

**DIOXYGEN ACTIVATION BY TRISPYRAZOLYLBORATE-SUPPORTED,
MONOVALENT NICKEL COMPLEXES AND ASSOCIATED REACTIVITY**

by

William L. Green

A dissertation submitted to the Faculty of the University of Delaware in partial fulfillment of the requirements for the degree of Doctor of Philosophy in Chemistry and Biochemistry

Summer 2016

© William L. Green
All Rights Reserved

ProQuest Number: 10156575

All rights reserved

INFORMATION TO ALL USERS

The quality of this reproduction is dependent upon the quality of the copy submitted.

In the unlikely event that the author did not send a complete manuscript and there are missing pages, these will be noted. Also, if material had to be removed, a note will indicate the deletion.



ProQuest 10156575

Published by ProQuest LLC (2016). Copyright of the Dissertation is held by the Author.

All rights reserved.

This work is protected against unauthorized copying under Title 17, United States Code
Microform Edition © ProQuest LLC.

ProQuest LLC.
789 East Eisenhower Parkway
P.O. Box 1346
Ann Arbor, MI 48106 - 1346

**DIOXYGEN ACTIVATION BY TRISPYRAZOLYLBORATE-SUPPORTED,
MONOVALENT NICKEL COMPLEXES AND ASSOCIATED REACTIVITY**

by

William L. Green

Approved: _____

Murray V. Johnston, Ph.D.
Chair of the Department of Chemistry and Biochemistry

Approved: _____

George H. Watson, Ph.D.
Dean of the College of Arts and Sciences

Approved: _____

Ann L. Ardis, Ph.D.
Senior Vice Provost for Graduate and Professional Education

I certify that I have read this dissertation and that in my opinion it meets the academic and professional standard required by the University as a dissertation for the degree of Doctor of Philosophy

Signed:

Charles G. Riordan, Ph.D.
Professor in charge of dissertation

I certify that I have read this dissertation and that in my opinion it meets the academic and professional standard required by the University as a dissertation for the degree of Doctor of Philosophy.

Signed:

Mary P. Watson, Ph.D.
Member of dissertation committee

I certify that I have read this dissertation and that in my opinion it meets the academic and professional standard required by the University as a dissertation for the degree of Doctor of Philosophy.

Signed:

Joel Rosenthal, Ph.D.
Member of dissertation committee

I certify that I have read this dissertation and that in my opinion it meets the academic and professional standard required by the University as a dissertation for the degree of Doctor of Philosophy.

Signed:

Robert Opila, Ph.D.
Member of dissertation committee

ACKNOWLEDGMENTS

The path of a chemistry graduate student is not an easy one to walk. It is a journey fraught with challenges both great and small, with no guarantee of success. Fortunately, it is also not a road which anyone is expected to walk alone. As I stand at the end of my own educational journey, I look back on the many years I have spent at UD and reflect on all of the people who have helped me to reach my destination.

There is no person to whom I owe more thanks than my advisor, Dr. Charles Riordan. His advice and encouragement have been absolutely invaluable. He has given me support whenever I needed it and repeatedly provided me with confidence when I couldn't find it for myself. He has been kind, thoughtful and endlessly patient through all my years in the Riordan lab. His mentorship has made me not only a better chemist, but a better person. I would also like to thank the members of my committee, Dr. Mary Watson, Dr. Joel Rosenthal and Dr. Robert Opila. Thank you all for your advice and suggestions, as well as for taking time out of your busy schedules to serve on my committee.

I want to thank all of the members of the Riordan lab, both current and former. The work I've done wouldn't have been possible without you. A special thank you to Molly Mock, Megan Shalaida, Yingxin Huang and Piyal Ariyananda who took time out of their own projects to teach me the finer points of wet chemistry. Thanks to Jess Wallick who was always there when I needed someone to talk to or bounce an idea off of. Thanks to Ann Ploskonka who has done beautiful work with the $Tp^{Ph,Me}$ complexes.

Thank you to everyone at UD who has provided instrumental or technical support/training. A huge thanks to Dr. Glenn P. A. Yap for X-ray crystallographic support. Thanks to Steve Bai for NMR training and help with day to day operations. Thanks to Jessie McAtee for LIFDI-MS support. A big thank you to Doug Nixon, Jim Draper and John Famiglietti (collectively, the Wizards in the Basement of Brown Lab) for technical support and repairs to everything from glassware to hot plates.

Lastly, I'd like to thank my family and friends. My parents deserve special mention for their tireless love and support. Thank you for always encouraging me to do my best and follow my dreams. Thanks to Dan Hess, A.J. Antonelli, Tony Doleman and Eric Sirianni for making my graduate experience memorable both inside and outside of lab. Lastly, I thank my fiancée Ashley for never letting me give up and for lending me her strength whenever I needed it.

TABLE OF CONTENTS

LIST OF TABLES	xi
LIST OF FIGURES	xiii
ABSTRACT	xxi

Chapter

1	INTRODUCTION	1
1.1	Ni-Dioxygen Interactions in Biological Systems	1
1.2	Nickel Based Substrate Oxidation – Applications and Industrial Relevance	9
1.3	Synthetic Strategies for the Preparation of Nickel-Dioxygen Complexes	13
1.4	Stabilizing Metal-Dioxygen Adducts with Trispyrazolylborates.....	18
2	EXPERIMENTAL PROCEDURES	22
2.1	General Procedures.....	22
2.1.1	Materials	22
2.1.2	Physical Methods.....	22
2.2	Synthesis of Ni(II) Halide Precursor Complexes	24
2.2.1	$[\text{Tp}^{\text{tBu,Me}}]\text{NiBr}$	24
2.2.2	$[\text{Tp}^{\text{tBu,Ph}}]\text{Ti}$	24
2.2.3	$[\text{Tp}^{\text{tBu,Ph}}]\text{NiBr}$	25
2.2.4	$[\text{Tp}^{\text{Ph,Me}}]\text{NiI}$	27
2.3	Synthesis of $[\text{Tp}^{\text{tBu,Me}}]\text{Ni}(\text{OH})$	27
2.4	$[\text{Tp}^{\text{tBu,Me}}]\text{Ni}(\text{NO}_3)$	28
2.5	$[\text{Tp}^{\text{tBu,Me}}]\text{Ni}(\text{NO}_2)$	28
2.6	Synthesis of $[\text{Tp}^{\text{tBu,Me}}]\text{Ni}(\text{OO}t\text{Bu})$	29
2.7	Synthesis of Metallacycle.....	30
2.8	Synthesis of Monovalent Nickel Complexes	30
2.8.1	$[\text{Tp}^{\text{tBu,Me}}]\text{Ni}(\text{CN}t\text{Bu})$	30
2.8.2	$[\text{Tp}^{\text{tBu,Me}}]\text{Ni}(\text{CNCy})$	31

2.8.3	Synthesis of $[\text{Tp}^{\text{tBu,Me}}]\text{Ni}(\text{CO})$	32
2.8.4	Synthesis of $[\text{Tp}^{\text{tBu,Ph}}]\text{Ni}(\text{CN}t\text{Bu})$	32
2.8.5	Synthesis of $[\text{Tp}^{\text{Ph,Me}}]\text{Ni}(\text{PPh}_3)$	33
2.8.6	Synthesis of $[\text{Tp}^{\text{Ph,Me}}]\text{Ni}(\text{CO})$	34
2.9	Synthesis of Carbamate Complexes, $[\text{Tp}^{\text{tBu,Me}}]\text{Ni}(\text{O}_2\text{CN}(\text{H})\text{R})$, R = <i>t</i> Bu, Cy.....	35
2.9.1	$[\text{Tp}^{\text{tBu,Me}}]\text{Ni}(\text{O}_2\text{CN}(\text{H})t\text{Bu})$	35
2.9.2	$[\text{Tp}^{\text{tBu,Me}}]\text{Ni}(\text{O}_2\text{CN}(\text{H})\text{Cy})$	35
2.10	Reaction of Monovalent Nickel Complexes with Dioxygen.....	36
2.10.1	$[\text{Tp}^{\text{tBu,Me}}]\text{Ni}(\text{O}_2)$	36
2.10.2	$[\text{Tp}^{\text{tBu,Ph}}]\text{Ni}(\text{O}_2)$	37
2.10.3	$[\text{Tp}^{\text{Ph,Me}}]\text{Ni}(\text{O}_2)$	38
2.11	O-Atom Transfer by $[\text{Tp}^{\text{tBu,Me}}]\text{Ni}(\text{O}_2)$	38
2.11.1	Reaction of $[\text{Tp}^{\text{tBu,Me}}]\text{Ni}(\text{O}_2)$ with PR_3 (R = Me, Et, Cy).....	38
2.11.1.1	Reaction of $[\text{Tp}^{\text{tBu,Me}}]\text{Ni}(\text{O}_2)$ with PMe_3 (Stoichiometric).....	38
2.11.1.2	Reaction of $[\text{Tp}^{\text{tBu,Me}}]\text{Ni}(\text{O}_2)$ with PEt_3	39
2.11.1.3	Reaction of $[\text{Tp}^{\text{tBu,Me}}]\text{Ni}(\text{O}_2)$ with PCy_3	39
2.11.1.4	Reaction of $[\text{Tp}^{\text{tBu,Me}}]\text{Ni}(\text{O}_2)$ with excess PMe_3	40
2.11.1.5	Reaction of $[\text{Tp}^{\text{tBu,Me}}]\text{Ni}(\text{O}_2)$ with excess PMe_3 and <i>t</i> - BuNC: Monovalent Trapping Experiment.....	40
2.11.1.6	Reaction of $[\text{Tp}^{\text{tBu,Me}}]\text{Ni}(\text{O}_2)$ with excess PMe_3 and excess O_2	41
2.11.2	Reaction of $[\text{Tp}^{\text{tBu,Me}}]\text{Ni}(\text{O}_2)$ with NO.....	42
2.11.3	Reaction of $[\text{Tp}^{\text{tBu,Me}}]\text{Ni}(\text{O}_2)$ with $[\text{Tp}^{\text{tBu,Me}}]\text{Ni}(\text{CN}t\text{Bu})$	43
2.12	C-H Activation by $[\text{Tp}^{\text{tBu,Me}}]\text{Ni}(\text{O}_2)$	43
2.12.1	Reaction of $[\text{Tp}^{\text{tBu,Me}}]\text{Ni}(\text{O}_2)$ with 1,4-cyclohexadiene (CHD)...	43
2.12.2	Reaction of $[\text{Tp}^{\text{tBu,Me}}]\text{Ni}(\text{O}_2)$ with 9,10-dihydroanthracene (DHA).....	44
2.12.3	Kinetic Studies of the Reaction $[\text{Tp}^{\text{tBu,Me}}]\text{Ni}(\text{O}_2)$ with DHA.....	45
2.12.4	Reaction of $[\text{Tp}^{\text{tBu,Me}}]\text{Ni}(\text{O}_2)$ with 9,10-dihydroxy-9,10- dihydroanthracene.....	46
2.12.5	Reaction of $[\text{Tp}^{\text{tBu,Me}}]\text{Ni}(\text{O}_2)$ with Xanthene.....	46
2.12.6	Reaction of $[\text{Tp}^{\text{tBu,Me}}]\text{Ni}(\text{O}_2)$ with 9-hydroxyxanthene.....	47

2.12.7	Reaction of $[\text{Tp}^{\text{tBu,Me}}]\text{Ni}(\text{O}_2)$ with 2-Phenylpropionaldehyde.....	48
2.13	X-Ray Crystallography.....	48
2.13.1	X-ray Structural Solution and Refinement	48
2.13.2	Crystallographic Data Collection and Structure Determination..	49
2.13.2.1	$[\text{Tp}^{\text{tBu,Me}}]\text{NiBr}$	49
2.13.2.2	$[\text{Tp}^{\text{tBu,Ph}}]\text{NiBr}$	49
2.13.2.3	$[\text{Tp}^{\text{tBu,Me}}]\text{Ni}(\text{OH})$	50
2.13.2.4	$[\text{Tp}^{\text{tBu,Me}}]\text{Ni}(\text{OO}t\text{Bu})$	50
2.13.2.5	Metallacycle	50
2.13.2.6	$[\text{Tp}^{\text{tBu,Me}}]\text{Ni}(\text{CN}t\text{Bu})$	50
2.13.2.7	$[\text{Tp}^{\text{tBu,Me}}]\text{Ni}(\text{CNCy})$	51
2.13.2.8	$[\text{Tp}^{\text{tBu,Ph}}]\text{Ni}(\text{CN}t\text{Bu})$	51
2.13.2.9	$[\text{Tp}^{\text{Ph,Me}}]\text{Ni}(\text{PPh}_3)$	51
2.13.2.10	$[\text{Tp}^{\text{Ph,Me}}]\text{Ni}(\text{CO})$	51
2.13.2.11	$[\text{Tp}^{\text{tBu,Me}}]\text{Ni}(\text{O}_2\text{CN}(\text{H})t\text{Bu})$	52
2.13.2.12	$[\text{Tp}^{\text{tBu,Me}}]\text{Ni}(\text{O}_2\text{CN}(\text{H})\text{Cy})$	52
2.13.2.13	$[\text{Tp}^{\text{tBu,Me}}]\text{Ni}(\text{O}_2)$	52
2.13.2.14	$[\text{Tp}^{\text{tBu,Ph}}]\text{Ni}(\text{O}_2)$	52
2.13.2.15	$[\text{Tp}^{\text{Ph,Me}}]\text{Ni}(\text{O}_2)$	53
2.13.2.16	$[\text{Tp}^{\text{tBu,Me}}]\text{Ni}(\text{NO}_2)$	53
2.13.2.17	$[\text{Tp}^{\text{tBu,Me}}]\text{Ni}(\text{NO}_3)$	53
3	SYNTHESIS, CHARACTERIZATION AND REACTIVITY OF TRISPYRAZOLYLBORATE SUPPORTED MONOVALENT NICKEL COMPLEXES	63
3.1	Introduction	63
3.2	$[\text{Tp}^{\text{tBu,Me}}]$ and $[\text{Tp}^{\text{tBu,Ph}}]$ Supported Monovalent Nickel Complexes	64
3.2.1	Synthesis and Structure of $[\text{Tp}^{\text{tBu,Me}}]\text{Ni}(\text{CN}t\text{Bu})$, $[\text{Tp}^{\text{tBu,Me}}]\text{Ni}(\text{CNCy})$, $[\text{Tp}^{\text{tBu,Me}}]\text{Ni}(\text{CO})$ and $[\text{Tp}^{\text{tBu,Ph}}]\text{Ni}(\text{CN}t\text{Bu})$	65
3.2.2	Molecular Structure of $[\text{Tp}^{\text{tBu,Me}}]\text{Ni}(\text{CN}t\text{Bu})$, $[\text{Tp}^{\text{tBu,Me}}]\text{Ni}(\text{CNCy})$ and $[\text{Tp}^{\text{tBu,Ph}}]\text{Ni}(\text{CN}t\text{Bu})$	72
3.2.2.1	^1H NMR Spectral Analysis.....	73
3.2.2.2	FT-IR Spectral Analysis.	74
3.2.3	Reactivity of $[\text{Tp}^{\text{tBu,Me}}]\text{Ni}(\text{CNR})$ with PhIO, R = <i>tert</i> -Bu, Cy.....	77

3.2.3.1	Synthesis of $[\text{Tp}^{\text{tBu,Me}}]\text{Ni}(\text{O}_2\text{CN}(\text{H})\text{R})$, $\text{R} = \text{tert-Bu, Cy}$	77
3.2.3.2	Structure, Alternative Synthesis and Mechanistic Implications.	82
3.3	$[\text{Tp}^{\text{Ph,Me}}]$ -Supported Monovalent Complexes	86
3.3.1	Synthesis and Structure of $[\text{Tp}^{\text{Ph,Me}}]\text{Ni}(\text{PPh}_3)$ and $[\text{Tp}^{\text{Ph,Me}}]\text{Ni}(\text{CO})$	89
3.3.2	Molecular Structures of $[\text{Tp}^{\text{Ph,Me}}]\text{Ni}(\text{PPh}_3)$ and $[\text{Tp}^{\text{Ph,Me}}]\text{Ni}(\text{CO})$	94
3.3.3	Proton NMR and FT-IR Spectral Analysis of $[\text{Tp}^{\text{Ph,Me}}]\text{Ni}(\text{PPh}_3)$ and $[\text{Tp}^{\text{Ph,Me}}]\text{Ni}(\text{CO})$	95
3.3.3.1	^1H NMR Spectral Analysis.....	95
3.3.3.2	FT-IR Spectral Analysis.	95
3.4	Summary.....	97
4	SYNTHESIS AND CHARACTERIZATION OF TRISPYRAZOLYLBORATE SUPPORTED SUPEROXONICKEL COMPLEXES	99
4.1	Introduction	99
4.2	Synthesis and Structure of $[\text{Tp}^{\text{tBu,R}}]\text{Ni}(\text{O}_2)$, $\text{R} = \text{Me, Ph}$	100
4.3	Molecular Structure of $[\text{Tp}^{\text{tBu,R}}]\text{Ni}(\text{O}_2)$, $\text{R} = \text{Me, Ph}$	105
4.4	^1H NMR, FT-IR, Electronic Absorption and L-Edge XAS Analysis of $[\text{Tp}^{\text{tBu,R}}]\text{Ni}(\text{O}_2)$, $\text{R} = \text{Me, Ph}$	107
4.4.1	^1H NMR Spectral Analysis.....	107
4.4.2	Electronic Absorption Analysis.....	109
4.4.3	FT-IR Analysis.	110
4.4.4	L-Edge X-ray Absorption Spectroscopy Analysis.	111
4.5	Thermal Stability of $[\text{Tp}^{\text{tBu,Me}}]\text{Ni}(\text{O}_2)$	113
4.6	Synthesis and Structure of $[\text{Tp}^{\text{Ph,Me}}]\text{Ni}(\text{O}_2)$	115
4.7	Molecular Structure of $[\text{Tp}^{\text{Ph,Me}}]\text{Ni}(\text{O}_2)$	119
4.8	Proton NMR, FT-IR and Electronic Absorption Analysis of $[\text{Tp}^{\text{Ph,Me}}]\text{Ni}(\text{O}_2)$	120
4.8.1	^1H NMR Analysis.....	120
4.8.2	Electronic Absorption Analysis.....	120
4.8.3	FT-IR Analysis	121

4.9	Summary.....	123
5	OXYGEN ATOM TRANSFER, C-H ACTIVATION AND ALDEHYDE DEFORMYLATION BY [Tp ^{tBu,Me}]Ni(O ₂).....	125
5.1	Introduction	125
5.2	Oxygen Atom Transfer by [Tp ^{tBu,Me}]Ni(O ₂)	125
5.2.1	Reaction of [Tp ^{tBu,Me}]Ni(O ₂) with PR ₃ (R = Me, Et, Cy)	125
5.2.2	Stoichiometric Reactions with Phosphines	126
5.2.3	Nickel Products of Phosphine Oxidation	127
5.2.4	Reaction of [Tp ^{tBu,Me}]Ni(O ₂) with NO	141
5.3	C-H Activation by [Tp ^{tBu,Me}]Ni(O ₂).....	144
5.3.1	Reaction of [Tp ^{tBu,Me}]Ni(O ₂) with 1,4-cyclohexadiene (CHD).	144
5.3.2	Independent Preparation of [Tp ^{tBu,Me}]Ni(OOH)	149
5.3.3	Preparation and Thermal Decomposition of [Tp ^{tBu,Me}]Ni(OO ^t Bu)	153
5.3.4	Reaction of [Tp ^{tBu,Me}]NiO ₂ with DHA	158
5.3.4.1	Mechanistic Insights into the Reaction of [Tp ^{tBu,Me}]NiO ₂ with DHA.....	161
5.3.4.2	Kinetic Study of the Reaction of [Tp ^{tBu,Me}]Ni(O ₂) with DHA	169
5.3.5	Reaction of [Tp ^{tBu,Me}]Ni(O ₂) with Xanthene.....	174
5.3.5.1	Mechanistic Analysis and Comparisons to DHA	176
5.4	Reaction of [Tp ^{tBu,Me}]Ni(O ₂) with 2-Phenylpropionaldehyde - Aldehyde Deformylation.....	181
5.5	Summary.....	189
	REFERENCES	192
	Appendix	
A	CHECK CIF FILES.....	200
B	PERMISSION FOR JOURNAL ARTICLE REPRINT.....	246

LIST OF TABLES

Table 2.1	Extent of oxygen atom transfer in reactions with excess PMe_3	40
Table 2.2	Extent of oxygen atom transfer in reactions with excess PMe_3 and excess O_2	42
Table 2.3	9,10-anthraquinone yield (AQ) versus reaction stoichiometry.	45
Table 2.4	Xanthone yield versus reaction stoichiometry.	47
Table 2.5	Crystallographic data for $[\text{Tp}^{\text{tBu,Me}}]\text{NiBr}$ and $[\text{Tp}^{\text{tBu,Ph}}]\text{NiBr}$	54
Table 2.6	Crystallographic data for $[\text{Tp}^{\text{tBu,Me}}]\text{Ni(OH)}$ and $[\text{Tp}^{\text{tBu,Me}}]\text{Ni(OOtBu)}$. ..	55
Table 2.7	Crystallographic data for Metallacycle and $[\text{Tp}^{\text{tBu,Me}}]\text{Ni(CN}t\text{Bu)}$	56
Table 2.8	Crystallographic data for $[\text{Tp}^{\text{tBu,Me}}]\text{Ni(NO}_2)$ and $[\text{Tp}^{\text{tBu,Me}}]\text{Ni(NO}_3)$	57
Table 2.9	Crystallographic data for $[\text{Tp}^{\text{tBu,Ph}}]\text{Ni(CN}t\text{Bu)}$ and $[\text{Tp}^{\text{Ph,Me}}]\text{Ni(PPh}_3)$...	58
Table 2.10	Crystallographic data for $[\text{Tp}^{\text{Ph,Me}}]\text{Ni(CO)}$ and $[\text{Tp}^{\text{tBu,Me}}]\text{Ni(O}_2\text{CN(H)}t\text{Bu)}$	59
Table 2.11	Crystallographic data for $[\text{Tp}^{\text{tBu,Me}}]\text{Ni(O}_2\text{CN(H)Cy)}$ and $[\text{Tp}^{\text{tBu,Me}}]\text{Ni(O}_2)$	60
Table 2.12	Crystallographic data for $[\text{Tp}^{\text{tBu,Ph}}]\text{Ni(O}_2)$ and $[\text{Tp}^{\text{Ph,Me}}]\text{Ni(O}_2)$	61
Table 2.13	Crystallographic data for $[\text{Tp}^{\text{tBu,Me}}]\text{Ni(CNCy)}$	62
Table 3.1	Selected bond lengths (\AA) for $[\text{Tp}^{\text{tBu,Me}}]\text{Ni(CN}t\text{Bu)}$, $[\text{Tp}^{\text{tBu,Me}}]\text{Ni(CNCy)}$, $[\text{Tp}^{\text{tBu,Ph}}]\text{Ni(CN}t\text{Bu)}$	72
Table 3.2	Selected bond angles (\AA) and τ values for $[\text{Tp}^{\text{tBu,Me}}]\text{Ni(CN}t\text{Bu)}$, $[\text{Tp}^{\text{tBu,Me}}]\text{Ni(CNCy)}$, $[\text{Tp}^{\text{tBu,Me}}]\text{Ni(CO)}$ and $[\text{Tp}^{\text{tBu,Ph}}]\text{Ni(CN}t\text{Bu)}$	72
Table 3.3	Selected ^1H NMR spectral features for $[\text{Tp}^{\text{tBu,Me}}]\text{Ni(CN}t\text{Bu)}$, $[\text{Tp}^{\text{tBu,Me}}]\text{Ni(CNCy)}$, $[\text{Tp}^{\text{tBu,Me}}]\text{Ni(CO)}$ and $[\text{Tp}^{\text{tBu,Ph}}]\text{Ni(CN}t\text{Bu)}$	76

Table 3.4	Selected FT-IR stretching frequencies for [Tp ^{tBu,Me}]Ni(CN <i>t</i> Bu), [Tp ^{tBu,Me}]Ni(CNCy), [Tp ^{tBu,Me}]Ni(CO) and [Tp ^{tBu,Ph}]Ni(CN <i>t</i> Bu).	77
Table 3.5	Selected bond lengths (Å) for [Tp ^{tBu,Me}]Ni(O ₂ CN(H) <i>t</i> Bu) and [Tp ^{tBu,Me}]Ni(O ₂ CN(H)Cy).	81
Table 3.6	Selected bond angles (Å) and τ values for [Tp ^{tBu,Me}]Ni(O ₂ CN(H) <i>t</i> Bu) and [Tp ^{tBu,Me}]Ni(O ₂ CN(H)Cy).	82
Table 3.7	Selected bond lengths, bond angles and τ values for [Tp ^{Ph,Me}]Ni(CO) and [Tp ^{Ph,Me}]Ni(PPh ₃).	94
Table 3.8	Selected ¹ H NMR spectral features for [Tp ^{Ph,Me}]Ni(CO) and [Tp ^{Ph,Me}]Ni(PPh ₃).	97
Table 4.1	Selected bond distances (Å) for [Tp ^{tBu,Me}]Ni(O ₂) and [Tp ^{tBu,Ph}]Ni(O ₂).	104
Table 4.2	Selected bond angles (°) for [Tp ^{tBu,Me}]Ni(O ₂) and [Tp ^{tBu,Ph}]Ni(O ₂).	104
Table 4.3	Selected bond distances (Å) and bond angles (°) for [Tp ^{Ph,Me}]Ni(O ₂). ..	119
Table 5.1	DHA yield versus reaction stoichiometry. #	160
Table 5.2	2 nd order rate constant, kinetic isotope effect and Eyring parameters from the reaction of [Tp ^{tBu,Me}]Ni(O ₂) with DHA.	172
Table 5.3	Xanthone yield versus reaction stoichiometry. #	175

LIST OF FIGURES

Figure 1.1	Transformation of 1,2-dihydroxy-3-keto-5-(methylthio)pentene by Fe-ARD (top) and Ni-ARD (bottom).	3
Figure 1.2	The active site of Ni containing acireductone dioxygenase (Ni-ARD). Adapted with permission, from Figure S1, Ragsdale, S. W. <i>The Journal of Biological Chemistry</i> . 2009 , 284, 18571, under the terms of the CC-BY license, http://creativecommons.org/licenses/by/4.0/legalcode	4
Figure 1.3	Transformation of quercetin by Ni-QED.	5
Figure 1.4	Mechanism of Nickel Superoxide Dismutase.	8
Figure 1.5	Examples of olefin epoxidation with divalent nickel complexes. ²⁰	10
Figure 1.6	Proposed mechanism of olefin epoxidation with nickel(II) complex and iodosylbenzene.	11
Figure 1.7	Synthetic metalloprotein cleaves DNA at the indicated sites (Top and Right). Nickel(II) macrocycles facilitate conversion of supercoiled plasmid to nicked, circular form (Bottom, Left). Images adapted with permission from Mack, D. P.; Dervan, P. B. <i>J. Am. Chem. Soc.</i> , 1990 , 112, 4604 and Morrow, J. R.; Kolasa, K. A. <i>Inorg. Chim. Acta</i> , 1992 , 195, 245 respectively	13
Figure 1.8	Preparation of the bis- μ -oxo dinickel complex, $[\text{Tp}^{\text{Me}_3}]_2\text{Ni}(\mu\text{-O})_2\text{Ni}[\text{Tp}^{\text{Me}_3}]$	15
Figure 1.9	Preparation of $[(\text{PhTt}^{\text{iBu}})\text{Ni}]_2(\mu\text{-O})_2$ and $[\text{PhTt}^{\text{Ad}}]\text{Ni}(\text{O}_2)$ from their monovalent precursors.	17
Figure 1.10	Preparation of Driess' nickel-superoxo complex, $[\text{Ni}^{\text{II}}(\beta\text{-diketiminato})(\text{O}_2)]$	18
Figure 1.11	General two dimensional structure of a trispyrazolylborate ligand. Substituents at the 3, 4 and 5 positions of the pyrazole ring can be used to tune steric and electronic properties.	20

Figure 1.12	Bridging the Dioxygen Adduct Gap: Copper and cobalt dioxygen adducts supported by the Tp ligand system have been prepared and fully characterized.	21
Figure 2.1	^1H NMR spectrum of crude $[\text{Tp}^{\text{tBu,Ph}}]\text{NiBr}$. * indicates residual solvent signals. ♣ indicates major isomer. # indicates minor isomer. Inset shows diamagnetic region.	26
Figure 3.1	Synthesis of $[\text{Tp}^{\text{tBu,Me}}]\text{Ni}(\text{CNR})$ complexes.	68
Figure 3.2	Illustration of $[\text{Tp}^{\text{tBu,Me}}]\text{Ni}(\text{CNR})$ preparation and isolation procedure. .	68
Figure 3.3	Synthesis of $[\text{Tp}^{\text{tBu,Me}}]\text{Ni}(\text{CO})$	68
Figure 3.4	Thermal ellipsoid diagram of $[\text{Tp}^{\text{tBu,Me}}]\text{Ni}(\text{CN}t\text{Bu})$ with atom labeling. Thermal ellipsoids are drawn to 30% probability. Hydrogen atoms are omitted for clarity with the exception of B-H.	69
Figure 3.5	Thermal ellipsoid diagram of $[\text{Tp}^{\text{tBu,Me}}]\text{Ni}(\text{CNCy})$ with atom labeling. Thermal ellipsoids are drawn to 30% probability. Hydrogen atoms are omitted for clarity with the exception of B-H.	70
Figure 3.6	Thermal ellipsoid diagram of $[\text{Tp}^{\text{tBu,Ph}}]\text{Ni}(\text{CN}t\text{Bu})$ with atom labeling. Thermal ellipsoids are drawn to 30% probability. Hydrogen atoms are omitted for clarity with the exception of B-H.	71
Figure 3.7	^1H NMR spectrum of $[\text{Tp}^{\text{tBu,Me}}]\text{Ni}(\text{CN}t\text{Bu})$. * indicates residual solvent signals and silicone grease.	76
Figure 3.8	Synthesis of $[\text{Tp}^{\text{tBu,Me}}]\text{Ni}(\text{O}_2\text{CN}(\text{H})\text{R})$ from $[\text{Tp}^{\text{tBu,Me}}]\text{Ni}(\text{CNR})$ and PhIO.	78
Figure 3.9	Thermal ellipsoid diagram of $[\text{Tp}^{\text{tBu,Me}}]\text{Ni}(\text{O}_2\text{CN}(\text{H})t\text{Bu})$ with atom labeling. Thermal ellipsoids are drawn to 30% probability. Hydrogen atoms are omitted for clarity with the exception of B-H and N-H.	79
Figure 3.10	Thermal ellipsoid diagram of $[\text{Tp}^{\text{tBu,Me}}]\text{Ni}(\text{O}_2\text{CN}(\text{H})\text{Cy})$ with atom labeling. Both molecules in the asymmetric unit are shown highlighting the intermolecular N—H—O bonds. Thermal ellipsoids are drawn to 30% probability. Hydrogen atoms are omitted for clarity with the exception of B-H and N-H.	80
Figure 3.11	Proposed mechanism for formation of Ni(II) carbamates upon treatment of $[\text{Tp}^{\text{tBu,Me}}]\text{Ni}(\text{CNR})$ with iodosylbenzene.	85

Figure 3.12	Alternative Synthesis of $[\text{Tp}^{\text{tBu,Me}}]\text{Ni}(\text{O}_2\text{CN}(\text{H})\text{R})$, $\text{R} = t\text{-Bu, Cy}$	86
Figure 3.13	Synthesis of $[\text{Tp}^{\text{Ph,Me}}]\text{Ni}(\text{PPh}_3)$	91
Figure 3.14	Synthesis of $[\text{Tp}^{\text{Ph,Me}}]\text{Ni}(\text{CO})$	91
Figure 3.15	Thermal ellipsoid diagram of $[\text{Tp}^{\text{Ph,Me}}]\text{Ni}(\text{PPh}_3)$ with atom labeling. Thermal ellipsoids are drawn to 30% probability. Hydrogen atoms are omitted for clarity with the exception of B-H.	92
Figure 3.16	Thermal ellipsoid diagram of $[\text{Tp}^{\text{Ph,Me}}]\text{Ni}(\text{CO})$ with atom labeling. Thermal ellipsoids are drawn to 30% probability. Hydrogen atoms are omitted for clarity with the exception of B-H.	93
Figure 3.17	^1H NMR spectrum of $[\text{Tp}^{\text{Ph,Me}}]\text{Ni}(\text{CO})$. * indicates residual solvent signals.	96
Figure 4.1	Synthesis of $[\text{Tp}^{\text{tBu,Me}}]\text{Ni}(\text{O}_2)$	101
Figure 4.2	Thermal ellipsoid diagram of $[\text{Tp}^{\text{tBu,Me}}]\text{Ni}(\text{O}_2)$ with atom labeling. Thermal ellipsoids are drawn to 30% probability. Hydrogen atoms are omitted for clarity with the exception of B-H. Positional disorder in the O_2 moiety is not depicted.	102
Figure 4.3	Thermal ellipsoid diagram of $[\text{Tp}^{\text{tBu,Ph}}]\text{Ni}(\text{O}_2)$ with atom labeling. Thermal ellipsoids are drawn to 30% probability. Hydrogen atoms are omitted for clarity with the exception of B-H.	103
Figure 4.4	Plot of oxygen-oxygen bond length versus stretching frequency for a number of reported metal-dioxygen adducts (Adapted from Rheingold et al., <i>Proc. Nat. Acad. Sci.</i> 2003 , <i>100</i> , 3635). ⁷³ Positions for $[\text{Tp}^{\text{tBu,Me}}]\text{Ni}(\text{O}_2)$ and $[\text{Tp}^{\text{tBu,Ph}}]\text{Ni}(\text{O}_2)$ have been superimposed in pink.	107
Figure 4.5	^1H NMR spectrum of $[\text{Tp}^{\text{tBu,Me}}]\text{Ni}(\text{O}_2)$. * Indicates residual solvent features.	108
Figure 4.6	Electronic absorption spectrum of $[\text{Tp}^{\text{tBu,Me}}]\text{Ni}(\text{O}_2)$ recorded in CHCl_3	109
Figure 4.7	FT-IR comparison of $\nu_{\text{O-O}}$ and $\nu_{\text{Ni-O}}$ for ^{16}O and ^{18}O isotopomers of $[\text{Tp}^{\text{tBu,Me}}]\text{Ni}(\text{O}_2)$	111

Figure 4.8	L-Edge XAS spectrum of $[\text{Tp}^{\text{tBu,Me}}]\text{Ni}(\text{O}_2)$. The spectrum of the Ni(II) reference material, $\text{Ni}[\text{Me}_4[12]\text{aneN}_4](\text{OTf})_2$, is overlaid for comparison.	113
Figure 4.9	^1H NMR study of $[\text{Tp}^{\text{tBu,Me}}]\text{Ni}(\text{O}_2)$ thermal stability over short time courses.	115
Figure 4.10	Synthesis of $[\text{Tp}^{\text{Ph,Me}}]\text{Ni}(\text{O}_2)$	118
Figure 4.11	Thermal ellipsoid diagram of $[\text{Tp}^{\text{Ph,Me}}]\text{Ni}(\text{O}_2)$ with atom labeling. Thermal ellipsoids are drawn to 30% probability. Hydrogen atoms are omitted for clarity with the exception of B–H. Only one orientation of the positionally disordered O_2 moiety is depicted.	118
Figure 4.12	^1H NMR spectrum of $[\text{Tp}^{\text{Ph,Me}}]\text{Ni}(\text{O}_2)$	122
Figure 4.13	UV-visible spectrum of $[\text{Tp}^{\text{Ph,Me}}]\text{Ni}(\text{O}_2)$ recorded in CHCl_3	122
Figure 5.1	Reaction of $[\text{Tp}^{\text{tBu,Me}}]\text{Ni}(\text{O}_2)$ with stoichiometric phosphine. *Reaction with PCy_3 was run at 55 °C.	134
Figure 5.2	$^{31}\text{P}\{^1\text{H}\}$ NMR spectrum of reaction mixture of 2 with PMe_3 after 24 hr. Inset: PMe_3 stock solution (control).	134
Figure 5.3	$^{31}\text{P}\{^1\text{H}\}$ NMR spectrum of reaction mixture of 2 with PEt_3 after 24 hr. Inset: PEt_3 stock solution (internal 85% aqueous H_3PO_4 , $\delta = 0$).	135
Figure 5.4	$^{31}\text{P}\{^1\text{H}\}$ NMR spectrum of reaction mixture of 2 with PCy_3 after 24 hours at 55 °C. Inset shows PCy_3 stock solution (internal 85% aqueous H_3PO_4 , $\delta = 0$).	136
Figure 5.5	^1H NMR spectral comparison of independently prepared $[\text{Tp}^{\text{tBu,Me}}]\text{Ni}(\text{OH})$ (top, green), metallacycle (middle, red) and residue from reaction of $[\text{Tp}^{\text{tBu,Me}}]\text{Ni}(\text{O}_2)$ with PMe_3 (bottom, blue).	137
Figure 5.6	Thermal ellipsoid diagram of $[\text{Tp}^{\text{tBu,Me}}]\text{Ni}(\text{OH})$ with atom labeling. Thermal ellipsoids are drawn to 30% probability. Hydrogen atoms are omitted for clarity with the exception of B–H and O–H.	137
Figure 5.7	Proposed mechanism for formation of $[\text{Tp}^{\text{tBu,Me}}]\text{Ni}(\text{OH})$ in reaction of $[\text{Tp}^{\text{tBu,Me}}]\text{Ni}(\text{O}_2)$ with 1 equiv. of phosphine.	138

Figure 5.8	Thermal ellipsoid diagram of metallacycle with atom labeling. Thermal ellipsoids are drawn to 30% probability. Hydrogen atoms are omitted for clarity with the exception of B–H. The <i>tert</i> -butyl groups were located disordered in two positions and treated to restraints based on non-crystallographic symmetry.....	138
Figure 5.9	¹ H NMR spectrum of independently prepared metallacycle with activated and unactivated <i>tert</i> -butyl pyrazole features labeled. Molecular structure is inset for reference.....	139
Figure 5.10	¹ H NMR spectral comparison of: A) Independently prepared [Tp ^{tBu,Me}]Ni(CN <i>t</i> Bu). B) Pentane extract of residue from reaction of [Tp ^{tBu,Me}]Ni(O ₂) with PMe ₃ in the presence of <i>t</i> BuCN purified via silica gel plug chromatography. C. Crude reaction residue.	139
Figure 5.11	Proposed mechanism for sequential O-atom transfer in reaction of [Tp ^{tBu,Me}]Ni(O ₂) and excess PMe ₃ with and without <i>t</i> BuNC as a trapping agent.....	140
Figure 5.12	¹ H NMR spectral comparison of nickel products resulting from reaction of [Tp ^{tBu,Me}]Ni(O ₂) with PMe ₃ (top, red), PEt ₃ and PCy ₃ . The ratio of metallacycle to [Tp ^{tBu,Me}]Ni(OH) increases with the increasing steric bulk of the phosphine.....	141
Figure 5.13	Reaction of [Tp ^{tBu,Me}]Ni(O ₂) with NO.....	143
Figure 5.14	¹ H NMR spectral comparison of: A) Independently prepared [Tp ^{tBu,Me}]Ni(NO ₂). B) Independently prepared [Tp ^{tBu,Me}]Ni(NO ₃). C) Residue from reaction of [Tp ^{tBu,Me}]Ni(O ₂) with NO.....	143
Figure 5.15	Possible mechanism for formation of [Tp ^{tBu,Me}]Ni(NO ₂) and [Tp ^{tBu,Me}]Ni(NO ₃) in the reaction of [Tp ^{tBu,Me}]Ni(O ₂) with NO.....	144
Figure 5.16	¹ H NMR spectral comparison of: A) 1,4-cyclohexadiene solution before addition of [Tp ^{tBu,Me}]Ni(O ₂). B) 1,4-cyclohexadiene solution after reaction.....	147
Figure 5.17	¹ H NMR spectral comparison of: A) Independently prepared [Tp ^{tBu,Me}]Ni(OH). B) Independently prepared metallacycle. C) Crude residue from reaction of [Tp ^{tBu,Me}]Ni(O ₂) and 1,4-cyclohexadiene.....	147
Figure 5.18	Reaction of [Tp ^{tBu,Me}]Ni(O ₂) with 1,4-cyclohexadiene.....	148

- Figure 5.19** Proposed mechanism for the reaction of $[\text{Tp}^{\text{tBu,Me}}]\text{Ni}(\text{O}_2)$ with 1,4-cyclohexadiene. Abstraction of an H atom from the ligand t-Bu group by hydroxyl radical results in the formation of the major product, metallacycle. Hydroxyl radical escape generates of the minor product, $[\text{Tp}^{\text{tBu,Me}}]\text{Ni}(\text{OH})$ 148
- Figure 5.20** Alternative mechanism for the reaction of $[\text{Tp}^{\text{tBu,Me}}]\text{Ni}(\text{O}_2)$ with 1,4-cyclohexadiene. Decomposition of $[\text{Tp}^{\text{tBu,Me}}]\text{Ni}(\text{OOH})$ proceeds through a transition state consisting of an extended ring structure. O–O and C–H bond breaking are concerted with O–H bond formation.... 149
- Figure 5.21** UV-Vis absorption analysis of the reaction $[\text{Tp}^{\text{tBu,Me}}]\text{Ni}(\text{OH})$ and H_2O_2 . Solid line: Intermediate produced upon addition of H_2O_2 to a solution of $[\text{Tp}^{\text{tBu,Me}}]\text{Ni}(\text{OH})$ in CH_2Cl_2 at $-55\text{ }^\circ\text{C}$ H_2O_2 . Dashed line: spectrum of solution after decomposition at room temperature. UV-Vis measurements and figure prepared by M. White.⁹³ 152
- Figure 5.22** ^1H NMR spectral comparison of: A) Independently prepared metallacycle. B) Independently prepared $[\text{Tp}^{\text{tBu,Me}}]\text{Ni}(\text{OH})$. C) Intermediate species produced upon treatment of $[\text{Tp}^{\text{tBu,Me}}]\text{Ni}(\text{OH})$ with H_2O_2 . For consistency, all spectra were collected at $-60\text{ }^\circ\text{C}$. Spectroscopic measurements performed by M. White under the supervision of W. Green. Figure prepared by W. Green..... 153
- Figure 5.23** Preparation of $[\text{Tp}^{\text{tBu,Me}}]\text{Ni}(\text{OOtBu})$ 155
- Figure 5.24** Mechanism for the thermal decomposition of $\text{Tp}^{\text{tBu,Me}}\text{Ni}(\text{OOtBu})$ 156
- Figure 5.25** ^1H NMR spectrum of $\text{Tp}^{\text{tBu,Me}}\text{Ni}(\text{OOtBu})$. Crystal structure is inset for reference. 156
- Figure 5.26** Thermal ellipsoid diagram of $[\text{Tp}^{\text{tBu,Me}}]\text{Ni}(\text{OOtBu})$ with atom labeling. Thermal ellipsoids are drawn to 30% probability. Hydrogen atoms are omitted for clarity with the exception of B–H. 157
- Figure 5.27** ^1H NMR spectral analysis of the thermal decomposition of $[\text{Tp}^{\text{tBu,Me}}]\text{Ni}(\text{OOtBu})$ with comparison to independently prepared products. 158
- Figure 5.28** ^1H NMR spectral analysis of organic products in the reaction of DHA with 2 equivalents of $[\text{Tp}^{\text{tBu,Me}}]\text{Ni}(\text{O}_2)$ 160
- Figure 5.29** ^1H NMR spectral analysis of nickel products in the reaction of DHA with 2 equivalents of $[\text{Tp}^{\text{tBu,Me}}]\text{Ni}(\text{O}_2)$ 161

Figure 5.30	¹ H NMR spectral comparison of organic products in the reaction of DHA with 2, 4 and 6 equivalents of [Tp ^{tBu,Me}]Ni(O ₂).	161
Figure 5.31	Proposed mechanism for the formation of 9,10-anthraquinone in the reaction of [Tp ^{tBu,Me}]Ni(O ₂) with 9,10-dihydroanthracene.	166
Figure 5.32	¹ H NMR spectral analysis of organic products in the reaction of 9,10-dihydroxy-9,10-dihydroanthracene with 2 equivalents of [Tp ^{tBu,Me}]Ni(O ₂).	167
Figure 5.33	¹ H NMR spectral analysis of nickel products in the reaction of 9,10-dihydroanthracene with 2 equivalents of [Tp ^{tBu,Me}]Ni(O ₂).	167
Figure 5.34	Proposed mechanism for the reaction of [Tp ^{tBu,Me}]Ni(O ₂) with 9,10-dihydroxy-9,10-dihydroanthracene.	168
Figure 5.35	Example of a typical kinetic run. Arrows indicate major absorbance changes. Red arrow indicates change at 505 nm which was the wavelength chosen for analysis in the kinetic study. Conditions in this run: [Tp ^{tBu,Me}]Ni(O ₂) at 2 mg/mL in toluene, 40 equivalents of DHA (156 mM), 45 °C.	170
Figure 5.36	Plot of k _{obs} vs [DHA] at 60 °C for the reaction of [Tp ^{tBu,Me}]Ni(O ₂) with DHA. DHA concentration was varied from 20 to 80 equivalents (78 – 311 mM) in 10 equivalent increments. The second order rate constant was derived from slope of the linear, least-squares fit of the data as indicated by the trend line. Data points shown are the average of triplicate kinetic runs. Error bars show the range of values obtained at each concentration.	171
Figure 5.37	Eyring plot of ln(k/T) vs. 1/T for the reaction of [Tp ^{tBu,Me}]Ni(O ₂) with DHA. All kinetics runs were conducted with an initial DHA concentration of 156 mM. Temperature was varied from 25 to 65 °C in 5 °C increments. Activation parameters, ΔH [‡] and ΔS [‡] , were derived from the slope and intercept, respectively, of the linear, least-squares fit of the data as indicated by the trend line. Data points shown are the average of triplicate kinetic runs. Error bars show the range of values obtained at each temperature.	172
Figure 5.38	¹ H NMR spectral analysis of organic products in the reaction of xanthene with 2 equivalents of [Tp ^{tBu,Me}]Ni(O ₂).	175
Figure 5.39	¹ H NMR spectral analysis of nickel products in the reaction of xanthene with 1 equivalent of [Tp ^{tBu,Me}]Ni(O ₂).	176

Figure 5.40	^1H NMR spectral comparison of organic products in the reaction of xanthene with 1, 2 and 3 equivalents of $[\text{Tp}^{\text{tBu,Me}}]\text{Ni}(\text{O}_2)$	176
Figure 5.41	^1H NMR spectral analysis of organic products in the reaction of 9-hydroxyxanthene with 1 equivalent of $[\text{Tp}^{\text{tBu,Me}}]\text{Ni}(\text{O}_2)$	179
Figure 5.42	^1H NMR spectral analysis of nickel products in the reaction of 9-hydroxyxanthene with 1 equivalent of $[\text{Tp}^{\text{tBu,Me}}]\text{Ni}(\text{O}_2)$	179
Figure 5.43	Proposed mechanism for the formation of xanthone in the reaction of $[\text{Tp}^{\text{tBu,Me}}]\text{Ni}(\text{O}_2)$ with xanthene.	180
Figure 5.44	Proposed mechanism for the reaction of $[\text{Tp}^{\text{tBu,Me}}]\text{Ni}(\text{O}_2)$ with 9-hydroxyxanthene. Note that the metallacycle is the only predicted nickel product.	181
Figure 5.45	Reaction of $[\text{Tp}^{\text{tBu,Me}}]\text{Ni}(\text{O}_2)$ with 2-PPA. Products boxed in blue have been confirmed. Product in red is suspected.	185
Figure 5.46	Excerpt from GC-MS spectrum of the reaction of $[\text{Tp}^{\text{tBu,Me}}]\text{Ni}(\text{O}_2)$ and 2-PPA showing production of acetophenone as well as residual 2-PPA. Peak identity was determined by spectral comparison to known compounds (see inset, right).....	186
Figure 5.47	^1H NMR spectral analysis of nickel products in the reaction of $[\text{Tp}^{\text{tBu,Me}}]\text{Ni}(\text{O}_2)$ and 2-PPA.	187
Figure 5.48	LIFDI-MS spectrum of the reaction of $[\text{Tp}^{\text{tBu,Me}}]\text{Ni}(\text{O}_2)$ and 2-PPA. Possible identities for major mass fragments are inset.....	187
Figure 5.49	Possible mechanism for the deformylation of 2 phenylpropionaldehyde by $[\text{Tp}^{\text{tBu,Me}}]\text{Ni}(\text{O}_2)$	188

ABSTRACT

The activation of dioxygen by transition metal complexes is an area of intense study due to the potentially invaluable synthetic utility such systems may provide. While a number of 1st row transition metals have been extensively investigated in this regard, the use of nickel to activate O₂ has seen considerably less development. The knowledge gap in this area is due in large part to the relatively small number of nickel systems known to display this type of reactivity as well as the even smaller number of stable, nickel-dioxygen adducts available for study.

This dissertation describes efforts towards the preparation of a new class of monovalent nickel complexes, supported by the trispyrazolylborate (Tp) ligand system, and the use of these complexes to facilitate dioxygen activation. The pursuit of this goal has led to the successful isolation and characterization of the first Tp supported monovalent nickel compounds. Furthermore, the study of these complexes has resulted in the discovery of numerous interesting derivative species including two superoxo-nickel complexes, [Tp^{tBu,Me}]Ni(O₂) and [Tp^{Ph,Me}]Ni(O₂). These new dioxygen adducts have been fully characterized and, in the case of [Tp^{tBu,Me}]Ni(O₂), have been extensively investigated with regard to potential avenues of reactivity.

Two trispyrazolylborate ligands with different steric and electronic environments were selected for study. The ligands chosen, Tp^{tBu,Me} and Tp^{Ph,Me}, were used to prepare divalent nickel complexes, which were then reduced in the presence of suitable trapping agents. These experiments resulted in the preparation of stable monovalent species including [Tp^{tBu,Me}]Ni(CN*t*Bu), [Tp^{tBu,Me}]Ni(CNCy),

$[\text{Tp}^{\text{tBu,Me}}]\text{Ni}(\text{CO})$, $[\text{Tp}^{\text{Ph,Me}}]\text{Ni}(\text{PPh}_3)$ and $[\text{Tp}^{\text{Ph,Me}}]\text{Ni}(\text{CO})$. All of these complexes have demonstrated the ability to activate dioxygen and, with the exception of $[\text{Tp}^{\text{Ph,Me}}]\text{Ni}(\text{PPh}_3)$, to yield dioxygen adducts amenable to structural characterization. In addition, the isonitrile trapped complexes were found to react with iodobenzene to generate nickel(II) carbamates. The putative mechanism of this transformation suggests the involvement of an oxo-nickel intermediate. Related studies also led to preparation of a monomeric nickel hydroxide complex, $[\text{Tp}^{\text{tBu,Me}}]\text{Ni}(\text{OH})$.

Treatment of $[\text{Tp}^{\text{tBu,Me}}]\text{Ni}(\text{CN}t\text{Bu})$ with dioxygen resulted in the isolation of a nickel- O_2 adduct, $[\text{Tp}^{\text{tBu,Me}}]\text{Ni}(\text{O}_2)$. This complex was characterized by ^1H NMR, FT-IR, elemental analysis, L-edge X-ray absorption spectroscopy and X-ray crystallography. Characterization led to the unequivocal assignment of the complex as nickel(II)-superoxide with the O_2 unit bound to nickel in a “side-on” fashion. The magnetic moment of the complex was determined to be $2.3(1) \mu_{\text{B}}$, indicating an $S = 1/2$ spin state. $[\text{Tp}^{\text{tBu,Me}}]\text{Ni}(\text{O}_2)$ is stable under ambient conditions, both in the solid state and in solution. In addition, the complex exhibits considerable resistance to thermally induced decomposition. A second superoxo-nickel complex, $[\text{Tp}^{\text{Ph,Me}}]\text{Ni}(\text{O}_2)$, was prepared from $[\text{Tp}^{\text{Ph,Me}}]\text{Ni}(\text{CO})$ under conditions similar to those used to generate $[\text{Tp}^{\text{tBu,Me}}]\text{Ni}(\text{O}_2)$. This complex, which has also been fully characterized, is stable under ambient conditions in the solid state but is unstable in solution. The divergence in stability between the two dioxygen adducts has been attributed primarily to differences in steric environment.

The reactivity of $[\text{Tp}^{\text{tBu,Me}}]\text{Ni}(\text{O}_2)$ was explored with a major focus on oxygen atom transfer, C-H activation and aldehyde deformylation. $[\text{Tp}^{\text{tBu,Me}}]\text{Ni}(\text{O}_2)$ facilitates O-atom transfer to both nitric oxide and alkylphosphines. In the latter case, the transfer

was shown to be catalytic in nature with strong implications for the involvement of an oxo-nickel intermediate. The complex was also competent in the C-H activation of multiple substrates including 1,4-cyclohexadiene (CHD), 9,10-dihydroanthracene (DHA) and xanthene. In the case of CHD, reaction with $[\text{Tp}^{\text{tBu,Me}}]\text{Ni}(\text{O}_2)$ resulted in the production of benzene. Investigations into the mechanism of this reaction implied the existence of a hydroperoxo-nickel species; a result supported by independent lines of reactivity. The reaction of $[\text{Tp}^{\text{tBu,Me}}]\text{Ni}(\text{O}_2)$ with DHA resulted in the unexpected generation of 9,10-anthraquinone. Mechanistic interrogation of the reaction suggests a complex, multistep process involving H-atom abstraction, radical rebound and the agency of both oxo-nickel and hydroperoxo-nickel intermediates. A kinetic analysis of the reaction reveals a KIE (kH/kD) of at least 12. Activation parameters, $\Delta H^\ddagger = 14(1)$ kcal/mol and $\Delta S^\ddagger = -117(10)$ J mol⁻¹K⁻¹, were determined from an Eyring analysis. A subsequent study of the reaction between $[\text{Tp}^{\text{tBu,Me}}]\text{Ni}(\text{O}_2)$ and xanthene show very strong similarities to the reaction with DHA and argues for the involvement of an analogous mechanistic pathway. Lastly, $[\text{Tp}^{\text{tBu,Me}}]\text{Ni}(\text{O}_2)$ was found to perform aldehyde deformylation when reacted with 2-phenylpropionaldehyde (2-PPA). In addition to the organic product, acetophenone, the reaction resulted in the formation of several divalent nickel derivatives. With regard to the nickel containing products, ¹H NMR and LIFDI analysis has resulted in the positive identification of metallacycle, hydroxo and formate complexes. Additional nickel derivatives remain unidentified.

Chapter 1

INTRODUCTION

The study of nickel-dioxygen species is a subject of tremendous importance and intense interest in both the academic and industrial communities. From utilization in biological systems to implications in industrial catalysis, this pairing of an Earth-abundant metal and a ubiquitous, potent oxidant provides a valuable platform for a wide range of chemical reactivity. Given their known and potential applications, Ni-O₂ adducts are tantalizing synthetic targets. The study of these always interesting, but often elusive species promises great rewards while offering up a number of synthetic challenges. Rising to these challenges advances not only the study of nickel-dioxygen systems, but also the field of metal-O₂ chemistry in general.

1.1 Ni-Dioxygen Interactions in Biological Systems

Great strides have been made in the last few decades in uncovering the identity and function of nickel-based systems in biology. Once thought to be of little importance in biological systems, nickel containing enzymes are now known to be intimately involved in the biological processes of a variety of plants, archaea and bacteria.¹ [NiFe] Hydrogenases are utilized by a number of bacteria for the purpose of metabolizing molecular hydrogen.² Nickel also serves as a metal cofactor in select varieties of the glyoxalase I enzyme.³ Methyl-coenzyme M reductase, the enzyme responsible for methane production in methanogenic archaea, is dependent on two units of the nickel containing cofactor, F₄₃₀.⁴ All known members of the urease

enzyme family, which facilitate the catalytic decomposition of urea into carbon dioxide and ammonia, contain nickel in their active sites.⁵ These examples serve to illustrate that while nickel may be underutilized in biology relative to other 1st row transition metals, it is nonetheless an essential element for a number of bioinorganic processes.

Of the known examples of Ni-based enzymes, only a very small number promote direct utilization of molecular O₂. One that does is acireductone dioxygenase (ARD). This class of enzyme plays an integral role in the methionine salvage pathway, the process by which many organisms generate methionine from 5'-methylthioadenosine (MTA). In humans, this process is essential for the recycling of endogenous sulfur. Two general types of ARD can be found in Nature with the only significant difference between them being the metal utilized in the active site; one using nickel and the other, iron. Both ARDs rely on 1,2-dihydroxy-3-keto-5-(methylthio)pentene as their substrate but they differ markedly in the products which they produce.⁶ In the case of iron-containing ARD, the substrate is transformed into a α -keto acid with concomitant formation of formic acid. The former of these products undergoes one final reaction to generate methionine, the final step in the methionine salvage pathway. By contrast, the nickel variant of ARD, Ni-ARD, catalyzes the so called "off-pathway" reaction wherein the substrate is converted to a methylthiocarboxylic acid, formic acid, and carbon monoxide. This process represents an exit to the methionine salvage pathway as these products do not go on to yield methionine.

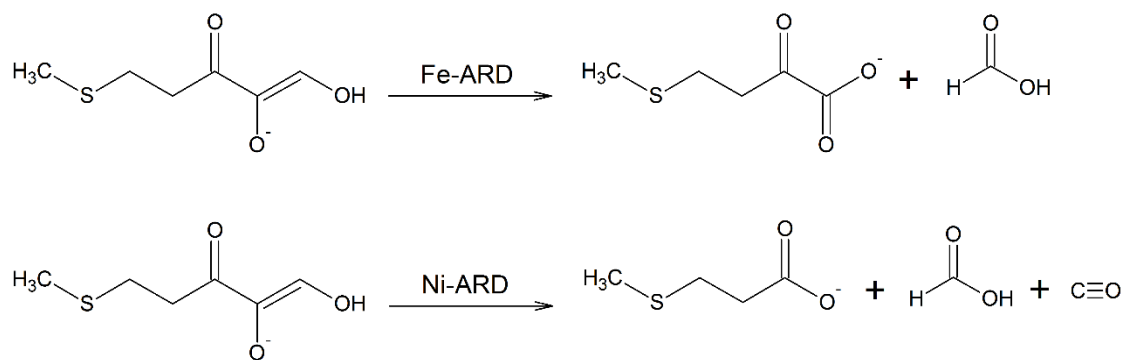


Figure 1.1 Transformation of 1,2-dihydroxy-3-keto-5-(methylthio)pentene by Fe-ARD (top) and Ni-ARD (bottom).

The identical sequence homology shared between Ni-ARD and Fe-ARD strongly suggests that the electronic environment created by the individual metals is responsible for the differences in the substrate transformation pathway. This rationale is further supported by studies utilizing small molecules mimics.^{7,8,9} The active site structure of the enzyme has been elucidated using a combination of NMR methods, X-ray absorption spectroscopy and conserved domain homology.¹⁰ As shown in Figure 1.2, these studies reveal a high spin Ni(II) center with an octahedral coordination environment consisting of one aspartic acid, three histidine residues, and two water molecules.¹¹

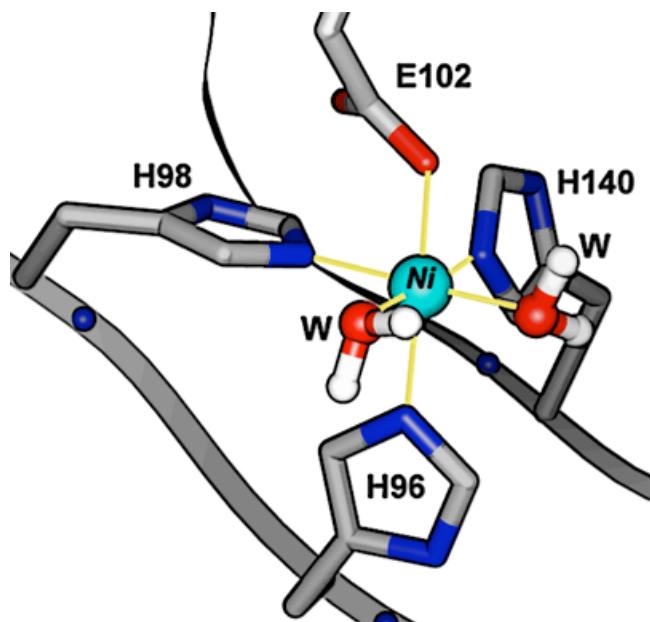


Figure 1.2 The active site of Ni containing acireductone dioxygenase (Ni-ARD). Adapted with permission, from Figure S1, Ragsdale, S. W. *The Journal of Biological Chemistry*. **2009**, *284*, 18571, under the terms of the CC-BY license, <http://creativecommons.org/licenses/by/4.0/legalcode>

Interestingly, while the presence of nickel in the active site is essential for “off-pathway” ARD activity, the metal center itself is redox inactive and does not bind O₂. Rather, the nickel-bound substrate reacts with O₂ directly to form a peroxo intermediate. The nickel acts as a Lewis acid, with the effect of encouraging this peroxo moiety to attack the metal-bound carbonyl group.

Recently, another nickel based dioxygenase has been discovered which plays a more direct role in dioxygen activation. Nickel containing quercetinase (Ni-QueD) is a variant of quercetin 2,4-dioxygenase (QueD), which is responsible for the metabolism of 3,5,7,3',4'-pentahydroxyflavone (QUE) as part of the aerobic decomposition of plant material. Ni-QueD was isolated from a strain of *Streptomyces* and, while possessed of the ability to bind several different transition metals, shows its highest

activity when utilizing nickel. An X-ray crystallographic study by Jeoung et al has revealed the structure of Ni-QueD's active site in stunning detail and is accompanied by detailed proposed mechanism.¹² In the resting state, the nickel ion is coordinated by three His residues, one glutamate residue and two water molecules to give a distorted octahedral configuration. Binding of quercetin displaces one of the water molecules and induces a conformational change which labilizes the second water and creates a channel for O₂ diffusion to the binding site. The active site having been primed in this fashion, dioxygen displaces the remaining water molecule to bind, side-on to nickel. The O₂ moiety subsequently undergoes 1-electron reduction, although the source of the electron (either quercetin or nickel) is currently unknown. The observed O–O bond length of up to 1.35 Å result in both dioxygen and superoxide being possible candidates for the bound state of O₂, while a peroxy assignment is precluded. Dioxygen binding and activation is followed by attack on the bound quercetin to give a peroxydate intermediate. Subsequent O–O and C–O bond cleavage liberates CO and the depside product.

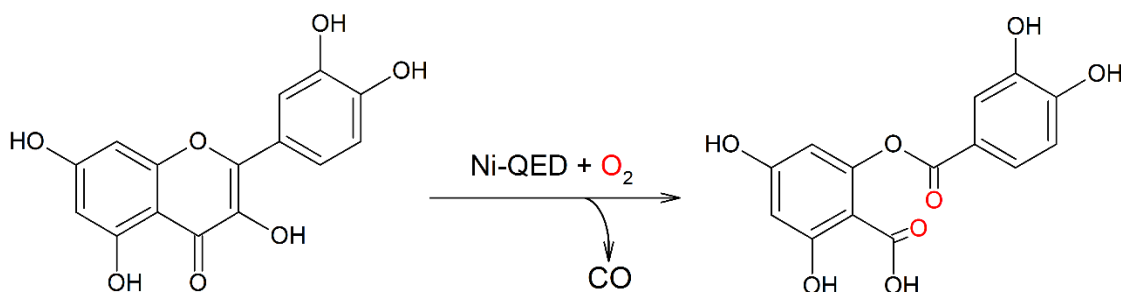
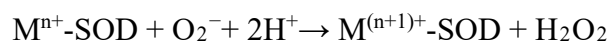
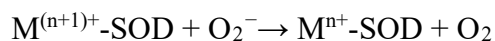


Figure 1.3 Transformation of quercetin by Ni-QED.

While both Ni-ARD and Ni-QueD facilitate the usage of dioxygen, at present neither of these systems is known, definitively, to utilize the nickel in a redox active capacity. In Ni-ARD, the evidence suggests a redox inactive nickel while in the case of Ni-QueD the electronic state of the O₂-bound complex is still unknown. Thus, in terms of biological significance, the system with somewhat greater relevance to the present work is the nickel-superoxide dismutase (NiSOD) enzyme. NiSOD belongs to the larger family of superoxide dismutase enzymes, all of which serve to catalyze the dismutation of superoxide into either dioxygen or hydrogen peroxide according to the following scheme:



Superoxide is an unavoidable byproduct of oxygen metabolism in biological systems. It is also a potent toxicant whose generation can result in lipid peroxidation, protein damage, enzyme deactivation and myriad forms of DNA damage. The long list of deleterious intracellular reactions caused by superoxide necessitates a robust and efficient detoxification mechanism. The SOD enzyme family provides this function via their incredibly facile dismutation of superoxide. Indeed, the SODs are among the most efficient enzymes known in biology, performing their function so rapidly that superoxide breakdown is diffusion limited. This ability serves to render these enzymes indispensable to nearly all organisms that either metabolize molecular oxygen or must otherwise survive in an aerobic environment. Given the importance of timely superoxide detoxification, Nature has evolved a number of SOD subtypes which are generally grouped into the following three classes based on amino acid sequence homology: Copper and Zinc SOD, Iron or Manganese SOD and Nickel SOD.

Eukaryotic life is most dependent on the copper and zinc SOD class. The first SOD for which a high resolution crystal structure was obtained¹³, the Cu-Zn-SOD active site ligands consist of six histidine and one aspartate side chain¹⁴ and operates by cycling between Cu^{I} and Cu^{II} . The Iron or Manganese SOD is used primarily by prokaryotes as well as by the mitochondria of eukaryotes. Active site architecture is largely the same for both the Fe and Mn variants, with each site containing a single metal ion bonded to three histidine residues, one aspartate (aspartic acid in Mn-SOD) and one water.¹⁵ The nature of the catalytic cycle is also consistent between the two variants, with superoxide dismutation being driven by the $\text{M}^{\text{II}}/\text{M}^{\text{III}}$ redox couple. In contrast with the more widely distributed nature of the other SOD classes, Ni-SOD is found almost exclusively in prokaryotes with the only known eukaryotic examples being certain types of green algae. NiSOD is unique among the SOD family in that it undergoes a significant change to its coordination sphere when cycling between the Ni^{II} and Ni^{III} oxidation states. This can be visualized in Figure 1.4 in the ligation and deligation of imidazole functionality of His1. The imidazole is bound to nickel in the 3+ oxidation state but deligated in the 2+ oxidation state. Like the Fe/Mn-SOD subtype, Ni-SOD functions by cycling between the Ni^{II} and Ni^{III} oxidation states. However, unlike Fe/Mn SOD, NiSOD utilizes two sulfur donors in the form of cysteine residues. This is another unique feature among the SOD enzymes whose coordination spheres are typically dominated by N and O donors such as histidine, aspartate and imidazole ligands. The reason for this striking difference is postulated to be due to the need to tune the redox properties of the active site such that the $\text{Ni}^{\text{II}}/\text{Ni}^{\text{III}}$ couple becomes a viable mechanistic pathway.¹⁶ This is in line with the more general observation that nickel containing enzymes which are thought to be redox active (such

as acetyl coenzyme A synthase and NiFe hydrogenase) consistently contain sulfur donors whereas those postulated to be redox inactive (such as Ni containing acireductone dioxygenase and urease) do not.¹⁷

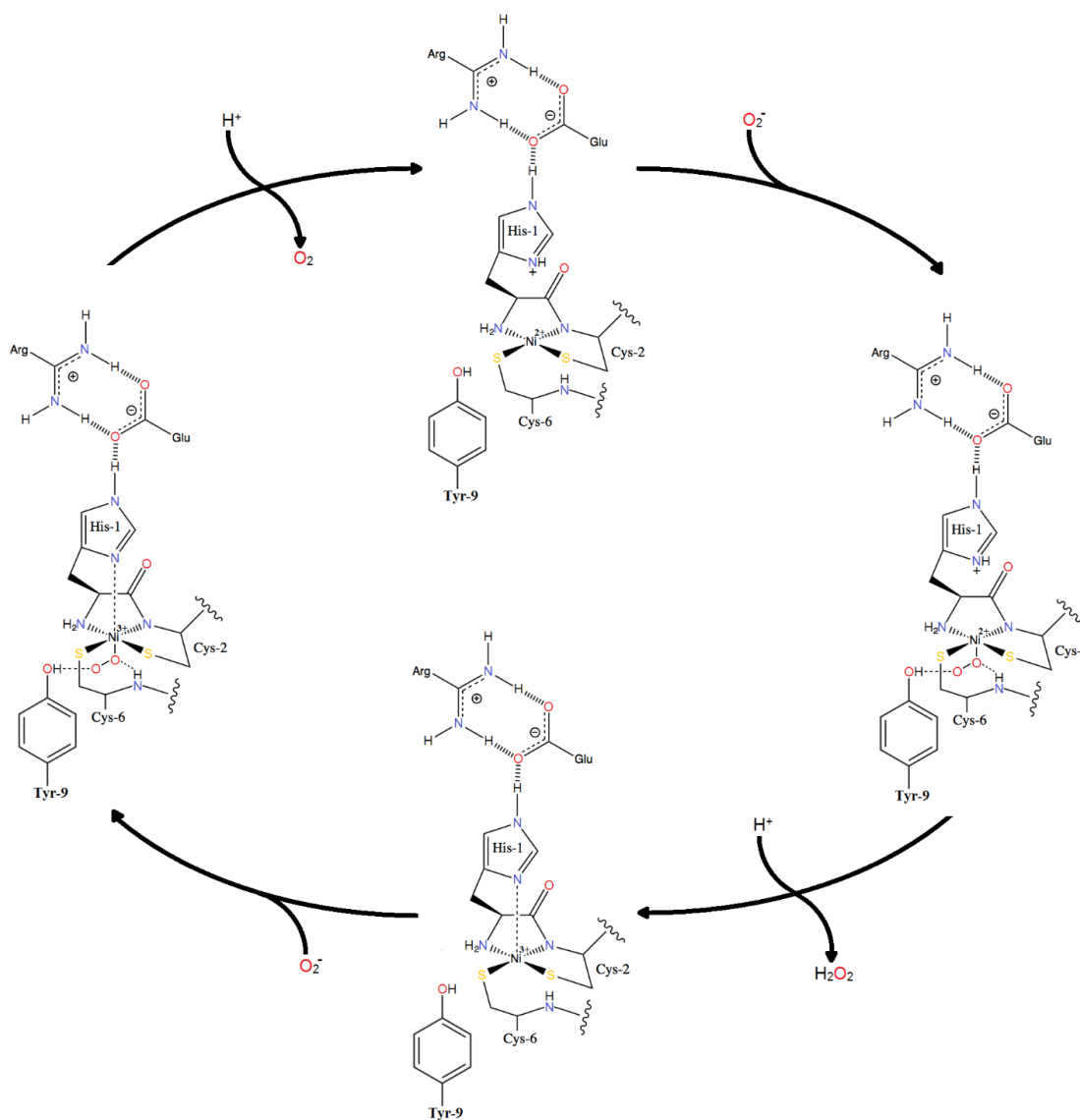


Figure 1.4 Mechanism of Nickel Superoxide Dismutase.

1.2 Nickel Based Substrate Oxidation – Applications and Industrial Relevance

The use of metal complexes to catalyze the oxidation of organic substrates is of great importance and broad relevance throughout many areas of chemistry.¹⁸ From the synthesis of commodity chemicals, to the preparation of pharmaceuticals, to innumerable biological functions, there are few areas of study where such complexes are not encountered. In biology, the environmentally abundant 1st row transition metals largely dominate these processes. Iron is particularly well represented, as evidenced by the ubiquitous presence and broad substrate scope of the cytochromes as well as the oxygen storage and transport properties of myoglobin and hemoglobin. Synthetic chemists, on the other hand, have been far more cosmopolitan in their choice of transition metals with examples of catalysis available from across the periodic table. Among these options, precious metals such as rhodium, ruthenium, platinum and palladium have seen particularly extensive use. Unfortunately, the expense of precious metal catalysts inherently limits their utility, especially in processes where the catalyst loading is high and/or the catalyst is irrecoverable. It is unsurprising then that Earth-abundant, 1st row transition metal replacements for these elements are of great interest in current inorganic chemistry research.¹⁹ Nickel is particularly important in this regard due to its chemical similarity to its heavier congener, palladium. However, replacing the established reactivity of precious metals with cheaper, 1st row alternatives requires significant research investments in order to circumvent the latter's often less active and selective nature.

One area where nickel based complexes have shown considerable promise is in the epoxidation of olefins. Work by Koola and Kochi demonstrated the ability of divalent nickel complexes supported by a number of different ligand systems to catalyze the epoxidation of several common alkenes.²⁰ The reactions, which used

iodosylbenzene as the oxidant, were most successful when performed using complexes supported by cyclam derivatives (Figure 1.5).

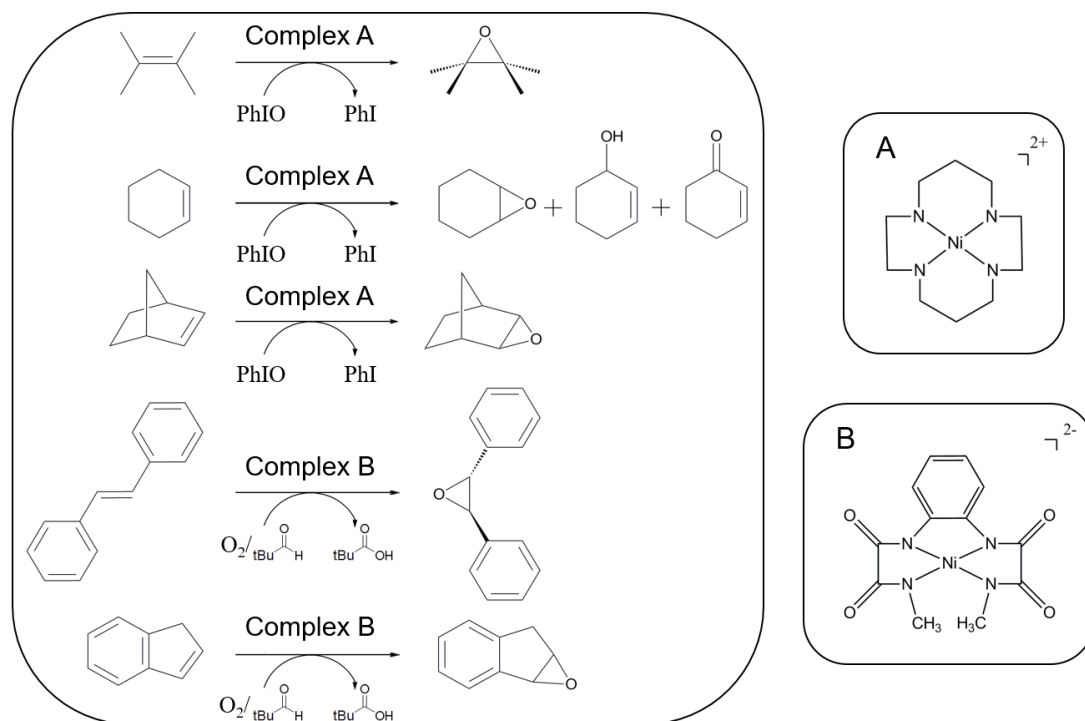


Figure 1.5 Examples of olefin epoxidation with divalent nickel complexes.

Produced along with the desired epoxide products were significant amounts of oxidized ligand and solvent. This indicated the formation of a powerful and fairly indiscriminant oxidant. A Ni(IV)-oxo species was postulated to be the active species with formation of the complex occurring via oxygen atom transfer from the iodosylbenzene to nickel, and subsequently, from nickel to the product, Figure 1.6.

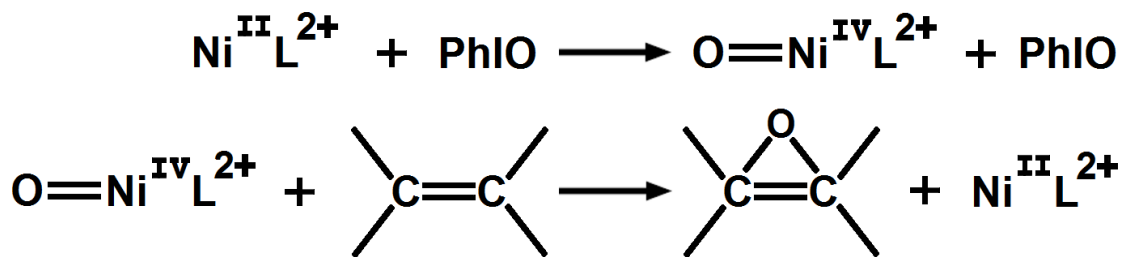


Figure 1.6 Proposed mechanism of olefin epoxidation with nickel(II) complex and iodosylbenzene.

This active species, however, was not spectroscopically observed. In another report, Fernandez et al. describe square-planar nickel(II) complexes of *o*-phenylenebis(*N*'-methyloxamidate) which catalyze the aerobic epoxidation of olefins in the presence of pivalaldehyde as a reductant. This is especially significant due to the use of dioxygen as the active oxidant. In this case, as in the work of Koola and Kochi, the active species is again proposed to be a Ni(IV)-oxo complex. These examples serve to illustrate the utility of nickel complexes in the facilitation of olefin epoxidation as well as to demonstrate the need for continued study towards elucidating the nature of the active species in these reactions.

Another novel use of nickel complexes in functional oxidations is the site specific cleavage of DNA. The ability to selectively target and cleave DNA at specific positions is an essential technique in the study and manipulation of genetic material. Several nickel complexes have demonstrated the ability to effect this cleavage in a remarkably controlled manner. A notable example of this is a report by Mack and Dervan in which they use a synthetic metalloprotein derived from naturally occurring α -amino acids.^{21,22} The nickel is introduced into the metalloprotein via the addition of nickel(II) acetate. Monoperoxyphthalic acid (MPPA) was used as the oxygen atom

donor. Once in solution, the metalloprotein selectively binds DNA. Subsequent addition of MPPA results in rapid cleavage at the binding site (Figure 1.7). As with the olefin epoxidation reactions, the active oxidant is speculated to be a high valent oxo-nickel moiety that abstracts a specific hydrogen atom on the deoxyribose backbone. In a later report by Morrow and Kolasa, divalent nickel complexes including, nickel salen, were used to effect a DNA cleavage that converted a supercoiled plasmid into the nicked circular form.²³ The conversion was accomplished in less than five minutes using iodosylbenzene as the oxygen atom donor. A high valent oxo-nickel species is again presented as a possible active agent although the authors do not rule out an activated iodosylbenzene complex. These examples serve to illustrate the utility of nickel complexes in the areas of biochemistry and bioinorganic chemistry as well as to highlight the need for further research regarding the formation of oxo-nickel species.

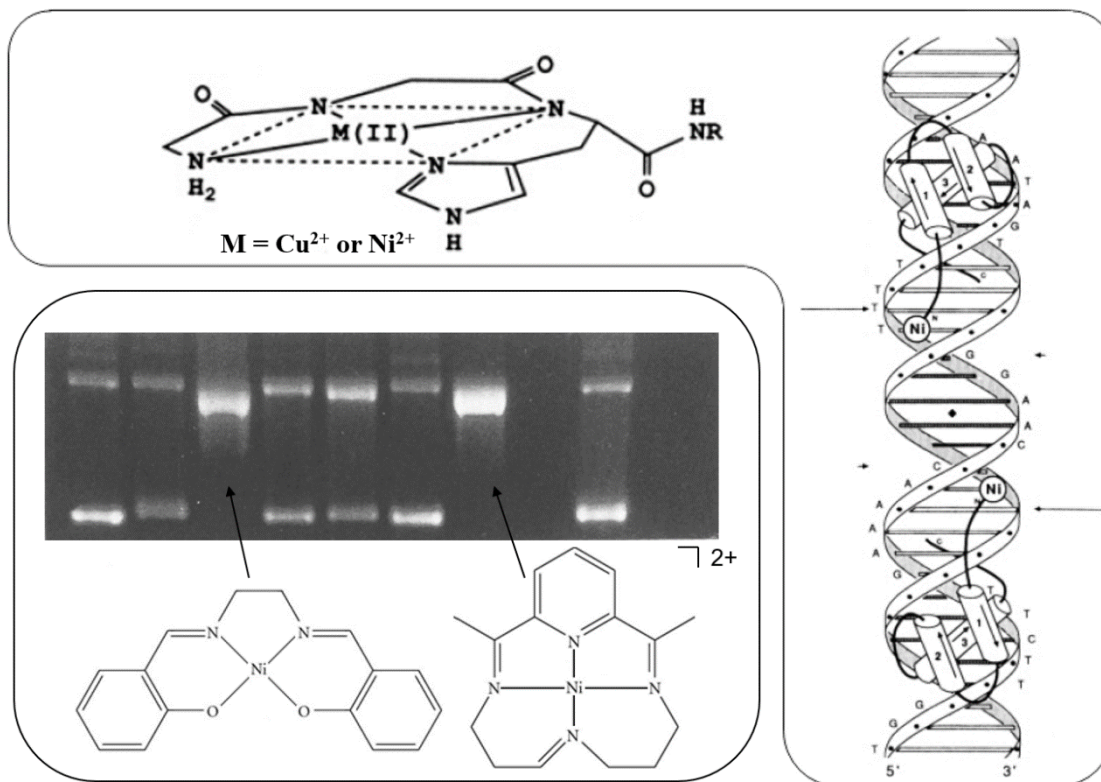


Figure 1.7 Synthetic metalloprotein cleaves DNA at the indicated sites (Top and Right). Nickel(II) macrocycles facilitate conversion of supercoiled plasmid to nicked, circular form (Bottom, Left). Images adapted with permission from Mack, D. P.; Dervan, P. B. *J. Am. Chem. Soc.*, **1990**, *112*, 4604 and Morrow, J. R.; Kolasa, K. A. *Inorg. Chim. Acta*, **1992**, *195*, 245 respectively

1.3 Synthetic Strategies for the Preparation of Nickel-Dioxygen Complexes

While the number of potential applications for dioxygen activation by nickel are vast, the development of such applications requires a significant depth of understanding in regard to their formation, stability and patterns of reactivity. With this in mind, a number of efforts have been made in the last several decades to generate examples of nickel-dioxygen adducts for study. This search for suitable candidates has not been an easy endeavor, with the task complicated by the often

unstable and highly reactive nature of these elusive species. The matter is made still more difficult by the paucity of preparation methods by which potential complexes may be prepared. Despite these difficulties, however, researchers in this area have developed a number of general strategies whereby nickel-dioxygen adducts may be realized.

One of the most widely used methods available for the preparation Ni-O₂ complexes is the treatment of divalent nickel complexes by hydrogen peroxide. Such preparation regimes have resulted in the successful characterization of a number of highly interesting species, predominantly of the nickel(III)-peroxo variety. An early prominent example of this approach is the preparation by Hikichi et al of the first bis- μ -oxo dinickel complex, [Tp^{Me}₃]₂Ni(μ -O)₂Ni[Tp^{Me}₃]. The complex was generated via treatment of the bis- μ -hydroxo precursor complex, [Tp^{Me}₃]₂Ni(μ -OH)₂Ni[Tp^{Me}₃], with H₂O₂ as shown in Figure 1.8.²⁴ This was followed by a report from Shiren and coworkers utilizing the tetradentate tripodal ligand, Me₃-tpa, wherein they demonstrated the conversion of a bis- μ -oxo to a bis- μ -superoxo core upon treatment with excess H₂O₂.²⁵ More recently, Nam and coworkers have used this technique to prepare both superoxo and peroxo nickel complexes. These tetraazamacrocyclic (TMC) supported complexes include examples of both “end-on” and “side-on” dioxygen binding motifs.^{26,27}

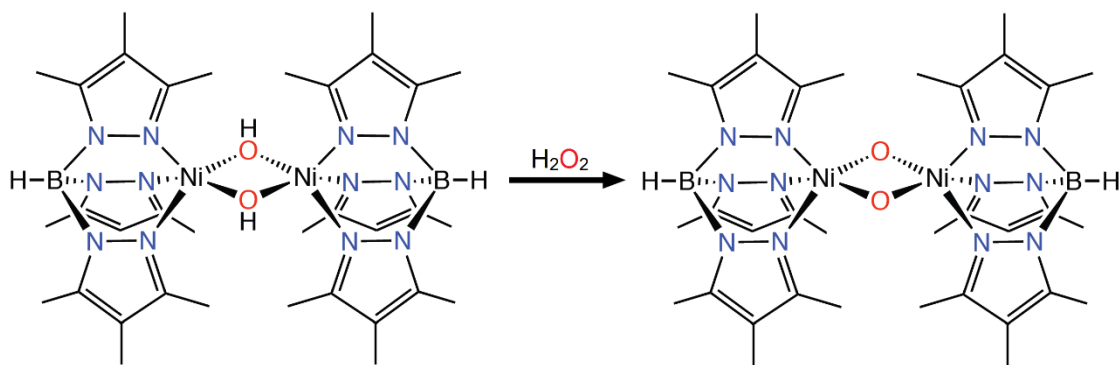


Figure 1.8 Preparation of the bis- μ -oxo dinickel complex, $[\text{Tp}^{\text{Me}_3}]_2\text{Ni}(\mu\text{-O})_2\text{Ni}[\text{Tp}^{\text{Me}_3}]$.

Another very effective, if less widely used, strategy for the preparation of nickel-dioxygen adducts is the direct reaction of low valent (zero or monovalent) nickel complexes with dioxygen. Such preparations are driven by the highly reducing nature of such low-valent species and have the advantage of activating dioxygen directly. The latter aspect makes this technique highly relevant to both industrial and biological areas of study as dioxygen is a cheap, plentiful and readily available oxidant. However, it is somewhat inconvenient with respect to the preparation, handling and storage of the low-valent precursor complexes as they are by design greatly sensitive to water and oxygen. The preparation of monovalent complexes in particular is often synthetically challenging and has led to the development of numerous strategies for selectively reducing nickel and discouraging disproportionation of the resulting complexes. Despite these challenges, this approach has provided some of the most stable and well characterized examples of nickel-dioxygen adducts, including the primary compounds described in the present work.

One of the first uses of low valent nickel to activate dioxygen can be found in the work of Otsuka et al.²⁸ In that report, the zero-valent complex, $\text{Ni}(t\text{-BuNC})_4$, was

reacted with dioxygen at -20°C to generate the peroxo complex, $\text{Ni}(\text{O}_2)(\text{t-BuNC})_2$ as pale green crystals. While the complex is fairly stable in the solid state at room temperature, it was found to be unstable in solution. Though a relatively simple system compared with those that have since been developed, this initial foray into dioxygen activation by nickel laid the groundwork for further exploration. More than three decades later the Riordan lab expanded on this concept through the preparation of two nickel-dioxygen adducts from monovalent precursors in a pair of landmark reports.^{29,30} Using two members of the phenyltris(thioether)borate (PhTt) ligand system, the monovalent complexes $[\text{PhTt}^{\text{tBu}}]\text{Ni}(\text{CO})$ and $[\text{PhTt}^{\text{Ad}}]\text{Ni}(\text{CO})$ were prepared and reacted with dioxygen (Figure 1.9). The results from these experiments are striking. When treated with O_2 , $[\text{PhTt}^{\text{tBu}}]\text{Ni}(\text{CO})$ went on to generate the bis- μ -oxo complex, $[(\text{PhTt}^{\text{tBu}})\text{Ni}]_2(\mu\text{-O})_2$. $[\text{PhTt}^{\text{Ad}}]\text{Ni}(\text{CO})$ on the other hand led to the monomeric side on superoxide complex, $[\text{PhTt}^{\text{Ad}}]\text{Ni}(\text{O}_2)$. These studies served to illustrate not only the effectiveness of using monovalent nickel to activate dioxygen, but also how steric effects could be used to direct and control the nature of the activated product. Unfortunately, while both complexes underwent extensive spectroscopic study, their thermal sensitivity precluded structural characterization via X-ray diffraction.

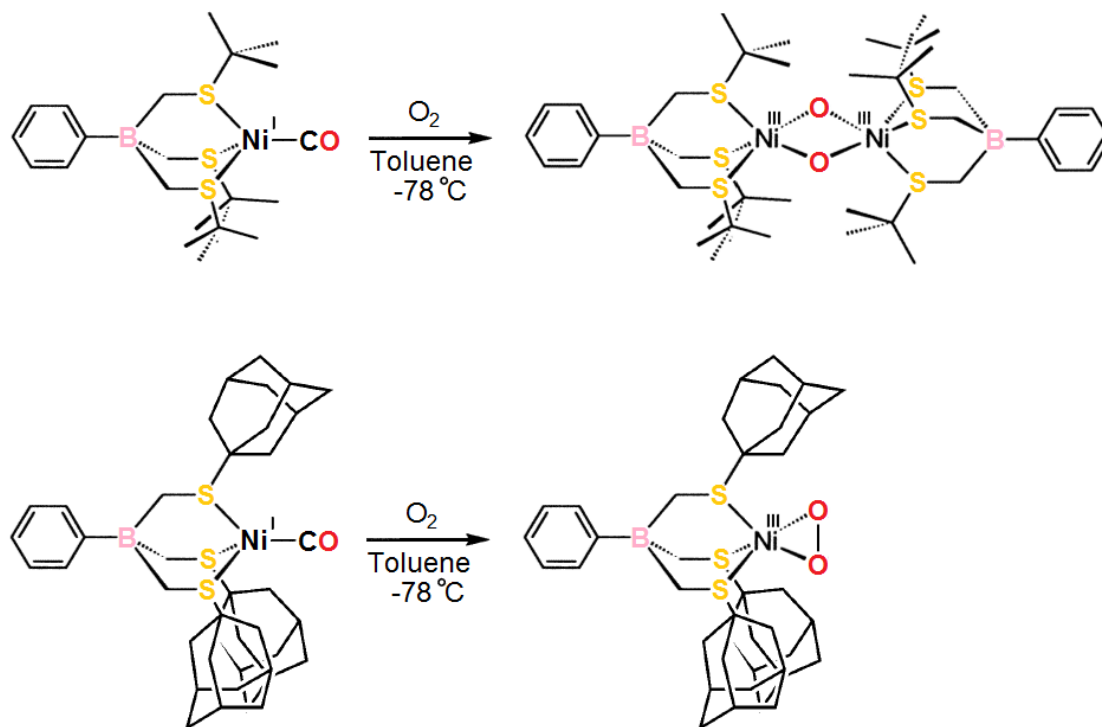


Figure 1.9 Preparation of $[(\text{PhTt}^{\text{tBu}})\text{Ni}]_2(\mu\text{-O})_2$ and $[\text{PhTt}^{\text{Ad}}]\text{Ni}(\text{O}_2)$ from their monovalent precursors.

The Riordan group made further progress in this area with the preparation of another superoxo-nickel complex. The tetraazamacrocycle (TMC) supported species, $[\text{Ni}(\text{tmc})(\text{O}_2)](\text{OTf})$, was the first reported “end-on” superoxo nickel coordination motif.³¹

A final prominent example of the low-valent nickel approach came from a report by Driess et al. This work focused on the beta-diketiminato (nacnac) ligand system, with the complex $[\text{((Nacnac)Ni)}_2(\mu\text{-}\eta^3\text{:}\eta^3\text{-C}_6\text{H}_5\text{-Me})]$ serving as the precursor.³² This formally divalent complex serves as a synthon for monovalent complexes and can itself be used like one. When treated with dioxygen the side-on superoxo complex, $[\text{Ni}^{\text{II}}(\beta\text{-diketiminato})(\text{O}_2)]$, is formed (Figure 1.10).⁴⁶ Remarkably,

the superoxide complex exhibits considerable thermal stability, tolerating temperatures as high as 60 °C in hexane. The high thermal stability of the complex relative to previous examples allowed for the first X-ray structural characterization of a mononuclear nickel-superoxide species.

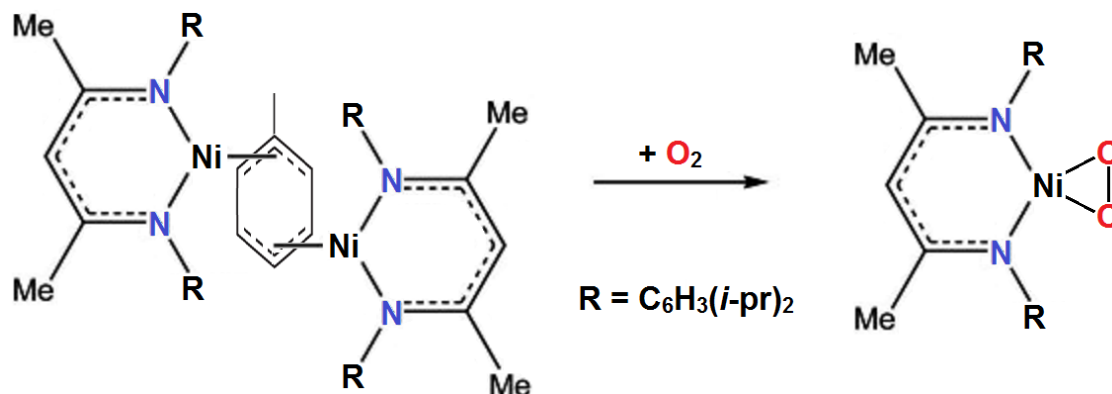


Figure 1.10 Preparation of Driess' nickel-superoxo complex, $[\text{Ni}^{\text{II}}(\beta\text{-diketiminato})(\text{O}_2)]$

1.4 Stabilizing Metal-Dioxygen Adducts with Trispyrazolylborates

In the study of transition metal-dioxygen complexes in general, no factor is of greater importance than the choice of ligand system. The ability to manipulate and control the patterns of reactivity displayed by a given transition metal is often limited solely by the corresponding ability to manipulate and control that metal's coordination environment and redox processes through clever ligand design. A great number of ligand systems have been used to study nickel based chemistry, each with their own advantages and drawbacks. With respect to the preparation of Ni-dioxygen adducts, previous examples have illustrated β -diketiminato (nacnac), TMC and PhTt ligands systems to be of particular importance and usefulness. Expanding the list of available

ligand systems with which nickel-dioxygen complexes can be prepared is of paramount importance in advancing this area of study.

One system in particular which shows great promise in this regard and which is the basis of the present work is the trispyrazolylborate ligand class. Trispyrazolylborates, or Tps as they are commonly known, are a class of tridentate, monoanionic ligands composed of three pyrazole substituents bound to a central boron. Originally prepared by Swatoslaw Trofimenko, who named them scorpionates for the manner in which they bind metals, Tp ligands represent one the most versatile and widely known ligands available in coordination chemistry.^{63,64} Their versatility stems from their highly modifiable nature. The pyrazole substituents (the claws and the stinger in scorpionate parlance) that constitute the bulk of the ligand are most often derived from diketones, which can be prepared in a nearly limitless number of variants. By altering the substituents on the pyrazole ring (and to a lesser extent the boron backbone), the steric and electronic properties of the resulting ligand can be tuned for a range of applications. This is a critical requirement for the preparing a nickel-dioxygen adduct.

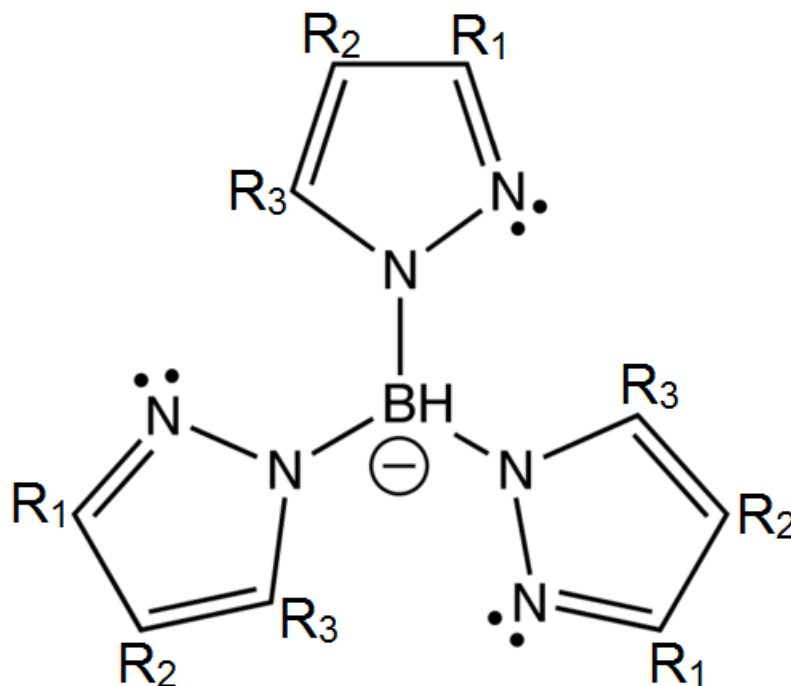


Figure 1.11 General two dimensional structure of a trispyrazolylborate ligand. Substituents at the 3, 4 and 5 positions of the pyrazole ring can be used to tune steric and electronic properties.

Tp ligands have also demonstrated support for a wide range of transition metal oxidation states. Another reason the Tp system was selected is its demonstrated history of supporting stable dimeric and monomeric metal-dioxygen complexes. Of particular note are the monomeric dioxygen adducts, $[\text{Tp}^{\text{tBu,Me}}]\text{Co}(\text{O}_2)$ and $[\text{Tp}^{\text{tBu,i-Pr}}]\text{Cu}(\text{O}_2)$.^{52,53} Both complexes were prepared from monovalent precursors and both are stable under ambient conditions. Earlier work from the Kitajima lab has already demonstrated that Tp can support bis- μ -oxo nickel complexes. The effects of differences in steric environment on nickel-dioxygen reaction patterns were clearly demonstrated in the divergent reactivity observed in the Tt supported Ni systems. In the case of Tp, these differences are paralleled in the reactivity observed in the Cu/Co systems versus that

displayed by the less bulky Ni complex. This begged the question of whether the more sterically encumbering ligands supporting the Co and Co adducts could be used to support a nickel-dioxygen adduct. This seemed a particularly attractive approach given the relative stability of the former complexes and the prior difficulties in preparing thermally robust NiO₂ species. Such a course of study would also likely necessitate the preparation of monovalent Tp complexes which were completely unexplored and offered a wealth of potential lines of reactivity. It was with these thoughts and the rich history of trispyrazolylborate chemistry in mind that we pursued a course targeting Tp supported nickel-dioxygen adducts.

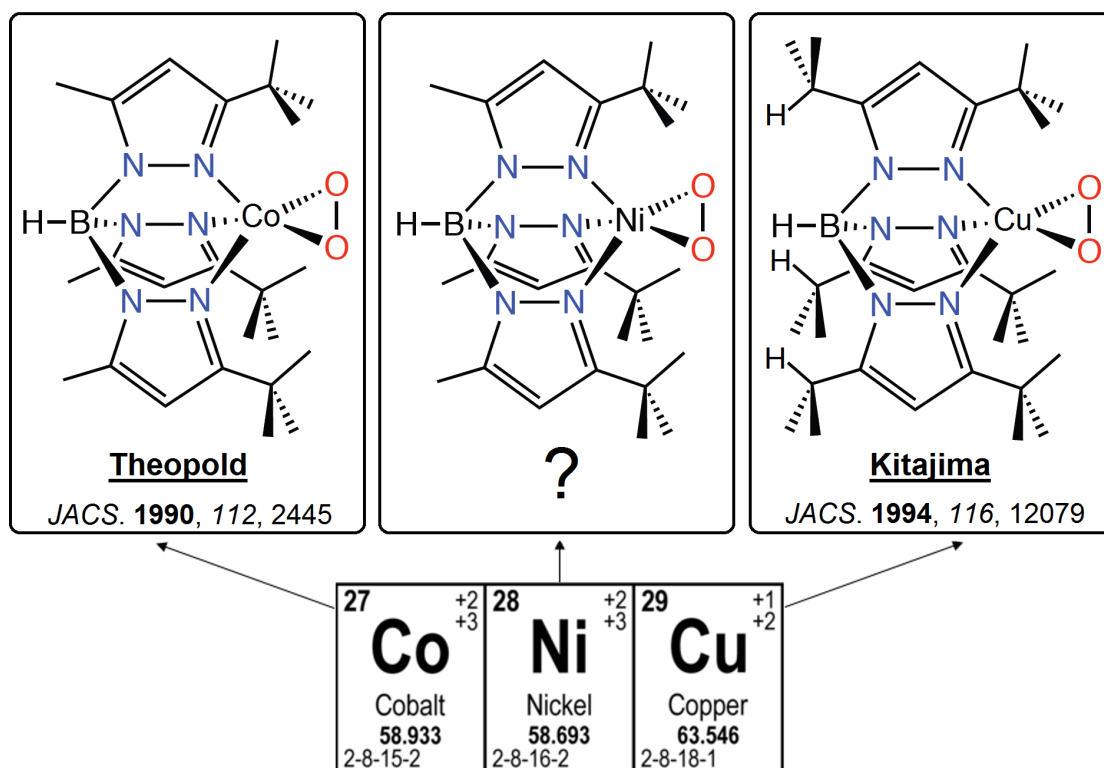


Figure 1.12 Bridging the Dioxygen Adduct Gap: Copper and cobalt dioxygen adducts supported by the Tp ligand system have been prepared and fully characterized.

Chapter 2

EXPERIMENTAL PROCEDURES

2.1 General Procedures

Unless otherwise indicated, all reactions were carried out under a nitrogen atmosphere either in a Vacuum Atmospheres glovebox or by using standard Schlenk techniques. All glassware was dried for a minimum of 4 hours at a temperature not less than 150 °C.

2.1.1 Materials

Solvents were dried by passage through activated alumina columns and purged with dry N₂ for 15 minutes immediately prior to collection. O₂ and CO were purchased from Keen Gas and dried by passage through a Dririte column. Elemental mercury was purified via vacuum distillation. (3-Aminopropyl)triethoxysilane (ATPS) coated silica gel,³³ cyclohexyl isocyanate,³⁴ [Tp^{tBu,Me}]K,³⁵ [Tp^{tBu,Me}]NiCl,³⁶ [Tp^{Ph,Me}]NiCl,³⁷ 9,10-dihydroxy-9,10-dihydroanthracene³⁸ and DHA-d₄³⁹ were prepared according to literature methods. Deuterated solvents were purchased from Cambridge Isotope Laboratories and dried over 4 Å molecular sieves. All other reagents were purchased from commercial sources and were used as received.

2.1.2 Physical Methods

NMR spectra were recorded at room temperature on a Bruker AVIII 400 MHz NMR spectrometer equipped with either a BBO or BBFO probe and on a Bruker AVIII 600 MHz spectrometer equipped with a 5-mm Bruker SMART probe. Spectra were processed using Bruker Topspin[®] software. NMR spectral signals were

referenced to the residual solvent signals, unless otherwise indicated. Chemical shifts are quoted in δ (ppm). Abbreviations for NMR spectral features are as follows: s, singlet; d, doublet; t, triplet; m, multiplet; br, broad. The ^{31}P NMR spectra were recorded with proton decoupling and were referenced to a phosphoric acid (85% in D_2O) internal standard. Columbia Analytical Services, Tucson, AZ and Intertek Pharmaceutical Services, Whitehouse, NJ performed combustion analyses. Infrared spectra were recorded on a Nicolet Magna 560 IR Spectrometer under a dry, CO_2 free, compressed air purge at room temperature. Solid-state FT-IR samples were prepared as KBr pellets. Electronic absorption measurements were recorded on either a HP Agilent 8453 Diode Array Spectrophotometer or a Varian Cary 50 Spectrophotometer using custom made, air free cuvettes. The locations of specific electronic absorption maxima (λ_{max}) are reported in nm with the associated extinction coefficients (ϵ) reported in units of $\text{M}^{-1}\text{cm}^{-1}$ and rounded to the nearest 50 units. Magnetic moments were obtained in solution by the Evans Method and are reported in Bohr magnetons (μ_{B}).⁴⁰ Mass spectra of metal complexes were acquired on a Waters GCT mass spectrometer with a liquid injection field desorption ionization⁴¹ (LIFDI) source. Mass spectra of organic species were acquired on an Agilent 6850 Series GC System coupled with an Agilent 5973 Network Mass Selective Detector.

X-ray Absorption Spectroscopy (XAS) was performed at the Advanced Light Source in Lawrence Berkeley National Laboratory on beamline 6.3.1 (ISSAC) by Professor Stephen Cramer (UC-Davis) and coworkers. Samples were prepared, stored and shipped under a nitrogen atmosphere. Samples were transferred to the beamline floor using scintillation vials capped under nitrogen and mounted to the sample holder inside an argon-filled glove bag. Measurements were performed through either photo

diode (total fluorescence yield, TFY), electron current (total electron yield, TEY), and/or silicon drift detector (total and partial fluorescence yield, TFY and PFY). NiF₂ and NiO samples located inside the ISACC chamber were used as calibrants.⁴²

2.2 Synthesis of Ni(II) Halide Precursor Complexes

2.2.1 [Tp^{tBu,Me}]NiBr

Finely ground, anhydrous NiBr₂ (4.96 g, 22.7 mmol) was added to a ~350 mL CH₃CN solution of potassium hydrotris(3-*tert*-butyl-5-methylpyrazolyl)borate (10.0 g, 21.6 mmol). The solution was stirred for 5 days, during which time the color turned to a deep purple and large amounts of precipitate were formed. The volatiles were removed under vacuum giving a dark purple residue, which was dissolved in 400 mL of THF and filtered through Celite to remove KBr and excess NiBr₂. The solvent was removed under vacuum and the remaining purple solid stirred in 100 mL of cold MeOH for 20 min. The product was recovered by filtration, washed with MeOH and dried under vacuum yielding [Tp^{tBu,Me}]NiBr as a purple powder, 9.26 g (76%). ¹H NMR (CDCl₃): δ 84.9 (4-*Pz*, s, 3H), 7.3 (5-*Me*, s, 9H), -0.1 (3-*t-Bu*, br, 27H), -8.6 (BH, br, 1H). UV-vis (CHCl₃), λ_{\max} (ϵ , M⁻¹cm⁻¹): 316 (2600), 535 (400), 827 (50), 954 (100). IR (KBr pellet, ν /cm⁻¹): 2558 (B-H). $\mu_{\text{eff}} = 3.5(1) \mu_{\text{B}}$. Anal. Calcd for C₂₄H₄₀N₆BNiBr: C, 51.28; H, 7.19; N, 14.95. Found: C, 51.18; H, 7.27; N, 14.73.

2.2.2 [Tp^{tBu,Ph}]Ti

This new ligand derivative was prepared using a modification of the one-pot procedure reported by Kitamura and coworkers.⁴³ To a 100-mL round bottom flask was added finely ground KBH₄ (663 mg, 12.3 mmol), 3-*tert*-butyl-5-phenylpyrazole (14.8 g, 73.7 mmol) and Ti₂(SO₄) (3.1 g, 6.14 mmol). The reaction vessel was heated

to 240°C in a sand bath under a constant nitrogen flow. The resulting melt was stirred vigorously for 6 days at a temperature maintained between 230-240°C. A heat gun was used twice daily to melt pyrazole, which collected at the top of the reaction vessel (heat gun use was discontinued and the pyrazole allowed to collect for the final 12 hours of heating). After 6 days, the reaction was cooled to room temperature. Pyrazole that collected at the top of the reaction vessel during the final 12 hours of heating was scraped from the flask for reuse and the remaining solids extracted into 200 mL of CHCl₃. The cloudy solution was filtered through Celite and the solvent removed under vacuum giving an off-white residue. The residue was further purified by stirring with 100 mL of cold MeOH, recovered by filtration and dried under vacuum yielding [Tp^{tBu,Ph}]Tl as a white powder, 7.75 g (78%). ¹H NMR (CDCl₃): δ 7.1 (*5-Ph*, t, 3H), 6.9 (*5-Ph*, d, 6H), 6.8 (*5-Ph*, t, 6H), 6.1 (*4-Pz*, s, 3H), 1.4 (*t-Bu*, br, 27H).

2.2.3 [Tp^{tBu,Ph}]NiBr

Finely ground, anhydrous NiBr₂ (2.07 g, 9.5 mmol) was added in one portion to a suspension of thallium hydrotris(3-*tert*-butyl-5-phenylpyrazolyl)borate (7.0 g, 8.6 mmol) in ~300 mL CH₃CN. The solution was stirred for 5 days, during which time the color turned to a deep purple and copious amounts of precipitate were formed. The volatiles were removed under vacuum giving a dark purple residue, which was dissolved in ~200 mL of THF and filtered through Celite to remove TlBr and excess NiBr₂. The solvent was removed under vacuum and the remaining purple solid stirred in ~100 mL of pentane for 10 min. The product was recovered by filtration, washed with cold pentane and dried under vacuum yielding [Tp^{tBu,Ph}]NiBr as a purple powder, 5.22 g (81%). As deduced by ¹H NMR spectroscopy, approximately 13% of the product was in the form of the "N-confused" isomer, in which one of the pyrazole

substituents has been isomerized, with the phenyl and *tert*-butyl substituents of the "N-confused" arm occupying the 3- and 5-positions, respectively Figure 2.1. ^1H NMR (Major isomer only, C_6D_6): δ 83.4 (*4-Pz*, s, 3H), 10.2 (*5-Ph*, br, 3H), 8.6 (*5-Ph*, s, 6H), 7.7 (*5-Ph*, t, 6H), 0.6 (*3-t-Bu*, br, 27H), -9.3 (*BH*, br, 1H). UV-vis (CHCl_3), λ_{max} (ϵ , $\text{M}^{-1}\text{cm}^{-1}$): 322 (3900), 533 (550), 826 (50), 951 (150). $\mu_{\text{eff}} = 3.4(2) \mu_{\text{B}}$ IR (KBr pellet, v/cm^{-1}): 2657 (B-H).

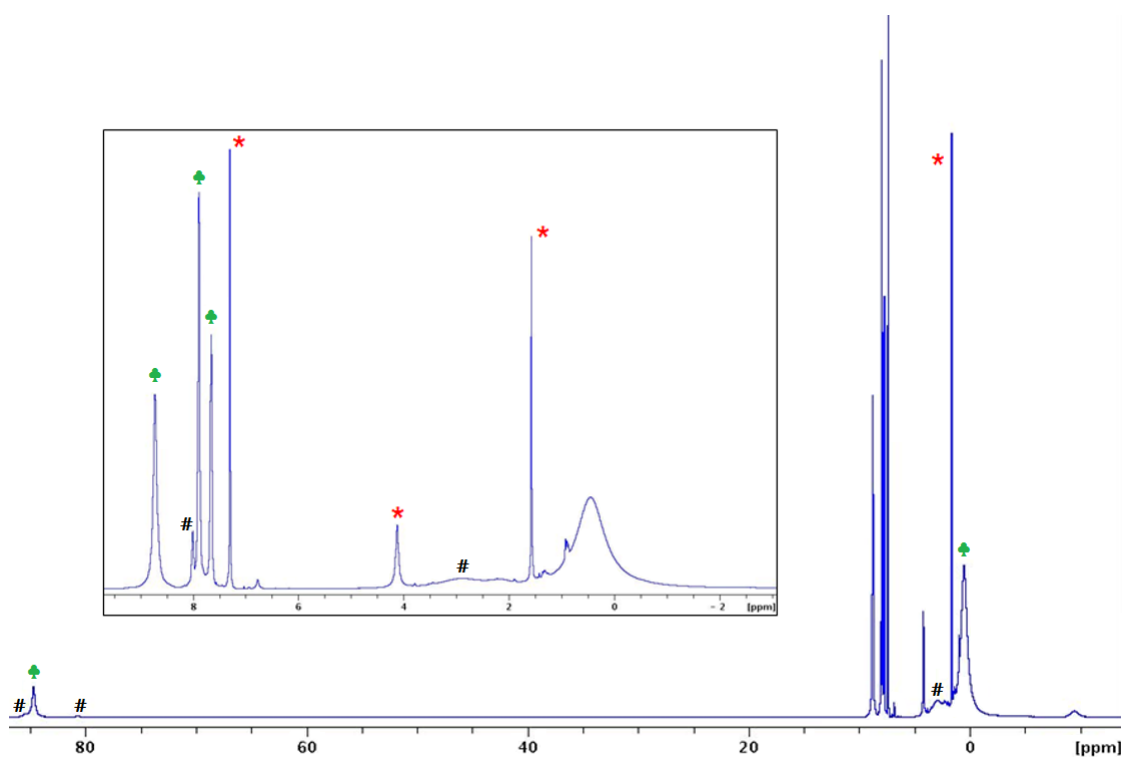


Figure 2.1 ^1H NMR spectrum of crude $[\text{Tp}^{\text{tBu,Ph}}]\text{NiBr}$. * indicates residual solvent signals. ♣ indicates major isomer. # indicates minor isomer. Inset shows diamagnetic region.

2.2.4 [Tp^{Ph,Me}]NiI

[Tp^{Ph,Me}]NiCl (2 g, 3.46 mmol) was added to a 250-mL round bottom flask and dissolved in ~150 mL of acetone. To this solution was added 8 equiv. of solid NaI (4.15 g, 27.70 mmol). The addition resulted in an immediate color change from pink-red to a much darker red and was accompanied by the generation of a white precipitate, NaCl. The reaction mixture was stirred for 4 hours, after which the solvent was removed under vacuum. The reddish-black residue was dissolved in toluene, filtered through Celite and the solvent removed under vacuum to give [Tp^{Ph,Me}]NiI as a dark reddish-black powder, 2.08 g (90%). ¹H NMR (C₆D₆): δ 75.3 (*4-Pz*, s, 3H), 8.7 (*m-Ph*, s, 6H), 8.2 (*5-Me*, s, 9H), 7.0 (*p-Ph*, s, 3H), 3.0 (*o-Ph*, br, 6H), -2.6 (BH, br, 1H). UV-vis (toluene), λ_{\max} (ϵ , M⁻¹cm⁻¹): 334 (1300) 392 (1700), 437 (1500), 519 (1150), 600 (300), 860 (150), 960 (150). IR (KBr pellet, v/cm⁻¹): 2545 (B-H). LIFDI-MS (*m/z*): Calc 668.08, Found 668.09.⁷²

2.3 Synthesis of [Tp^{tBu,Me}]Ni(OH)

A solution of [Tp^{tBu,Me}]NiCl (5.00 g, 9.66 mmol) in 150 mL of CHCl₃ was added to 50 mL of aqueous NaOH (3.09g, 77.27 mmol). The sealed reaction mixture was stirred vigorously for 3 days, during which time the color of the CHCl₃ layer changed from purple to red-brown. The CHCl₃ layer was removed, washed twice with distilled water and once with brine and filtered through Celite. The solvent was removed under vacuum giving a light brown residue, which was further purified by washing with pentane. The solid was recovered by filtration and dried under vacuum yielding [Tp^{tBu,Me}]Ni(OH) as a light brown powder, 4.2 g (87%). X-ray quality crystals were grown by slow evaporation of a concentrated CHCl₃ solution of the metal complex. ¹H NMR (C₆D₆): δ 74.5 (*4-Pz*, s, 3H), 6.5 (*3-t-Bu*, br, 27H), -3.0 (*5-Me*, s,

9H), -22.7 (BH, br, 1H). UV-vis (CHCl₃), λ_{\max} (ϵ , M⁻¹cm⁻¹): 271 (2600), 435 (350), 569 (50), 977 (100). IR (KBr pellet, v/cm⁻¹): 3687 (O–H), 2540 (B–H). $\mu_{\text{eff}} = 3.4(1) \mu_{\text{B}}$. Anal. Calcd for C₂₄H₄₁N₆OBNi: C, 57.74; H, 8.30; N, 16.84. Found: C, 57.80; H, 8.67; N, 16.77.

2.4 [Tp^{tBu,Me}]Ni(NO₃)

Ni(NO₃)₂•6H₂O (7.54 g, 25.9 mmol) was added to a 300 mL methanol solution of potassium hydrotris(3-*tert*-butyl-5-methylpyrazolyl)borate (10 g, 21.6 mmol). Addition of Ni(NO₃)₂•6 H₂O resulted in the rapid precipitation of an orange solid. The solution was stirred for ~2 hours after which the formed solids were recovered by filtration, washed thoroughly with methanol and dried under vacuum. The orange recovered material was dissolved in toluene and filtered through Celite. The solvent was removed under vacuum to give the crude product as an orange powder. The crude material was recrystallized by dissolution in chloroform and layering with methanol. Orange crystals, suitable for X-ray crystallography, grew over the course of four days. The product was recovered by decanting the mother liquor and drying the crystals under vacuum to give 8.47 g (72%) of [Tp^{tBu,Me}]Ni(NO₃). ¹H NMR (CDCl₃): δ 78.6 (4-*Pz*, s, 3H), 2.3 (5-*Me*, s, 9H), 0.3 (3-*t-Bu*, br, 27H), -11.5 (BH, br, 1H). UV-vis (C₆D₆), λ_{\max} (ϵ , M⁻¹cm⁻¹): 348 (400), 433 (100), 482 (150), 746 (50). IR (KBr pellet, v/cm⁻¹): 2549 (B–H).

2.5 [Tp^{tBu,Me}]Ni(NO₂)

To a 100-mL THF solution of [Tp^{tBu,Me}]NiBr (500 mg, 0.89 mmol) was added dropwise 100 mL of a methanol solution of NaNO₂ (491 mg, 7.12 mmol). During the addition the color of the solution changed from deep purple to orange. After stirring

for 15 min, the solvent was removed under vacuum and the orange residue dissolved in toluene. The toluene extract was filtered through Celite to remove formed NaBr and excess NaNO₂ followed by removal of the toluene under vacuum giving [Tp^{tBu,Me}]Ni(NO₂) as an orange powder, (394 mg, 84%). X-ray quality crystals were grown by layering methanol on a CH₂Cl₂ solution of the complex. ¹H NMR (CDCl₃): δ 77.0 (4-Pz, s, 3H), 3.5 (5-Me, s, 9H), -0.2 (3-*t*-Bu, br, 27H), -9.5 (BH, br, 1H). UV-vis (CHCl₃), λ_{max} (ε, M⁻¹cm⁻¹): 505 (150). IR (KBr pellet, ν/cm⁻¹): 2546 (B–H).

2.6 Synthesis of [Tp^{tBu,Me}]Ni(OO*t*Bu)

This new complex was prepared using a modification of the procedure reported by Hikichi, et al.⁴⁴ for the preparation of the analogous [Tp^{iPr₂}]Ni(OO*t*Bu). [Tp^{tBu,Me}]Ni(OH) (500 mg, 1.0 mmol) in 50 mL of toluene was treated with 0.55 mL of a *tert*-BuOOH solution (~5.5 M in decane; ~3 equivalents). Addition of the *tert*-BuOOH resulted in an immediate color change from red-brown to a darker red-orange. The reaction mixture was stirred for 30 min, after which the solvent was removed under vacuum giving a red-brown solid. This crude product was washed with ~2 mL of cold pentane and dried under vacuum yielding [Tp^{tBu,Me}]Ni(OO*t*Bu) as a red-brown powder, 492 mg (86%). X-ray quality crystals were grown by cooling a concentrated pentane solution of the metal complex in a -30 °C freezer for several days. ¹H NMR (C₆D₆): δ 71.4 (4-Pz, s, 3H), 5.8 (3-*t*-Bu, br, 27H), 2.3 (*t*-Bu, s, 9H), 0.5 (5-Me, s, 9H), -16.5 (BH, br, 1H). UV-vis (THF), λ_{max} (ε, M⁻¹cm⁻¹): 271 (1800), 387 (1900), 540 (100), 944 (100). IR (KBr pellet, ν/cm⁻¹): 2541 (B–H).

2.7 Synthesis of Metallacycle

To a 50-mL CH₂Cl₂ solution of [Tp^{tBu,Me}]Ni(OH) (1.0 g, 2.0 mmol), was added aqueous H₂O₂ (30% H₂O₂; 0.4 mL, ~2 equivalents). The mixture was stirred vigorously for 30 min, during which time the color of the solution changed from red-brown to a deeper red. The volatiles were removed under vacuum affording a red powder. The crude powder was further purified by stirring in ~50 mL of pentane for 10 min, then recovered by filtration and dried under vacuum yielding 0.89 g (89%) of metallacycle. ¹H NMR (C₆D₆): δ 73.2 (4-Pz, br, 1H), 70.1 (4-Pz, br, 2H), 15.5 (3-tBu, br, 18H), 5.8 (5-Me, s, 3H), -0.1 (3-t-Bu, br, 6H), -4.6 (5-Me, s, 6H), -15.9 (BH, br, 1H). UV-vis (CHCl₃), λ_{max} (ε, M⁻¹cm⁻¹): 273 (3100), 400 (150), 445 (200), 537 (100), 882 (100). IR (KBr pellet, ν/cm⁻¹): 2517 (B-H). μ_{eff} = 3.3(1) μ_B. Anal. Calcd for C₂₄H₃₉N₆OBNi: C, 57.97; H, 7.92; N, 16.91. Found: C, 57.62; H, 7.44; N, 16.53.

2.8 Synthesis of Monovalent Nickel Complexes

2.8.1 [Tp^{tBu,Me}]Ni(CN*t*Bu)

A suspension of [Tp^{tBu,Me}]NiBr (500 mg, 0.89 mmol) in 50 mL of toluene was added to a 100-mL round bottom flask containing 4 equivalents of a 0.3% sodium-mercury amalgam (Na, 82 mg; Hg, 27.3 g). To this was added ~0.1 mL THF and *tert*-butyl isocyanide (121 μL, 1.07 mmol). (*nota bene*, total reaction time and yield are highly dependent on the amount of THF added. Addition of THF in excess of ~0.1-0.2 mL resulted in significant over-reduction and reduced yields). The reaction mixture was stirred for 3 hours, during which time all of the [Tp^{tBu,Me}]NiBr was drawn into solution and the color of the reaction mixture changed from purple to yellow. The yellow solution was separated from the amalgam via cannula transfer and filtered through Celite. The solvent was removed under vacuum yielding a yellow residue,

which was dissolved in ~40 mL of pentane and filtered through an APTS silica gel plug. The plug was washed with pentane, the filtrate and washings combined and the solvent removed under vacuum giving $[\text{Tp}^{\text{tBu,Me}}]\text{Ni}(\text{CN}t\text{Bu})$ as a light yellow powder, 455 mg (90%). X-ray quality crystals were grown by slow evaporation of a concentrated benzene solution of the metal complex. ^1H NMR (C_6D_6): δ 38.8 (BH, br, 1H) 17.5 (4-Pz, s, 3H), 15.8 (*t*-Bu, s, 9H), 15.4 (5-Me, s, 9H), -10.0 (3-*t*-Bu, br, 27H). UV-vis (THF), λ_{max} (ϵ , $\text{M}^{-1}\text{cm}^{-1}$): 263 (9800). IR (KBr pellet, v/cm^{-1}): 2546 (B-H), 2065 ($\text{C}\equiv\text{N}$). $\mu_{\text{eff}} = 2.26(8) \mu_{\text{B}}$. LIFDI-MS (m/z): Calc 564.35, Found 564.39.

2.8.2 $[\text{Tp}^{\text{tBu,Me}}]\text{Ni}(\text{CNCy})$

A suspension of $[\text{Tp}^{\text{tBu,Me}}]\text{NiBr}$ (500 mg, 0.89 mmol) in 50 mL of toluene was added to a 100-mL round bottom flask containing 4 equivalents of a 0.3% sodium mercury amalgam (Na, 82 mg; Hg, 27.3 g). To this was added, ~0.1 mL THF and cyclohexyl isocyanide (133 μL , 1.07 mmol). The reaction mixture was stirred for 4 hours, during which time all of the $[\text{Tp}^{\text{tBu,Me}}]\text{NiBr}$ was drawn into solution and the color of the reaction mixture changed from purple to yellow. The yellow solution was separated from the amalgam via cannula transfer and filtered through Celite. The solvent was removed under vacuum yielding a yellow residue which was dissolved in ~150 mL of pentane and filtered through an APTS coated silica gel plug. The plug was washed with pentane, the filtrate and washings combined and the solvent removed under vacuum giving $[\text{Tp}^{\text{tBu,Me}}]\text{Ni}(\text{CNCy})$ as a light yellow solid, 416 mg (79%). X-ray quality crystals were grown by slow evaporation of a concentrated benzene solution of the metal complex. ^1H NMR (C_6D_6): δ 38.2 (BH, br, 1H), 20.4 (Cy, s, 2H), 17.6 (4-Pz, s, 3H), 16.3 (Cy, br, 2H), 15.2 (5-Me, s, 9H), 10.7 (Cy, br, 1H), 8.0 (Cy, s, 2H), 6.7 (Cy, s, 1H), -9.8 (3-*t*-Bu, br, 27H), -11.6 (Cy, br, 1H). UV-vis (THF), λ_{max} (ϵ ,

$M^{-1}cm^{-1}$): 263 (9700). IR (KBr pellet, ν/cm^{-1}): 2544 (B–H), 2085 (C \equiv N). $\mu_{eff} = 2.24(8)$ μ_B . LIFDI-MS (m/z): Calc 590.37, Found 590.41.

2.8.3 Synthesis of [Tp^{tBu,Me}]Ni(CO)

[Tp^{tBu,Me}]NiBr (500 mg, 0.89 mmol) and KC₈ (0.144 g, 1.07 mmol) were combined by grinding their solids in a mortar and pestle and transferred, along with a stir bar, to one side of a double-sided Schlenk flask. To the other side of the flask was added ~50 mL of THF. The flask was flushed with CO gas for 2 minutes then transferred to a stir plate. While stirring, the flask was tilted such that the THF spilled over into the side containing the [Tp^{tBu,Me}]NiBr and KC₈. The color of the resulting solution changed from violet to pale yellow over the course of ~2 min. The mixture was stirred for an additional 30 minutes, after which the solution was removed from the reaction vessel via cannula transfer and filtered through Celite. The solvent was removed under vacuum yielding a pale yellow residue, which was dissolved in pentane and filtered through an APTS coated silica gel plug. The plug was washed with pentane, the filtrate and washings combined and the solvent removed under vacuum giving [Tp^{tBu,Me}]Ni(CO) as a pale yellow solid, 342 mg (75%). ¹H NMR (C₆D₆): δ 45.7 (BH, br, 1H) 17.8 (4-Pz, s, 3H), 21.3 (5-Me, s, 9H), -11.5 (3-t-Bu, br, 27H). UV-vis (THF), λ_{max} (ϵ , $M^{-1}cm^{-1}$): 351 (2200). IR (KBr pellet, ν/cm^{-1}): 2559 (B–H), 1993 (C \equiv O). $\mu_{eff} = 2.17(5)$ μ_B .

2.8.4 Synthesis of [Tp^{tBu,Ph}]Ni(CNtBu)

A suspension of [Tp^{tBu,Ph}]NiBr (500 mg, 0.67 mmol, ~87:13 mixture of isomers, *vide supra*) in 50 mL of toluene was added to a 100-mL round bottom flask containing 5 equivalents of a 0.3% sodium mercury amalgam (Na, 77 mg; Hg, 25.6 g).

To this solution was added *tert*-butyl isocyanide (113 μL , 1.0 mmol). The reaction mixture was stirred for 3 hours, during which time all of the $[\text{Tp}^{\text{tBu,Ph}}]\text{NiBr}$ was drawn into solution and the color of the reaction mixture changed from purple to yellow. The yellow solution was separated from the amalgam via cannula transfer and filtered through Celite. The volatiles were removed under vacuum giving a yellow residue, which was dissolved in 60 mL of pentane and filtered through an APTS coated silica gel plug. The plug was washed with pentane, the filtrate and washings combined and cooled to -30°C in a freezer. Over the course of one week, yellow crystals precipitated from the solution and were recovered by filtration, yielding 298 mg of $[\text{Tp}^{\text{tBu,Ph}}]\text{Ni}(\text{CN}t\text{Bu})$. The filtrate was concentrated to 20 mL under vacuum and subjected to a second week at -30°C affording an additional 54 mg of crystals for a total yield of 352 mg (70%) (the crystals consisted of a single isomer, $[\text{Tp}^{\text{tBu,Ph}}]\text{Ni}(\text{CN}t\text{Bu})$ as deduced by ^1H NMR spectroscopy, *vide infra*). X-ray quality crystals were selected from the bulk recrystallization of the metal complex. ^1H NMR (C_6D_6): δ 38.1 (BH, br, 1H), 17.8 (4-Pz, s, 3H), 15.4 (*t*-Bu, s, 9H), 14.9 (5-Ph, s, 6H), 10.9 (5-Ph, s, 6H), 10.0 (5-Ph, s, 3H), -9.5 (3-*t*-Bu, br, 27H). UV-vis (THF), λ_{max} (ϵ , $\text{M}^{-1}\text{cm}^{-1}$): 241 (9900), 314 (sh, 1850). IR (KBr pellet, v/cm^{-1}): 2611 (B-H), 2100 ($\text{C}\equiv\text{N}$). $\mu_{\text{eff}} = 2.12(9) \mu_{\text{B}}$.

2.8.5 Synthesis of $[\text{Tp}^{\text{Ph,Me}}]\text{Ni}(\text{PPh}_3)$

$[\text{Tp}^{\text{Ph,Me}}]\text{NiI}$ (500 mg, 0.75 mmol) and PPh_3 (216 mg, 0.82 mmol) were suspended in ~ 20 mL of toluene. To this mixture was added 5 equivalents of a 0.3% sodium mercury amalgam (Na, 86 mg; Hg, 28.7 g). The reaction mixture was stirred vigorously for 45 min during which time all of the starting material was drawn into solution and the color changed from dark red to bright yellow. The reaction solution

was separated from the amalgam by filtration through Celite, transferred to a 250-mL round bottom flask and layered with ~120 mL of pentane. The product, $[\text{Tp}^{\text{Ph,Me}}]\text{Ni}(\text{PPh}_3)$, precipitated as a bright yellow, microcrystalline powder over the course of 1 week. The product was collected by filtration and dried under vacuum giving $[\text{Tp}^{\text{Ph,Me}}]\text{Ni}(\text{PPh}_3)$ as a bright yellow powder, 433 mg (72%). $^1\text{H NMR}$ (C_6D_6): δ 49.2 (BH, b, 1), 18.5 (5-Me, s, 9), 13.9 (4-Pz, s, 3), 9.0 (3-Ph, s, 3), 8.2 (Ph, b, 6), 7.6 (3-Ph, s, 6), 5.3 (Ph, s, 3), 4.0 (Ph, s, 6), -18.15 (3-Ph, s, 6H). UV-vis (toluene), λ_{max} (ϵ , $\text{M}^{-1}\text{cm}^{-1}$): 391 (3318) nm. IR (KBr pellet, v/cm^{-1}): 2542 (B-H). $\mu_{\text{eff}} = 2.2(2) \mu_{\text{B}}$. LIFDI-MS (m/z): Calc 803.27, Found 803.27.⁷²

2.8.6 Synthesis of $[\text{Tp}^{\text{Ph,Me}}]\text{Ni}(\text{CO})$

$[\text{Tp}^{\text{Ph,Me}}]\text{Ni}(\text{PPh}_3)$ (180 mg, 0.22 mmol) was added to a 50-mL Schlenk flask and dissolved in ~5 mL of THF. The flask was purged with CO for 2 minutes, followed by stirring for 30 minutes. The addition of CO resulted in a color change from bright yellow to a much paler yellow. The solvent and excess CO were removed under vacuum and the product washed with pentane to remove free PPh_3 . After washing, the product was dried under vacuum giving $[\text{Tp}^{\text{Ph,Me}}]\text{Ni}(\text{CO})$ as a pale yellow powder, 106 mg (83%). $^1\text{H NMR}$ (C_6D_6): δ 32.8 (BH, br, 1H), 19.0 (4-Pz, s, 3H), 16.9 (5-Me, s, 9.0), 8.0 (*m*-Ph, s, 6H), 7.3 (*p*-Ph, s, 3H), -8.9 (*o*-Ph, b, 6H). UV-vis (THF), λ_{max} (ϵ , $\text{M}^{-1}\text{cm}^{-1}$): 237 (47,500), 343 (sh, 2600 cm^{-1}). IR (KBr pellet, v/cm^{-1}): 2527 (B-H), 2005 ($\text{C}\equiv\text{O}$). $\mu_{\text{eff}} = 2.1(1) \mu_{\text{B}}$. LIFDI-MS (m/z): Calc 569.18, Found 569.18.⁷²

2.9 Synthesis of Carbamate Complexes, [Tp^{tBu,Me}]Ni(O₂CN(H)R), R = *t*Bu, Cy

2.9.1 [Tp^{tBu,Me}]Ni(O₂CN(H)*t*Bu).

Route A: PhIO (319 mg, 1.45 mmol) was added in one portion to a toluene (15 mL) solution of [Tp^{tBu,Me}]Ni(CN*t*Bu) (410 mg, 0.73 mmol). The reaction mixture was stirred for 1 day during which time the color changed from yellow to a deeper, yellow-orange. The reaction mixture was filtered through Celite and the volatiles removed under vacuum giving an oily, yellow-orange residue. The residue was dissolved in a minimal volume of pentane, transferred to a scintillation vial and cooled in a -30 °C freezer. Cube shaped, yellow crystals deposited on the reaction vessel walls over a period of 2 days. The solvent was decanted and the crystals dried under vacuum affording [Tp^{tBu,Me}]Ni(O₂CN(H)*t*Bu), 278 mg (64%). ¹H NMR (C₆D₆): δ 80.7 (NH, br, 1H), 69.9 (4-*Pz*, s, 3H), 0.8 (*t*-BuNH, s, 9H), 0.4 (3-*t*-Bu, br, 27H), -0.7 (5-*Me*, s, 9H), -13.0 (BH, br, 1H). UV-vis (CHCl₃), λ_{max} (ε, M⁻¹cm⁻¹): 433 (200), 755 (50). IR (KBr pellet, ν/cm⁻¹): 3275 (N-H), 2544 (B-H). Anal. Calcd for C₂₉H₅₀N₇O₂BNi: C, 58.21; H, 8.44; N, 16.39. Found: C, 58.66; H, 8.47; N, 16.44.

Route B: To a suspension of [Tp^{tBu,Me}]Ni(OH) (500 mg, 1.00 mmol) in 10 mL of THF, was added *tert*-butyl isocyanate (137 μL, 1.2 mmol). The reaction was stirred for 1 day, during which time the color of the solution changed from red-brown to bright yellow. The volatiles were removed under vacuum affording a yellow powder. The crude product was recrystallized from pentane at -30 °C, in the same manner as *Route A*, yielding [Tp^{tBu,Me}]Ni(O₂CN(H)*t*Bu), 454 mg (80%).

2.9.2 [Tp^{tBu,Me}]Ni(O₂CN(H)Cy).

Route A: PhIO (277 mg, 1.3 mmol) was added in one portion to a toluene (15 mL) solution of [Tp^{tBu,Me}]Ni(CNCy) (372 mg, 0.6 mmol). The reaction mixture was

stirred for 1 day, during which time the color changed from yellow to orange. The reaction mixture was filtered through Celite and the volatiles removed under vacuum giving a red-orange residue. The residue was washed with a small volume of pentane and dried under vacuum yielding $[\text{Tp}^{\text{tBu,Me}}]\text{Ni}(\text{O}_2\text{CN}(\text{H})\text{Cy})$ as a yellow powder, 229 mg (58%). ^1H NMR (C_6D_6): δ 70.1 (NH, br, 1H), 68.7 (4-Pz, s, 3H), 13.1 (Cy, br, 1H), 4.2 (Cy, s, 2H), 3.8 (Cy, s, 2H), 3.3 (Cy, s, 4H), 0.4 (3-*t*-Bu, br, 27H), -0.5 (5-Me, s, 9H), -12.6 (BH, br, 1H). UV-vis (CHCl_3), λ_{max} (ϵ , $\text{M}^{-1}\text{cm}^{-1}$): 429 (150), 756 (50). IR (KBr pellet, v/cm^{-1}): 3271 (N–H), 2542 (B–H). Anal. Calcd for $\text{C}_{31}\text{H}_{52}\text{N}_7\text{O}_2\text{BNi}$: C, 59.63; H, 8.41; N, 15.71. Found: C, 59.68; H, 8.42; N, 15.48.

Route B: To a suspension of $[\text{Tp}^{\text{tBu,Me}}]\text{Ni}(\text{OH})$ (500 mg, 1.00 mmol) in 10 mL of THF, was added cyclohexyl isocyanate (192 μL , 1.5 mmol). The reaction was stirred for 1 day, during which time the color of the solution changed from red-brown to an orange-yellow. The solvent was removed under vacuum giving a yellow powder. The crude product was washed with a small amount of pentane and dried under vacuum yielding $[\text{Tp}^{\text{tBu,Me}}]\text{Ni}(\text{O}_2\text{CN}(\text{H})\text{Cy})$ as a yellow powder, 453 mg (72%).

2.10 Reaction of Monovalent Nickel Complexes with Dioxygen

2.10.1 $[\text{Tp}^{\text{tBu,Me}}]\text{Ni}(\text{O}_2)$

A suspension of $[\text{Tp}^{\text{tBu,Me}}]\text{Ni}(\text{CN}t\text{Bu})$ (508 mg, 1.0 mmol) in 10 mL of pentane was cooled to -78 °C. Dry dioxygen was bubbled through the solution for 5 minutes, during which time the color changed from yellow to brown with the formation of a brown precipitate. The reaction mixture was allowed to warm to room temperature and stirred for an additional 20 minutes. The precipitate was recovered by filtration, washed with MeOH and pentane and dried under vacuum yielding $[\text{Tp}^{\text{tBu,Me}}]\text{Ni}(\text{O}_2)$ as

a brown, air- and moisture-stable powder, 427 mg (92%). X-ray quality crystals were grown by slow vapor diffusion of Et₂O into a concentrated CHCl₃ solution of the metal complex. ¹H NMR (CDCl₃): δ 38.4 (*4-Pz*, br, 3H), 2.9 (*5-Me*, s, 9H), 1.0 (*3-t-Bu*, br, 27H), -2.0 (*BH*, br, 1H). UV-vis (CHCl₃), λ_{max} (ε, M⁻¹cm⁻¹): 325 (900), 870 (150). IR (KBr pellet, v/cm⁻¹): 2544 (B–H), 1000 (¹⁶O–¹⁶O) (945 (¹⁸O–¹⁸O)). μ_{eff} = 2.3(1) μ_B. Anal. Calcd for C₂₄H₄₀O₂N₆BNi: C, 56.06; H, 7.86; N, 16.35. Found: C, 56.16; H, 8.04; N, 16.15.

2.10.2 [Tp^{tBu,Ph}]Ni(O₂)

A solution of [Tp^{tBu,Ph}]Ni(CN*t*Bu) (185 mg, 0.246 mmol) in ~3 mL of toluene was cooled to -78 °C. Dry dioxygen was passed through the solution for 2 minutes, during which time the color changed from yellow to brown with the formation of a brown precipitate. The reaction mixture was warmed to room temperature and stirred for an additional 20 minutes. 15 mL of pentane were added to precipitate additional product and the reaction vessel was placed in a -20°C freezer overnight. The product was recovered by filtration, washed with cold pentane and dried under vacuum yielding [Tp^{tBu,Ph}]Ni(O₂) as a brown, air- and moisture-stable powder, 164 mg (95%). X-ray quality crystals were grown by layering pentane on a concentrated C₆D₆ solution of the metal complex in an NMR tube. ¹H NMR (C₆D₆): δ 38.0 (*4-Pz*, br, 3H), 7.3 (*5-Ph*, s, 6H), 7.0 (*5-Ph*, s, 9H), 1.4 (*3-t-Bu*, br, 27H), -1.8 (*BH*, br, 1H). UV-vis (CHCl₃), λ_{max} (ε, M⁻¹cm⁻¹): 325 (1000), 873 (150). IR (KBr pellet, v/cm⁻¹): 2627 (B–H), 1001 (O–O). μ_{eff} = 2.2(1) μ_B. Anal. Calcd for C₃₉H₄₆N₆O₂BNi: C, 66.87; H, 6.63; N, 12.00. Found: C, 66.75; H, 6.51; N, 11.49.

2.10.3 [Tp^{Ph,Me}]Ni(O₂)

[Tp^{Ph,Me}]Ni(CO) (150 mg, 0.26 mmol) was added to a 20-mL scintillation vial and suspended in ~15 mL of pentane. Dry dioxygen was bubbled through the suspension for 5 minutes and the mixture stirred for an additional 20 minutes. Upon addition of O₂, the color of the suspended material changed from pale yellow to brown. The product, which had very poor solubility in pentane, was recovered by filtration and dried under vacuum giving [Tp^{Ph,Me}]Ni(O₂) as a brown powder, 137 mg (91%). ¹H NMR (C₆D₆): δ 34.9 (*4-Pz*, br, 3H), 7.6 (*p-Ph*, s, 3H), 7.4 (*o-Ph*, br), 6.9 (*m-Ph*, s, 6H), 2.5 (*5-Me*, s, 9H), -1.8 (*BH*, br, 1H). UV-vis (CHCl₃), λ_{max} (ε, M⁻¹cm⁻¹): 311 (sh, 1550), 874 (150). μ_{eff} = 2.3(1) μ_B. IR (KBr pellet, ν/cm⁻¹): 2531 (B–H), 991 (O–O).

2.11 O-Atom Transfer by [Tp^{tBu,Me}]Ni(O₂)

2.11.1 Reaction of [Tp^{tBu,Me}]Ni(O₂) with PR₃ (R = Me, Et, Cy)

2.11.1.1 Reaction of [Tp^{tBu,Me}]Ni(O₂) with PMe₃ (Stoichiometric).

[Tp^{tBu,Me}]Ni(O₂) (100 mg, 0.19 mmol) was added to 10 mL of a toluene stock solution containing trimethylphosphine (0.019 M) and pyridine (1.0 M), in a 25 mL scintillation vial. The pyridine was added to preclude OPMe₃ binding to the metallacycle, a minor product resulting from C-H activation of a ligand *tert*-butyl group. The reaction mixture was stirred for 24 hours at room temperature. Stirring was discontinued and aliquots from both the crude reaction mixture and the PMe₃ stock solution were removed and subjected to ³¹P{¹H} NMR and ¹H NMR analysis. ³¹P{¹H} NMR analysis was performed directly on the stock and reaction solutions respectively, with a capillary tube containing phosphoric acid (85% H₃PO₄ in D₂O)

used as a spectral reference and internal standard. $^{31}\text{P}\{^1\text{H}\}$ NMR spectral analysis indicated production of $\text{O}=\text{PMe}_3$ in 90% yield. ^1H NMR analysis was performed on samples of the reaction mixture after the volatiles were removed under vacuum. The major nickel-containing products were $[\text{Tp}^{\text{tBu,Me}}]\text{Ni}(\text{OH})$ and the metallacycle, which accounted for ~87% and ~13% of the nickel containing products, respectively. Metal products were identified on the basis of ^1H NMR spectral comparison of the crude reaction material to independently prepared samples.

2.11.1.2 Reaction of $[\text{Tp}^{\text{tBu,Me}}]\text{Ni}(\text{O}_2)$ with PEt_3 .

$[\text{Tp}^{\text{tBu,Me}}]\text{Ni}(\text{O}_2)$ (100 mg, 0.19 mmol) was added to 10 mL of a toluene stock solution containing triethylphosphine (0.019 M) and pyridine (1.0 M), in a 25 mL scintillation vial. The pyridine was added to preclude OPEt_3 binding to the metallacycle. The reaction and workup were performed according to the same procedure used for PMe_3 , *vide supra*. $^{31}\text{P}\{^1\text{H}\}$ NMR spectroscopy established a 75% yield of $\text{O}=\text{PEt}_3$. The major metal products were determined to be $[\text{Tp}^{\text{tBu,Me}}]\text{Ni}(\text{OH})$ and the metallacycle, which accounted for ~77% and ~23% of the nickel containing products, respectively.

2.11.1.3 Reaction of $[\text{Tp}^{\text{tBu,Me}}]\text{Ni}(\text{O}_2)$ with PCy_3 .

$[\text{Tp}^{\text{tBu,Me}}]\text{Ni}(\text{O}_2)$ (100 mg, 0.19 mmol) was added to 10 mL of a toluene stock solution containing tricyclohexylphosphine (0.019 M) and pyridine (1.0 M), in a 25 mL scintillation vial. The reaction mixture was stirred for 24 hours at 55 °C. After 24 hours, heating was discontinued and the reaction was worked up according to the procedure used for PMe_3 and PEt_3 , *vide supra*. $^{31}\text{P}\{^1\text{H}\}$ NMR spectroscopy established a 62% yield of PCy_3 . The major metal products were determined to be

$[\text{Tp}^{\text{tBu,Me}}]\text{Ni}(\text{OH})$ and the metallacycle, which accounted for ~67% and ~33% of the nickel containing products, respectively.

2.11.1.4 Reaction of $[\text{Tp}^{\text{tBu,Me}}]\text{Ni}(\text{O}_2)$ with excess PMe_3 .

$[\text{Tp}^{\text{tBu,Me}}]\text{Ni}(\text{O}_2)$ (100 mg, 0.19 mmol) was added to 10 mL of a toluene stock solution containing trimethylphosphine (0.039 M) and pyridine (1.0 M, to prevent $\text{O}=\text{PMe}_3$ ligating to metal products) in a 25 mL scintillation vial. The reaction and workup were performed according to the same procedure used in the stoichiometric reactions. This procedure was repeated with stock solutions containing higher PMe_3 concentrations (0.078 M and 0.389 M, 4 equivalents and 20 equivalents, respectively). Results are summarized in Table 2.1.

Table 2.1 Extent of oxygen atom transfer in reactions with excess PMe_3 .

Ratio of $[\text{Tp}^{\text{tBu,Me}}]\text{Ni}(\text{O}_2)$ to PMe_3	Equivalents of OPMe_3 generated per equivalent of $[\text{Tp}^{\text{tBu,Me}}]\text{Ni}(\text{O}_2)$
1:2	1.26
1:4	1.54
1:20	1.98

2.11.1.5 Reaction of $[\text{Tp}^{\text{tBu,Me}}]\text{Ni}(\text{O}_2)$ with excess PMe_3 and t-BuNC: Monovalent Trapping Experiment.

$[\text{Tp}^{\text{tBu,Me}}]\text{Ni}(\text{O}_2)$ (100 mg, 0.19 mmol) was added to 10 mL of a toluene stock solution containing trimethylphosphine (0.389 M) and tert-butyl isonitrile (44 μL , 0.39 mmol). The reaction was stirred for 24 hours during which time the color changed

from red-brown to yellow. The volatiles were removed under vacuum to give a yellow-orange residue. A sample of the crude residue was taken for direct ^1H NMR analysis. The remainder of the residue was extracted into pentane and filtered through a silica gel plug to give a bright yellow solution. Solvent was removed from the filtered sample under vacuum to give a yellow powder which was also analyzed by ^1H NMR. The major nickel-containing product in both the crude and purified samples was determined to be $[\text{Tp}^{\text{tBu,Me}}]\text{Ni}(\text{CNtBu})$ with identification made on the basis of ^1H NMR spectral to the independently prepared complex.

2.11.1.6 Reaction of $[\text{Tp}^{\text{tBu,Me}}]\text{Ni}(\text{O}_2)$ with excess PMe_3 and excess O_2 .

$[\text{Tp}^{\text{tBu,Me}}]\text{Ni}(\text{O}_2)$ (100 mg, 0.19 mmol) was transferred to a scintillation vial and placed under a dry dioxygen purge. To the vial was added 10 mL of a toluene stock solution containing trimethylphosphine (0.389 M) via gas-tight syringe. The reaction was stirred for 10 min during which time the color changed from red-brown to yellow-orange. An aliquot was removed from the reaction and subjected to $^{31}\text{P}\{^1\text{H}\}$ NMR analysis following the same procedures used in the stoichiometric reactions. This procedure was repeated with stock solutions containing one and two equivalents of *tert*-butyl isonitrile (44 μL , 0.39 mmol and 88 μL , 0.78 mmol), respectively. A control sample without $[\text{Tp}^{\text{tBu,Me}}]\text{Ni}(\text{O}_2)$ was run under otherwise identical conditions and resulted in negligible auto-oxidation of the phosphine. Results are shown in Table 2.2.

Table 2.2 Extent of oxygen atom transfer in reactions with excess PMe_3 and excess O_2 .

Equivalents of <i>tert</i> -butyl isonitrile added per molecule of $[\text{Tp}^{\text{tBu,Me}}]\text{Ni}(\text{O}_2)$	Equivalents of OPMe_3 generated per equivalent of $[\text{Tp}^{\text{tBu,Me}}]\text{Ni}(\text{O}_2)$
0	3.3
2	5.6
4	8

2.11.2 Reaction of $[\text{Tp}^{\text{tBu,Me}}]\text{Ni}(\text{O}_2)$ with NO.

$[\text{Tp}^{\text{tBu,Me}}]\text{Ni}(\text{O}_2)$ (100 mg, 0.19 mmol) was added to a custom made reaction flask and dissolved ~50 mL of toluene. The reaction flask was attached to a glass bulb of known volume for use as a gas reservoir. The gas bulb was separated from the reaction compartment by a lower stopcock and from its ground glass vacuum joint by an upper stopcock. The reaction vessel was attached to a high vacuum line and degassed via three freeze-pump-thaw cycles. The gas bulb was isolated from the reaction compartment by closing the lower stopcock. The bulb was charged with 1.5 equivalents of NO gas from a NO tank attached to the high vacuum line, using a mercury barometer to measure the pressure. Once charged and isolated from the high-vacuum line, the stopcock separating the gas bulb from the reaction compartment was opened to deliver the NO to the $[\text{Tp}^{\text{tBu,Me}}]\text{Ni}(\text{O}_2)$ solution. The reaction solution was stirred for 24 hours, during which time the color of the solution changed from red-brown to yellow-green. The volatiles were removed under vacuum to give a green residue, which was subjected to ^1H NMR analysis. The major products were determined to be $[\text{Tp}^{\text{tBu,Me}}]\text{Ni}(\text{NO}_3)$ and $[\text{Tp}^{\text{tBu,Me}}]\text{Ni}(\text{NO}_2)$ in an approximate ratio of

2:1. Product identification was made by comparing the ^1H NMR spectrum of the crude reaction mixture to spectra of the independently prepared complexes.

2.11.3 Reaction of $[\text{Tp}^{\text{tBu,Me}}]\text{Ni}(\text{O}_2)$ with $[\text{Tp}^{\text{tBu,Me}}]\text{Ni}(\text{CN}t\text{Bu})$.

$[\text{Tp}^{\text{tBu,Me}}]\text{Ni}(\text{CN}t\text{Bu})$ (55 mg, 9.7×10^{-2} mmol) and $[\text{Tp}^{\text{tBu,Me}}]\text{Ni}(\text{O}_2)$ (50 mg, 9.7×10^{-2} mmol) were added to a scintillation vial and dissolved in ~ 10 mL of toluene. The solution was stirred for 24 hours, during which time the color of the solution changed from a red-brown to a lighter red-orange. The volatiles were removed under vacuum to give a red-orange residue, which was subjected to analysis by ^1H NMR. The major product was determined to be $[\text{Tp}^{\text{tBu,Me}}]\text{Ni}(\text{OH})$ with smaller quantities of metallacycle and $[\text{Tp}^{\text{tBu,Me}}]\text{Ni}(\text{O}_2\text{CN}(\text{H})t\text{Bu})$ also present. The approximate ratio of species in the crude product mixture was 6:2:1 for $[\text{Tp}^{\text{tBu,Me}}]\text{Ni}(\text{OH})$, metallacycle and $[\text{Tp}^{\text{tBu,Me}}]\text{Ni}(\text{O}_2\text{CN}(\text{H})t\text{Bu})$, respectively. Product identification was made by comparing the ^1H NMR spectrum of the crude reaction mixture to spectra of the independently prepared complexes.

2.12 C-H Activation by $[\text{Tp}^{\text{tBu,Me}}]\text{Ni}(\text{O}_2)$

2.12.1 Reaction of $[\text{Tp}^{\text{tBu,Me}}]\text{Ni}(\text{O}_2)$ with 1,4-cyclohexadiene (CHD)

A solution of 1,4-cyclohexadiene (CHD) was prepared by injecting 9.2 μL (9.7×10^{-2} mmol) of CHD into 10 mL of *d*₈-toluene in a scintillation vial, followed by addition of hexamethylbenzene as an internal standard. An aliquot was removed and transferred to a J. Young tube for initial ^1H NMR analysis to determine the initial concentration of benzene impurity and the ratio of CHD to hexamethylbenzene. The aliquot was returned to the bulk solution, to which was added $[\text{Tp}^{\text{tBu,Me}}]\text{Ni}(\text{O}_2)$ (100 mg, 0.19 mmol). The reaction vial was heated to 60 $^\circ\text{C}$ in a temperature-controlled oil

bath and stirred for 24 hours, during which time the color of the solution changed from a red-brown to a lighter red-orange. Following the reaction, a 2nd aliquot was removed from the bulk solution and subjected to analysis by ¹H NMR spectroscopy. The major product was determined to be the metallacycle along with a lesser quantity of [Tp^{tBu,Me}]Ni(OH) with the two products forming in a 6:1 ratio, respectively. Metal product identification was made by comparing the ¹H NMR spectrum of the crude reaction mixture to spectra of the independently prepared complexes. Analysis of the aromatic region showed a large increase in the concentration of benzene (65% yield based on comparison to HMB), consistent with C-H activation of CHD forming C₆H₆.

2.12.2 Reaction of [Tp^{tBu,Me}]Ni(O₂) with 9,10-dihydroanthracene (DHA)

[Tp^{tBu,Me}]Ni(O₂) (50 mg, 9.7×10⁻² mmol) was added to 10 mL of a benzene stock solution containing 9,10-dihydroanthracene (0.88 mg/mL, 4.9 mM) and hexamethylbenzene in a 25 mL scintillation vial. The reaction mixture was stirred for 5 min at room temperature to completely dissolve the [Tp^{tBu,Me}]Ni(O₂). An aliquot was removed for initial ¹H NMR spectral analysis, after which the reaction vial was sealed and heated to 40 °C in a temperature-controlled oil bath. The reaction temperature was maintained at 40 °C for ~72 hours, after which the temperature was raised to 60 °C and maintained for an additional 48 hours. Aliquots were removed from the reaction during and after the heating period for ¹H NMR analysis in order to determine reaction progress. This procedure was repeated with double and triple the concentration of [Tp^{tBu,Me}]Ni(O₂). The production of 9,10-anthraquinone was verified by GC-MS and ¹H NMR spectral comparison to authentic material. Yield of anthraquinone was based on comparison to the hexamethylbenzene internal standard. Results are summarized in Table 2.3.

Table 2.3 9,10-anthraquinone yield (AQ) versus reaction stoichiometry.

Ratio of [Tp ^{tBu,Me}]NiO ₂ to DHA	Yield of AQ (% , average of triplicate trials)	Amount of [Tp ^{tBu,Me}]Ni(O ₂) Remaining After Reaction (%)
2	43	0
4	75	0
6	95	22

2.12.3 Kinetic Studies of the Reaction [Tp^{tBu,Me}]Ni(O₂) with DHA

All kinetic runs were conducted under pseudo-first order conditions with DHA present in at least twenty-fold excess. In a typical run, the requisite quantity of DHA was weighed into a 20-mL scintillation vial and dissolved in 5 mL of a stock solution containing [Tp^{tBu,Me}]Ni(O₂) at a concentration of 2 mg/mL (3.89 mM) in toluene. This solution was transferred to an air-free cuvette, which was subsequently inserted into a Unisoku CoolSpeK UV Cryostat attached to a Varian Cary 50 UV-vis Spectrophotometer. For variable DHA concentration runs, the solution was heated to 60 °C. For variable temperature runs, the solution was heated to the target temperature. The progress of the reaction was monitored by tracking the decrease in absorbance at 505 nm. Pseudo first-order rate constants (k_{obs} , s⁻¹) were determined via the initial rate method. The absorbance at 505 nm was plotted against reaction time for the first 10% of each kinetic run giving linear plots. Data analysis was performed following the procedure outlined by Borovik and coworkers.⁹⁷ Values for k_{obs} were determined from the slope/4 of the least-square fit of the aforementioned plots, where $A = 4(k_{\text{obs}})(t)$. The factor of 4 was included to account for the stoichiometry of the reaction (4:1, [Tp^{tBu,Me}]Ni(O₂):DHA). The second-order rate constant at 60 °C (k , M⁻¹s⁻¹) was derived from the slope of the linear least-square fit of k_{obs} data at various concentrations of DHA (78 – 311 mM) using the relationship $k_{\text{obs}} = k[\text{DHA}]$. The

second-order rate constant was divided by 4 to normalize for the 4 reactive C—H bonds per DHA molecule. The enthalpy and entropy of activation (ΔH^\ddagger and ΔS^\ddagger , respectively) were derived from an Eyring plot of $\ln(k/T)$ vs $1/T$ where T is the temperature (K) at which the experiments were carried out (25 to 65 °C in 5 °C increments) and k is the second-order rate constant (determined from $k_{\text{obs}}/[\text{DHA}]$, $[\text{DHA}] = 156 \text{ mM}$) for each reaction.

2.12.4 Reaction of $[\text{Tp}^{\text{tBu,Me}}]\text{Ni}(\text{O}_2)$ with 9,10-dihydroxy-9,10-dihydroanthracene.

$[\text{Tp}^{\text{tBu,Me}}]\text{Ni}(\text{O}_2)$ (50 mg, 9.7×10^{-2} mmol) was added to 10 mL of a benzene stock solution containing 9,10-dihydroxy-9,10-dihydroanthracene (1.03 mg/mL, 4.9 mM) and hexamethylbenzene (internal standard) in a 25 mL scintillation vial. The reaction mixture was stirred for 24 hours at room temperature, during which time the color of the solution changed from red-brown to bright red. An aliquot was removed from the reaction vial and subjected to ^1H NMR analysis. The major nickel containing product was determined to be the metallacycle, with small traces of $[\text{Tp}^{\text{tBu,Me}}]\text{Ni}(\text{OH})$ observed as a secondary component. The organic product was identified as anthraquinone (48% yield) based on ^1H NMR spectral comparison to authentic material. Yield of anthraquinone was based on comparison to the hexamethylbenzene internal standard.

2.12.5 Reaction of $[\text{Tp}^{\text{tBu,Me}}]\text{Ni}(\text{O}_2)$ with Xanthene

$[\text{Tp}^{\text{tBu,Me}}]\text{Ni}(\text{O}_2)$ (25 mg, 4.9×10^{-2} mmol) was added to 10 mL of a benzene stock solution containing xanthene (0.88 mg/mL, 4.9 mM) and hexamethylbenzene (2 mg, internal standard) in a 25-mL scintillation vial. The reaction mixture was stirred for 5 min at room temperature in order to completely dissolve the $[\text{Tp}^{\text{tBu,Me}}]\text{Ni}(\text{O}_2)$. An

aliquot was removed for initial ^1H NMR spectral analysis, after which the reaction vial was sealed and heated to 40 °C in a temperature-controlled oil bath. The reaction temperature was maintained at 40 °C for ~72 hours, after which the temperature was raised to 60 °C and maintained for an additional 48 hours. Aliquots were removed from the reaction during and after the heating period for ^1H NMR analysis in order to determine reaction progress. This procedure was repeated with double and triple the concentration of $[\text{Tp}^{\text{tBu,Me}}]\text{Ni}(\text{O}_2)$. The presence of xanthone as a reaction product was verified by GC-MS and ^1H NMR spectral comparison to authentic material. Yield of xanthone was based on comparison to the hexamethylbenzene internal standard. Results are summarized in Table 2.4.

Table 2.4 Xanthone yield versus reaction stoichiometry.

Ratio of $[\text{Tp}^{\text{tBu,Me}}]\text{Ni}(\text{O}_2)$ to Xanthene	Yield of Xanthone (% average of triplicate trials)	Amount of $[\text{Tp}^{\text{tBu,Me}}]\text{Ni}(\text{O}_2)$ Remaining After Reaction (% average of triplicate trials)
1	48	0
2	83	0
3	97	24

2.12.6 Reaction of $[\text{Tp}^{\text{tBu,Me}}]\text{Ni}(\text{O}_2)$ with 9-hydroxyxanthene.

$[\text{Tp}^{\text{tBu,Me}}]\text{Ni}(\text{O}_2)$ (50 mg, 9.7×10^{-2} mmol) was added to 10 mL of a benzene stock solution containing 9-hydroxyxanthene (1.93 mg/mL, 9.7 mM) and hexamethylbenzene (2 mg, internal standard) in a 25 mL scintillation vial. The reaction mixture was stirred for 24 hours at room temperature, during which time the color of the solution changed from red-brown to bright red. An aliquot was removed from the reaction vial and subjected to ^1H NMR spectral analysis. The nickel containing product was determined to be almost exclusively metallacycle, with only

traces of $[\text{Tp}^{\text{tBu,Me}}]\text{Ni}(\text{OH})$ observed. The organic product was identified as xanthone (49% yield) based on ^1H NMR spectral comparison to authentic material. Yield of xanthone was based on comparison to the hexamethylbenzene internal standard.

2.12.7 Reaction of $[\text{Tp}^{\text{tBu,Me}}]\text{Ni}(\text{O}_2)$ with 2-Phenylpropionaldehyde

To a 10 ml toluene solution of $[\text{Tp}^{\text{tBu,Me}}]\text{Ni}(\text{O}_2)$ (100 mg, 0.19 mmol) in a scintillation vial, 2-PPA (26 μL , 0.19 mmol) was added via microliter syringe. The solution was stirred for 24 hours, during which time the color of the solution changed from red-brown to dark purple. Following the reaction period, aliquots were removed from the solution for analysis by GC-MS and LIFDI-MS. The solvent from the remainder of the solution was removed under vacuum and the residue taken up into C_6D_6 for ^1H NMR analysis. The GC-MS spectrum of the reaction indicated acetophenone as the major organic product, consistent with the deformylation of 2-phenylpropionaldehyde. The spectrum also revealed the presence of unreacted 2-PPA. The LIFDI-MS spectrum displayed prominent mass fragments centered on m/z values of 481.28, 496.26, 526.27 and 614.34. The paramagnetic ^1H NMR spectrum showed the presence of several complexes consistent with $[\text{Tp}^{\text{tBu,Me}}]\text{Ni}^{\text{II}}(\text{X})$ type formulations. Of these, the hydroxo and formate complexes ($[\text{Tp}^{\text{tBu,Me}}]\text{Ni}(\text{OH})$ and $[\text{Tp}^{\text{tBu,Me}}]\text{Ni}(\text{O}_2\text{CH})$) were positively identified via comparison of the reaction NMR spectrum to the spectra of the independently prepared compounds.

2.13 X-Ray Crystallography

2.13.1 X-ray Structural Solution and Refinement

Crystals were selected, sectioned, mounted using viscous oil onto a plastic mesh, and cooled to the data collection temperature. Data were collected on a Bruker-

AXS APEX 2 DUO CCD diffractometer with Mo-K α radiation ($\lambda = 0.71073 \text{ \AA}$) monochromated with graphite. Unit cell parameters were obtained from 36 data frames, $0.5^\circ \omega$, from three different sections of the Ewald sphere. The data-sets were treated with multi-scan absorption corrections (Apex2 software suite, Madison, WI, 2005). The structures were solved using direct methods or by intrinsic phasing and refined with full-matrix, least-squares procedures on F^2 .⁴⁵ All non-hydrogen atoms were refined with anisotropic displacement parameters. All hydrogen atoms were treated as idealized contributions. Atomic scattering factors are contained in various versions of the SHELXTL 6.12 program library.⁴⁵ Data collection, analysis and solving of structures was performed by Dr. Glenn P. A. Yap with assistance from Eric R. Sirianni and Bryan D. Klebon.

2.13.2 Crystallographic Data Collection and Structure Determination

2.13.2.1 [Tp^{tBu,Me}]NiBr

Crystal data collection and refinement parameters are given in Table 2.5. Purple blocks were grown by layering methanol on a concentrated chloroform solution of the metal complex. The systematic absences in the diffraction data are consistent with the rhombohedral space group, R3m.

2.13.2.2 [Tp^{tBu,Ph}]NiBr

Crystal data collection and refinement parameters are given in Table 2.5. Purple blocks were grown by layering pentane on a concentrated benzene solution of the metal complex. The systematic absences in the diffraction data are consistent with the monoclinic space group, C2/c. The compound co-crystallized with a molecule of pentane.

2.13.2.3 [Tp^{tBu,Me}]Ni(OH)

Crystal data collection and refinement parameters are given in Table 2.6. Red blocks were grown by slow evaporation of a concentrated chloroform solution of the metal complex. The systematic absences in the diffraction data are consistent with the monoclinic space group, P2(1)/n.

2.13.2.4 [Tp^{tBu,Me}]Ni(OOtBu)

Crystal data collection and refinement parameters are given in Table 2.6. Red plates were grown by cooling a concentrated pentane solution of the metal complex to -30 °C. The systematic absences in the diffraction data are consistent with the trigonal space group, R3m.

2.13.2.5 Metallacycle

Crystal data collection and refinement parameters are given in Table 2.7. Red plates were grown by slow evaporation of a concentrated chloroform solution of the metal complex. The systematic absences in the diffraction data are consistent with the monoclinic space group, P2(1)/n. The *tert*-butyl groups were located disordered in two positions and treated to restraints based on non-crystallographic symmetry.

2.13.2.6 [Tp^{tBu,Me}]Ni(CNtBu)

Crystal data collection and refinement parameters are given in Table 2.7. Yellow blocks were grown by slow evaporation of a concentrated benzene solution of the metal complex. The systematic absences in the diffraction data are consistent with the monoclinic space group, P2(1)/n. The compound co-crystallized with a molecule of benzene.

2.13.2.7 [Tp^{tBu,Me}]Ni(CNCy)

Crystal data collection and refinement parameters are given in Table 2.13. Yellow blocks were grown by slow evaporation of a concentrated benzene solution of the metal complex. The systematic absences in the diffraction data are consistent with the monoclinic space group, P2(1)/c. Two symmetry unique molecules were located in the asymmetric unit.

2.13.2.8 [Tp^{tBu,Ph}]Ni(CNtBu)

Crystal data collection and refinement parameters are given in Table 2.9. Yellow plates were grown by cooling a concentrated pentane solution of the metal complex to -30° C. The systematic absences in the diffraction data are consistent with the monoclinic space group, P2(1)/c. The compound co-crystallized with a molecule of pentane.

2.13.2.9 [Tp^{Ph,Me}]Ni(PPh₃)

Crystal data collection and refinement parameters are given in Table 2.9. Yellow blocks were grown by layering pentane on a concentrated toluene solution of the metal complex. The systematic absences in the diffraction data are consistent with the rhombohedral space group, R3c.

2.13.2.10 [Tp^{Ph,Me}]Ni(CO)

Crystal data collection and refinement parameters are given in Table 2.10. Yellow plates were grown by vapor diffusion of pentane into a concentrated toluene solution of the metal complex. The systematic absences in the diffraction data are consistent with the monoclinic space group, P2(1)/n.

2.13.2.11 [Tp^{tBu,Me}]Ni(O₂CN(H)*t*Bu)

Crystal data collection and refinement parameters are given in Table 2.10. Yellow blocks were grown by cooling a concentrated pentane solution to -20 °C. The systematic absences in the diffraction data are consistent with the monoclinic space group, P2(1)/c. The compound co-crystallized with a molecule of diethyl ether, likely a result of ethereal contamination of the pentane.

2.13.2.12 [Tp^{tBu,Me}]Ni(O₂CN(H)Cy)

Crystal data collection and refinement parameters are given in Table 2.11. Orange blocks were grown by slow evaporation of a toluene solution of the metal complex. The systematic absences in the diffraction data are consistent with the monoclinic space group, P2(1)/c. Two symmetry unique molecules were located in the asymmetric unit.

2.13.2.13 [Tp^{tBu,Me}]Ni(O₂)

Crystal data collection and refinement parameters are given in Table 2.11. Brown blocks were grown by vapor diffusion of diethyl ether into a concentrated chloroform solution of the metal complex. The systematic absences in the diffraction data are consistent with the monoclinic space group, P2(1)/n. The dioxygen moiety was located disordered in two positions and treated to restraints based on non-crystallographic symmetry.

2.13.2.14 [Tp^{tBu,Ph}]Ni(O₂)

Crystal data collection and refinement parameters are given in Table 2.12. Red blocks were grown by layering pentane on a C₆D₆ solution of the metal complex in an NMR tube. The systematic absences in the diffraction data are consistent with the

monoclinic space group, $C2/c$. The compound co-crystallized with a molecule of pentane.

2.13.2.15 [Tp^{Ph,Me}]Ni(O₂)

Crystal data collection and refinement parameters are given in Table 2.12. Brown blocks were grown by layering pentane on a benzene solution of the metal complex. The systematic absences in the diffraction data are consistent with the monoclinic space group, $P2(1)/n$.

2.13.2.16 [Tp^{tBu,Me}]Ni(NO₂)

Crystal data collection and refinement parameters are given in Table 2.8. Orange blocks were grown by layering methanol on a CH₂Cl₂ solution of the metal complex. The systematic absences in the diffraction data are consistent with the monoclinic space group, $P2(1)/m$.

2.13.2.17 [Tp^{tBu,Me}]Ni(NO₃)

Crystal data collection and refinement parameters are given in Table 2.8. Orange blocks were grown by layering methanol on a CHCl₃ solution of the metal complex. The systematic absences in the diffraction data are consistent with the orthorhombic space group, $Pca2(1)$.

Table 2.5 Crystallographic data for [Tp^{tBu,Me}]NiBr and [Tp^{tBu,Ph}]NiBr.

Compound	[Tp ^{tBu,Me}]NiBr	[Tp ^{tBu,Ph}]NiBr • C ₅ H ₁₂
Identification Code	char351	char429
Empirical Formula	C ₂₄ H ₄₀ N ₆ BNiBr	C ₄₄ H ₅₈ N ₆ BNiBr
Formula Weight	562.05	820.39
Color, Habit	Purple, blocks	Purple, blocks
Crystal System	Rhombohedral	Monoclinic
Space Group	R3m	C2/c
<i>a</i> , Å	15.924(2)	44.049(2)
<i>b</i> , Å	15.924(2)	9.6989(5)
<i>c</i> , Å	9.576(3)	24.3038(13)
<i>α</i> , deg	90	90
<i>β</i> , deg	90	123.2880(10)
<i>γ</i> , deg	120	90
<i>V</i> (Å ³)	2102.8(8)	8679.7(8)
<i>Z</i>	3	8
Temperature (K)	200(2)	200(2)
Density _{calc} (g cm ⁻³)	1.331	1.256
θ range, deg	2.56 to 28.26	1.68 to 29.65
GOF (F ²)	1.047	1.01
μ(Mo, Kα), mm ⁻¹	2.139	1.404
R(F)/Rw(F)	0.0220/0.0547	0.0549/0.1737

Quantity minimized = $R(wF^2) = \Sigma[w(F_0^2 - F_c^2)^2] / \Sigma[(wF_0^2)^2]^{0.5}$; $R = \Sigma\Delta / \Sigma(F_0)$, $\Delta = |(F_0 - F_c)|$, $w = 1/[\sigma^2(F_0^2) + (aP)^2 + bP]$, $P = [2F_c^2 = \text{Max}(F_0, 0)]/3$

Table 2.6 Crystallographic data for [Tp^{tBu,Me}]Ni(OH) and [Tp^{tBu,Me}]Ni(OOtBu).

Compound	[Tp ^{tBu,Me}]Ni(OH)	[Tp ^{tBu,Me}]Ni(OOtBu)
Identification Code	char318	char390
Empirical Formula	C ₂₄ H ₄₁ N ₆ BNiO	C ₂₈ H ₄₉ N ₆ BNiO ₂
Formula Weight	499.15	571.25
Color, Habit	Red, blocks	Red, plates
Crystal System	Monoclinic	Trigonal
Space Group	P2(1)/n	R3m:H
<i>a</i> , Å	9.521(2)	30.638(8)
<i>b</i> , Å	30.307(7)	30.638(8)
<i>c</i> , Å	9.585(2)	9.773(3)
<i>α</i> , deg	90	90
<i>β</i> , deg	101.706(5)	90
<i>γ</i> , deg	90	120
<i>V</i> (Å ³)	2708.1(11)	7945(5)
<i>Z</i>	4	9
Temperature (K)	200(2)	200(2)
Density _{calc} (g cm ⁻³)	1.224	1.075
<i>θ</i> range, deg	2.27 to 28.30	1.329 to 28.275
GOF (F ²)	1.044	1.055
<i>μ</i> (Mo, K α), mm ⁻¹	0.743	0.579
R(F)/Rw(F)	0.0565/0.1200	0.0430/0.1189

Quantity minimized = $R(wF^2) = \Sigma[w(F_0^2 - F_c^2)^2] / \Sigma[(wF_0^2)^2]^{0.5}$; $R = \Sigma\Delta / \Sigma(F_0)$, $\Delta = |(F_0 - F_c)|$, $w = 1/[\sigma^2(F_0^2) + (aP)^2 + bP]$, $P = [2F_c^2 = \text{Max}(F_0, 0)]/3$

Table 2.7 Crystallographic data for Metallacycle and [Tp^{tBu,Me}]Ni(CNtBu).

Compound	Metallacycle	[Tp ^{tBu,Me}]Ni(CNtBu) • C ₆ H ₆
Identification Code	char387	char313
Empirical Formula	C ₂₄ H ₃₉ N ₆ BNiO	C ₃₅ H ₅₅ N ₇ BNi
Formula Weight	497.13	643.38
Color, Habit	Red, blocks	Yellow, blocks
Crystal System	Monoclinic	Monoclinic
Space Group	P2(1)/n	P2(1)/n
<i>a</i> , Å	9.3513(16)	14.654(3)
<i>b</i> , Å	30.260(5)	16.383(3)
<i>c</i> , Å	9.5648(16)	16.034(3)
<i>α</i> , deg	90	90
<i>β</i> , deg	102.279(3)	101.924(3)
<i>γ</i> , deg	90	90
<i>V</i> (Å ³)	2644.6(8)	3766.4(12)
<i>Z</i>	4	4
Temperature (K)	200(2)	200(2)
Density _{calc} (g cm ⁻³)	1.249	1.135
<i>θ</i> range, deg	2.24 to 28.30	1.71 to 28.29
GOF (F ²)	1.008	1.013
<i>μ</i> (Mo, K α), mm ⁻¹	0.760	0.547
R(F)/Rw(F)	.0664/0.1734	0.0484/0.1144

Quantity minimized = $R(wF^2) = \Sigma[w(F_0^2 - F_c^2)^2] / \Sigma[(wF_0^2)^2]^{0.5}$; $R = \Sigma\Delta / \Sigma(F_0)$, $\Delta = |(F_0 - F_c)|$, $w = 1 / [\sigma^2(F_0^2) + (aP)^2 + bP]$, $P = [2F_c^2 = \text{Max}(F_0, 0)] / 3$

Table 2.8 Crystallographic data for [Tp^{tBu,Me}]Ni(NO₂) and [Tp^{tBu,Me}]Ni(NO₃)

Compound	[Tp ^{tBu,Me}]Ni(NO ₂)	[Tp ^{tBu,Me}]Ni(NO ₃)
Identification Code	char310	Char311a
Empirical Formula	C ₂₄ H ₄₀ N ₇ BNiO ₂	C ₂₄ H ₄₀ N ₇ BNiO ₃
Formula Weight	528.15	544.15
Color, Habit	Orange, blocks	Orange, blocks
Crystal System	Monoclinic	Orthorhombic
Space Group	P2(1)/m	Pca2(1)
<i>a</i> , Å	9.684(3)	19.013(7)
<i>b</i> , Å	16.978(4)	9.872(4)
<i>c</i> , Å	17.258(4)	29.865(11)
<i>α</i> , deg	90	90
<i>β</i> , deg	99.131(4)	90
<i>γ</i> , deg	90	90
<i>V</i> (Å ³)	2801.7(12)	5606(3)
<i>Z</i>	4	8
Temperature (K)	200(2)	200(2)
Density _{calc} (g cm ⁻³)	1.252	1.290
<i>θ</i> range, deg	2.13 to 28.29	1.36 to 28.24
GOF (F ²)	1.062	1.038
<i>μ</i> (Mo, K α), mm ⁻¹	0.725	0.730
R(F)/Rw(F)	0.0425/0.1227	0.0469/0.1360

Quantity minimized = $R(wF^2) = \Sigma[w(F_0^2 - F_c^2)^2] / \Sigma[(wF_0^2)^2]^{0.5}$; $R = \Sigma\Delta / \Sigma(F_0)$, $\Delta = |(F_0 - F_c)|$, $w = 1 / [\sigma^2(F_0^2) + (aP)^2 + bP]$, $P = [2F_c^2 = \text{Max}(F_0, 0)] / 3$

Table 2.9 Crystallographic data for [Tp^{tBu,Ph}]Ni(CN*t*Bu) and [Tp^{Ph,Me}]Ni(PPh₃).

Compound	[Tp ^{tBu,Ph}]Ni(CN <i>t</i> Bu) • C ₅ H ₁₂	[Tp ^{Ph,Me}]Ni(PPh ₃)
Identification Code	char457	char451
Empirical Formula	C ₄₉ H ₆₇ N ₇ BNi	C ₄₈ H ₄₃ N ₆ BNiP
Formula Weight	823.62	804.37
Color, Habit	Yellow, plates	Yellow, blocks
Crystal System	Monoclinic	Rhombohedral
Space Group	P2(1)/c	R3c
<i>a</i> , Å	9.7125(7)	17.0376(15)
<i>b</i> , Å	28.446(2)	17.0376(15)
<i>c</i> , Å	17.9486(13)	24.734(2)
<i>α</i> , deg	90	90
<i>β</i> , deg	100.1680(10)	90
<i>γ</i> , deg	90	120
<i>V</i> (Å ³)	4880.9(6)	6217.7(9)
<i>Z</i>	4	6
Temperature (K)	200(2)	200(2)
Density _{calc} (g cm ⁻³)	1.121	1.289
<i>θ</i> range, deg	1.84 to 27.55	2.15 to 27.50
GOF (F ²)	1.043	1.028
<i>μ</i> (Mo, K α), mm ⁻¹	0.436	0.548
R(F)/Rw(F)	0.0455/0.1173	0.0220/0.0629

Quantity minimized = $R(wF^2) = \Sigma[w(F_0^2 - F_c^2)^2] / \Sigma[(wF_0^2)^2]^{0.5}$; $R = \Sigma\Delta / \Sigma(F_0)$, $\Delta = |(F_0 - F_c)|$, $w = 1/[\sigma^2(F_0^2) + (aP)^2 + bP]$, $P = [2F_c^2 = \text{Max}(F_0, 0)]/3$

Table 2.10 Crystallographic data for [Tp^{Ph,Me}]Ni(CO) and [Tp^{tBu,Me}]Ni(O₂CN(H)*t*Bu).

Compound	[Tp ^{Ph,Me}]Ni(CO)	[Tp ^{tBu,Me}]Ni(O ₂ CN(H) <i>t</i> Bu) • Et ₂ O
Identification Code	char465	char341
Empirical Formula	C ₃₁ H ₂₈ N ₆ BNiO	C ₃₃ H ₆₀ N ₇ BNiO ₃
Formula Weight	570.11	672.40
Color, Habit	Yellow, plates	Yellow, blocks
Crystal System	Monoclinic	Monoclinic
Space Group	P2(1)/n	P2(1)/c
<i>a</i> , Å	11.5283(16)	11.970(7)
<i>b</i> , Å	16.056(2)	18.076(9)
<i>c</i> , Å	15.933(2)	18.509(9)
<i>α</i> , deg	90	90
<i>β</i> , deg	100.204(2)	103.241(8)
<i>γ</i> , deg	90	90
<i>V</i> (Å ³)	2902.5(7)	3898(4)
<i>Z</i>	4	4
Temperature (K)	200(2)	200(2)
Density _{calc} (g cm ⁻³)	1.305	1.146
<i>θ</i> range, deg	1.82 to 26.37	1.75 to 28.35
GOF (F ²)	1.019	1.033
<i>μ</i> (Mo, K α), mm ⁻¹	0.703	0.536
R(F)/Rw(F)	0.0470/0.1057	0.0443/0.1271

Quantity minimized = $R(wF^2) = \Sigma[w(F_0^2 - F_c^2)^2] / \Sigma[(wF_0^2)^2]^{0.5}$; $R = \Sigma\Delta / \Sigma(F_0)$, $\Delta = |(F_0 - F_c)|$, $w = 1 / [\sigma^2(F_0^2) + (aP)^2 + bP]$, $P = [2F_c^2 = \text{Max}(F_0, 0)] / 3$

Table 2.11 Crystallographic data for [Tp^{tBu,Me}]Ni(O₂CN(H)Cy) and [Tp^{tBu,Me}]Ni(O₂).

Compound	[Tp ^{tBu,Me}]Ni(O ₂ CN(H)Cy)	[Tp ^{tBu,Me}]Ni(O ₂)
Identification Code	char329	char340
Empirical Formula	C ₃₁ H ₅₂ N ₇ BNiO ₂	C ₂₄ H ₄₀ N ₆ BNiO ₂
Formula Weight	624.32	514.14
Color, Habit	Orange, blocks	Brown, blocks
Crystal System	Monoclinic	Monoclinic
Space Group	P2(1)/c	P2(1)/n
<i>a</i> , Å	21.892(8)	9.501(8)
<i>b</i> , Å	12.062(4)	30.03(3)
<i>c</i> , Å	26.556(10)	9.546(8)
<i>α</i> , deg	90	90
<i>β</i> , deg	105.327(7)	100.876(13)
<i>γ</i> , deg	90	90
<i>V</i> (Å ³)	6763(4)	2675(4)
<i>Z</i>	8	4
Temperature (K)	200(2)	90(2)
Density _{calc} (g cm ⁻³)	1.226	1.277
<i>θ</i> range, deg	1.59 to 28.32	2.28 to 28.34
GOF (F ²)	1.013	1.023
<i>μ</i> (Mo, K α), mm ⁻¹	0.611	0.757
R(F)/Rw(F)	0.0656/0.1634	0.0443/0.1047

Quantity minimized = $R(wF^2) = \Sigma[w(F_0^2 - F_c^2)^2] / \Sigma[(wF_0^2)^2]^{0.5}$; $R = \Sigma\Delta / \Sigma(F_0)$, $\Delta = |(F_0 - F_c)|$, $w = 1 / [\sigma^2(F_0^2) + (aP)^2 + bP]$, $P = [2F_c^2 = \text{Max}(F_0, 0)] / 3$

Table 2.12 Crystallographic data for [Tp^{tBu,Ph}]Ni(O₂) and [Tp^{Ph,Me}]Ni(O₂).

Compound	[Tp ^{tBu,Ph}]Ni(O ₂) • C ₅ H ₁₂	[Tp ^{Ph,Me}]Ni(O ₂)
Identification Code	char377	char509
Empirical Formula	C ₄₄ H ₅₈ N ₆ BNiO ₂	C ₃₀ H ₂₈ N ₆ BNiO ₂
Formula Weight	772.48	574.10
Color, Habit	Red, blocks	Brown, blocks
Crystal System	Monoclinic	Monoclinic
Space Group	C2/c	P2(1)/n
<i>a</i> , Å	43.670(5)	11.493(2)
<i>b</i> , Å	9.4871(10)	16.075(3)
<i>c</i> , Å	23.700(3)	15.643(3)
<i>α</i> , deg	90	90
<i>β</i> , deg	122.604(7)	99.808(3)
<i>γ</i> , deg	90	90
<i>V</i> (Å ³)	8271.7(16)	2847.8(9)
<i>Z</i>	8	4
Temperature (K)	100(2)	200(2)
Density _{calc} (g cm ⁻³)	1.241	1.339
<i>θ</i> range, deg	1.72 to 28.35	2.40 to 27.59
GOF (F ²)	1.028	1.011
<i>μ</i> (Mo, K α), mm ⁻¹	0.513	0.719
R(F)/Rw(F)	0.0464/0.1116	0.0299/0.0739

Quantity minimized = $R(wF^2) = \Sigma[w(F_0^2 - F_c^2)^2] / \Sigma[(wF_0^2)^2]^{0.5}$; $R = \Sigma\Delta / \Sigma(F_0)$, $\Delta = |(F_0 - F_c)|$, $w = 1 / [\sigma^2(F_0^2) + (aP)^2 + bP]$, $P = [2F_c^2 = \text{Max}(F_0, 0)] / 3$

Table 2.13 Crystallographic data for [Tp^{tBu,Me}]Ni(CNCy).

Compound	[Tp ^{tBu,Me}]Ni(CNCy)
Identification Code	char316
Empirical Formula	C ₃₁ H ₅₁ N ₇ BNi
Formula Weight	591.31
Color, Habit	Yellow, blocks
Crystal System	Monoclinic
Space Group	P2(1)/c
<i>a</i> , Å	18.236(4)
<i>b</i> , Å	18.931(4)
<i>c</i> , Å	19.090(5)
<i>α</i> , deg	90
<i>β</i> , deg	91.561(4)
<i>γ</i> , deg	90
<i>V</i> (Å ³)	6588(3)
<i>Z</i>	8
Temperature (K)	200(2)
Density _{calc} (g cm ⁻³)	1.192
<i>θ</i> range, deg	1.87 to 28.35
GOF (F ²)	1.017
<i>μ</i> (Mo, K α), mm ⁻¹	0.620
R(F)/Rw(F)	0.0632/0.1429

Quantity minimized = $R(wF^2) = \Sigma[w(F_0^2 - F_c^2)^2] / \Sigma[(wF_0^2)^2]^{0.5}$; $R = \Sigma\Delta / \Sigma(F_0)$, $\Delta = |(F_0 - F_c)|$, $w = 1 / [\sigma^2(F_0^2) + (aP)^2 + bP]$, $P = [2F_c^2 - \text{Max}(F_0, 0)] / 3$

Chapter 3

SYNTHESIS, CHARACTERIZATION AND REACTIVITY OF TRISPYRAZOLYLBORATE SUPPORTED MONOVALENT NICKEL COMPLEXES

3.1 Introduction

The study of nickel-dioxygen species has been plagued by stability issues^{28,30,31} as well as by a dearth of synthetic methods by which they can be prepared. While the treatment of Ni(II) complexes with hydrogen peroxide has been, and continues to be a productive method for producing such species,^{24,25,26,27} in recent years the use of monovalent nickel complexes to activate dioxygen directly, first reported in these laboratories,²⁹ has been of increasing importance to this area of study.^{30,31,46}

A number of ligands that support this relatively uncommon nickel oxidation state have been discovered.^{32,47,48,49,50,51} The most commonly used systems for stabilizing Ni(I) are tetradentate, macrocyclic amine ligands in which the nickel is bound in a roughly square planar fashion (square pyramidal in the case of an ancillary donor ligand).^{47,49,50} Other coordination environments are less prevalent in the literature and include tetrahedral ($[\text{PhTt}^{\text{R}}]\text{NiL}$ and $(\text{PPh}_3)_3\text{NiX}$)^{29,48} and trigonal planar $((\text{Nacnac})\text{Ni}(\text{L}))$ ³² geometries.

Even among systems that show support for the monovalent oxidation state of nickel's close neighbors, cobalt and copper, demonstrated support for monovalent nickel is often lacking. Perhaps nowhere is this disparity more evident than in the case of trispyrazolylborate (Tp) ligands. This versatile and robust ligand system has shown

broad oxidation state support for a number of first row transition metals. In particular, both monovalent and divalent complexes of cobalt and copper have been prepared, with the monovalent complexes, $[\text{Tp}^{\text{tBu,Me}}]\text{Co}(\text{N}_2)$ and $[\text{Tp}^{\text{tBu,iPr}}]\text{Cu}(\text{DMF})$, being utilized to generate stable dioxygen adducts.^{52,53} By contrast, and despite an extensive library of reported Ni(II) complexes, support for monovalent nickel on Tp has yet to be reported.

This knowledge gap in one of inorganic chemistry's most widely used ligand systems, combined with the general scarcity of Ni(I) species, provides substantial motivation for the pursuit of Tp-supported, monovalent nickel complexes. It was with this in mind that I aimed to prepare such species; an endeavor that has resulted in the isolation of several new Ni(I) complexes whose synthesis, structure and reactivity are discussed herein.

3.2 $[\text{Tp}^{\text{tBu,Me}}]$ and $[\text{Tp}^{\text{tBu,Ph}}]$ Supported Monovalent Nickel Complexes

I began initial investigations by utilizing the $\text{Tp}^{\text{tBu,Me}}$ aka Tp' ligand. As mentioned above, this ligand and similar variants have been used to great effect with Co and Cu, with both the monovalent complex and its corresponding dioxygen adduct isolated in each case. A large part of the success of this ligand in these pursuits is due to the effects of the 3-*tert*-butyl groups. In addition to being a useful proton NMR spectroscopic handle, this substituent provides for metal complexes with distinct preference for four-coordinate complexes.⁵⁴ The steric bulk also serves to discourage the formation of bis-ligand species, i.e. $[\text{Tp}^{\text{tBu,Me}}]_2\text{M}$, in the preparation of first row transition metal complexes. The properties conferred to the $\text{Tp}^{\text{tBu,Me}}$ by its steric demands have earned it a place among the so called "tetrahedral enforcers."⁶³ In terms of this study, however, perhaps the most important role of the 3-*tert*-butyl groups is

their ability to stabilize metal-dioxygen adducts by preventing potential decomposition pathways, e.g. via dimerization.

As described below, the Tp'Ni(II) halide complexes have shown themselves to be satisfactory precursors for reduction to Ni(I), with the bromide, $[\text{Tp}^{\text{tBu,Me}}]\text{NiBr}$, being used almost exclusively due to its ease of synthesis and relatively fast reduction. The chloride complex can also be used, however, its reduction was associated with much longer reaction times, lower yields and substantial difficulties in product isolation. Reduction was facilitated, with varying degrees of success, by a number of reducing agents including methyl lithium, Grignard reagents, sodium naphthalenide, potassium graphite and sodium amalgam. Of these, KC_8 and Na/Hg were by far the most effective. Successful reduction to Ni(I) could only be accomplished by using a suitable donor ligand to act as a trapping agent, thereby ensuring that the monovalent product was protected against disproportionation. Carbon monoxide and isonitriles with large substituents, $t\text{BuNC}$ and C_7NC , served this role well. Each of the monovalent species was unreactive to the O-atom transfer agents N_2O and pyridine-N-oxide. The isonitrile-bound complexes reacted with PhIO, however, resulting in the formation of Ni(II) carbamates. Most importantly, all of the monovalent complexes were highly reactive towards dioxygen, allowing for the isolation of thermally stable Ni-O₂ adducts (see Chapter 4).

3.2.1 Synthesis and Structure of $[\text{Tp}^{\text{tBu,Me}}]\text{Ni}(\text{CN}t\text{Bu})$, $[\text{Tp}^{\text{tBu,Me}}]\text{Ni}(\text{CNCy})$, $[\text{Tp}^{\text{tBu,Me}}]\text{Ni}(\text{CO})$ and $[\text{Tp}^{\text{tBu,Ph}}]\text{Ni}(\text{CN}t\text{Bu})$

Synthesis of the monovalent complexes $[\text{Tp}^{\text{tBu,Me}}]\text{Ni}(\text{CN}t\text{Bu})$ and $[\text{Tp}^{\text{tBu,Me}}]\text{Ni}(\text{CNCy})$ was accomplished by sodium amalgam reduction of $[\text{Tp}^{\text{tBu,Me}}]\text{NiBr}$ in the presence of ~1.2 equivalents of the isonitrile in toluene or

benzene, Figure 3.1. Addition of THF, in roughly the same quantity as the isonitrile, to the benzene or toluene solutions accelerated the reaction rate. This reduced the reaction time by half, with complete reduction occurring in 3-4 hours with THF as opposed to 6-8 hours without THF. However, addition of THF in excess of that described in Section 2.6 resulted in significant amounts of over-reduction and greatly reduced yields. Reduction with THF as the sole solvent resulted in rapid and complete over-reduction with no monovalent product isolated. The course of the reaction can be easily followed via observation of the dramatic, but gradual color change from the deep violet of the starting material to the bright yellow of the product. Upon completion of the reduction, the reaction solution was separated from the sodium amalgam via cannula filtration through Celite and the solvent removed under vacuum. The residue was taken up into pentane and filtered through an APTS silica gel plug. This process served to remove $[\text{Tp}^{\text{tBu,Me}}]\text{Na}$, formed as a result of over-reduction, as well as any trace oxidation products and unreacted starting material. Unmodified silica gel can be used in place of the APTS coated version, albeit with reduced yields. Final solvent removal under vacuum gave the monovalent complexes as yellow powders in good to excellent yields (79-90%). This process was adapted for preparation of the closely related $[\text{Tp}^{\text{tBu,Ph}}]\text{Ni}(\text{CN}t\text{Bu})$. These paramagnetic complexes are stable under N_2 , but are highly reactive toward both H_2O and O_2 .

In addition to the isonitrile complexes, the CO-trapped monovalent complex, $[\text{Tp}^{\text{tBu,Me}}]\text{Ni}(\text{CO})$, was prepared. Unlike its isonitrile analogs, Na/Hg reduction was not an effective method of preparation. Instead, the complex was prepared in good yield via KC_8 reduction of $[\text{Tp}^{\text{tBu,Me}}]\text{NiBr}$. This was accomplished via addition of THF to a mixture KC_8 and $[\text{Tp}^{\text{tBu,Me}}]\text{NiBr}$, in the form of a homogeneous powder, under an

atmosphere of CO, Figure 3.3. Reduction to the CO complex was quite fast, proceeding to completion in under two minutes. This process was characterized by a rapid color change from violet to pale yellow. The isolation method employed for this species was very similar to that of the isonitrile complexes. Filtration of the crude reaction solution through Celite was followed by solvent removal, dissolution in pentane and elution through an APTS coated silica gel plug. Final solvent removal under vacuum gave the CO complex as a pale yellow powder in good yield (75%).

X-ray quality crystals were grown by slow evaporation of concentrated benzene solutions in the case of $[\text{Tp}^{\text{tBu,Me}}]\text{Ni}(\text{CN}t\text{Bu})$ and $[\text{Tp}^{\text{tBu,Me}}]\text{Ni}(\text{CNCy})$, and by cooling of concentrated pentane solutions to $-30\text{ }^{\circ}\text{C}$ in the case of $[\text{Tp}^{\text{tBu,Ph}}]\text{Ni}(\text{CN}t\text{Bu})$. The molecular structures of these compounds are found in Figures 3.4-3.6 with selected bond distances in Table 3.1 and selected bond angles and τ values in Table 3.2. Crystals of $[\text{Tp}^{\text{tBu,Me}}]\text{Ni}(\text{CO})$ were grown by vapor diffusion of pentane into a concentrated toluene solution of the metal complex. However, while the data collected from these crystals was sufficient to elucidate the general structure of $[\text{Tp}^{\text{tBu,Me}}]\text{Ni}(\text{CO})$, it was of too low a quality for reliable metric parameters.

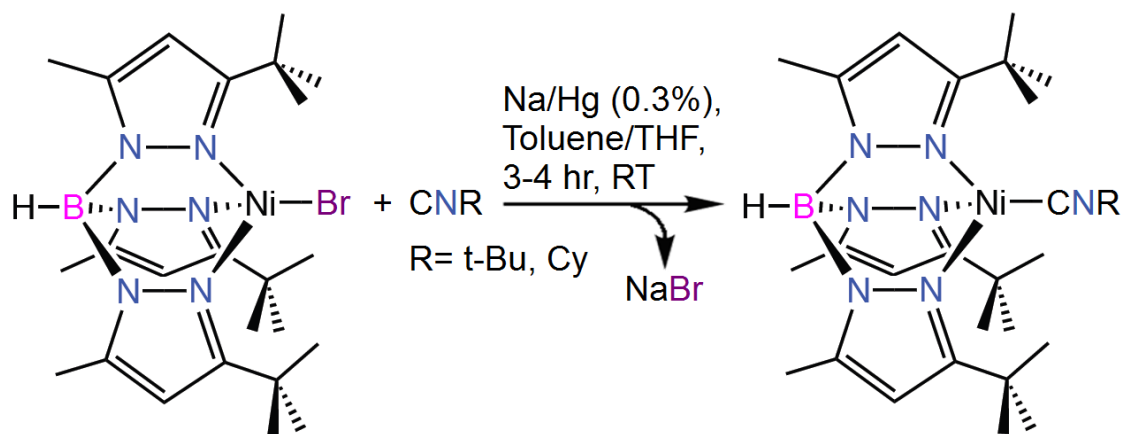


Figure 3.1 Synthesis of $[\text{Tp}^{\text{tBu,Me}}]\text{Ni}(\text{CNR})$ complexes.

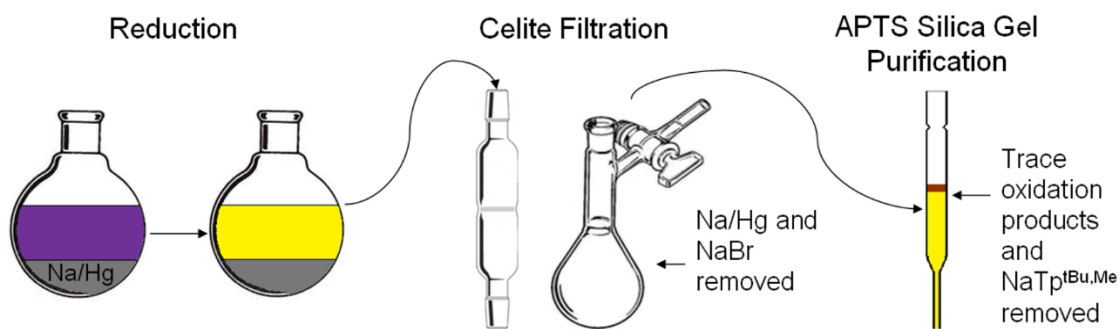


Figure 3.2 Illustration of $[\text{Tp}^{\text{tBu,Me}}]\text{Ni}(\text{CNR})$ preparation and isolation procedure.

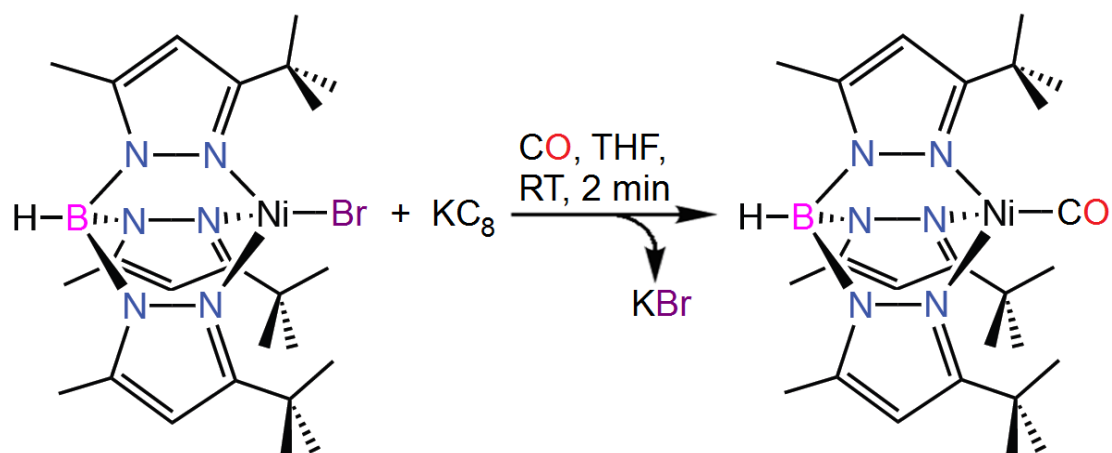


Figure 3.3 Synthesis of $[\text{Tp}^{\text{tBu,Me}}]\text{Ni}(\text{CO})$.

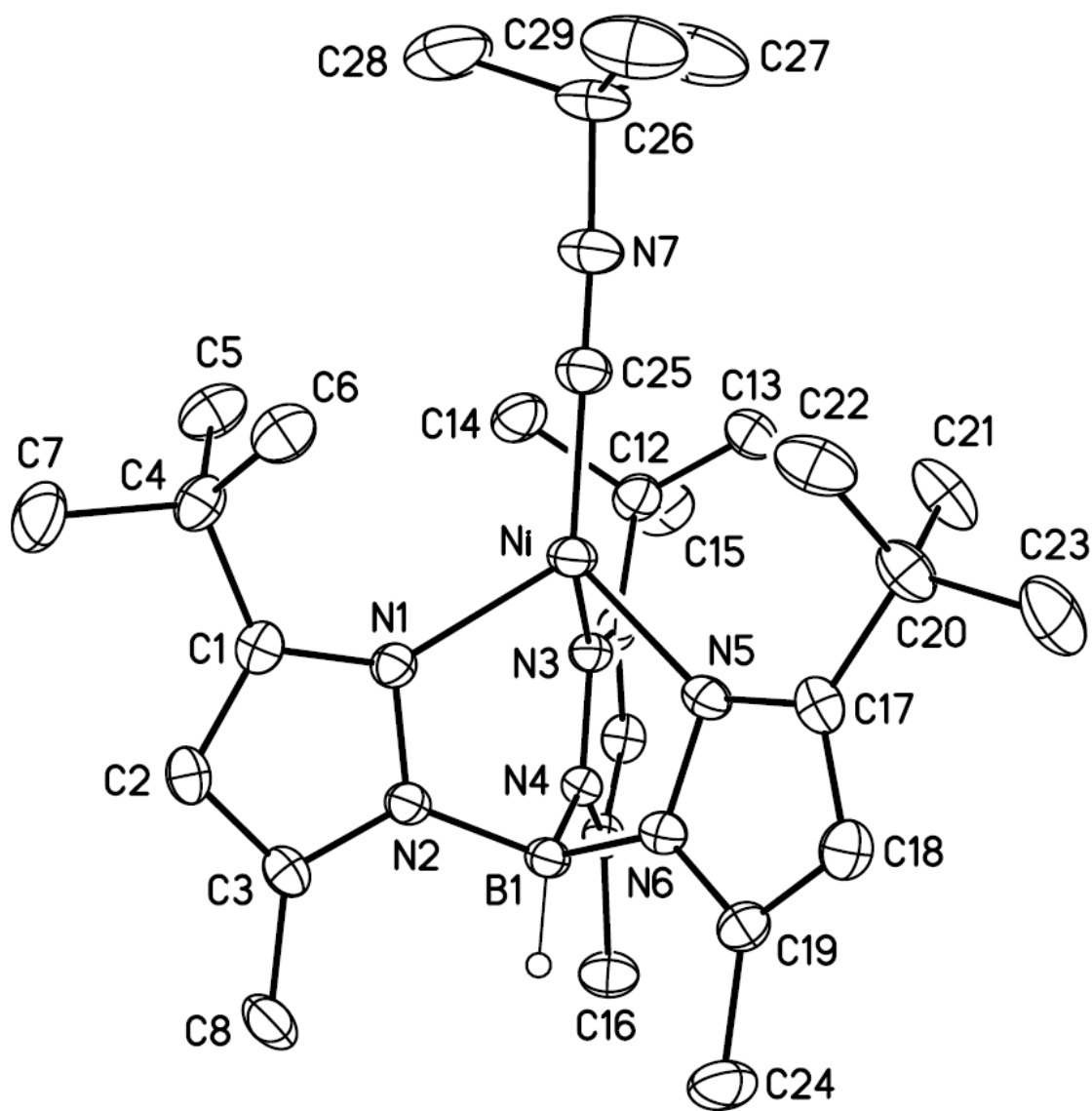


Figure 3.4 Thermal ellipsoid diagram of $[\text{Tp}^{\text{tBu,Me}}]\text{Ni}(\text{CN}^{\text{t}}\text{Bu})$ with atom labeling. Thermal ellipsoids are drawn to 30% probability. Hydrogen atoms are omitted for clarity with the exception of B-H.

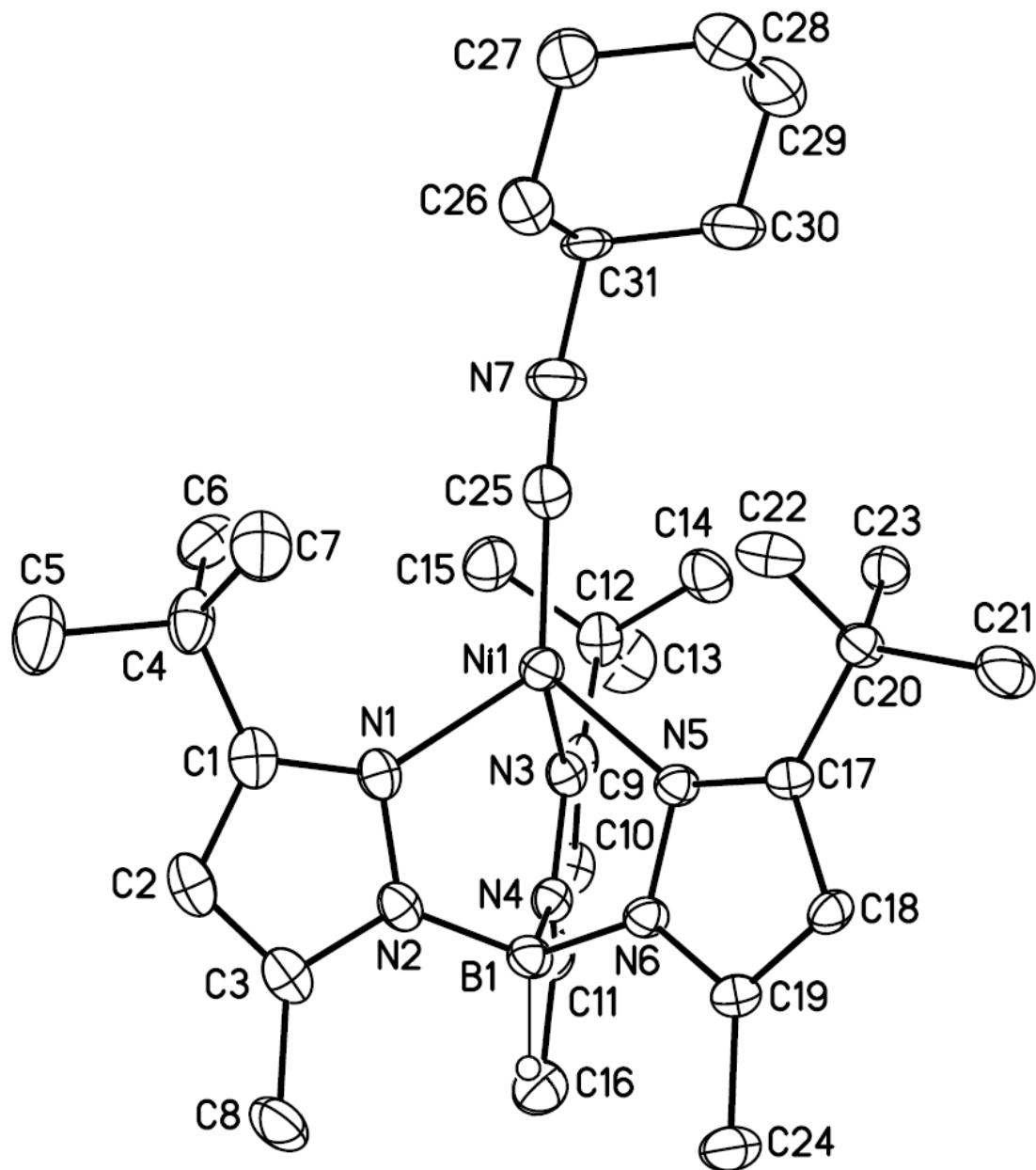


Figure 3.5 Thermal ellipsoid diagram of $[\text{Tp}^{\text{tBu,Me}}]\text{Ni}(\text{CNCy})$ with atom labeling. Thermal ellipsoids are drawn to 30% probability. Hydrogen atoms are omitted for clarity with the exception of B-H.

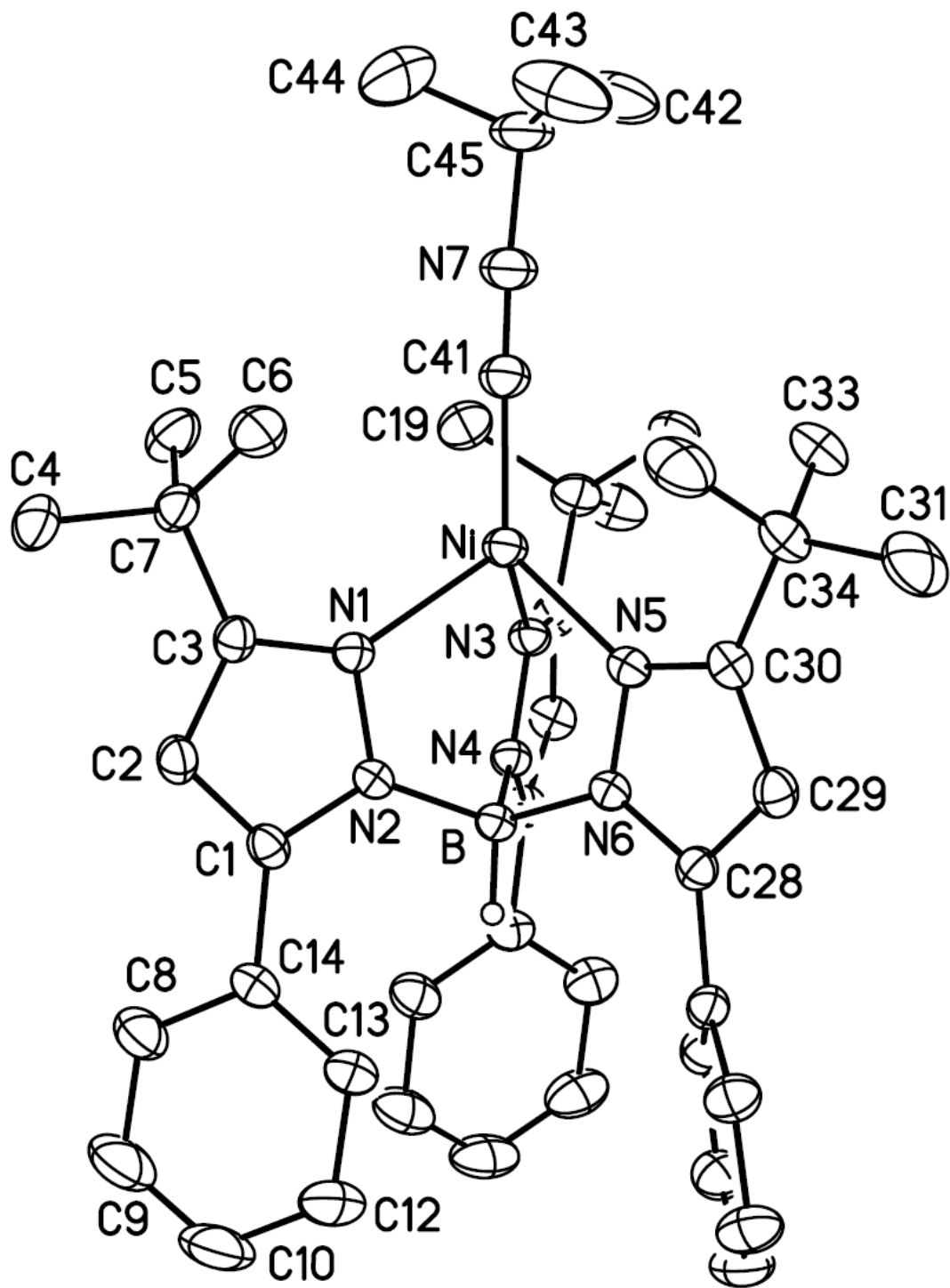


Figure 3.6 Thermal ellipsoid diagram of [Tp^{tBu,Ph}]Ni(CN^tBu) with atom labeling. Thermal ellipsoids are drawn to 30% probability. Hydrogen atoms are omitted for clarity with the exception of B-H.

Table 3.1 Selected bond lengths (Å) for [Tp^{tBu,Me}]Ni(CN*t*Bu), [Tp^{tBu,Me}]Ni(CNCy) [Tp^{tBu,Ph}]Ni(CN*t*Bu).

	[Tp ^{tBu,Me}]Ni(CN <i>t</i> Bu)	[Tp ^{tBu,Me}]Ni(CNCy)	[Tp ^{tBu,Ph}]Ni(CN <i>t</i> Bu)
Ni–N1	2.065(2)	2.067(3)	2.0467(15)
Ni–N3	2.045(2)	2.048(3)	2.0508(15)
Ni–N5	2.071(2)	2.057(3)	2.0598(15)
Ni–C _{Isonitrile}	1.830(2)	1.822(4)	1.830(2)
C–N _{Isonitrile}	1.161(3)	1.166(4)	1.150(3)

Table 3.2 Selected bond angles (°) and τ values for [Tp^{tBu,Me}]Ni(CN*t*Bu), [Tp^{tBu,Me}]Ni(CNCy), [Tp^{tBu,Me}]Ni(CO) and [Tp^{tBu,Ph}]Ni(CN*t*Bu).

Complex	Angles (°)	τ_4 value
	Ni–C–N	
[Tp ^{tBu,Me}]Ni(CN <i>t</i> Bu)	179.7(3)	0.35
[Tp ^{tBu,Me}]Ni(CNCy)	176.0(3)	0.42
[Tp ^{tBu,Ph}]Ni(CN <i>t</i> Bu)	177.8(2)	0.37

3.2.2 Molecular Structure of [Tp^{tBu,Me}]Ni(CN*t*Bu), [Tp^{tBu,Me}]Ni(CNCy) and [Tp^{tBu,Ph}]Ni(CN*t*Bu)

The geometry of the isonitrile-bound complexes, [Tp^{tBu,Me}]Ni(CN*t*Bu), [Tp^{tBu,Me}]Ni(CNCy) and [Tp^{tBu,Ph}]Ni(CN*t*Bu) is best described as distorted tetrahedral with τ_4 values of 0.35, 0.42 and 0.37, respectively. All of the compounds are bound in

a κ^3 fashion to the Tp ligand by its three nitrogen donors as well as to the carbon of the ancillary, "trapping", ligand (isonitrile). In addition to helping stabilizing the monovalent oxidation state, the isonitrile ligand also effectively prevents the approach of large substrates and neighboring nickel complexes (through its steric bulk) while still allowing small molecules (such as O₂) access to the metal center. The average Ni–N distance of 2.051 Å does not differ substantially from that of the divalent precursor, [Tp^{tBu,Me}]NiBr. The average Ni–C bond length of 1.827(8) Å is somewhat shorter than that of the monovalent, phenyltris((adamantylthio)methyl)borate (PhTt^{Ad}) complex, [PhTt^{Ad}]Ni(CN*t*Bu) (1.849(7) Å).⁵⁵ The B---Ni–C bond angles are all very nearly linear, indicating an almost idealized C_{3v}. Likewise, the average Ni–C–N angles deviate only slightly from linearity, with [Tp^{tBu,Me}]Ni(CNCy) showing the greatest deviation (176.0(3)°). [Tp^{tBu,Me}]Ni(CNCy) also shows the most distortion from the ideal tetrahedral geometry. Both of these characteristics are likely the result of steric interactions between the cyclohexyl ring and the 3-*t*Bu groups of the Tp ligand.

3.2.2.1 ¹H NMR Spectral Analysis

Although some features in ¹H NMR spectra show significant broadening and are dispersed over a large chemical shift range, the proton resonances for the monovalent species are well resolved, Figure 3.7. Interestingly, while both the monovalent complexes and their divalent precursors are paramagnetic, they show substantial differences in the location of certain ¹H NMR spectral features. These differences can be illustrated by comparing the chemical shifts for the various substituents of [Tp^{tBu,Me}]Ni(CN*t*Bu) and its precursor [Tp^{tBu,Me}]NiBr. The *tert*-butyl group of the supporting ligand, located at $\delta = -0.1$ in [Tp^{tBu,Me}]NiBr, is found at $\delta = -10.0$ in [Tp^{tBu,Me}]Ni(CN*t*Bu). The pyrazole and methyl protons are located at $\delta = 84.9$

and 7.3, respectively in $[\text{Tp}^{\text{tBu,Me}}]\text{NiBr}$ and at $\delta = 17.5$ and 15.4 in $[\text{Tp}^{\text{tBu,Me}}]\text{Ni}(\text{CN}t\text{Bu})$. Lastly, and perhaps the most notable, is the *BH* resonance, which is shifted significantly upfield in virtually all Ni(II) Tp complexes ($\delta = -8.6$ in $[\text{Tp}^{\text{tBu,Me}}]\text{NiBr}$) and downfield in all Ni(I) Tp complexes ($\delta = 38.8$ in $[\text{Tp}^{\text{tBu,Me}}]\text{Ni}(\text{CN}t\text{Bu})$).

Despite these differences, the chemical shifts of various substituents are quite similar within a given oxidation state. This is particularly true for the monovalent complexes, Table 3.3. The similarity in the chemical shifts of species in a given oxidation state, combined with the significant differences between the chemical shifts of Ni(I) and Ni(II) compounds, allows for oxidation state identification via proton NMR spectroscopy. This approach is especially useful when identifying products in solutions containing both monovalent and divalent components.

In addition to substituent assignment, ^1H NMR spectroscopy was used to determine the magnetic moment of the monovalent complexes via the Evans Method.⁶ The effective magnetic moments of $[\text{Tp}^{\text{tBu,Me}}]\text{Ni}(\text{CN}t\text{Bu})$, $[\text{Tp}^{\text{tBu,Me}}]\text{Ni}(\text{CNCy})$, $[\text{Tp}^{\text{tBu,Ph}}]\text{Ni}(\text{CN}t\text{Bu})$ and $[\text{Tp}^{\text{tBu,Me}}]\text{Ni}(\text{CO})$ are displayed in Table 3.3. The values, which ranged from $2.1\text{-}2.3 \mu_{\text{B}}$, indicate an $S = 1/2$ spin state, which is consistent with the oxidation state assignment of Ni(I). For comparison, the effective magnetic moments of the divalent precursors, $[\text{Tp}^{\text{tBu,Me}}]\text{NiBr}$ and $[\text{Tp}^{\text{tBu,Ph}}]\text{NiBr}$, were $3.5(1) \mu_{\text{B}}$ and $3.4(2) \mu_{\text{B}}$ respectively.

3.2.2.2 FT-IR Spectral Analysis.

Selected IR spectral features for $[\text{Tp}^{\text{tBu,Me}}]\text{Ni}(\text{CN}t\text{Bu})$, $[\text{Tp}^{\text{tBu,Me}}]\text{Ni}(\text{CNCy})$, $[\text{Tp}^{\text{tBu,Me}}]\text{Ni}(\text{CO})$ and $[\text{Tp}^{\text{tBu,Ph}}]\text{Ni}(\text{CN}t\text{Bu})$ are contained in Table 3.4. In the case of $[\text{Tp}^{\text{tBu,Me}}]\text{Ni}(\text{CO})$, the $\nu_{\text{CO}} = 1993 \text{ cm}^{-1}$ falls between those of the analogous cobalt and

copper complexes, $[\text{Tp}^{\text{tBu,Me}}]\text{Co}(\text{CO})$ and $[\text{Tp}^{\text{tBu,Me}}]\text{Cu}(\text{CO})$,⁵⁶ which have values of $\nu_{\text{CO}} = 1942 \text{ cm}^{-1}$ and 2059 cm^{-1} , respectively. This stretching frequency indicates a weakening of the carbon-oxygen bond relative to free carbon monoxide (2143 cm^{-1}), due to the effects of metal $d\pi$ to $\text{CO } \pi^*$ donation (i.e. Π backbonding). Given that the extent of backdonation into the $\text{CO } \pi^*$ orbital increases with lower metal ionization potential (IP)⁵⁷, the observed trend in ν_{CO} , $\text{Co} < \text{Ni} < \text{Cu}$, is consistent with the increase in IP as one moves left to right across the 1st transition series from Co to Cu. A analogous trend can be seen in the structurally similar $[\text{PhTt}^{\text{tBu}}]\text{M}(\text{CO})$ complexes where $\nu_{\text{CO}} = 1966 \text{ cm}^{-1}$, 1999 cm^{-1} and 2078 cm^{-1} for $[\text{PhTt}^{\text{tBu}}]\text{Co}(\text{CO})$, $[\text{PhTt}^{\text{tBu}}]\text{Ni}(\text{CO})$ and $[\text{PhTt}^{\text{tBu}}]\text{Cu}(\text{CO})$, respectively.^{55,58,59} The isonitrile complexes exhibit similar trends. The isonitrile ν_{CN} of $[\text{Tp}^{\text{tBu,Me}}]\text{Ni}(\text{CN}t\text{Bu})$ occurs at 2065 and 2094 cm^{-1} (two stretching features result from solid state splitting) as opposed to 2126 cm^{-1} in free *tert*-BuNC. In the related complex, $[\text{Tp}^{\text{tBu,Ph}}]\text{Ni}(\text{CN}t\text{Bu})$, the electron withdrawing effects of the 5-Ph substituent manifest in the higher ν_{CN} (2100 cm^{-1}), where the slightly lower electron density at the metal results in a small, but quantifiable reduction in the degree of backbonding.

Table 3.3 Selected ^1H NMR spectral features for $[\text{Tp}^{\text{tBu,Me}}]\text{Ni}(\text{CN}t\text{Bu})$, $[\text{Tp}^{\text{tBu,Me}}]\text{Ni}(\text{CNCy})$, $[\text{Tp}^{\text{tBu,Me}}]\text{Ni}(\text{CO})$ and $[\text{Tp}^{\text{tBu,Ph}}]\text{Ni}(\text{CN}t\text{Bu})$.

Functional Group	Chemical Shifts (δ)				Magnetic Moment (μ_B)
	<i>3-tert-Bu</i>	<i>4-Pz</i>	<i>5-Me</i>	<i>B-H</i>	
$[\text{Tp}^{\text{tBu,Me}}]\text{Ni}(\text{CN}t\text{Bu})$	-10.0	17.5	15.4	-38.8	2.26(8)
$[\text{Tp}^{\text{tBu,Me}}]\text{Ni}(\text{CNCy})$	-9.8	17.6	15.2	38.2	2.24(8)
$[\text{Tp}^{\text{tBu,Ph}}]\text{Ni}(\text{CN}t\text{Bu})$	-9.5	17.8	N/A	38.1	2.12(9)
$[\text{Tp}^{\text{tBu,Me}}]\text{Ni}(\text{CO})$	-11.5	17.8	21.3	45.7	2.17(5)

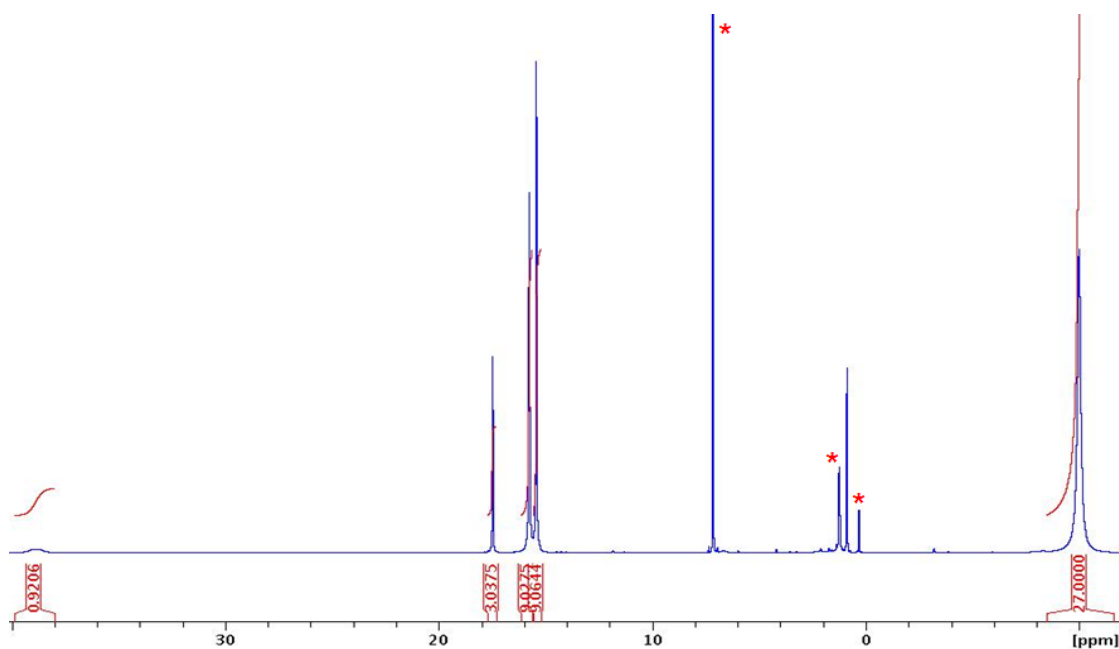


Figure 3.7 ^1H NMR spectrum of $[\text{Tp}^{\text{tBu,Me}}]\text{Ni}(\text{CN}t\text{Bu})$. * indicates residual solvent signals and silicone grease.

Table 3.4 Selected FT-IR stretching frequencies for $[\text{Tp}^{\text{tBu,Me}}]\text{Ni}(\text{CN}t\text{Bu})$, $[\text{Tp}^{\text{tBu,Me}}]\text{Ni}(\text{CNCy})$, $[\text{Tp}^{\text{tBu,Me}}]\text{Ni}(\text{CO})$ and $[\text{Tp}^{\text{tBu,Ph}}]\text{Ni}(\text{CN}t\text{Bu})$.

Complex	Stretching Frequencies (cm^{-1})		
	$\nu_{\text{C}\equiv\text{N}}$	$\nu_{\text{C}\equiv\text{O}}$	$\nu_{\text{B-H}}$
$[\text{Tp}^{\text{tBu,Me}}]\text{Ni}(\text{CN}t\text{Bu})$	2065, 2094	N/A	2546
$[\text{Tp}^{\text{tBu,Me}}]\text{Ni}(\text{CNCy})$	2085	N/A	2544
$[\text{Tp}^{\text{tBu,Ph}}]\text{Ni}(\text{CN}t\text{Bu})$	2100	N/A	2611
$[\text{Tp}^{\text{tBu,Me}}]\text{Ni}(\text{CO})$	N/A	1993	2559

3.2.3 Reactivity of $[\text{Tp}^{\text{tBu,Me}}]\text{Ni}(\text{CNR})$ with PhIO, R = *tert*-Bu, Cy.

3.2.3.1 Synthesis of $[\text{Tp}^{\text{tBu,Me}}]\text{Ni}(\text{O}_2\text{CN}(\text{H})\text{R})$, R = *tert*-Bu, Cy

Treatment of the monovalent complexes, $[\text{Tp}^{\text{tBu,Me}}]\text{Ni}(\text{CNR})$ (R = *tert*-Bu, Cy) with two equivalents of iodosylbenzene in toluene led to the formation of the Ni(II) carbamates, $[\text{Tp}^{\text{tBu,Me}}]\text{Ni}(\text{O}_2\text{CN}(\text{H})\text{R})$, Figure 3.8. After addition of the iodosylbenzene and stirring for 24 hours, the color of the solution changed from yellow to yellow-orange. The volatiles were then removed under vacuum and the product subjected to further purification. $[\text{Tp}^{\text{tBu,Me}}]\text{Ni}(\text{O}_2\text{CN}(\text{H})t\text{Bu})$ was isolated by recrystallization from pentane at $-20\text{ }^\circ\text{C}$ over the course of 1 week. The bright yellow, cube shaped crystals that formed were collected by decanting the mother liquor and drying the crystals under vacuum: crystalline yield (64%). For $[\text{Tp}^{\text{tBu,Me}}]\text{Ni}(\text{O}_2\text{CN}(\text{H})\text{Cy})$, purification was accomplished via washing with minimal amounts of pentane and drying under vacuum giving the product in 58% yield. The

incorporation of two oxygen atoms, via oxidation of the isonitrile ligand, is consistent with the iodosylbenzene stoichiometry, while the carbamate hydrogen is most likely derived from H-atom abstraction by an intermediate (*vide infra*).

X-ray quality crystals of $[\text{Tp}^{\text{tBu,Me}}]\text{Ni}(\text{O}_2\text{CN}(\text{H})\text{Cy})$ were grown by slow evaporation of a concentrated toluene solution. For $[\text{Tp}^{\text{tBu,Me}}]\text{Ni}(\text{O}_2\text{CN}(\text{H})\text{tBu})$, suitable crystals were selected from the bulk, low temperature recrystallization. The molecular structures of $[\text{Tp}^{\text{tBu,Me}}]\text{Ni}(\text{O}_2\text{CN}(\text{H})\text{tBu})$ and $[\text{Tp}^{\text{tBu,Me}}]\text{Ni}(\text{O}_2\text{CN}(\text{H})\text{Cy})$ are depicted in Figures 3.9 and 3.10, respectively. Selected bond distances are contained in Table 3.5 with selected bond angles and τ values in Table 3.6.

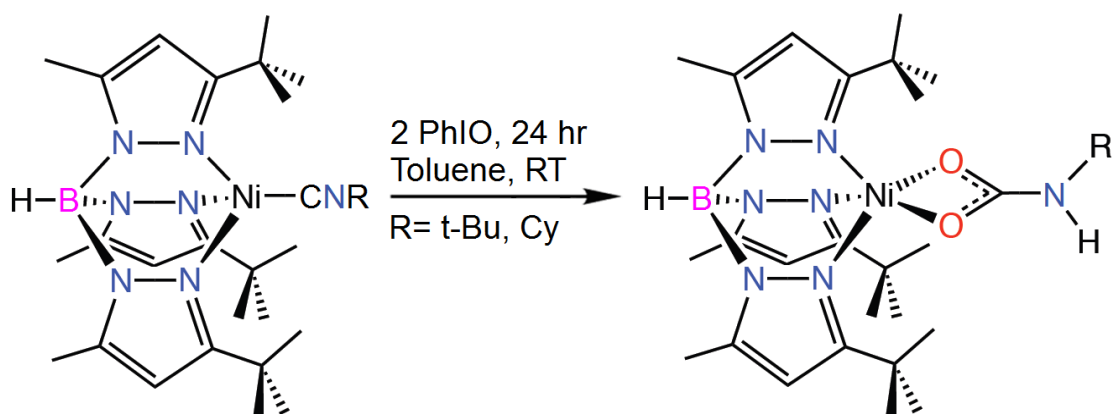


Figure 3.8 Synthesis of $[\text{Tp}^{\text{tBu,Me}}]\text{Ni}(\text{O}_2\text{CN}(\text{H})\text{R})$ from $[\text{Tp}^{\text{tBu,Me}}]\text{Ni}(\text{CNR})$ and PhIO.

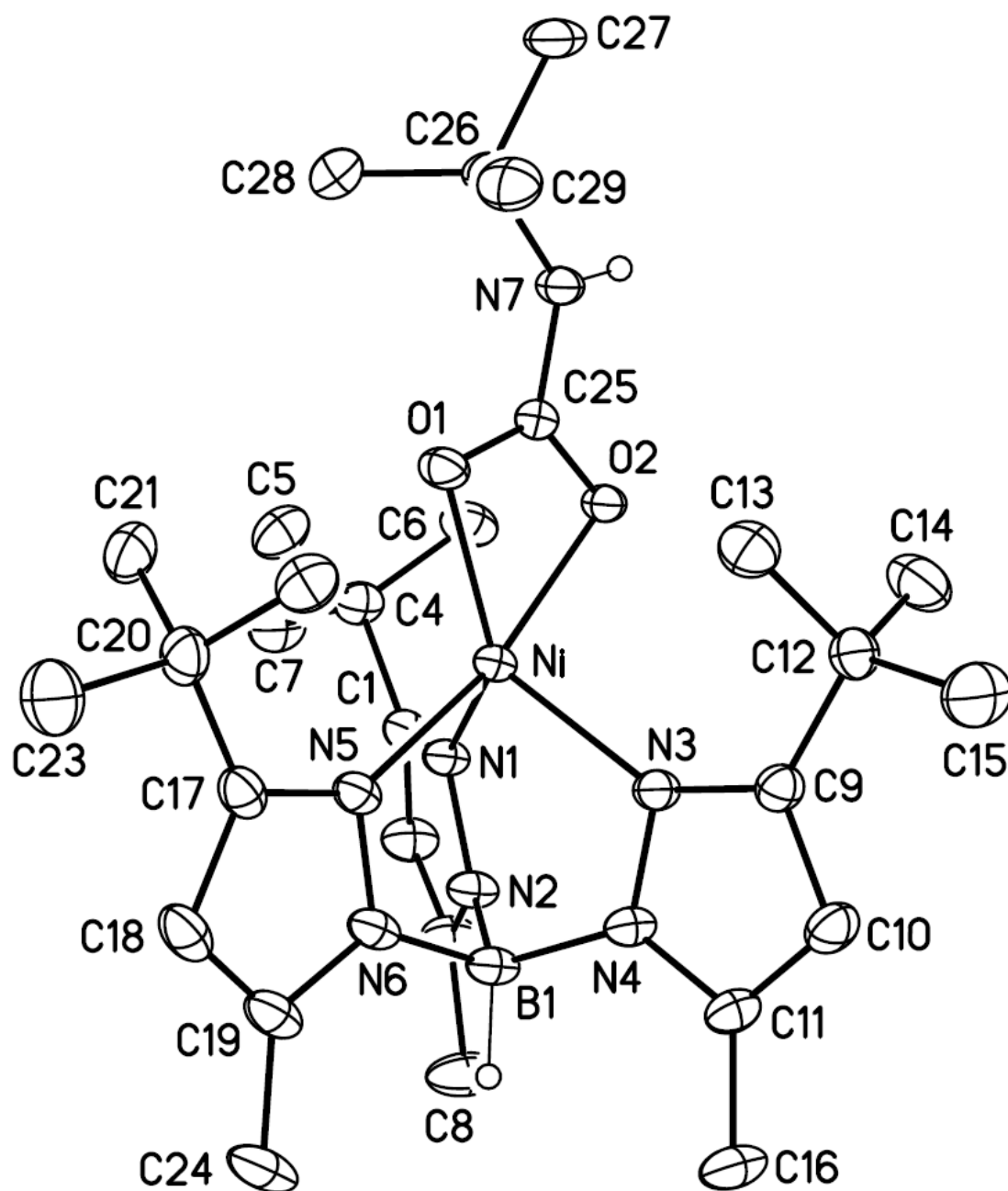


Figure 3.9 Thermal ellipsoid diagram of [Tp^{tBu,Me}]Ni(O₂CN(H)tBu) with atom labeling. Thermal ellipsoids are drawn to 30% probability. Hydrogen atoms are omitted for clarity with the exception of B-H and N-H.

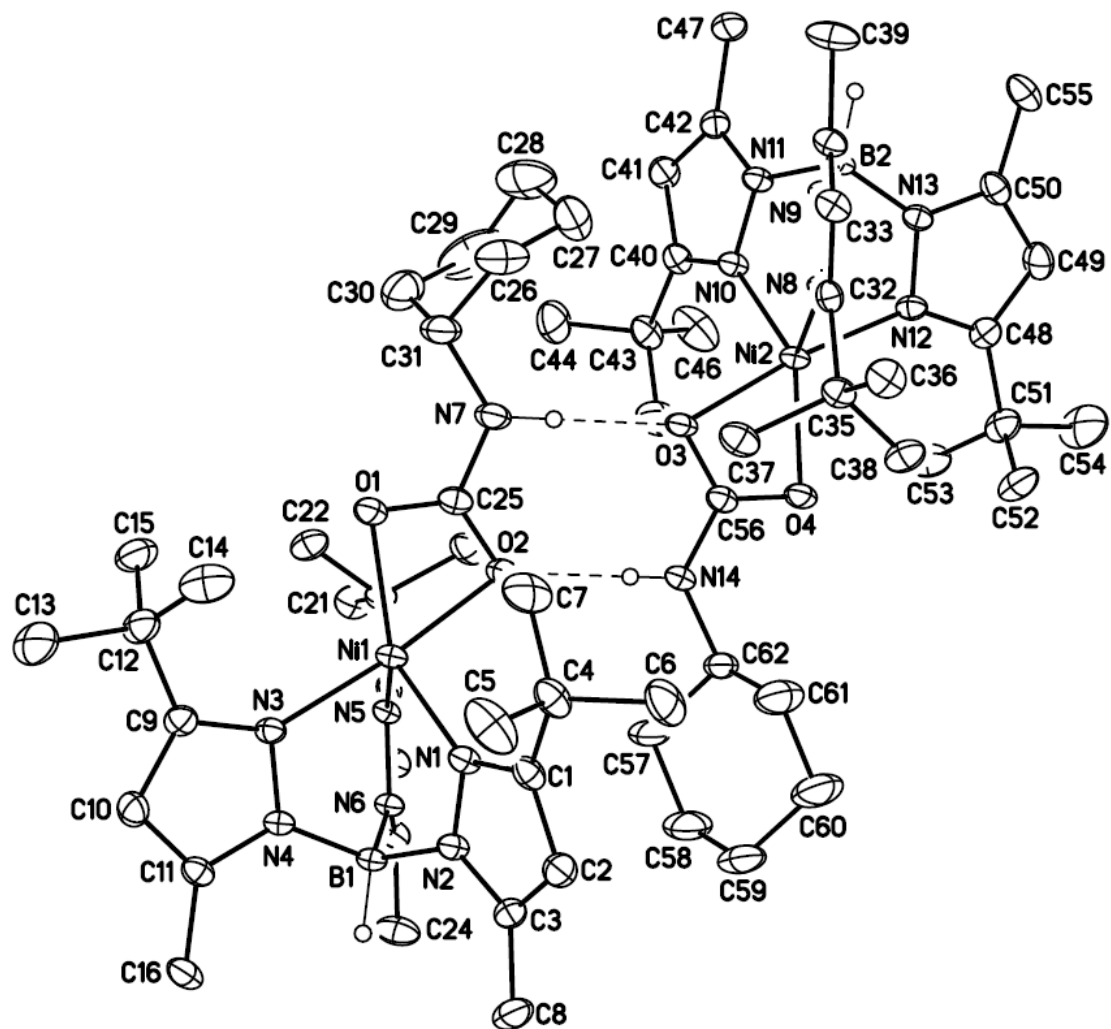


Figure 3.10 Thermal ellipsoid diagram of [Tp^{tBu,Me}]Ni(O₂CN(H)Cy) with atom labeling. Both molecules in the asymmetric unit are shown highlighting the intermolecular N–H—O bonds. Thermal ellipsoids are drawn to 30% probability. Hydrogen atoms are omitted for clarity with the exception of B–H and N–H.

Table 3.5 Selected bond lengths (Å) for [Tp^{tBu,Me}]Ni(O₂CN(H)tBu) and [Tp^{tBu,Me}]Ni(O₂CN(H)Cy).

	Bond Lengths (Å)	
	[Tp ^{tBu,Me}]Ni(O ₂ CN(H)tBu)	[Tp ^{tBu,Me}]Ni(O ₂ CN(H)Cy)*
Ni-N1	2.038(2)	2.058(2), 2.066(2)
Ni-N3	2.062(2)	2.056(2), 2.061(2)
Ni-N5	2.075(2)	2.062(2), 2.061(2)
Ni-O1	2.037(2)	2.109(2), 2.081(2)
Ni-O2	2.107(1)	2.053(2), 2.076(2)
O1-C25	1.279(2)	1.287(4), 1.283(3)
O2-C25	1.274(2)	1.274(3), 1.272(4)
C25-N7	1.337(2)	1.341(4), 1.342(4)

* Values reported for both of two symmetry unique molecules in the asymmetric unit.

Table 3.6 Selected bond angles (Å) and τ values for $[\text{Tp}^{\text{tBu,Me}}]\text{Ni}(\text{O}_2\text{CN}(\text{H})\text{tBu})$ and $[\text{Tp}^{\text{tBu,Me}}]\text{Ni}(\text{O}_2\text{CN}(\text{H})\text{Cy})$.

	Bond Angles ($^\circ$)	
	$[\text{Tp}^{\text{tBu,Me}}]\text{Ni}(\text{O}_2\text{CN}(\text{H})\text{tBu})$	$[\text{Tp}^{\text{tBu,Me}}]\text{Ni}(\text{O}_2\text{CN}(\text{H})\text{Cy})^*$
N1-Ni-O1	129.81(6)	133.52(9), 95.70(8)
N1-Ni-O2	98.48(6)	97.52(8), 119.46(9)
N3-Ni-O1	129.39(6)	110.25(9), 98.75(9)
N3-Ni-O2	100.04(6)	174.23(9), 135.64(9)
N5-Ni-O1	103.79(6)	121.10(9), 173.15(8)
N5-Ni-O2	167.23(5)	94.60(8), 109.36(9)
τ_5 value	0.69	0.68, 0.63

*Values reported for both of two symmetry unique molecules in the asymmetric unit.

3.2.3.2 Structure, Alternative Synthesis and Mechanistic Implications.

Single crystal XRD analysis of the carbamate complexes' structure indicates the usual κ^3 coordination to the Tp ligand as well as coordination through both oxygen atoms of the carbamate ligand itself. The manner of bonding to the carbamate moiety is reminiscent of the binding motif found in tetraazacycloalkane supported nickel dialkyl carbamates.⁶⁰ The calculated τ_5 values of 0.69 and 0.66 (average of two molecules in asymmetric unit), for $[\text{Tp}^{\text{tBu,Me}}]\text{Ni}(\text{O}_2\text{CN}(\text{H})\text{tBu})$ and $[\text{Tp}^{\text{tBu,Me}}]\text{Ni}(\text{O}_2\text{CN}(\text{H})\text{Cy})$, respectively, indicate a distorted, trigonal bipyramidal

geometry with one of the carbamate oxygen donors and one Tp nitrogen donor occupying the apical positions. The structure of $[\text{Tp}^{\text{tBu,Me}}]\text{Ni}(\text{O}_2\text{CN}(\text{H})\text{Cy})$ is notable in that it crystallizes as a dimer with hydrogen bonding occurring between the N-H and O atoms of adjacent molecules.

One possible mechanism for the formation of the carbamate complexes from $[\text{Tp}^{\text{tBu,Me}}]\text{Ni}(\text{CNR})$ and PhIO is shown in Figure 3.11. The mechanism begins with oxidation of the isonitrile ligand to isocyanate. Three potential scenarios have been considered for this step. One possibility is that the O atom is transferred directly to the isonitrile via an activated iodosylbenzene complex. The second possibility entails discrete transfer of the O atom to nickel to generate a transient oxo-nickel species, which then in turn transfers the O atom to the isonitrile. Yet a third possibility is that the iodosylbenzene oxidizes the isonitrile directly with the monovalent complex playing no role (i.e. “metal free” oxidation). While the exact nature of the isonitrile oxidation has yet to be elucidated, the possibility that the reaction proceeds through an oxo-nickel intermediate is of particular interest. Although definitive proof for an oxo-nickel species has yet to be provided, other lines of reactivity suggest the existence of this intermediate (see Chapter 5). Both direct O atom transfer from an activated iodosylbenzene complex and indirect transfer via an oxo-nickel intermediate would result in return to the Ni(I) oxidation state. At this point, a second equivalent of iodosylbenzene reacts with the monovalent nickel center ultimately resulting in the generation of a Ni(II) hydroxide complex after H atom abstraction by the oxo-nickel. Here, again, both an activated iodosylbenzene complex and an oxo-nickel species are possible intermediates, with the latter being invoked in Figure 3.11. Both of these would likely lead to the production of the Ni(II) hydroxo complex, $[\text{Tp}^{\text{tBu,Me}}]\text{Ni}(\text{OH})$,

via hydrogen atom abstraction from either the ligand (3-*tert*-butyl substituent) or the solvent. If the H-atom is ligand derived, the resulting *tert*-butyl radical must be quenched by another source, potentially the solvent or a carbamate alkyl substituent. The mechanism is completed by nucleophilic attack by the hydroxide on the isocyanate, followed by proton migration giving the carbamate.

Although the metal promoted reaction of CO₂ and amines is a more common route to carbamates,^{60,61} precedents for metal-hydroxide transformations, such as that proposed in this case, exist. For example, treatment of the dimeric, rare-earth hydroxide complexes, [Cp₂Ln(μ-OH)(THF)]₂ (Ln = Y, Er, Yb), with phenyl isocyanate, results in the generation of the bridging species, [Cp₂Ln(THF)]₂(μ-η²:η²-O₂CNPh).⁶² A bridging carbamate complex is the proposed intermediate with subsequent elimination of CpH and rearrangement generating the observed products.

In keeping with the last step of the mechanism, treatment of independently prepared [Tp^{tBu,Me}]Ni(OH) with *tert*-butyl or cyclohexyl isocyanate at room temperature results in the clean generation of the respective carbamates. Attempts at determining the source of the carbamate hydrogen atom in samples prepared with PhIO have, as yet, been unsuccessful. FT-IR spectral analysis of [Tp^{tBu,Me}]Ni(O₂CN(H)R) samples prepared in deuterated solvent displayed a ν_{NH} but not a ν_{ND} stretching mode. This argues against solvent being the H-atom source. ²H NMR spectral analysis of the same samples failed to locate evidence for deuterium incorporation into any ligand position, as might be expected for a solvent quenched *tert*-butyl radical. One possible explanation for this result is that a single deuteron might well be masked by the paramagnetic nickel (the 27 protons typically present

from the three *tert*-butyl groups are highly broadened in both the monovalent and divalent complexes).

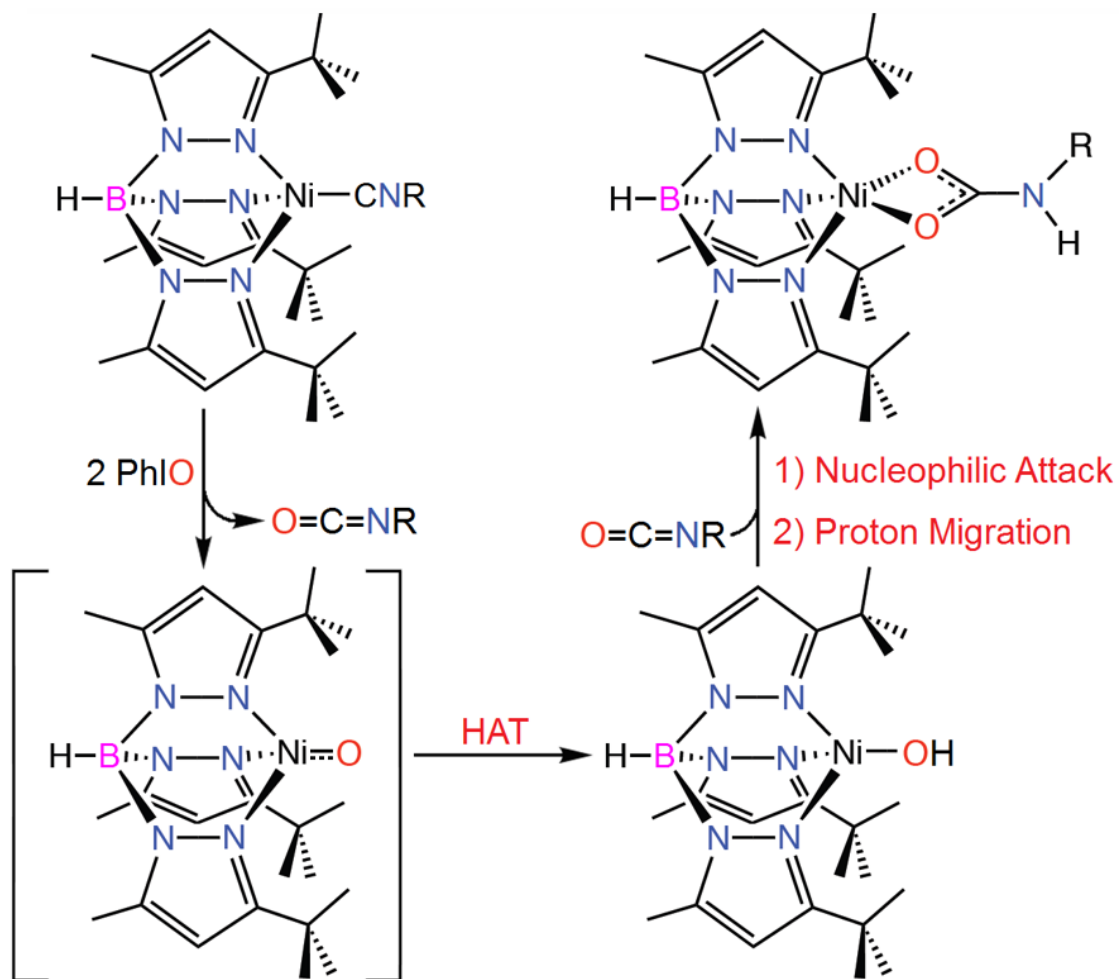


Figure 3.11 Proposed mechanism for formation of Ni(II) carbamates upon treatment of [Tp^{tBu,Me}]Ni(CNR) with iodosylbenzene.

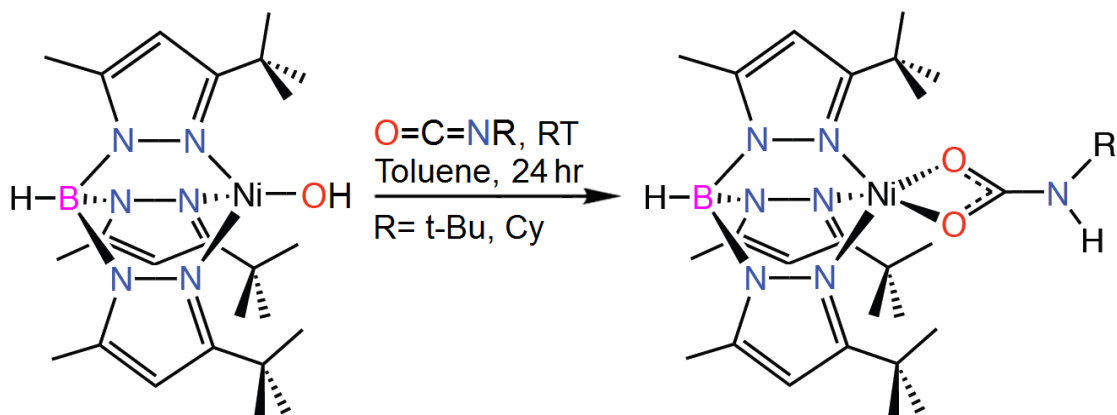


Figure 3.12 Alternative Synthesis of $[\text{Tp}^{\text{tBu,Me}}]\text{Ni}(\text{O}_2\text{CN}(\text{H})\text{R})$, $\text{R} = t\text{-Bu, Cy}$.

3.3 $[\text{Tp}^{\text{Ph,Me}}]$ -Supported Monovalent Complexes

The use of the $\text{Tp}^{\text{tBu,Me}}$ system, while offering a number of advantages, also presents certain limitations. The steric bulk imparted by the *tert*-butyl groups, which so effectively suppresses the generation of the bis-ligand complex and other detrimental bimolecular transformations, is a double-edged sword. It is inherently limiting in terms of the size of trapping agents and ancillary ligands that can be used with the system. It also limits access to the metal center in the case of the nickel-dioxygen adduct derivative, $[\text{Tp}^{\text{tBu,Me}}]\text{Ni}(\text{O}_2)$, and thus may limit the approach of larger substrates of interest for facile intermolecular oxidations. Fortunately, the Tp ligand class offers tremendous tunability, with a large and varied number of derivatives having been reported.^{63,64} For these reasons it seemed worthwhile to determine whether the techniques developed for preparation of the $[\text{Tp}^{\text{tBu,Me}}]\text{Ni}(\text{L})$ ($\text{L} = \text{CO}$, *tert*-BuNC, CyNC) series of complexes could be applied to other Tp ligands.

Another widely used ligand in the trispyrazolylborate class is the $\text{Tp}^{\text{Ph,Me}}$ system. The $\text{Tp}^{\text{Ph,Me}}$ ligand is both sterically and electronically distinct from $\text{Tp}^{\text{tBu,Me}}$. These features make for a significant contrast to $\text{Tp}^{\text{tBu,Me}}$. By extension, they also

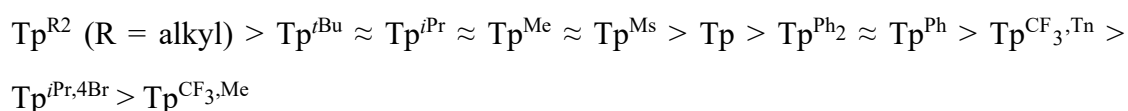
make $\text{Tp}^{\text{Ph,Me}}$ an intriguing candidate for use in preparing a second series of Tp supported, monovalent nickel complexes.

When discussing the steric properties of Tp ligands, the typical approach is to compare cone and wedge angles.⁶⁵ The lines which define a cone angle in a Tp ligand are derived from X-ray structural data. These lines connect the metal center to the outermost point of the R-group, taking into account its van der Waals radii. The larger the cone angle, the more difficult it is for a ligand or substrate to make a frontal approach to the metal center. The wedge angle, on the other hand, defines the space between R-groups, and by extension the ease of side-on access to the metal center.

While cone angles for the two nickel systems have not as yet been determined, the cone angles for related cobalt complexes supported by Tp^{tBu} and Tp^{Ph} were calculated to be 244° and 235° respectively.⁶⁶ Although Tp^{tBu} does indeed possess the larger cone angle, Calabrese et al have described the magnitude of the difference as being experimentally insignificant and have cautioned against the practice of comparing the cone angles of Tp ligands bearing planar R-groups with those having non-planer substituents. Thus, in the case of $\text{Tp}^{\text{tBu,Me}}$ and $\text{Tp}^{\text{Ph,Me}}$, it would appear that the wedge angles would make a better basis for comparison. Unfortunately, while the wedge angle for $\text{Tp}^{\text{tBu,Me}}$ is known (31° in the Tl complex), calculating the wedge angles for Tp ligands bearing 3-aryl substituents is complicated owing to multiple orientations in which such substituents may position themselves. Despite these difficulties, qualitative comparisons can be made regarding access to the metal center in the two complexes. Simply by examining the 3-dimensional structure of $\text{Tp}^{\text{Ph,Me}}$, one can see that certain orientations of the Ph groups provide greater access (larger wedge angle) than others. By comparison, the symmetrical *tert*-butyl groups of

$\text{Tp}^{\text{tBu,Me}}$ present a constant, small wedge angle which is much more restrictive in allowing access to the metal center. These generalizations are borne out by the coordination chemistry displayed by the two systems. Nickel(II) complexes of $\text{Tp}^{\text{Ph,Me}}$ easily bind an additional ancillary ligand or solvent whereas $\text{Tp}^{\text{tBu,Me}}$ complexes do not.^{67,68} Furthermore, $\text{Tp}^{\text{Ph,Me}}$ is capable of forming the bis-ligand complex, $[\text{Tp}^{\text{Ph,Me}}]_2\text{M}$, with numerous metals (including nickel).⁶⁹ Such complexes are sterically precluded in the case of $\text{Tp}^{\text{tBu,Me}}$, except in such cases where a pyrazole arm from one or both participating ligands is deligated.

With regard to electronic effects, the most significant change between $\text{Tp}^{\text{tBu,Me}}$ and $\text{Tp}^{\text{Ph,Me}}$ is a result of the differences in electron donating capabilities of the respective R-groups. A study by Tolman and Kitajima, comparing ν_{CO} data from a number of Tp supported metal-carbonyl complexes differing only in their R groups, is helpful in making a qualitative assessment of the relative electronic effects of the two systems.⁷⁰ Given that lower values of ν_{CO} represent higher electron density at the metal center, Pettinari and coworkers have used the data from this study to generate the following trend in ligand electron donating ability:⁶⁴



In addition to the more general observation that the phenyl rings of $\text{Tp}^{\text{Ph,Me}}$ are electron withdrawing whereas the *tert*-butyl groups on $\text{Tp}^{\text{tBu,Me}}$ are electron donating, this trend clearly demonstrates that $\text{Tp}^{\text{tBu,Me}}$ falls on the high end of the electronic donating spectrum while $\text{Tp}^{\text{Ph,Me}}$ likely falls somewhere in the middle. The latter complex is certainly not as electron withdrawing as the fluorinated species and the

presence of its electron releasing 5-Me substituent likely places it slightly higher in the series than the monosubstituted Tp^{Ph} .

3.3.1 Synthesis and Structure of $[\text{Tp}^{\text{Ph,Me}}]\text{Ni}(\text{PPh}_3)$ and $[\text{Tp}^{\text{Ph,Me}}]\text{Ni}(\text{CO})$

As with its larger, $\text{Tp}^{\text{tBu,Me}}$ -supported relatives, the first $\text{Tp}^{\text{Ph,Me}}$ -supported monovalent nickel complexes were prepared by sodium amalgam reduction of a Ni(II) precursor. $[\text{Tp}^{\text{Ph,Me}}]\text{NiI}$ was employed due to its ease of synthesis from $[\text{Tp}^{\text{Ph,Me}}]\text{NiCl}$, good solubility in toluene/benzene and rapid reduction to Ni(I). While *tert*-BuNC served as an effective trapping agent, the resulting complex, $[\text{Tp}^{\text{Ph,Me}}]\text{Ni}(\text{CN}t\text{Bu})$, was ineffective as a precursor to a stable O_2 adduct. While the reason for this has not been definitely established, oxidation of the isonitrile ligand by a transient superoxo-nickel species seems likely. Slow oxidation of *tert*-BuNC occurs when solutions of $[\text{Tp}^{\text{tBu,Me}}]\text{Ni}(\text{O}_2)$ are exposed to the isonitrile over extended periods at ambient temperature. Given that the metal center in $[\text{Tp}^{\text{Ph,Me}}]$ complexes is more accessible, due to smaller steric constraints imposed by the 3-Ph substituents, it seems probable that isonitrile oxidation also occurs in this system, possibly at an accelerated rate relative to the $[\text{Tp}^{\text{tBu,Me}}]$ system. However, it should be noted that unlike $\text{Tp}^{\text{tBu,Me}}$, carbamate complexes were not isolated in the $\text{Tp}^{\text{Ph,Me}}$ system.

Due to the difficulties encountered in preparing a stable dioxygen adduct with $[\text{Tp}^{\text{Ph,Me}}]\text{Ni}(\text{CN}t\text{Bu})$, the carbonyl complex, $[\text{Tp}^{\text{Ph,Me}}]\text{Ni}(\text{CO})$, was prepared as an alternative precursor. Direct synthesis of $[\text{Tp}^{\text{Ph,Me}}]\text{Ni}(\text{CO})$ via Na/Hg and KC_8 reduction of $[\text{Tp}^{\text{Ph,Me}}]\text{NiI}$ under CO proved troublesome, therefore the monovalent species, $[\text{Tp}^{\text{Ph,Me}}]\text{Ni}(\text{PPh}_3)$, was prepared first and used as a precursor to the carbonyl complex.

Synthesis of $[\text{Tp}^{\text{Ph,Me}}]\text{Ni}(\text{PPh}_3)$ was accomplished via reduction of $[\text{Tp}^{\text{Ph,Me}}]\text{NiI}$ in toluene with 5 equivalents of a 0.3% sodium amalgam in the presence of ~ 1.1 equivalents of PPh_3 . The reduction was finished in approximately 45 min, with completion indicated by a drastic color change from dark red to bright yellow. The crude product solution was separated from the amalgam via filtration through Celite. $[\text{Tp}^{\text{Ph,Me}}]\text{Ni}(\text{PPh}_3)$ is sensitive to silica gel, therefore purification was accomplished by layering pentane onto the filtered toluene solution. The product precipitated as a bright yellow microcrystalline powder over the course of one week. The powder was collected by filtration and dried under vacuum affording $[\text{Tp}^{\text{Ph,Me}}]\text{Ni}(\text{PPh}_3)$ in 72% yield.

$[\text{Tp}^{\text{Ph,Me}}]\text{Ni}(\text{CO})$ was prepared via ligand substitution by treating a THF solution of $[\text{Tp}^{\text{Ph,Me}}]\text{Ni}(\text{PPh}_3)$ with an excess of CO. Purging the $[\text{Tp}^{\text{Ph,Me}}]\text{Ni}(\text{PPh}_3)$ solution with CO for 2 min followed by stirring for 30 min led to a color change from bright yellow to a much paler yellow. The solvent and excess CO were removed under vacuum. Subsequently, the crude product was washed with pentane to remove free PPh_3 . After drying under vacuum, $[\text{Tp}^{\text{Ph,Me}}]\text{Ni}(\text{CO})$ was isolated as a pale yellow powder in high yield (83%). As is the case with their larger brethren, both $[\text{Tp}^{\text{Ph,Me}}]\text{Ni}(\text{CO})$ and $[\text{Tp}^{\text{Ph,Me}}]\text{Ni}(\text{PPh}_3)$ are stable under N_2 but are highly reactive toward water and dioxygen.

X-ray quality crystals of $[\text{Tp}^{\text{Ph,Me}}]\text{Ni}(\text{PPh}_3)$ and $[\text{Tp}^{\text{Ph,Me}}]\text{Ni}(\text{CO})$ were grown by vapor diffusion of pentane into a concentrated toluene solution of the respective metal complex. The molecular structures of $[\text{Tp}^{\text{Ph,Me}}]\text{Ni}(\text{PPh}_3)$ and $[\text{Tp}^{\text{Ph,Me}}]\text{Ni}(\text{CO})$ are depicted in Figures 3.15 and 3.16, respectively. Selected bond distances, bond angles and τ values are contained in Table 3.7.

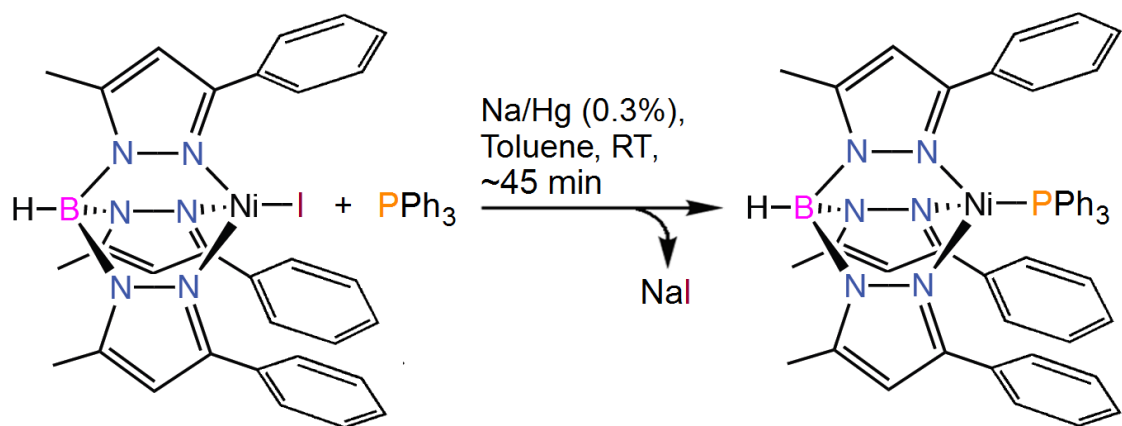


Figure 3.13 Synthesis of $[\text{Tp}^{\text{Ph,Me}}]\text{Ni}(\text{PPh}_3)$.

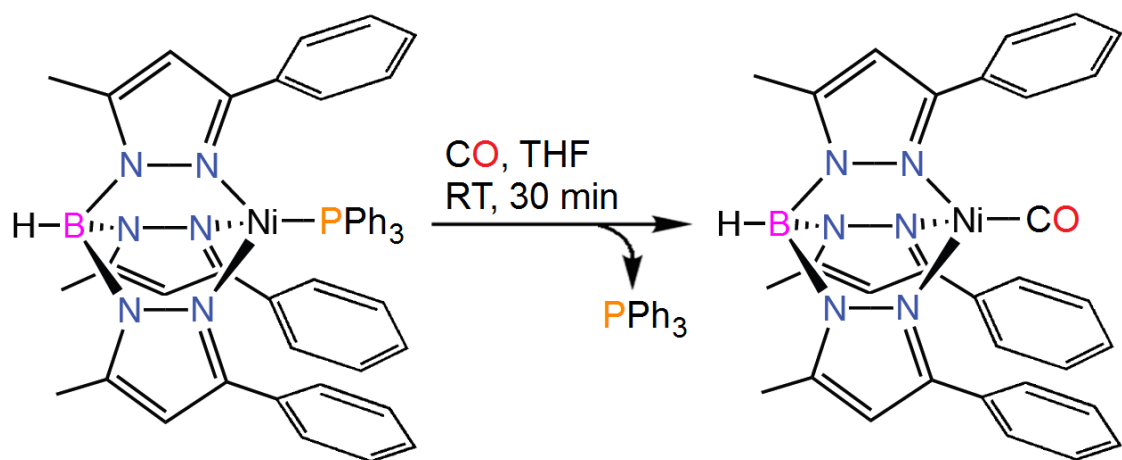


Figure 3.14 Synthesis of $[\text{Tp}^{\text{Ph,Me}}]\text{Ni}(\text{CO})$.

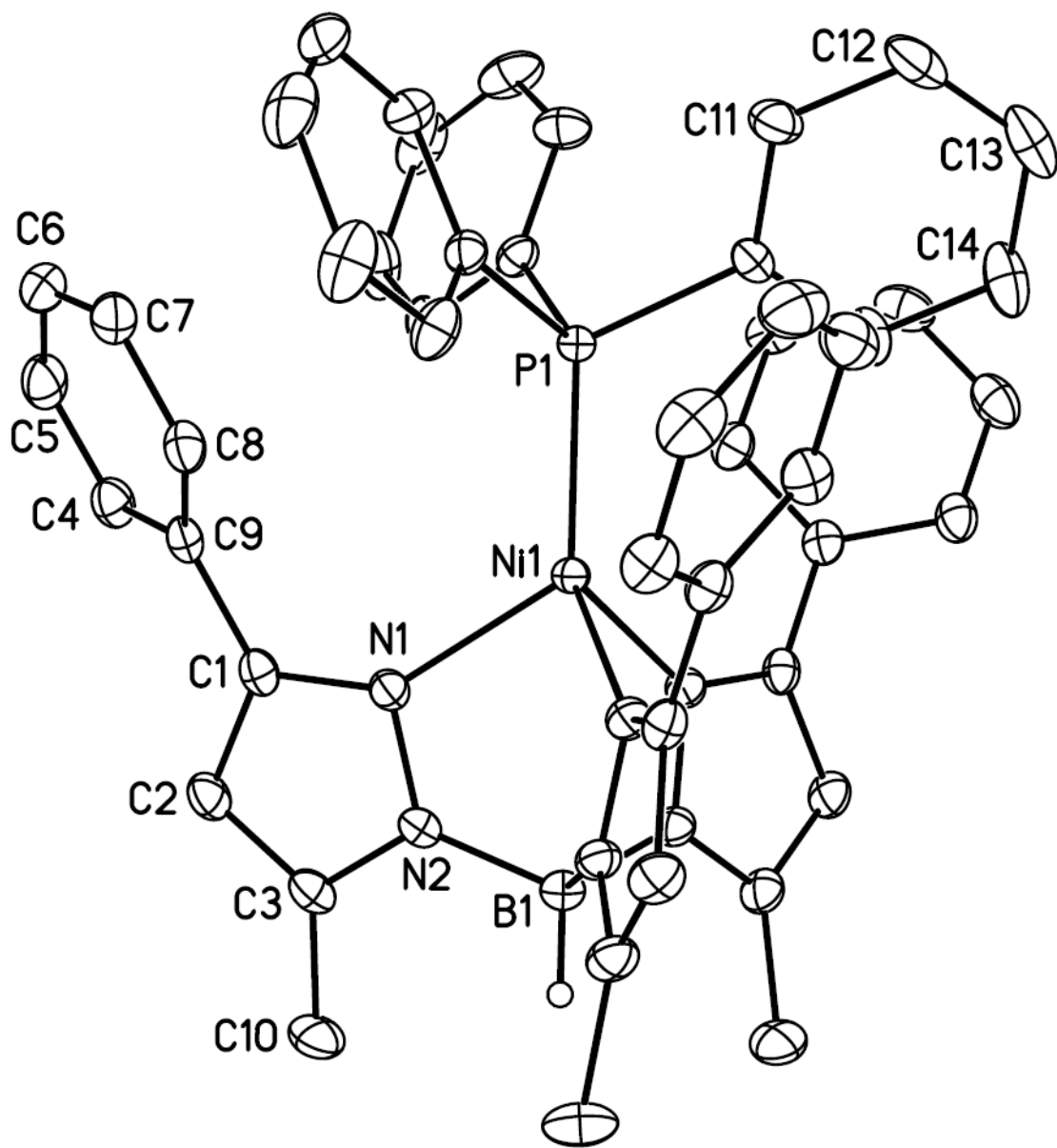


Figure 3.15 Thermal ellipsoid diagram of $[\text{Tp}^{\text{Ph,Me}}]\text{Ni}(\text{PPh}_3)$ with atom labeling. Thermal ellipsoids are drawn to 30% probability. Hydrogen atoms are omitted for clarity with the exception of B-H.

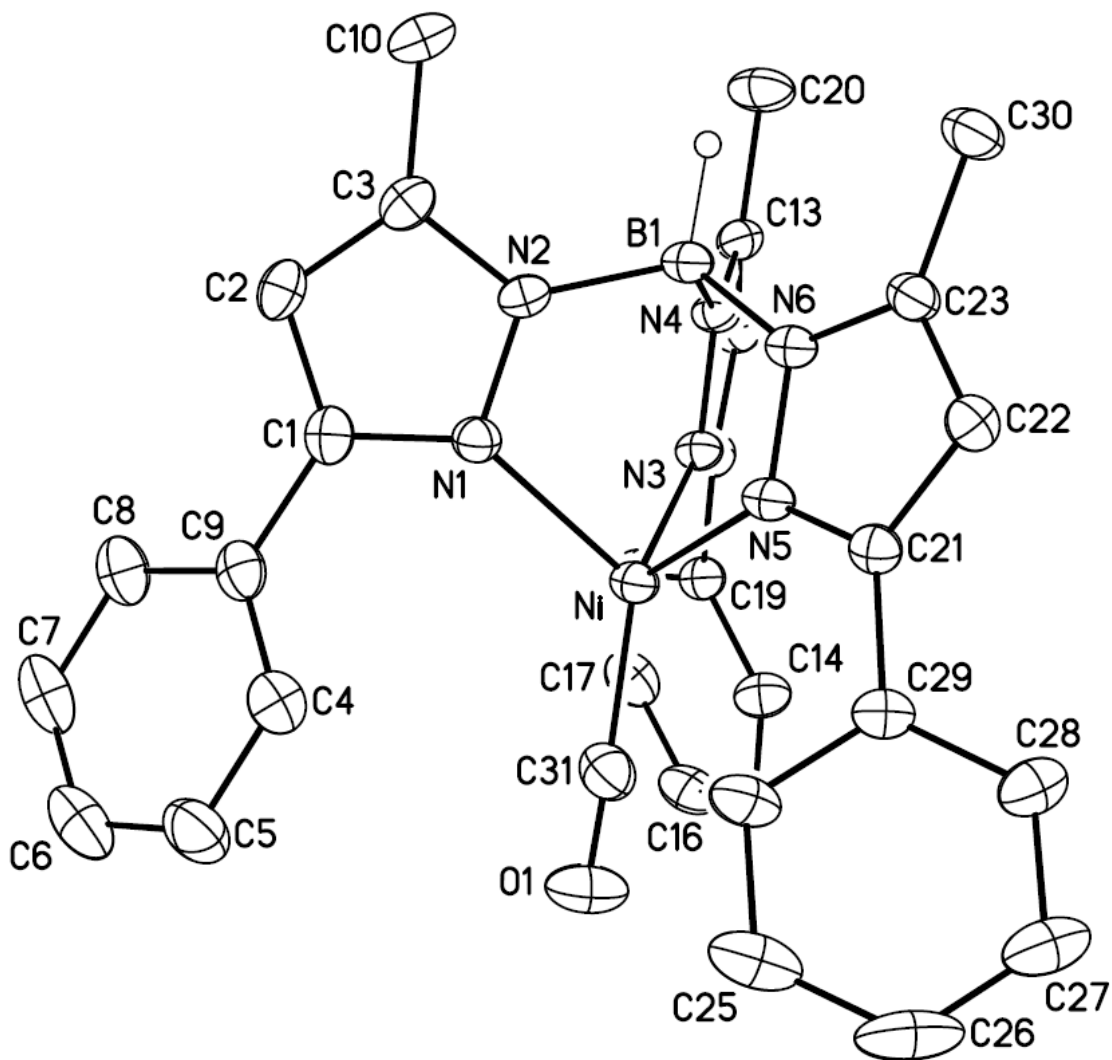


Figure 3.16 Thermal ellipsoid diagram of $[\text{Tp}^{\text{Ph,Me}}]\text{Ni}(\text{CO})$ with atom labeling. Thermal ellipsoids are drawn to 30% probability. Hydrogen atoms are omitted for clarity with the exception of B-H.

Table 3.7 Selected bond lengths, bond angles and τ values for $[\text{Tp}^{\text{Ph,Me}}]\text{Ni}(\text{CO})$ and $[\text{Tp}^{\text{Ph,Me}}]\text{Ni}(\text{PPh}_3)$.

		$[\text{Tp}^{\text{Ph,Me}}]\text{Ni}(\text{CO})$	$[\text{Tp}^{\text{Ph,Me}}]\text{Ni}(\text{PPh}_3)$
Bond Lengths	Ni–N1	2.022(2)	2.100(1)
	Ni–N3	2.048(2)	2.100(1)
	Ni–N5	2.017(2)	2.100(1)
	Ni–P	N/A	2.189(1)
	Ni–C	1.783(3)	N/A
	C–O	1.108(4)	N/A
Bond Angles	Ni–C–O	175.8(3)	N/A
τ_4 value		0.42	0.35

3.3.2 Molecular Structures of $[\text{Tp}^{\text{Ph,Me}}]\text{Ni}(\text{PPh}_3)$ and $[\text{Tp}^{\text{Ph,Me}}]\text{Ni}(\text{CO})$.

The molecular structures of $[\text{Tp}^{\text{Ph,Me}}]\text{Ni}(\text{PPh}_3)$ and $[\text{Tp}^{\text{Ph,Me}}]\text{Ni}(\text{CO})$ are best described as distorted tetrahedral, as indicated by their τ_4 values of 0.35 and 0.42, respectively. For $[\text{Tp}^{\text{Ph,Me}}]\text{Ni}(\text{PPh}_3)$, the Ni–P distance is 2.1887(6) Å. The three Ni–N distances are equivalent as demanded by crystallographic symmetry with a value of 2.100(1) Å. In $[\text{Tp}^{\text{Ph,Me}}]\text{Ni}(\text{CO})$, the average Ni–N distance was found to be 2.029(2) with a Ni–C bond length of 1.783(3) Å. The latter value compares well with that of $[\text{PhTt}^{\text{tBu}}]\text{Ni}(\text{CO})$ with a Ni–C bond length of 1.764(6) Å.

3.3.3 Proton NMR and FT-IR Spectral Analysis of [Tp^{Ph,Me}]Ni(PPh₃) and [Tp^{Ph,Me}]Ni(CO).

3.3.3.1 ¹H NMR Spectral Analysis.

Selected ¹H NMR spectral features for [Tp^{Ph,Me}]Ni(CO) and [Tp^{Ph,Me}]Ni(PPh₃) are contained in Table 3.8. While there are some differences in the magnitude of chemical shifts, with regard to the general locations of common substituents, the ¹H NMR spectra of the Tp^{Ph,Me}-supported Ni(I) complexes are similar in appearance to those of the Tp^{tBu,Me}-supported species. In [Tp^{Ph,Me}]Ni(CO), the 4-Pz, 5-Me and B-H substituents are located at $\delta = 19.0, 16.9, 32.8$, respectively (Figure 3.17), versus 17.8, 21.3 and 45.7 for the same protons in [Tp^{tBu,Me}]Ni(CO). The differences observed in the Tp^{tBu,Me} ligand between the monovalent complexes and their divalent precursors are also exhibited in Tp^{Ph,Me}, with major spectral differences between the oxidation states, but consistency within each oxidation state.

In both [Tp^{Ph,Me}]Ni(CO) and [Tp^{Ph,Me}]Ni(PPh₃), the *ortho* protons on the 3-phenyl group show a significant disparity in chemical shift and peak shape versus the neighboring *meta* and *para* protons. The latter two are relatively sharp and occur in the aromatic region while the former are shifted upfield of zero, and exhibit significant broadening. In [Tp^{Ph,Me}]Ni(PPh₃), the *ortho* protons on the triphenylphosphine ligand are similarly broadened compared with the other two positions on the phenyl ring. This discrepancy is most likely due to dipolar coupling as a consequence of the proximity of the *ortho* protons to the paramagnetic Ni(I) core.⁷¹

3.3.3.2 FT-IR Spectral Analysis.

[Tp^{Ph,Me}]Ni(CO) displays $\nu_{\text{CO}} = 2005 \text{ cm}^{-1}$. As with the [Tp^{tBu,Me}]Ni(CO) analog, this stretching frequency indicates a weakened carbon-oxygen bond relative to

free carbon monoxide (2143 cm^{-1}). The relatively minor difference in ν_{CO} between $[\text{Tp}^{\text{tBu,Me}}]\text{Ni}(\text{CO})$ and $[\text{Tp}^{\text{Ph,Me}}]\text{Ni}(\text{CO})$ is likely the result of the electron withdrawing nature of the phenyl rings in the latter, which slightly reduces the extent of Π -backbonding.

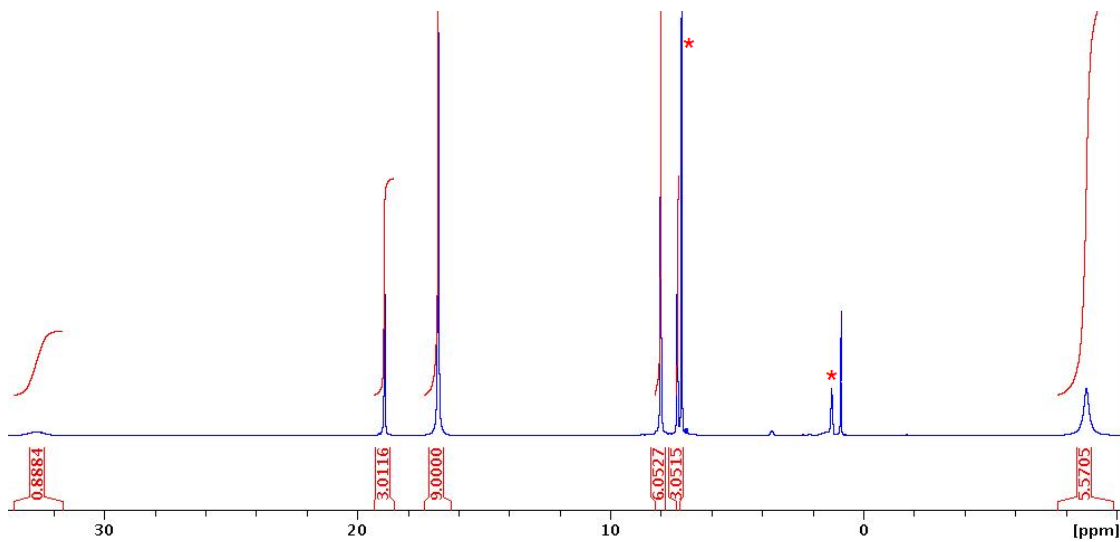


Figure 3.17 ^1H NMR spectrum of $[\text{Tp}^{\text{Ph,Me}}]\text{Ni}(\text{CO})$. * indicates residual solvent signals.

Table 3.8 Selected ^1H NMR spectral features for $[\text{Tp}^{\text{Ph,Me}}]\text{Ni}(\text{CO})$ and $[\text{Tp}^{\text{Ph,Me}}]\text{Ni}(\text{PPh}_3)$.

Functional Group	Chemical Shift (δ , ppm)					
	<i>3-o-Ph</i>	<i>3-m-Ph</i>	<i>3-p-Ph</i>	<i>4-Pz</i>	<i>5-Me</i>	<i>B-H</i>
$[\text{Tp}^{\text{Ph,Me}}]\text{Ni}(\text{PPh}_3)$	-18.1	7.6	9.0	13.4	18.5	49.2
$[\text{Tp}^{\text{Ph,Me}}]\text{Ni}(\text{CO})$	-8.9	8.0	7.3	19.0	16.9	32.8

3.4 Summary

The purpose of this study was two-fold. The primary objective was the preparation of nickel(I) complexes supported by the trispyrazolylborate (Tp) ligand. The secondary goal was to assess the reactivity of these monovalent species towards O atom transfer agents. The $\text{Tp}^{\text{tBu,Me}}$ (Tp') variant was chosen for the initial work due to its steric properties and its documented ability to support the monovalent oxidation states of other first row transition metals.^{52,53} The procedures developed for $\text{Tp}^{\text{tBu,Me}}$ were then adapted for use with $\text{Tp}^{\text{tBu,Ph}}$ and $\text{Tp}^{\text{Ph,Me}}$.

$[\text{Tp}^{\text{tBu,Me}}]\text{NiBr}$ provided a viable precursor for preparation of monovalent species. Sodium amalgam reduction of $[\text{Tp}^{\text{tBu,Me}}]\text{NiBr}$ in the presence of the isonitriles with large substituents, *tBuNC* and *CyNC*, resulted in the successful preparation of the monovalent complexes, $[\text{Tp}^{\text{tBu,Me}}]\text{Ni}(\text{CN}t\text{Bu})$ and $[\text{Tp}^{\text{tBu,Me}}]\text{Ni}(\text{CNCy})$. Potassium graphite reduction of $[\text{Tp}^{\text{tBu,Me}}]\text{NiBr}$ under an atmosphere of CO led to the isolation of $[\text{Tp}^{\text{tBu,Me}}]\text{NiCO}$. X-ray crystallographic analysis of the isonitrile bound Ni(I) species

revealed a distorted tetrahedral environment in all cases, as well as metric parameters consistent with the previously reported species, $[\text{Tt}^{\text{R}}]\text{Ni}^{\text{I}}(\text{L})$ ($\text{R} = \text{tBu}, \text{Ad}; \text{L} = \text{tBuNC}$). Further spectroscopic analysis showed that the monovalent complexes have $S = 1/2$ ground state and display highly distinctive ^1H NMR spectra, which are consistent across the series. The distinctiveness of these spectra permit assignment of the metal oxidation state by ^1H NMR spectral analysis.

$[\text{Tp}^{\text{tBu,Me}}]\text{Ni}(\text{CNtBu})$ and $[\text{Tp}^{\text{tBu,Me}}]\text{Ni}(\text{CNCy})$ were unreactive toward the oxygen atom transfer agents N_2O and pyridine-N-oxide, but reacted with PhIO generating the nickel(II) carbamates, $[\text{Tp}^{\text{tBu,Me}}]\text{Ni}(\text{O}_2\text{CN}(\text{H})\text{tBu})$ and $[\text{Tp}^{\text{tBu,Me}}]\text{Ni}(\text{O}_2\text{CN}(\text{H})\text{Cy})$. X-ray crystallography showed that the carbamate species display distorted trigonal bipyramidal geometries. The carbamates were prepared independently via treatment of $[\text{Tp}^{\text{tBu,Me}}]\text{Ni}(\text{OH})$ with isocyanates, implicating the hydroxide complex as a likely intermediate in reactions of the isonitrile bound, Ni(I) species with PhIO.

The nickel(I) complex, $[\text{Tp}^{\text{Ph,Me}}]\text{Ni}(\text{PPh}_3)$, was prepared from $[\text{Tp}^{\text{Ph,Me}}]\text{NiI}$ by sodium amalgam reduction, using techniques developed for the $\text{Tp}^{\text{tBu,Me}}$ supported species. $[\text{Tp}^{\text{Ph,Me}}]\text{Ni}(\text{CO})$ was prepared by treating $[\text{Tp}^{\text{Ph,Me}}]\text{Ni}(\text{PPh}_3)$ with carbon monoxide. X-ray crystallography revealed a distorted tetrahedral geometry about the nickel in both complexes. Further spectroscopic analysis showed the complexes to have ^1H NMR and FT-IR spectra highly similar to their larger $\text{Tp}^{\text{tBu,Me}}$ supported relatives. The reactivity of $[\text{Tp}^{\text{Ph,Me}}]\text{Ni}(\text{PPh}_3)$ and $[\text{Tp}^{\text{Ph,Me}}]\text{Ni}(\text{CO})$ has been investigated by Ann Ploskonka.⁷²

Chapter 4

SYNTHESIS AND CHARACTERIZATION OF TRISPYRAZOLYLBORATE SUPPORTED SUPEROXONICKEL COMPLEXES

4.1 Introduction

The first example of a low valent nickel complex activating dioxygen was Otsuka's report²⁸ in 1969 of accessing the Ni(0)/Ni(II) redox couple. More recently, the use of monovalent nickel complexes in particular has come to prominence for this purpose. First utilized in the Riordan lab,²⁹ this approach to dioxygen activation has proven to be one of the few synthetically useful methods for accessing nickel-dioxygen adducts of sufficient stability for spectroscopic and structural characterization.

Despite the utility of the technique, however, the generation of nickel-dioxygen adducts displaying stability under ambient conditions has proven quite difficult and has thus necessitated that the majority of studies concerning these species be performed under carefully controlled, low temperature conditions. This is, of course, inherently limiting in terms of the nature of studies that can be performed with these complexes, as it presents both thermal and, in many cases, temporal barriers to certain lines of reactivity. For this reason, the pursuit of a more thermally robust nickel-dioxygen complex was deemed advantageous.

The success shown in using trispyrazolylborate-supported monovalent complexes of cobalt and copper to generate stable dioxygen adducts, first demonstrated in the landmark reports by Theopold⁵² and Kitajima,⁵³ persuaded us that

a similar approach using monovalent nickel could be a fruitful course of study in the pursuit of a thermally stable nickel-dioxygen species. To this end, suitable Ni(I) starting materials were targeted utilizing the trispyrazolylborate ligands, $\text{Tp}^{\text{tBu,Me}}$ and $\text{Tp}^{\text{Ph,Me}}$. To the best of our knowledge, when this work commenced there were no examples of Ni(I) trispyrazolylborate complexes. The reduction of the divalent precursors, $[\text{Tp}^{\text{tBu,Me}}]\text{NiBr}$ and $[\text{Tp}^{\text{Ph,Me}}]\text{NiI}$, in the presence of suitable donor ligands resulted in the isolation and full characterization of the first Tp supported monovalent nickel complexes (for details, see Chapter 3). Preparation of these species subsequently allowed access to the superoxo-nickel(II) compounds, $[\text{Tp}^{\text{tBu,Me}}]\text{Ni}(\text{O}_2)$ and $[\text{Tp}^{\text{Ph,Me}}]\text{Ni}(\text{O}_2)$, whose synthesis, structure, and properties are described herein.

4.2 Synthesis and Structure of $[\text{Tp}^{\text{tBu,R}}]\text{Ni}(\text{O}_2)$, R = Me, Ph

The superoxo-nickel(II) complex, $[\text{Tp}^{\text{tBu,Me}}]\text{Ni}(\text{O}_2)$, was synthesized by treating its Ni(I) precursor, $[\text{Tp}^{\text{tBu,Me}}]\text{Ni}(\text{CN}t\text{Bu})$, with O_2 , Figure 4.1. Preparation of the superoxo complex was accomplished by cooling a solution of $[\text{Tp}^{\text{tBu,Me}}]\text{Ni}(\text{CN}t\text{Bu})$ in pentane to $-78\text{ }^\circ\text{C}$ followed by addition of a large excess of dry dioxygen. O_2 addition was accompanied by a color change in the solution from yellow to brown. The nickel-dioxygen adduct is poorly soluble in pentane and rapidly crashed out as a brown precipitate. The crude product was recovered by filtration, washed with MeOH and pentane and dried under vacuum giving $[\text{Tp}^{\text{tBu,Me}}]\text{Ni}(\text{O}_2)$ as a brown, air- and moisture-stable powder, in excellent yield (92%). The $\text{Tp}^{\text{tBu,Ph}}$ supported analog, $[\text{Tp}^{\text{tBu,Ph}}]\text{Ni}(\text{O}_2)$, was prepared in a similar fashion from $[\text{Tp}^{\text{tBu,Ph}}]\text{Ni}(\text{CN}t\text{Bu})$. It should be noted that $[\text{Tp}^{\text{tBu,Me}}]\text{Ni}(\text{CNCy})$ and $[\text{Tp}^{\text{tBu,Me}}]\text{Ni}(\text{CO})$ can also be used to prepare $[\text{Tp}^{\text{tBu,Me}}]\text{Ni}(\text{O}_2)$, however, the superior yield of $[\text{Tp}^{\text{tBu,Me}}]\text{Ni}(\text{CN}t\text{Bu})$, as well its

higher solubility in pentane, made it the most convenient precursor for bulk preparation.

For $[\text{Tp}^{\text{tBu,Me}}]\text{Ni}(\text{O}_2)$, X-ray quality crystals were grown by vapor diffusion of Et_2O into a concentrated CHCl_3 solution of the metal complex. In the case of $[\text{Tp}^{\text{tBu,Ph}}]\text{Ni}(\text{O}_2)$, crystals were grown by layering pentane on a C_6D_6 solution of the metal complex in an NMR tube. The molecular structures of $[\text{Tp}^{\text{tBu,Me}}]\text{Ni}(\text{O}_2)$ and $[\text{Tp}^{\text{tBu,Ph}}]\text{Ni}(\text{O}_2)$ are found in Figures 4.2 and 4.3, respectively. Selected bond distances are contained in Table 4.1 with selected bond angles and τ values in Table 4.2.

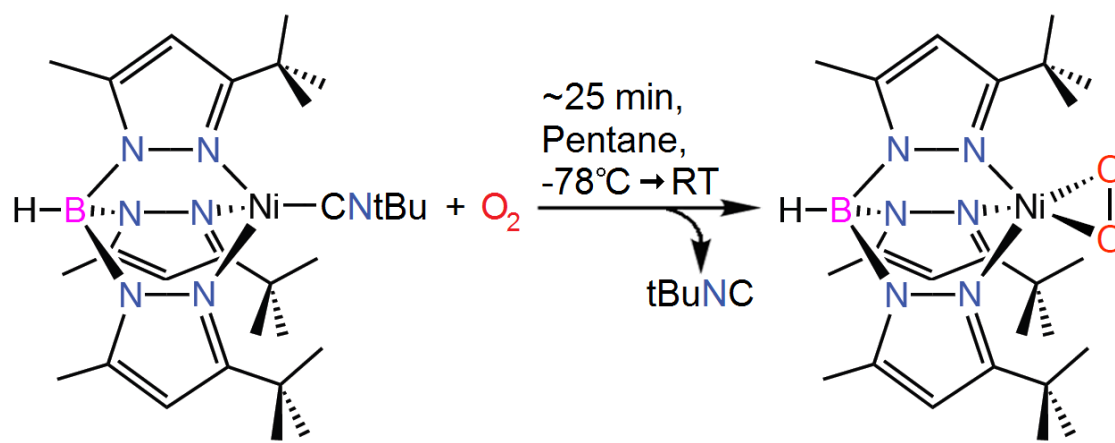


Figure 4.1 Synthesis of $[\text{Tp}^{\text{tBu,Me}}]\text{Ni}(\text{O}_2)$.

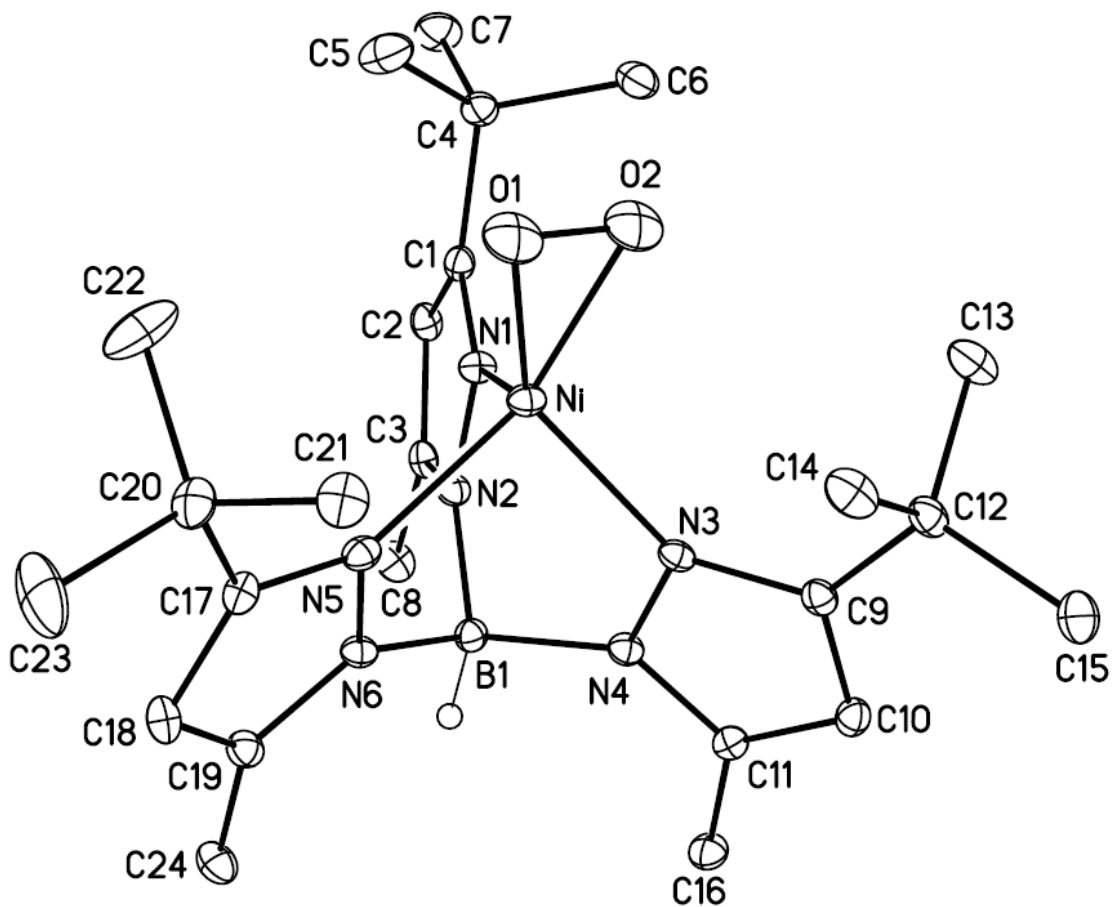


Figure 4.2 Thermal ellipsoid diagram of $[\text{Tp}^{\text{tBu,Me}}]\text{Ni}(\text{O}_2)$ with atom labeling. Thermal ellipsoids are drawn to 30% probability. Hydrogen atoms are omitted for clarity with the exception of B-H. Positional disorder in the O_2 moiety is not depicted.

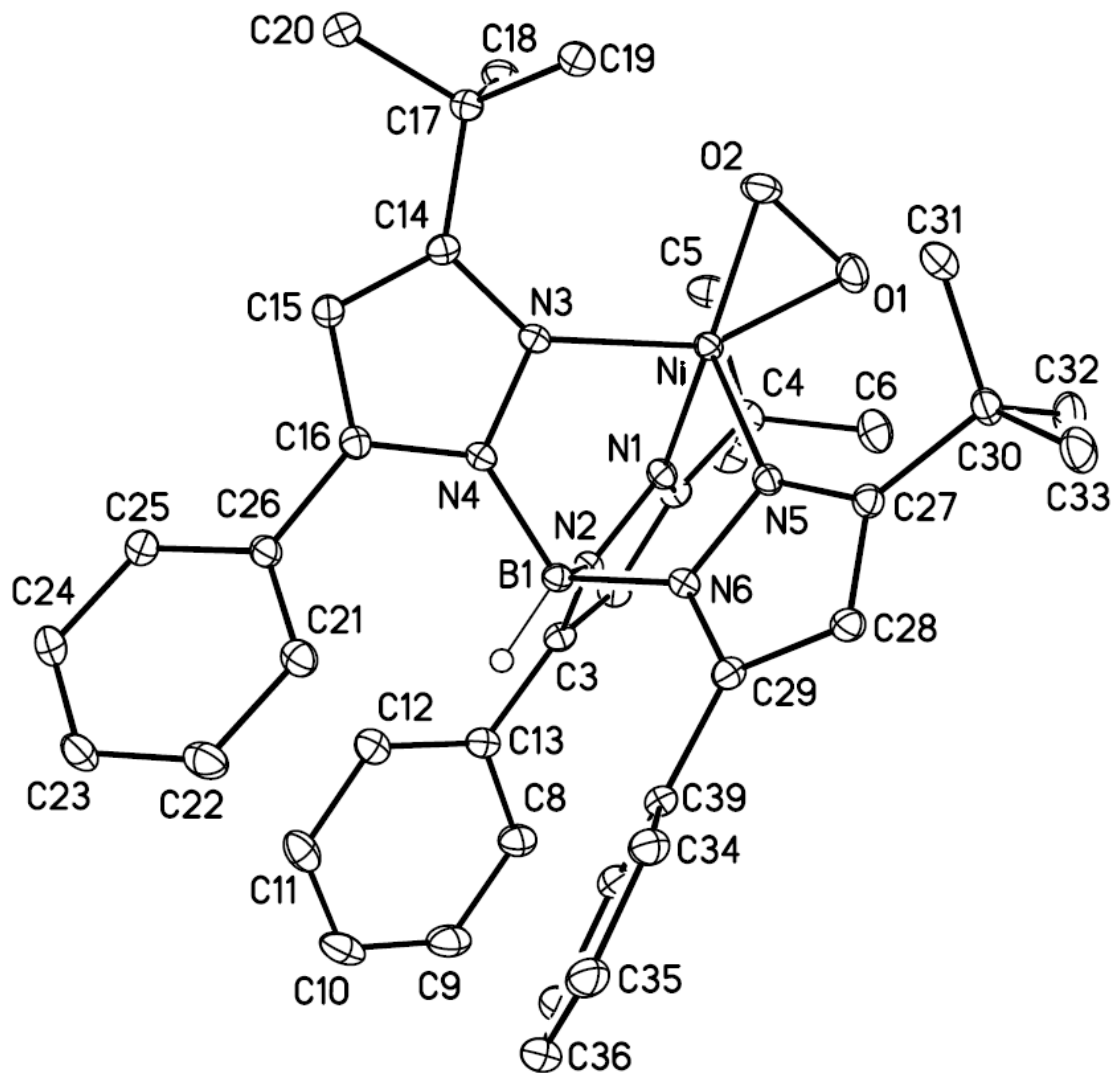


Figure 4.3 Thermal ellipsoid diagram of $[\text{Tp}^{\text{tBu,Ph}}]\text{Ni}(\text{O}_2)$ with atom labeling. Thermal ellipsoids are drawn to 30% probability. Hydrogen atoms are omitted for clarity with the exception of B-H.

Table 4.1 Selected bond distances (Å) for [Tp^{tBu,Me}]Ni(O₂) and [Tp^{tBu,Ph}]Ni(O₂).

		[Tp ^{tBu,Me}]Ni(O ₂)	[Tp ^{tBu,Ph}]Ni(O ₂)
Bond Length	Ni–N1	2.046(2)	2.0381(16)
	Ni–N3	1.997(2)	1.9706(15)
	Ni–N5	1.993(2)	1.9909(15)
	Ni–O1	1.872(4)	1.8706(14)
	Ni–O2	1.855(3)	1.8492(14)
	O–O	1.268(4)*	1.359(2)

* Apparent O–O distance is uncharacteristically short due to librational motion and modeling of positional disorder (*vide infra*).

Table 4.2 Selected bond angles (°) for [Tp^{tBu,Me}]Ni(O₂) and [Tp^{tBu,Ph}]Ni(O₂).

	Bond Angle (°)	
	[Tp ^{tBu,Me}]Ni(O ₂)	[Tp ^{tBu,Ph}]Ni(O ₂).
N1–Ni–O1	121.84(14)	105.20(6)
N1–Ni–O2	105.96(14)	123.26(7)
N3–Ni–O1	135.13(15),	152.56(6)
N3–Ni–O2	107.49(14),	109.87(6)
N5–Ni–O1	111.60(13)	105.70(6)
N5–Ni–O2	151.17(15)	134.58(7)
τ ₅ value	0.27	0.30

4.3 Molecular Structure of $[\text{Tp}^{\text{tBu,R}}]\text{Ni}(\text{O}_2)$, $\text{R} = \text{Me, Ph}$

The molecule structure of $[\text{Tp}^{\text{tBu,Me}}]\text{Ni}(\text{O}_2)$ reveals a five coordinate nickel bound by the 3 nitrogen donors of the Tp ligand and by the O_2 moiety, which is coordinated in a side-on, $\eta^2\text{-O}_2$, fashion to the metal. This dioxygen binding mode mirrors that of the analogous cobalt and copper complexes, $[\text{Tp}^{\text{tBu,Me}}]\text{Co}(\text{O}_2)$ and $[\text{Tp}^{\text{tBu,iPr}}]\text{Cu}(\text{O}_2)$ ^{52,53}. The τ_5 value of 0.27 is indicative of a square pyramidal geometry. The average Ni–N and Ni–O bond lengths are 2.012(2) and 1.864(4) respectively, with the latter value being similar to the nickel-oxygen distance in the four-coordinate Ni(II) species, $[\text{Tp}^{\text{tBu,Me}}]\text{Ni}(\text{OH})$ (1.842 Å). Further, the similar Ni–O distances point to symmetric binding of the O_2 ligand. While most aspects of the molecular structure of $[\text{Tp}^{\text{tBu,Me}}]\text{Ni}(\text{O}_2)$ are well resolved, the O_2 unit suffers from both positional disorder and librational motion. These issues conspire to produce an apparent O–O bond length that, relative to other metal-dioxygen adducts⁷³, appears shorter than expected given the complex's vibrational data (Figure 4.4). The librational motion has also proved problematic in the aforementioned cobalt and copper dioxygen adducts and has been cited by Theopold and coworkers as the source of what appear to be uncharacteristically short O–O bonds in the original X-ray crystal structures of those species.⁷³ In $[\text{Tp}^{\text{tBu,Me}}]\text{Co}(\text{O}_2)$, X-ray data collection on a crystal at low temperature was sufficient to minimize librational motion and subsequently resulted in a more well resolved O_2 unit.⁷³ In $[\text{Tp}^{\text{tBu,Me}}]\text{Ni}(\text{O}_2)$, however, the dual problems of librational motion and positional disorder precluded such a solution and thereby frustrated efforts to accurately assess the O–O bond distance. In order to circumvent this issue, a close analog of $[\text{Tp}^{\text{tBu,Me}}]\text{Ni}(\text{O}_2)$ was prepared in the form of $[\text{Tp}^{\text{tBu,Ph}}]\text{Ni}(\text{O}_2)$. The expectation of this variant was that the phenyl groups might act to produce a more confined O_2 binding pocket, as the addition of a larger 5-position

substituent would increase the ligand "bite" at the metal. This would serve both to reduce librational motion as well to lower the molecule's symmetry, in an attempt to eliminate the positional disorder. This effort proved successful as can be seen in the metric parameters of $[\text{Tp}^{\text{tBu,Ph}}]\text{Ni}(\text{O}_2)$ contained in Tables 4.1 and 4.2 (*vide supra*).

As is the case with $[\text{Tp}^{\text{tBu,Me}}]\text{Ni}(\text{O}_2)$, the molecular structure of $[\text{Tp}^{\text{tBu,Ph}}]\text{Ni}(\text{O}_2)$ displays $\eta^2\text{-O}_2$ ligation. The average Ni–N and Ni–O bond lengths, 2.000(2) Å and 1.860(1) Å respectively, are nearly identical to those found in $[\text{Tp}^{\text{tBu,Me}}]\text{Ni}(\text{O}_2)$ (2.012(2) Å and 1.864(4) Å). The τ_5 value of 0.3 indicates that the geometry is best described as square pyramidal, with N1 occupying the apical position. The O_2 unit of $[\text{Tp}^{\text{tBu,Ph}}]\text{Ni}(\text{O}_2)$ is well resolved, displaying an O–O bond length of 1.359(2) Å. This value is similar to a nickel-superoxo complex from the Driess group,⁴⁶ the latter with a O–O bond length of 1.347(2) Å. It is slightly shorter than two TMC supported nickel-dioxygen adducts reported by Nam and coworkers, $[\text{Ni}^{\text{III}}(12\text{-TMC})(\text{O}_2)]^+$ (1.386 Å) and $[\text{Ni}^{\text{II}}(13\text{-TMC})(\text{O}_2)]^+$ (1.383 Å).^{26,27}

Given that the O_2 moiety in $[\text{Tp}^{\text{tBu,Me}}]\text{Ni}(\text{O}_2)$ is poorly resolved, it is important to note that $[\text{Tp}^{\text{tBu,Me}}]\text{Ni}(\text{O}_2)$ and $[\text{Tp}^{\text{tBu,Ph}}]\text{Ni}(\text{O}_2)$ have identical ν_{OO} frequencies (*vide infra*). While this does not necessarily guarantee similar O–O bond lengths, the relatively minor structural and electronic differences between the two compounds, combined with their similar Ni–O and Ni–N metric parameters, make a large disparity in O–O bond lengths unlikely. When taken together, the O–O bond length and the associated ν_{OO} values are consistent with a Ni(II)-superoxo formulation. It is important to note, however, that the aforementioned dioxygen adducts prepared by the Nam group display similar metric parameters, yet have been described as Ni(III)-peroxo on the basis of reactivity and DFT.^{26,27}

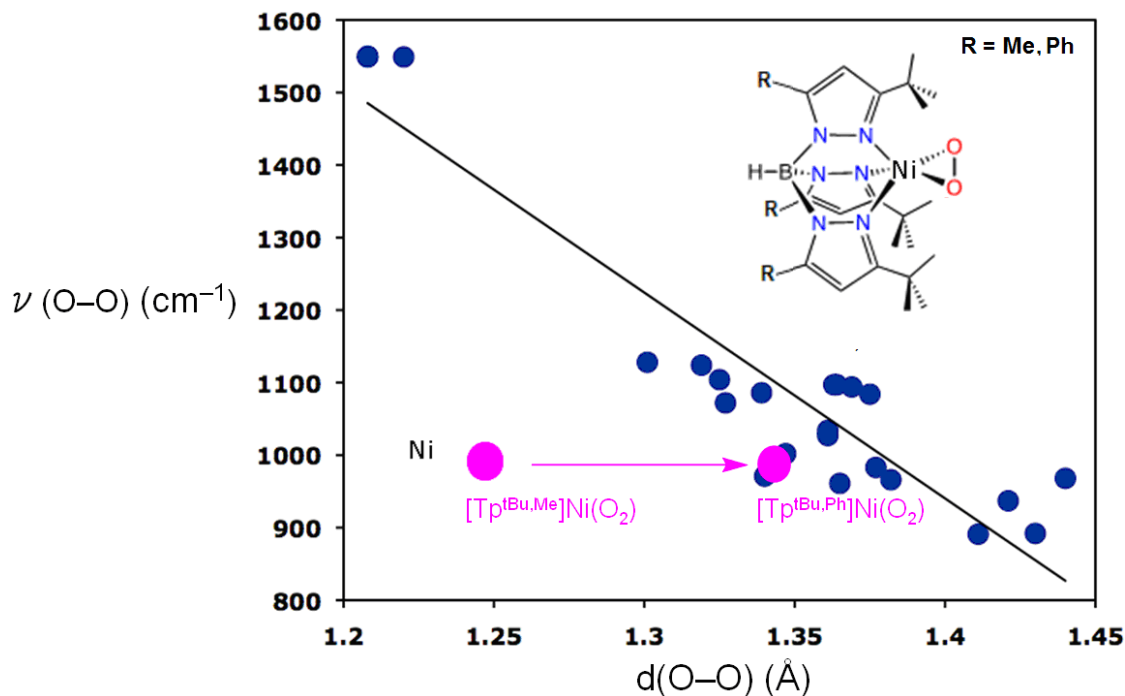


Figure 4.4 Plot of oxygen-oxygen bond length versus stretching frequency for a number of reported metal-dioxygen adducts (Adapted from Rheingold et al., *Proc. Nat. Acad. Sci.* **2003**, *100*, 3635).⁷³ Positions for $[\text{Tp}^{\text{tBu,Me}}]\text{Ni}(\text{O}_2)$ and $[\text{Tp}^{\text{tBu,Ph}}]\text{Ni}(\text{O}_2)$ have been superimposed in pink.

4.4 ^1H NMR, FT-IR, Electronic Absorption and L-Edge XAS Analysis of $[\text{Tp}^{\text{tBu,R}}]\text{Ni}(\text{O}_2)$, R = Me, Ph

4.4.1 ^1H NMR Spectral Analysis.

Both $[\text{Tp}^{\text{tBu,Me}}]\text{Ni}(\text{O}_2)$ and $[\text{Tp}^{\text{tBu,Ph}}]\text{Ni}(\text{O}_2)$ display well resolved, paramagnetic ^1H NMR spectra. Comparison of the two spectra reveal considerable similarity in their shared features, but also a distinctiveness that sets them apart from both their monovalent precursors as well as typical $\text{Tp}^{\text{tBu,Me}}$ supported Ni(II) complexes. The pyrazole proton is located just upfield of 40 ppm in both complexes. This position falls between the usual range for Ni(I) and Ni(II) species, with the former occurring upfield of 40 ppm, between 15-20 ppm, and the latter downfield of

20 ppm, in the 65-85 ppm region. The normally sharp pyrazole resonance is also highly broadened. The *t*-butyl groups are located in the 0-2 ppm region for both [Tp^{tBu,Me}]Ni(O₂) and [Tp^{tBu,Ph}]Ni(O₂), a position not terribly uncommon for a Ni(II) species. The B–H resides just upfield of zero, at -2 ppm. This value is further downfield than is seen in most Ni(II) Tp complexes yet far upfield of what would be expected for a Ni(I) species.

The rather unique ¹H NMR spectra of [Tp^{tBu,Me}]Ni(O₂) and [Tp^{tBu,Ph}]Ni(O₂) are undoubtedly a consequence of their distinct magnetic properties. The magnetic moment of [Tp^{tBu,Me}]Ni(O₂) was determined by the Evans' method to be 2.3(1) μ_B. This indicates a low-spin, *S* = 1/2 spin state, which results from the antiferromagnetic coupling of the high-spin Ni(II) core (*S* = 1) with the O₂^{•-} ligand (*S* = 1/2). Strong covalency between the metal and the superoxide ligand is also observed in the analogous Co and Cu systems reported by reports by Theopold⁵² and Kitajima.⁵³

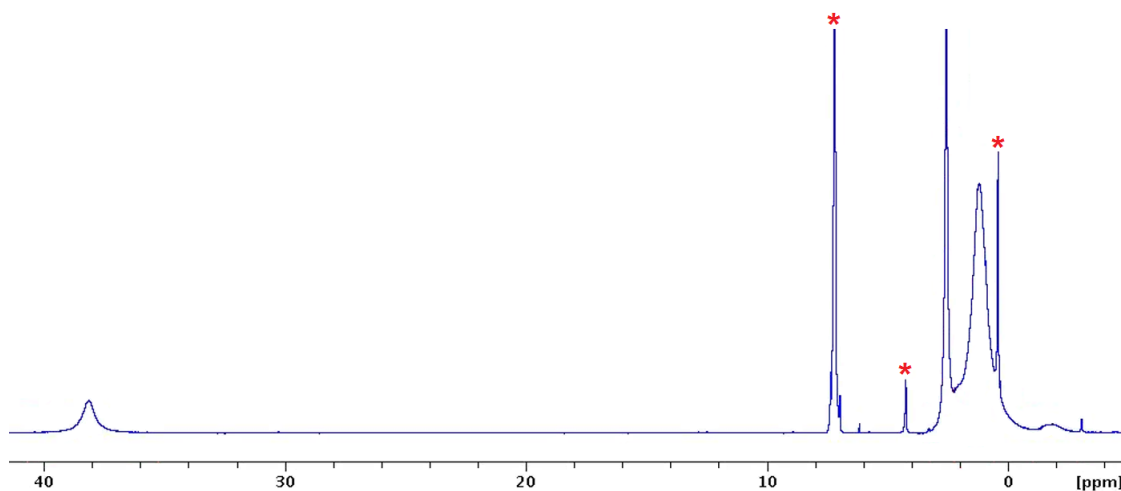


Figure 4.5 ¹H NMR spectrum of [Tp^{tBu,Me}]Ni(O₂). * Indicates residual solvent features.

4.4.2 Electronic Absorption Analysis.

The UV-visible spectrum of $[\text{Tp}^{\text{tBu,Me}}]\text{Ni}(\text{O}_2)$, Figure 4.6, exhibits two characteristic absorption bands at 325 and 870 nm with absorption coefficients of 900 and $150 \text{ M}^{-1}\text{cm}^{-1}$ respectively. The feature at 325 nm has been assigned as a superoxide to Ni charge transfer transition (LMCT). The less intense feature at 870 nm has been assigned as a ligand field transition. There are also strong shoulder features at ca. 370 and 485 nm. $[\text{Tp}^{\text{tBu,Ph}}]\text{Ni}(\text{O}_2)$ exhibits a very similar spectrum with characteristic absorption bands at 325 and 873 nm ($\epsilon = 1000$ and $150 \text{ M}^{-1}\text{cm}^{-1}$, respectively) and shoulders at ca. 370 and 480 nm. The spectral features of both complexes resemble those reported for the copper analogue, $[\text{Tp}^{\text{tBu,Me}}]\text{Cu}(\text{O}_2)$, as well as the structurally similar, PhTt supported nickel complex, $[\text{PhTt}^{\text{Ad}}]\text{Ni}(\text{O}_2)$.

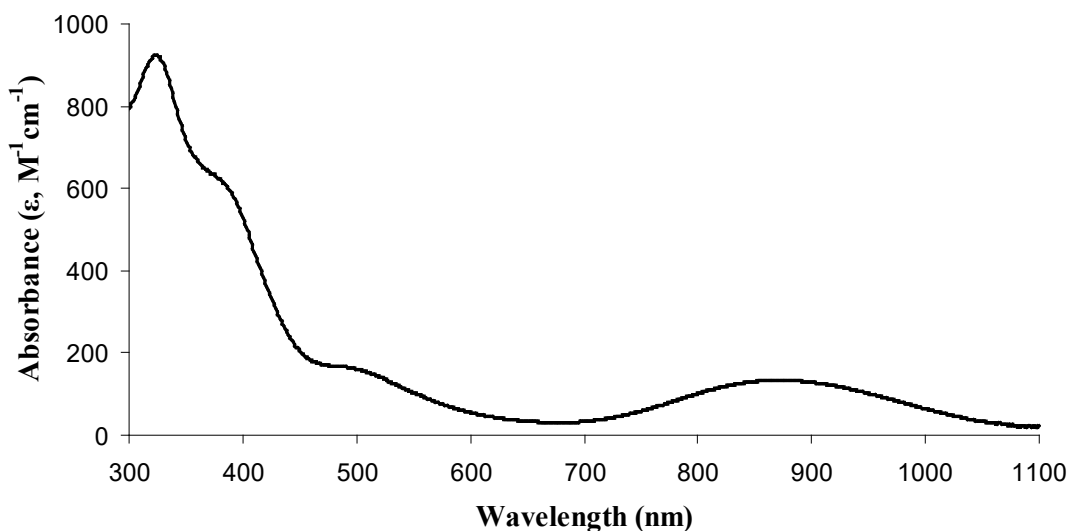


Figure 4.6 Electronic absorption spectrum of $[\text{Tp}^{\text{tBu,Me}}]\text{Ni}(\text{O}_2)$ recorded in CHCl_3 .

4.4.3 FT-IR Analysis.

Acquisition of the solid state, FT-IR spectrum of $[\text{Tp}^{\text{tBu,Me}}]\text{Ni}(\text{O}_2)$ revealed a strong, sharp feature at 1000 cm^{-1} , which was tentatively assigned as the dioxygen stretching frequency, $\nu(^{16}\text{O}^{16}\text{O})$. A virtually identical feature was found at the same position in the $\text{Tp}^{\text{tBu,Ph}}$ supported analog. The assignment as a dioxygen stretch was confirmed by examination of the spectrum of the ^{18}O -labeled complex, $[\text{Tp}^{\text{tBu,Me}}]\text{Ni}(^{18}\text{O}_2)$, in which the $\nu(\text{OO})$ value shifts to 945 cm^{-1} . This energy is in good agreement with the calculated value of 942 cm^{-1} , for a simple diatomic harmonic oscillator. Comparison of the labeled and unlabeled complexes also revealed a second isotope sensitive feature, occurring at 448 and 431 cm^{-1} in $[\text{Tp}^{\text{tBu,Me}}]\text{Ni}(^{32}\text{O}_2)$ and $[\text{Tp}^{\text{tBu,Me}}]\text{Ni}(^{18}\text{O}_2)$, respectively. This feature has been assigned as the Ni–O stretch, $\nu(\text{Ni}-\text{O})$. The calculated $\nu(\text{Ni}-^{18}\text{O})$ value of 428 cm^{-1} further supports this assignment. In comparison to $[\text{Tp}^{\text{tBu,Me}}]\text{Ni}(\text{O}_2)$, the nickel-superoxo complex reported by Driess⁴⁶ has a slightly lower dioxygen stretching frequency of 971 cm^{-1} , while a previous "end-on" adduct³¹ from our lab has a $\nu(^{16}\text{O}^{16}\text{O})$ value of 1131 cm^{-1} . The higher stretching frequency value in the latter complex is consistent with the differences in the dioxygen binding mode. Nam's TMC supported nickel-dioxygen adducts are the most similar to $[\text{Tp}^{\text{tBu,Me}}]\text{Ni}(\text{O}_2)$ in terms of OO stretching frequency with the complexes $[\text{Ni}^{\text{III}}(12\text{-TMC})(\text{O}_2)]^+$ and $[\text{Ni}^{\text{II}}(13\text{-TMC})(\text{O}_2)]^+$ possessing $\nu(^{16}\text{O}^{16}\text{O})$ values of 1002 and 1008 cm^{-1} , respectively.

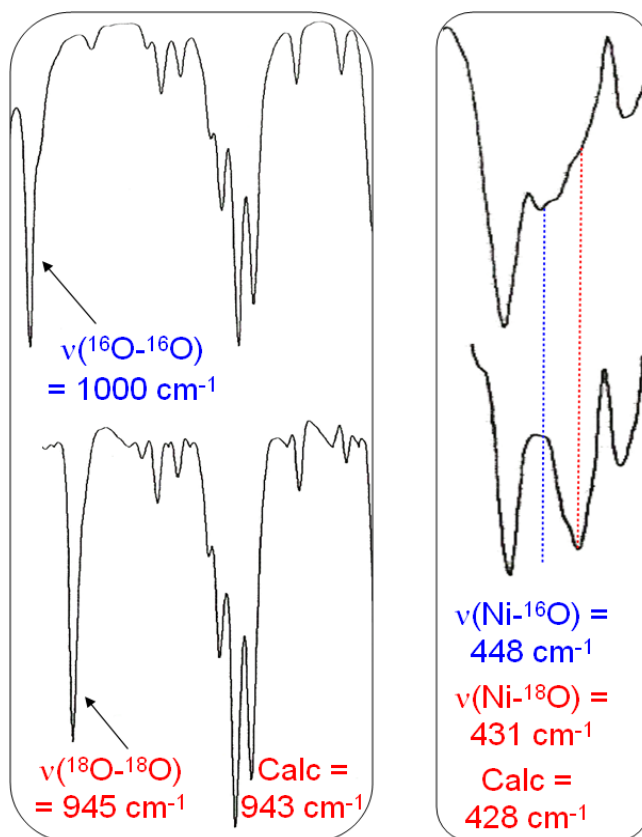


Figure 4.7 FT-IR comparison of $\nu_{\text{O-O}}$ and $\nu_{\text{Ni-O}}$ for ^{16}O and ^{18}O isotopomers of $[\text{Tp}^{\text{tBu,Me}}]\text{Ni}(\text{O}_2)$.

4.4.4 L-Edge X-ray Absorption Spectroscopy Analysis.

As with K-edge XAS, L-edge XAS spectroscopy involves excitation of a metal core electron to the d-manifold. However, unlike K-edge, where the core electron transition ($1s \rightarrow 3d$) is electric-dipole forbidden,⁷⁴ the core electron excitation in L-edge is derived from a metal 2p orbital and so the transition ($2p \rightarrow 3d$) is electric-dipole allowed. The consequences of this are two-fold. First, the electric-dipole allowed transition results in the L-edge being considerably more intense, i.e. much better signal-to-noise than the K-edge. Second, the lower required energy results in a

higher resolution spectrum with more defined features.⁷⁵ These qualities make L-edge XAS a valuable technique for probing the transition metal electronic structure in both biological and synthetic complexes.

A sample of $[\text{Tp}^{\text{tBu,Me}}]\text{Ni}(\text{O}_2)$ underwent L-edge XAS analysis at Lawrence Berkeley National Laboratory. The L-edge spectra of $[\text{Tp}^{\text{tBu,Me}}]\text{Ni}(\text{O}_2)$ and a Ni(II) reference compound, $\text{Ni}[\text{Me}_4[12]\text{aneN}_4](\text{OTf})_2$, are displayed in Figure 4.8. Both the L_3 and L_2 regions are consistent with a Ni^{II} oxidation state as indicated by the excellent overlap with the reference compound. In the L_3 region, the multiplet structure indicated by the shoulder on the high energy side of the L_3 feature, is indicative of a high spin configuration. In terms of the L_2 region, a low-spin Ni^{II} complex would be expected to present as a sharp feature, whereas the observed spectrum displays a broad, slightly split L_2 edge. This is also consistent with a high spin Ni^{II} configuration.

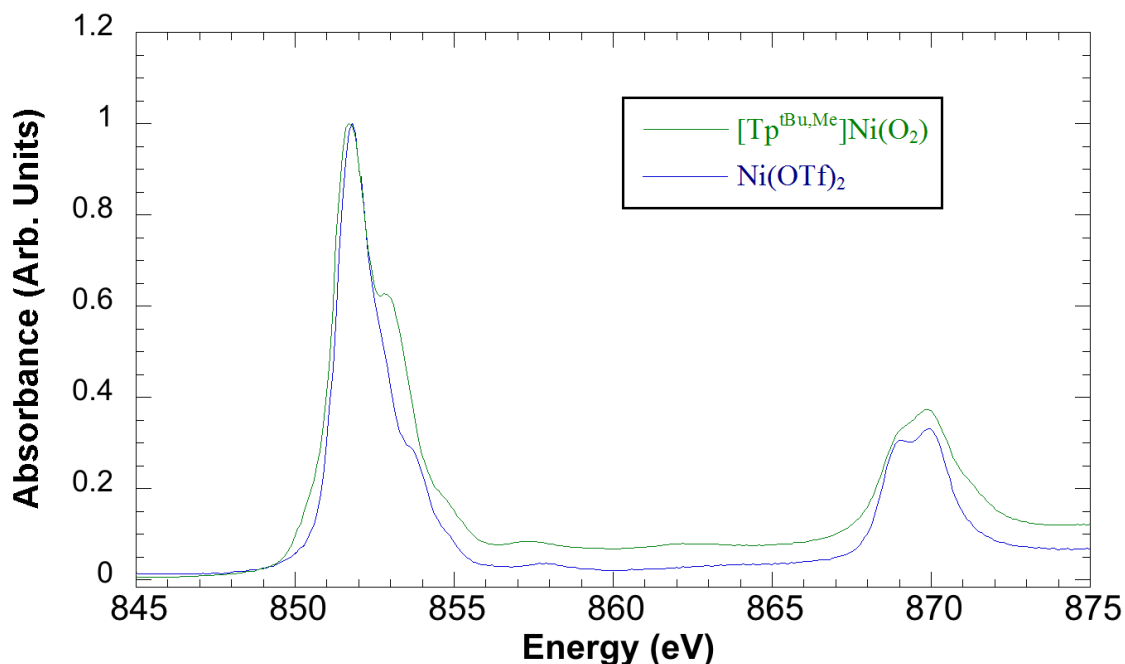


Figure 4.8 L-Edge XAS spectrum of $[\text{Tp}^{\text{tBu,Me}}]\text{Ni}(\text{O}_2)$. The spectrum of the Ni(II) reference material, $\text{Ni}[\text{Me}_4[12]\text{aneN}_4](\text{OTf})_2$, is overlaid for comparison.

4.5 Thermal Stability of $[\text{Tp}^{\text{tBu,Me}}]\text{Ni}(\text{O}_2)$

The study of nickel-dioxygen adducts is complicated by their somewhat notorious instability. Previous examples from our lab provide ample evidence. An "end-on" nickel-dioxygen adduct supported by the TMC ([1,4,8,11-tetramethyl-1,4,8,11-tetraazacyclotetradecane]) ligand system persists for a matter of hours at ambient temperature, while the PhTt-supported complex, $[\text{PhTt}^{\text{Ad}}]\text{Ni}(\text{O}_2)$ has a room temperature half-life of just 5 minutes. As a consequence, most spectroscopic analysis of these complexes must be performed at low temperature. A smaller relative of the latter species, $[\text{PhTt}^{\text{tBu}}]\text{Ni}(\text{O}_2)$, could not be stabilized even at low temperature and instead proceeds rapidly to the bis- μ -oxo dimer, $[(\text{PhTt}^{\text{tBu}})_2\text{Ni}_2(\mu\text{-O})_2]$. What has become clear from these, as well as other, studies is that in the case of nickel-dioxygen

adducts, bimolecular reactions are detrimental to stability. DFT calculations performed using the PhTi^{Me} system (Me substituted for larger substituents for simplified calculation) have helped to rationalize dimerization to the bis- μ -oxo dinickel(III) core. If the ligand steric environment allows for the formation of dimers, a bridging peroxo complex is the likely result. In the case of the DFT modeled, hypothetical complex, $[(\text{PhTi}^{\text{Me}})_2\text{Ni}_2(\mu\text{-}\eta^2\text{:}\eta^2\text{-O}_2)]$, rupture of the O–O bond affording $[(\text{PhTi}^{\text{Me}})_2\text{Ni}_2(\mu\text{-O})_2]$ is energetically favored by 32 kcal/mol. Thus, if dimerization is allowed by the steric environment at the nickel-dioxygen core, decomposition of the adduct is likely to follow.

By sterically "locking out" dimerization through the use of an appropriate ligand, the stability of the supported nickel-dioxygen adduct can be dramatically increased. This was demonstrated by Driess and coworkers with their beta-diketiminato supported nickel-superoxo adduct, where the ligand employs sterically imposing 2,6-diisopropylphenyl substituents.⁴⁶ This complex is stable to 60 °C in hexanes, indicating the effectiveness of steric protection of the Ni-dioxygen core.

Analogous to the results from the Driess group, the employment of the sterically demanding, tetrahedral enforcing $\text{Tp}^{\text{tBu,Me}}$ allowed for the preparation of a nickel-dioxygen adduct with considerable thermal stability. $[\text{Tp}^{\text{tBu,Me}}]\text{Ni}(\text{O}_2)$ is stable indefinitely at room temperature/humidity and exhibits substantial resistance to decomposition at elevated temperatures. ¹H NMR thermolysis experiments resulted in negligible degradation of the complex in d^8 -toluene at temperatures of up to 80° C, Figure 4.9. While heating toluene solutions of the complex at 60 °C for an extended duration led to minor decomposition (10-15% over 24 hours), the resistance of $[\text{Tp}^{\text{tBu,Me}}]\text{Ni}(\text{O}_2)$ to thermal degradation is nonetheless superior to nearly all other

reported Ni-dioxygen adducts, with only Driess's beta-diketiminato supported species sharing comparable stability.⁴⁶

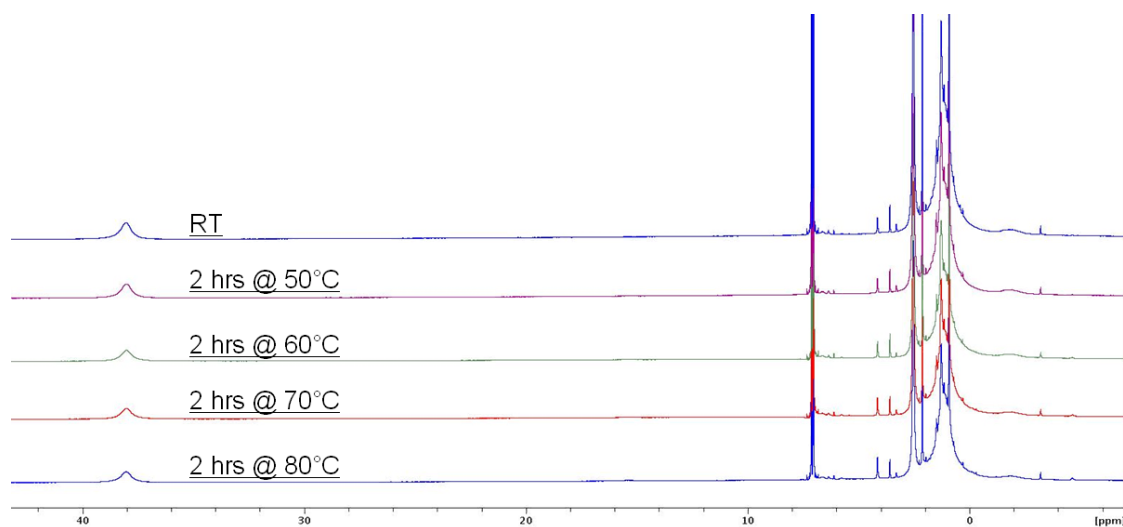


Figure 4.9 ¹H NMR study of [Tp^{tBu,Me}]Ni(O₂) thermal stability over short time courses.

4.6 Synthesis and Structure of [Tp^{Ph,Me}]Ni(O₂)

[Tp^{Ph,Me}]Ni(O₂) was prepared in a similar fashion to [Tp^{tBu,Me}]Ni(O₂) by treating a pentane suspension of finely powdered [Tp^{Ph,Me}]Ni(CO) with an excess of dry O₂, Figure 4.10. Both starting material and product are poorly soluble in pentane, making the reaction nearly heterogeneous in nature. The low solubility of [Tp^{Ph,Me}]Ni(CO) and [Tp^{Ph,Me}]Ni(O₂) also serves to minimize decomposition via interaction of the two; so much so that low temperature addition of O₂ provides little tangible benefit in terms of product yield or purity. Upon purging the reaction vessel with O₂ for 5 minutes and stirring for 20 min, the color of the suspended material changed from pale yellow to brown. The product was recovered by filtration and dried

under vacuum giving $[\text{Tp}^{\text{Ph,Me}}]\text{Ni}(\text{O}_2)$ as a brown powder in excellent yield (91%). $[\text{Tp}^{\text{Ph,Me}}]\text{Ni}(\text{O}_2)$ is air, moisture and vacuum stable in the solid state. However, the complex is unstable in solution under ambient conditions, undergoing decomposition to a mixture of products over the course of several days. The nature of the decomposition, including mechanism and products was probed by Ann Ploskonka as part of her master's thesis.⁷²

At present, known $[\text{Tp}^{\text{Ph,Me}}]\text{Ni}(\text{O}_2)$ decomposition products include the bis-ligand complex, $[\text{Tp}^{\text{Ph,Me}}]_2\text{Ni}$, and a Ni(II) metallacycle resulting from C–H activation at the *ortho* position of the 3-phenyl substituent with Ni bound to an oxygen atom, which is in turn bound to the ligand.⁷² The latter species constitutes the bulk decomposition product. The substantially diminished stability of $[\text{Tp}^{\text{Ph,Me}}]\text{Ni}(\text{O}_2)$ relative to $[\text{Tp}^{\text{tBu,Me}}]\text{Ni}(\text{O}_2)$ is likely a consequence of the reduced steric protection of the Ni(O₂) core in the former. $\text{Tp}^{\text{tBu,Me}}$, by virtue of its bulky 3-*tert*-butyl substituents, is highly effective at precluding dimer formation in the majority of its complexes. By contrast, the 3-phenyl substituents of $\text{Tp}^{\text{Ph,Me}}$ offer much more modest steric protection and thus are not sufficient to completely deter potentially deleterious dimerizations. Previous work from the Theopold lab, utilizing Tp-supported cobalt complexes, illustrates the pronounced effect that the steric environment can have on the stability of metal-dioxygen adducts. As mentioned previously, the treatment of $[\text{Tp}^{\text{tBu,Me}}]\text{Co}(\text{N}_2)$ with dioxygen resulted in the isolation of a stable superoxo-cobalt complex. Later, Theopold and coworkers prepared a similar, but less sterically hindered dioxygen adduct, $[\text{Tp}^{\text{iPr,Me}}]\text{Co}(\text{O}_2)$.⁷⁶ While this species was stable in the solid state, it was unstable in solution. Further study indicated that dimerization of the complex led to expulsion of one O₂ and further activation of the other, with the

resulting dimer then undergoing C-H activation at the ligand.⁷⁶ Given the similar steric environments of [Tp^{Ph,Me}] and [Tp^{iPr,Me}], as well as the isolation of products consistent with ligand C-H activation in both systems, the possibility of a similar decomposition route cannot be ignored.

In addition to the examples from the analogous cobalt chemistry, dependence of nickel-dioxygen complex stability on steric constraints also has precedent in the PhTt ligand system. Previous studies from the Riordan lab showed that the highly unstable dioxygen adduct, [PhTt^{tBu}]Ni(O₂), undergoes rapid conversion to the bis-μ-oxo dimer, [(PhTt^{tBu})Ni]₂(μ-O)₂.⁷⁷ Replacement of the *tert*-butyl substituent with 1-adamantyl made possible the preparation of the related species, [PhTt^{Ad}]Ni(O₂), the enhanced stability of which allowed for complete spectroscopic characterization. The observed increased stability in the more sterically encumbered complex was attributed to a greater resistance against dimerization and is, in ways, a parallel to the stability differences observed between [Tp^{Ph,Me}]Ni(O₂) and [Tp^{tBu,Me}]Ni(O₂).

X-ray quality crystals of [Tp^{Ph,Me}]Ni(O₂) were grown by layering pentane onto a concentrated benzene solution of the metal complex. The molecular structure of [Tp^{Ph,Me}]Ni(O₂) is found in Figure 4.11. Selected bond distances and bond angles value are located in Table 4.3.

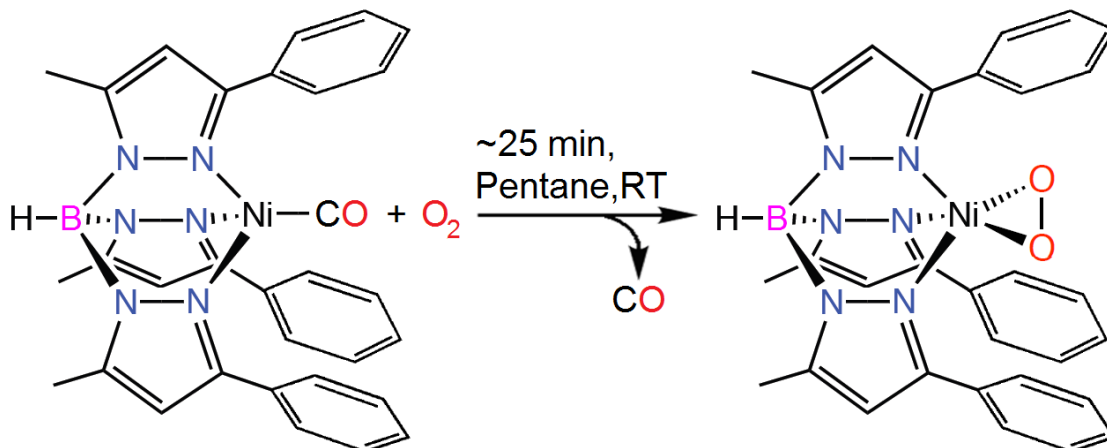


Figure 4.10 Synthesis of $[\text{Tp}^{\text{Ph,Me}}]\text{Ni}(\text{O}_2)$.

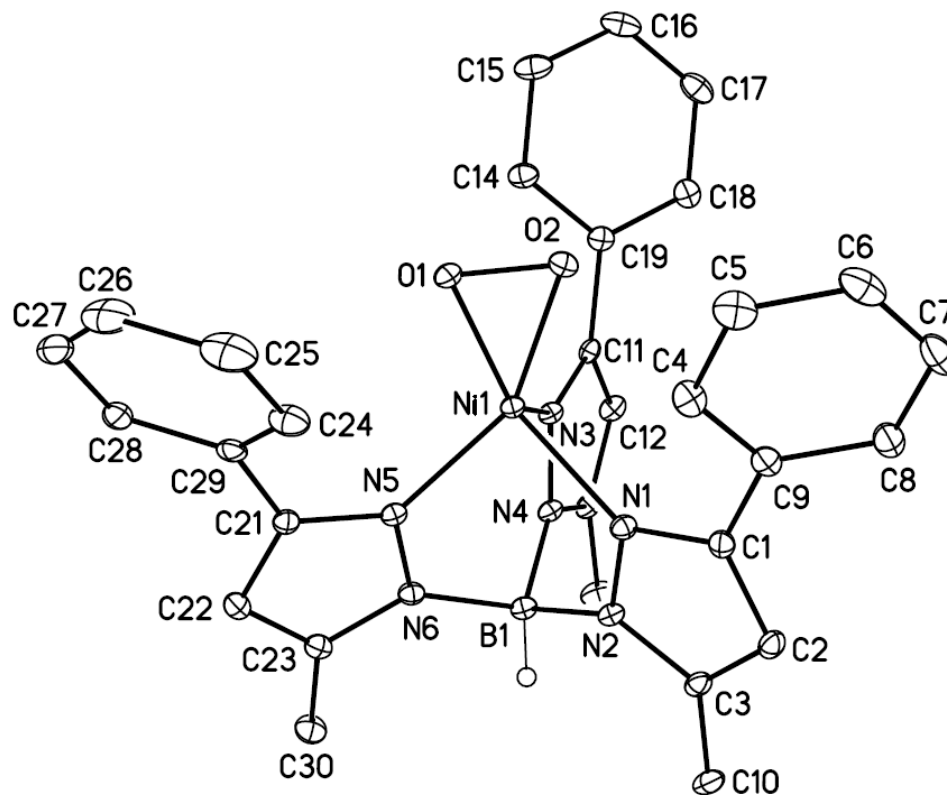


Figure 4.11 Thermal ellipsoid diagram of $[\text{Tp}^{\text{Ph,Me}}]\text{Ni}(\text{O}_2)$ with atom labeling. Thermal ellipsoids are drawn to 30% probability. Hydrogen atoms are omitted for clarity with the exception of B–H. Only one orientation of the positionally disordered O_2 moiety is depicted.

Table 4.3 Selected bond distances (Å) and bond angles (°) for [Tp^{Ph,Me}]Ni(O₂).

Bond Length (Å)		Bond Angle (°)	
Ni–N1	1.9849(12)	N1–Ni–O1	148.76(19)
Ni–N3	2.0589(12)	N1–Ni–O2	113.24(5)
Ni–N5	1.9440(12)	N3–Ni–O1	114.9(2)
Ni–O1	1.8247(13)	N3–Ni–O2	103.54(5)
Ni–O2	1.8784(10)	N5–Ni–O1	106.15(5)
O–O	1.3793(18)	N5–Ni–O2	149.14(5)

4.7 Molecular Structure of [Tp^{Ph,Me}]Ni(O₂)

As is the case in [Tp^{tBu,Me}]Ni(O₂), the molecular structure of [Tp^{tBu,Me}]Ni(O₂) displays a five coordinate nickel center bound by the 3 nitrogen donors of the Tp ligand and by the O₂ moiety which is coordinated in a side-on, η^2 -O₂ fashion to the metal. The O₂ moiety in [Tp^{Ph,Me}]Ni(O₂) is positionally disordered, precluding an accurate assessment of the O–O bond length. While the positional disorder also prevents calculation of a formal τ_5 value, a visual inspection of the modeled molecular structure and comparison to the structurally similar compounds, [Tp^{tBu,Me}]Ni(O₂) and [Tp^{tBu,Ph}]Ni(O₂), suggests that the coordination environment most closely resembles a distorted square pyramidal geometry. The average Ni–N and Ni–O bond lengths are 1.996(4) and 1.835(2) Å, respectively.

4.8 Proton NMR, FT-IR and Electronic Absorption Analysis of [Tp^{Ph,Me}]Ni(O₂)

4.8.1 ¹H NMR Analysis

[Tp^{Ph,Me}]Ni(O₂) displays a well resolved, paramagnetic ¹H NMR spectrum, Figure 4.12. As is the case with [Tp^{tBu,Me}]Ni(O₂), the pyrazole proton, located at 34.9 ppm, is shifted downfield relative to its position in the monovalent precursor, but well upfield of where it typically resides in Ni(II) species. The pyrazole resonance is highly broadened, a feature that is also consistent with the spectrum of [Tp^{tBu,Me}]Ni(O₂). The B–H can be found just upfield of zero at -1.8 ppm. This value is further downfield than in most Ni(II) Tp^{Ph,Me} complexes and far upfield of the monovalent species. The *meta* and *para* protons on the phenyl ring are both located in the aromatic region and are fairly sharp. The *ortho* proton, centered at 7.4 ppm, is highly broadened as a consequence of a dipolar coupling interaction with the paramagnetic center and overlaps with the chemical shifts of the neighboring *meta* and *para* protons. The much lower stability of [Tp^{Ph,Me}]Ni(O₂) relative to [Tp^{tBu,Me}]Ni(O₂) is apparent in the proton spectrum in the form of trace decomposition products. These appear even in freshly prepared samples of the complex and further illustrate the importance of steric protection in stabilizing the nickel-superoxo core structure.

4.8.2 Electronic Absorption Analysis

The UV-visible spectrum of [Tp^{Ph,Me}]Ni(O₂) is shown in Figure 4.13. The complex exhibits two characteristic absorption bands. The first is a shoulder at 311 nm with an absorption coefficient of 1550 M⁻¹cm⁻¹, which has been assigned as a superoxide to nickel charge transfer transition. This feature, which presumably extends into the UV beyond the detection limits of the spectrometer, is reminiscent of a similar absorption band in [Tp^{tBu,Me}]Ni(O₂) at 325 nm, albeit with a higher extinction

coefficient. The second feature at 874 nm ($150 \text{ M}^{-1}\text{cm}^{-1}$) was assigned as a ligand field transition. This latter absorption band is also similar to one at 870 nm for $[\text{Tp}^{\text{tBu,Me}}]\text{Ni}(\text{O}_2)$ with both features sharing identical extinction coefficients. As with $[\text{Tp}^{\text{tBu,Me}}]\text{Ni}(\text{O}_2)$, the electronic absorption features of $[\text{Tp}^{\text{Ph,Me}}]\text{Ni}(\text{O}_2)$ resemble those for the similar, but more sterically imposing copper complex, $[\text{Tp}^{\text{tBu,Me}}]\text{Cu}(\text{O}_2)$,²⁸ as well as the PhTt-supported nickel complex, $[\text{PhTt}^{\text{Ad}}]\text{Ni}(\text{O}_2)$.

4.8.3 FT-IR Analysis

Acquisition of the solid state, FT-IR spectrum of $[\text{Tp}^{\text{Ph,Me}}]\text{Ni}(\text{O}_2)$ revealed a strong, sharp feature at 991 cm^{-1} . This feature has been tentatively assigned as the dioxygen stretching frequency, $\nu(^{16}\text{O}^{16}\text{O})$, although verification by ^{18}O labeling was not performed. Compared with $[\text{Tp}^{\text{tBu,Me}}]\text{Ni}(\text{O}_2)$, the dioxygen stretching frequency in $[\text{Tp}^{\text{Ph,Me}}]\text{Ni}(\text{O}_2)$ is somewhat counter intuitive, as one might expect the electron withdrawing nature of the phenyl rings to result in less activated O_2 moiety and a correspondingly higher stretching frequency. It is possible that this discrepancy is a result of the diminished steric effects present in $\text{Tp}^{\text{Ph,Me}}$, with the more open binding pocket allowing for a closer approach of the O_2^- ligand and consequently better orbital overlap.

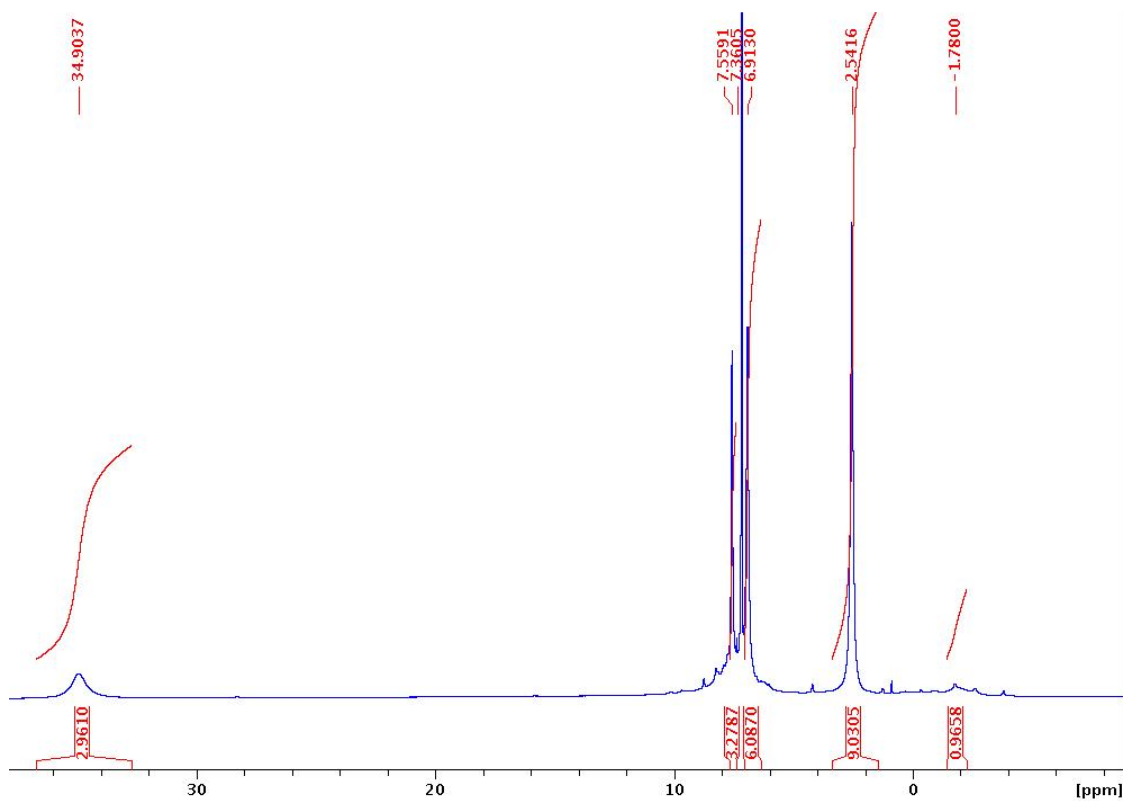


Figure 4.12 ^1H NMR spectrum of $[\text{Tp}^{\text{Ph,Me}}]\text{Ni}(\text{O}_2)$.

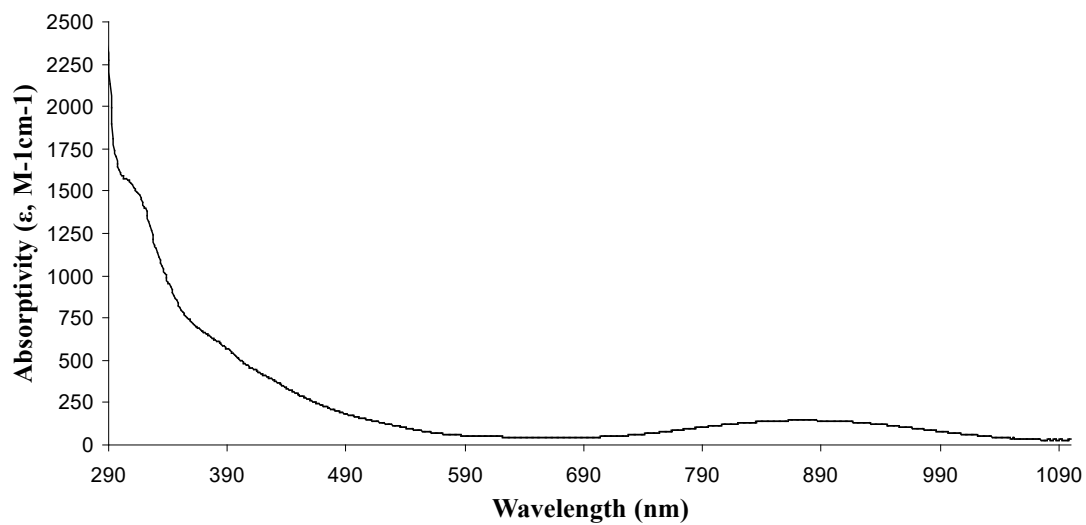


Figure 4.13 UV-visible spectrum of $[\text{Tp}^{\text{Ph,Me}}]\text{Ni}(\text{O}_2)$ recorded in CHCl_3 .

4.9 Summary

The synthesis of a series of monovalent nickel complexes, supported by the $\text{Tp}^{\text{tBu,Me}}$ and $\text{Tp}^{\text{Ph,Me}}$ ligands, provided access to such adducts by enabling direct activation of molecular O_2 . Low temperature treatment of the monovalent species, $[\text{Tp}^{\text{tBu,Me}}]\text{Ni}(\text{L})$ ($\text{L} = t\text{BuNC}$, CyNC , CO), with dry dioxygen generated a nickel-dioxygen adduct, $[\text{Tp}^{\text{tBu,Me}}]\text{Ni}(\text{O}_2)$. $[\text{Tp}^{\text{tBu,Me}}]\text{Ni}(\text{O}_2)$ is stable indefinitely under ambient conditions and exhibits remarkable resistance to decomposition at elevated temperatures. X-ray crystallographic analysis showed the dioxygen moiety to be bound to the nickel center in a side-on fashion. Preparation of the closely related compound, $[\text{Tp}^{\text{tBu,Ph}}]\text{Ni}(\text{O}_2)$, allowed for illumination of the O–O bond distance (1.359 Å) which was obscured in $[\text{Tp}^{\text{tBu,Me}}]\text{Ni}(\text{O}_2)$ by a combination librational motion and positional disorder in the O_2 moiety.

The structure and spectroscopic properties of $[\text{Tp}^{\text{tBu,Me}}]\text{Ni}(\text{O}_2)$ and $[\text{Tp}^{\text{tBu,Ph}}]\text{Ni}(\text{O}_2)$ were investigated by ^1H NMR, FT-IR and UV-Vis analysis. $[\text{Tp}^{\text{tBu,Me}}]\text{Ni}(\text{O}_2)$ displays a well resolved ^1H NMR spectrum, which is distinct from both its monovalent precursor as well as common Ni(II) Tp complexes. The vibrational data and metric parameters for $[\text{Tp}^{\text{tBu,Me}}]\text{Ni}(\text{O}_2)$ are consistent with an assignment as Ni(II)-superoxo. $[\text{Tp}^{\text{tBu,Me}}]\text{Ni}(\text{O}_2)$ was found to have an $S = 1/2$ spin state which results from the coupling of a high-spin nickel(II) core to $S = 1/2$ superoxide ligand.

A third nickel- O_2 adduct, $[\text{Tp}^{\text{Ph,Me}}]\text{Ni}(\text{O}_2)$, was prepared from $[\text{Tp}^{\text{Ph,Me}}]\text{Ni}(\text{CO})$ and dry dioxygen using a strategy similar to that developed for the $\text{Tp}^{\text{tBu,Me}}$ system. $[\text{Tp}^{\text{Ph,Me}}]\text{Ni}(\text{O}_2)$ is stable indefinitely in the solid state under ambient conditions, but

undergoes gradual decomposition in solution. X-ray crystallographic analysis revealed the core structure to be highly congruous with that of $[\text{Tp}^{\text{tBu,Me}}]\text{Ni}(\text{O}_2)$ with $[\text{Tp}^{\text{Ph,Me}}]\text{Ni}(\text{O}_2)$ possessing an O_2 moiety bound to the nickel center in an η^2 fashion. Analysis of $[\text{Tp}^{\text{Ph,Me}}]\text{Ni}(\text{O}_2)$ by ^1H NMR spectroscopy also showed considerable similarity to $[\text{Tp}^{\text{tBu,Me}}]\text{Ni}(\text{O}_2)$. The FT-IR spectrum of $[\text{Tp}^{\text{Ph,Me}}]\text{Ni}(\text{O}_2)$ revealed a dioxygen stretching frequency that is lower in energy than that of the O_2 moiety in $[\text{Tp}^{\text{tBu,Me}}]\text{Ni}(\text{O}_2)$, a result which is counter-intuitive given the more electron withdrawing nature of the $\text{Tp}^{\text{Ph,Me}}$ system.

Chapter 5

OXYGEN ATOM TRANSFER, C-H ACTIVATION AND ALDEHYDE DEFORMYLATION BY $[\text{Tp}^{\text{tBu,Me}}]\text{Ni}(\text{O}_2)$

5.1 Introduction

In biology and chemistry, an ultimate goal of dioxygen activation by transition metal species is often substrate oxidation. The nature of the transformations, in terms of the specific target molecule and mechanism, can take myriad forms, but the core transformations often concern the activation of C–H bonds and/or the transfer of oxygen atom(s).

Among the limited number of nickel-dioxygen adducts, the reported types of reactivity include O-atom transfer to phosphines and nitric oxide, activation of weak C–H bonds (e.g. 9,10-dihydroanthracene and 1,4-cyclohexadiene), phenol oxidation and, in at least one case, aldehyde deformylation. In this section, the reactivity of $[\text{Tp}^{\text{tBu,Me}}]\text{Ni}(\text{O}_2)$ towards a range of exogenous substrates is described. These studies illuminate a broad range of reactivity and serve to demonstrate while $[\text{Tp}^{\text{tBu,Me}}]\text{Ni}(\text{O}_2)$ is thermally robust, it reacts with a range of exogenous substrates.

5.2 Oxygen Atom Transfer by $[\text{Tp}^{\text{tBu,Me}}]\text{Ni}(\text{O}_2)$

5.2.1 Reaction of $[\text{Tp}^{\text{tBu,Me}}]\text{Ni}(\text{O}_2)$ with PR_3 (R = Me, Et, Cy)

Of the O-atom transfer reactions performed by dioxygen adducts, among the most common is the transfer of an oxygen atom to trialkyl and/or triaryl phosphines, generating the corresponding phosphine oxide.

It was thus surprising that $[\text{Tp}^{\text{tBu,Me}}]\text{Ni}(\text{O}_2)$ does not oxidize PPh_3 . The reaction does not proceed even at elevated temperatures. Nonetheless, $[\text{Tp}^{\text{tBu,Me}}]\text{Ni}(\text{O}_2)$ oxidizes alkyl phosphines including PMe_3 , PEt_3 and PCy_3 . The reaction generates the corresponding phosphine oxide as well as two previously unreported nickel compounds, $[\text{Tp}^{\text{tBu,Me}}]\text{Ni}(\text{OH})$ and a metallacycle, $[\text{Tp}^{\text{tBu,Me}}\text{O}]\text{Ni}$. (*vide infra*).

5.2.2 Stoichiometric Reactions with Phosphines

As detailed in Chapter 2, reactions of $[\text{Tp}^{\text{tBu,Me}}]\text{Ni}(\text{O}_2)$ with PR_3 (PMe_3 , PEt_3 and PCy_3) were initiated by combining toluene stock solutions containing the respective alkyl phosphine and pyridine with a stoichiometric quantity of the solid, powdered nickel-superoxo complex (Figure 5.1). The pyridine was added to prevent ligation of the phosphine oxide product to the nickel products as explained below. The resulting solutions were stirred for 24 hours at room temperature (55 °C for PCy_3) to ensure complete consumption of $[\text{Tp}^{\text{tBu,Me}}]\text{Ni}(\text{O}_2)$. As the reactions progressed, a color change from dark red-brown to a lighter red-orange was observed. Upon completion, aliquots were removed from the reaction solution and subjected to $^{31}\text{P}\{^1\text{H}\}$ and ^1H NMR spectral analyses to determine both the extent of $\text{O}=\text{PR}_3$ formation as well as the identity and relative amounts of nickel products. $\text{O}=\text{PR}_3$ quantification was accomplished by obtaining the $^{31}\text{P}\{^1\text{H}\}$ NMR spectra of both the stock and reaction solutions, the latter sampled directly from the crude reaction, and integrating the phosphine and phosphine oxide signals against the phosphoric acid internal standard, Figures 5.2, 5.3 and 5.4. Corrections were made, where applicable, for the presence of phosphine oxide impurities in the stock solutions. Yields of phosphine oxide were high to moderate with conversions of 90%, 75% and 62% for PMe_3 , PEt_3 and PCy_3 ,

respectively. The trend in yield follows the steric demands of the substrates with the larger phosphines resulting in lower conversion. Analysis of the nickel products was accomplished by removing the volatiles from aliquots of the reaction solution, dissolution of the resulting residue in C₆D₆ and acquisition of the paramagnetic ¹H NMR spectrum.

From a qualitative standpoint, the rate of reaction is inversely proportional to the steric bulk of the phosphine substrate with PMe₃ reacting faster than PEt₃ which, in turn, reacts much faster than PCy₃, the latter requiring heating in order for the reaction to proceed to completion within 24 hr. This trend is rationalized in terms of the ability of the phosphine to access the nickel-superoxo core. The *tert*-butyl groups of the Tp^{tBu,Me} ligand present more of an obstacle to the bulkier phosphines than they do to the smaller, less sterically encumbered substrates, and thus, the smaller phosphines can more easily approach the O₂ moiety. Additionally, the preference for more electron rich substrates, evidenced by the oxidation of PCy₃ but not PPh₃, despite the larger steric bulk of the former, illustrates the electrophilic character of [Tp^{tBu,Me}]Ni(O₂).

5.2.3 Nickel Products of Phosphine Oxidation

In all cases of stoichiometric phosphine oxidation, analysis by ¹H NMR spectroscopy indicates the presence of two paramagnetic species with features consistent with complexes of the [Tp^{tBu,Me}]NiX type. Of these two products, the major nickel derivative was determined to be the hydroxide complex, [Tp^{tBu,Me}]Ni(OH), which accounted for approximately 87%, 77% and 67% of the nickel containing products in reactions with PMe₃, PEt₃ and PCy₃, respectively. This species has been prepared independently by treatment of [Tp^{tBu,Me}]NiCl with NaOH and has been fully

characterized. The ^1H NMR spectrum of the residue obtained from phosphine oxidation by $[\text{Tp}^{\text{tBu,Me}}]\text{Ni}(\text{O}_2)$ contains features that match those of the independently prepared hydroxo complex, Figure 5.5. In addition, the residue displays an O-H stretching vibration in the FT-IR spectrum, which is identical to that of authentic $[\text{Tp}^{\text{tBu,Me}}]\text{Ni}(\text{OH})$. Finally, slow evaporation of pentane extracts from the reaction residue yielded crystals with a unit cell matching that of $[\text{Tp}^{\text{tBu,Me}}]\text{Ni}(\text{OH})$. Taken together, this evidence supports the unequivocal assignment of the primary nickel-containing product as $[\text{Tp}^{\text{tBu,Me}}]\text{Ni}(\text{OH})$.

The molecular structure of $[\text{Tp}^{\text{tBu,Me}}]\text{Ni}(\text{OH})$ deduced by X-ray diffraction, Figure 5.6, shows the complex to be monomeric with the nickel coordination environment consisting of the usual κ^3 binding to the Tp ligand, via its 3 nitrogen donors, as well as ligation to the oxygen of the ancillary hydroxo ligand. The τ_4 value of 0.39 indicates a pseudo-tetrahedral geometry about the nickel, which is typical of 4-coordinate nickel complexes supported by the $\text{Tp}^{\text{tBu,Me}}$ ligand. The Ni–O bond length of 1.842(2) Å is slightly longer than that reported for the less sterically encumbered bis- μ -hydroxo-nickel species¹³, $[\text{Tp}^{\text{Me}_3}\text{Ni}(\mu\text{-OH})]_2$ (1.964(3), 1.977(3)), and in fact is more in line with its bis- μ -oxo derivative, $[\text{Tp}^{\text{Me}_3}\text{Ni}(\mu\text{-O})]_2$ (1.841(7); 1.870(8)). $[\text{Tp}^{\text{tBu,Me}}]\text{Ni}(\text{OH})$ is the first example of a monomeric nickel hydroxide complex supported by the Tp ligand. Examples of hydroxo-nickel complexes utilizing smaller 3-substituent Tp variants contain bis- μ -hydroxo dinickel(II) cores.⁷⁸ This distinction serves to highlight the role of the $\text{Tp}^{\text{tBu,Me}}$ ligand in preventing dimerization.

Mechanistically, direct O-atom transfer to phosphine affording an oxonickel intermediate followed by H-atom abstraction seems a plausible avenue to formation of $[\text{Tp}^{\text{tBu,Me}}]\text{Ni}(\text{OH})$, Figure 5.7. Alternatively, O–H bond making could be concerted

with O–O bond breaking, obviating the need for an oxonickel species as a discreet intermediate. However, the observation that $[\text{Tp}^{\text{tBu,Me}}]\text{Ni}(\text{O}_2)$ can transfer both O-atoms under conditions of excess phosphine (*vide infra*) makes this latter scenario less likely, as the highly reactive oxonickel complex would be unavailable for a second O-atom transfer. The source of the H-atom has not yet been definitively established. Reactions performed in deuterated solvent yielded only $[\text{Tp}^{\text{tBu,Me}}]\text{Ni}(\text{OH})$, which suggests that the likely origin of the hydrogen atom is the Tp ligand *tert*-butyl group, although HAT from trace proteo solvent and/or the phosphine alkyl groups cannot be excluded.

In addition to $[\text{Tp}^{\text{tBu,Me}}]\text{Ni}(\text{OH})$, reactions of $[\text{Tp}^{\text{tBu,Me}}]\text{Ni}(\text{O}_2)$ and alkyl phosphines also produce a second nickel product in lower yields; a metallacycle resulting from C–H activation of the ligand *tert*-butyl group. An analogous cobalt complex has been reported by Theopold and coworkers.⁷⁹ In the case of the cobalt species, ligand C–H activation is proposed to result from formation and subsequent decomposition of a hydroperoxocobalt complex. This latter species, formed from the reaction of dioxygen $[\text{Tp}^{\text{tBu,Me}}]\text{Co}(\text{H})$ has significant implications in the present work which are detailed later in this Chapter. As with $[\text{Tp}^{\text{tBu,Me}}]\text{Ni}(\text{OH})$, the metallacycle has been independently prepared and fully characterized. Independent preparation entails the treatment of $[\text{Tp}^{\text{tBu,Me}}]\text{Ni}(\text{OH})$ with a slight excess of aqueous hydrogen peroxide (30% w/w H_2O_2). Due to its asymmetric structure, the metallacycle has a distinctive ^1H NMR spectrum, which makes its identification, even in complex, multiple product mixtures, fairly straightforward. In phosphine oxidation, this species is a minor product whose prevalence is proportional to the steric bulk of the phosphine being oxidized. It accounts for roughly 13% of the nickel-containing products in the

case of PMe_3 oxidation and increases to 23% and 33% for PEt_3 and PCy_3 oxidation, respectively. In the case of PCy_3 , a small portion of the metallacycle yield may be explained by minor thermal decomposition, however, the primary mechanistic pathway effecting this conversion is currently unknown. Direct C–H activation of phosphine alkyl groups by the superoxo-nickel moiety followed by decomposition of the resulting hydroperoxo-nickel species is an intriguing, albeit untested, possible explanation.

The structure of the metallacycle, Figure 5.8, highlights a 4-coordinate nickel center with an atypical κ^4 ligation including a C–H activated *tert*-butyl group of the Tp ligand. In addition to the Tp donor nitrogens, the ligand is also bound to Ni via the oxygen of the activated *tert*-butyl group to form a six membered ring. The *tert*-butyl groups, including the one containing the C–H activated position, are disordered in the crystal, preventing accurate assessment of the Ni–O and O–C distances. This disorder is also present in the isostructural cobalt complex reported by Theopold and coworkers.⁷³ The unusual structure breaks the typical C_{3v} symmetry associated with the Tp ligand and thus results in the non-equivalence of the protons in activated and unactivated pyrazole subunits. The consequence of the reduced symmetry is that all the ligand features in the ^1H NMR spectrum, with the exception of the B–H resonance, are split in 2:1 ratio, Figure 5.9.

The presence of the metallacycle presented a challenge to quantifying $\text{PR}_3 \rightarrow \text{O}=\text{PR}_3$ conversion in the case of reactions with PMe_3 and PEt_3 . Coordination of $\text{O}=\text{PMe}_3$ and $\text{O}=\text{PEt}_3$ with the paramagnetic metallacycle resulted in the phosphine oxide signal being broadened into the baseline in $^{31}\text{P}\{^1\text{H}\}$ NMR spectra. This phenomenon has been demonstrated independently via treatment of $\text{O}=\text{PMe}_3$ solutions

with independently prepared metallacycle, where the phosphine oxide signal disappears upon metallacycle addition. Similar experiments demonstrated that $[\text{Tp}^{\text{tBu,Me}}]\text{Ni}(\text{OH})$ does not have a similar effect. In order to resolve this issue, experiments for quantification of phosphine oxide production were conducted in the presence of 1M pyridine, which functions as a competitive ligand, thereby precluding $\text{O}=\text{PR}_3$ ligation. This approach resulted in the presence of the phosphine oxide signal and allowed for effective quantification. Control experiments performed without pyridine showed no discernable difference in the identity of the nickel derivatives or the final product distribution and addition of pyridine to NMR solutions of these experiments resulted in the reappearance of the phosphine oxide signal. Experiments with PCy_3 did not suffer from the same difficulty, presumably because the steric bulk of PCy_3 prevents effective coordination to the metallacycle. Nevertheless, these trials were also run in the presence of excess pyridine for the sake of consistency.

The invocation of an oxonickel species in the mechanism of phosphine oxidation poses an interesting question. Given that such a species should be a powerful oxidant, can this complex react with another equivalent of phosphine to generate a total of two equivalents of phosphine oxide? To investigate this possibility, solutions of the superoxo were treated with an excess of PMe_3 . This methodology successfully demonstrated that both oxygen atoms of the O_2 moiety can be transferred. This second O-atom transfer is evident even with a very modest excess of phosphine. With just two equivalents of PMe_3 , approximately 26% of superoxo-nickel units transferred both of their O-atoms. Product formation increased to 54% at four equivalents of PMe_3 . At twenty equivalents of PMe_3 , nearly every superoxonickel unit (98%) transferred both O-atoms. In terms of reaction mechanism, the involvement of

the aforementioned oxonickel intermediate seems the most straightforward pathway. Following the transfer of the first O-atom in the initial reaction of $[\text{Tp}^{\text{tBu,Me}}]\text{Ni}(\text{O}_2)$ and PMe_3 , a second O-atom transfer is performed by this oxonickel species. Given that $[\text{Tp}^{\text{tBu,Me}}]\text{Ni}(\text{OH})$ is the primary product in the case of reactions with stoichiometric PMe_3 , this second O-atom transfer must be kinetically competitive with H-atom abstraction forming the hydroxo complex. Successful transfer of the second O-atom equivalent presumably results in the generation of a Ni(I) fragment, which appears to be unstable under the reaction conditions. Consistent with this interpretation, ^1H NMR spectra of reaction solutions containing excess PMe_3 show large amounts of free ligand, while both $[\text{Tp}^{\text{tBu,Me}}]\text{Ni}(\text{OH})$ and metallacycle formation are virtually eliminated at the highest excess PMe_3 concentration, e.g. 20 equivalents. The presence of the monovalent product was confirmed by addition of the trapping agent, *tert*-butyl isonitrile, to the phosphine solution prior to the reaction with $[\text{Tp}^{\text{tBu,Me}}]\text{Ni}(\text{O}_2)$. Under these conditions, NMR spectral analysis, Figure 5.10, reveals that the Ni(I) species is stabilized as $[\text{Tp}^{\text{tBu,Me}}]\text{Ni}(\text{CNtBu})$ and formation of the free Tp ligand is reduced.

In reactions with excess phosphine, the confirmation that the nickel product is monovalent prompted further investigation into whether phosphine oxidation could be catalytic in the presence of excess O_2 . Experiments demonstrated that catalytic activity is possible, but are hampered by both the high reactivity of the putative oxonickel intermediate and by the relatively facile decomposition of the unstabilized three-coordinate $[\text{Tp}^{\text{tBu,Me}}]\text{Ni}$. If the reaction between $[\text{Tp}^{\text{tBu,Me}}]\text{Ni}(\text{O}_2)$ and excess PMe_3 is performed under a dry dioxygen purge, but without a capping fourth ligand for Ni(I), 3.3 equivalents of $\text{O}=\text{PMe}_3$ are produced per nickel. Auto-oxidation of the

phosphine was negligible under these conditions and is therefore insufficient to explain the additional ~1.3 units of phosphine oxide formed. This result indicates that a small, but significant number of nickel sites acquire a second O₂ molecule. The ¹H NMR spectrum of the reaction residue displays large amounts of free ligand consistent with decomposition of the monovalent nickel complex. This appears to be the predominant mode of catalyst failure, although the concomitant detection of the Ni(II) hydroxo complex, [Tp^{tBu,Me}]Ni(OH), indicates that competition between phosphine oxidation and hydrogen atom abstraction by the putative oxonickel may also play a role. When the reaction is performed in the presence of two equivalents of *t*BuNC, the number of O=PMe₃ equivalents per nickel increases to 5.6. Doubling the amount of isonitrile further boosted the phosphine oxide yield to 8 equivalents per nickel. ¹H NMR spectral analysis of the isonitrile-doped reactions showed a decrease in the amount of free ligand relative to intact Ni(II) complexes. The latter consisted of roughly equal portions of [Tp^{tBu,Me}]Ni(OH) and [Tp^{tBu,Me}]Ni(O₂CN(H)*t*Bu). The carbamate complex is likely the result of isonitrile oxidation and subsequent reaction of the isocyanate with [Tp^{tBu,Me}]Ni(OH). These results suggest that although stabilizing the monovalent nickel state improves performance, deleterious reactions involving the highly reactive oxonickel intermediate, and possibly the superoxo complex itself, eventually result in catalyst degradation.

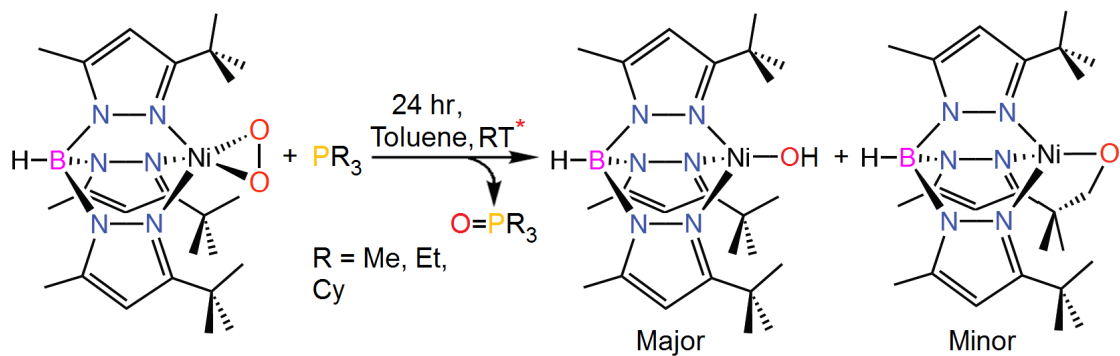


Figure 5.1 Reaction of $[\text{Tp}^{\text{tBu,Me}}]\text{Ni}(\text{O}_2)$ with stoichiometric phosphine. *Reaction with PCy_3 was run at 55°C .

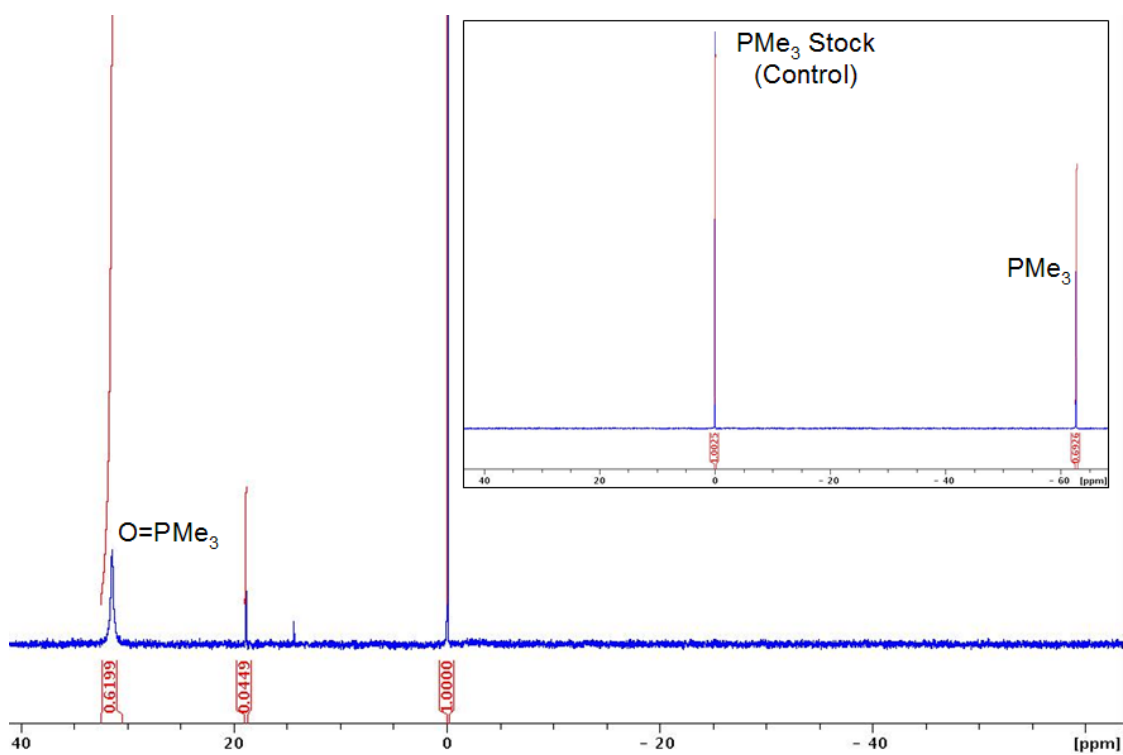


Figure 5.2 $^{31}\text{P}\{^1\text{H}\}$ NMR spectrum of reaction mixture of **2** with PMe_3 after 24 hr. Inset: PMe_3 stock solution (control).

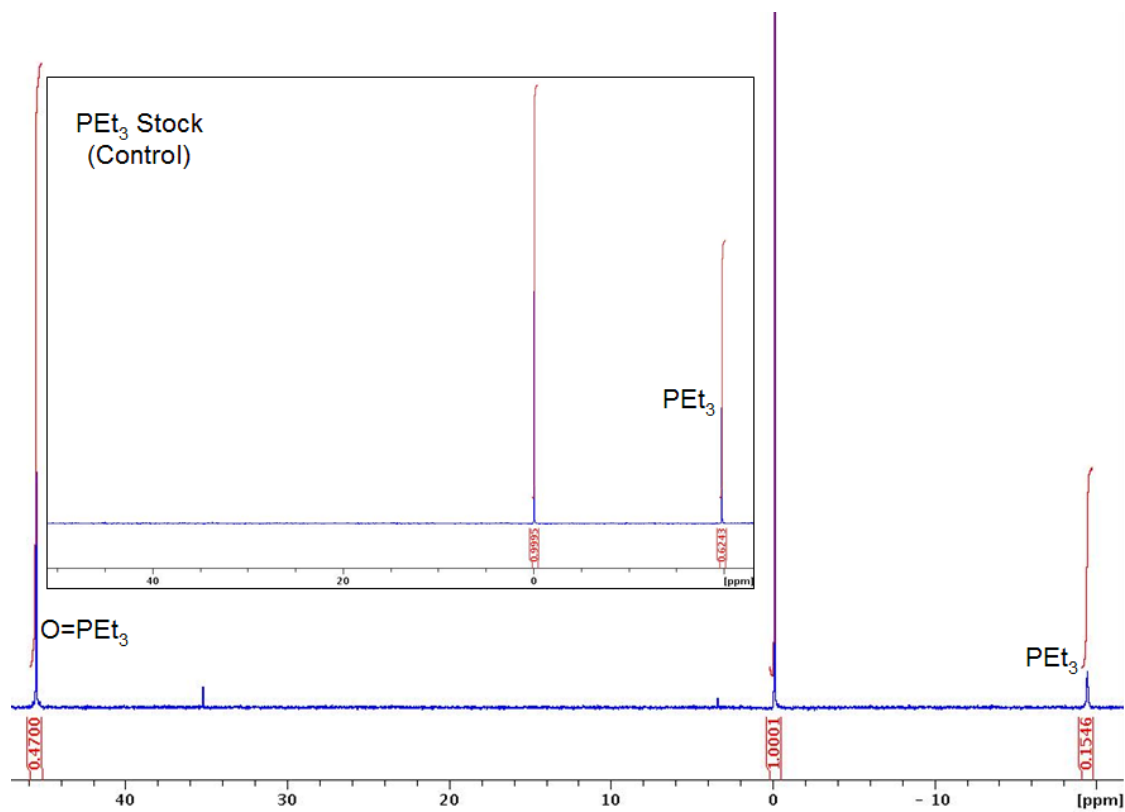


Figure 5.3 $^{31}\text{P}\{^1\text{H}\}$ NMR spectrum of reaction mixture of **2** with PEt_3 after 24 hr. Inset: PEt_3 stock solution (internal 85% aqueous H_3PO_4 , $\delta = 0$).

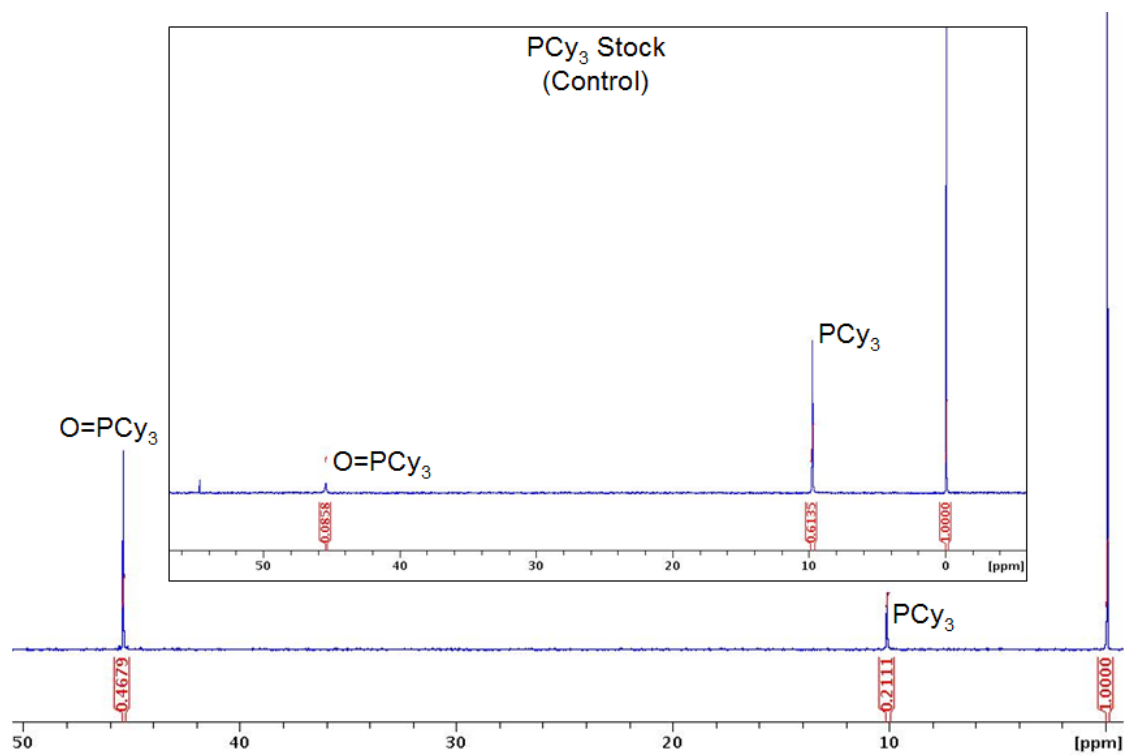


Figure 5.4 $^{31}\text{P}\{^1\text{H}\}$ NMR spectrum of reaction mixture of **2** with PCy_3 after 24 hours at $55\text{ }^\circ\text{C}$. Inset shows PCy_3 stock solution (internal 85% aqueous H_3PO_4 , $\delta = 0$).

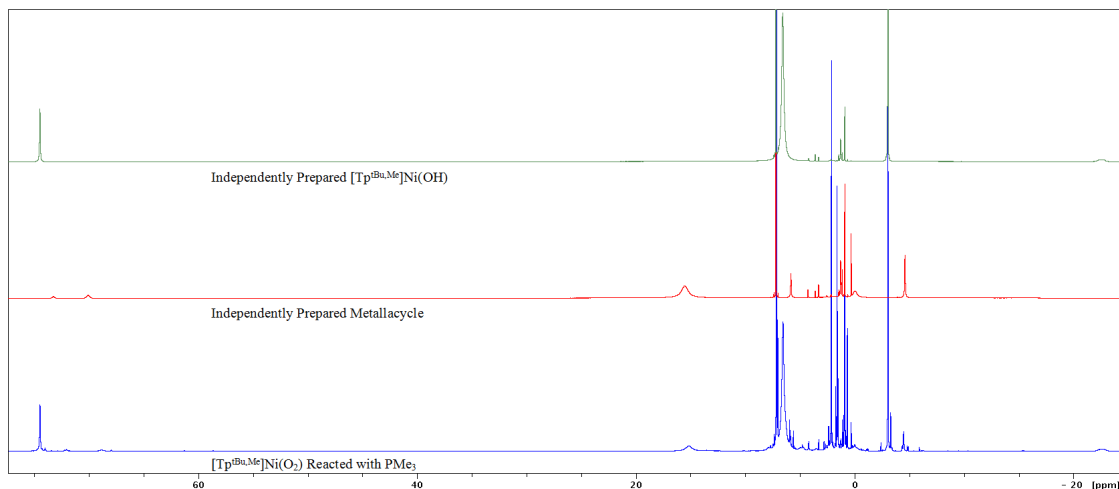


Figure 5.5 ^1H NMR spectral comparison of independently prepared $[\text{Tp}^{\text{tBu,Me}}]\text{Ni}(\text{OH})$ (top, green), metallacycle (middle, red) and residue from reaction of $[\text{Tp}^{\text{tBu,Me}}]\text{Ni}(\text{O}_2)$ with PMe_3 (bottom, blue).

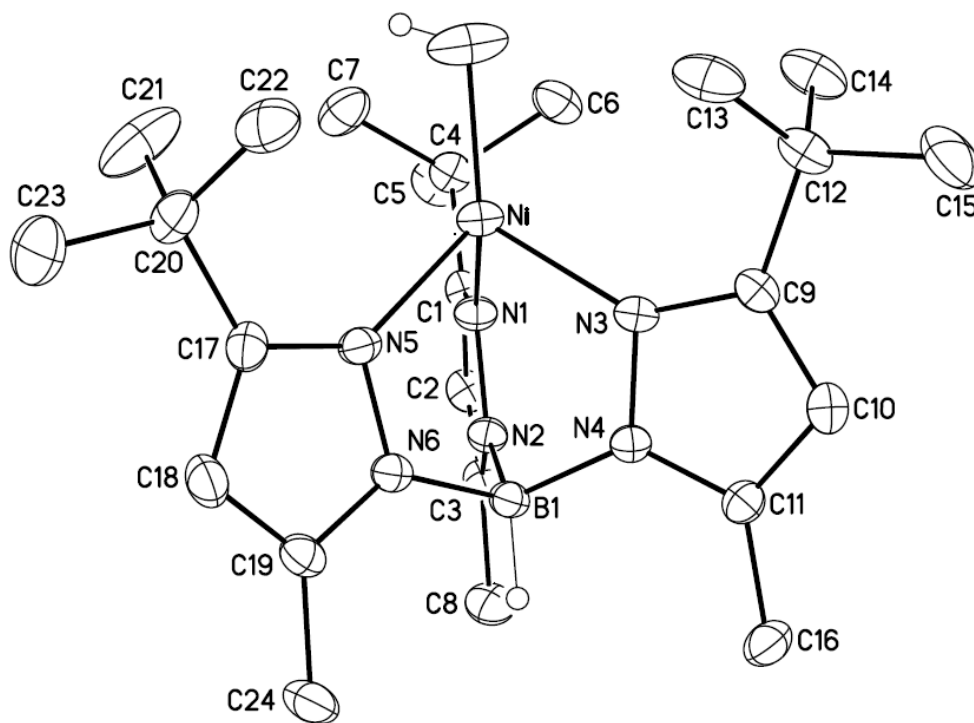


Figure 5.6 Thermal ellipsoid diagram of $[\text{Tp}^{\text{tBu,Me}}]\text{Ni}(\text{OH})$ with atom labeling. Thermal ellipsoids are drawn to 30% probability. Hydrogen atoms are omitted for clarity with the exception of B–H and O–H.

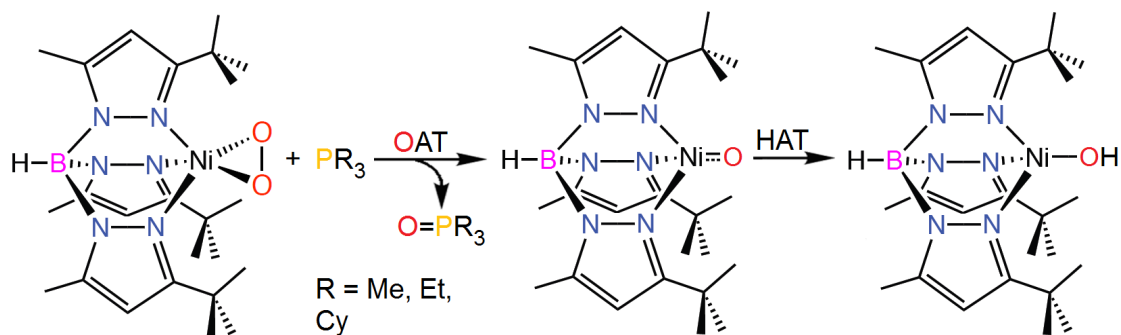


Figure 5.7 Proposed mechanism for formation of $[\text{Tp}^{\text{tBu,Me}}]\text{Ni(OH)}$ in reaction of $[\text{Tp}^{\text{tBu,Me}}]\text{Ni(O}_2\text{)}$ with 1 equiv. of phosphine.

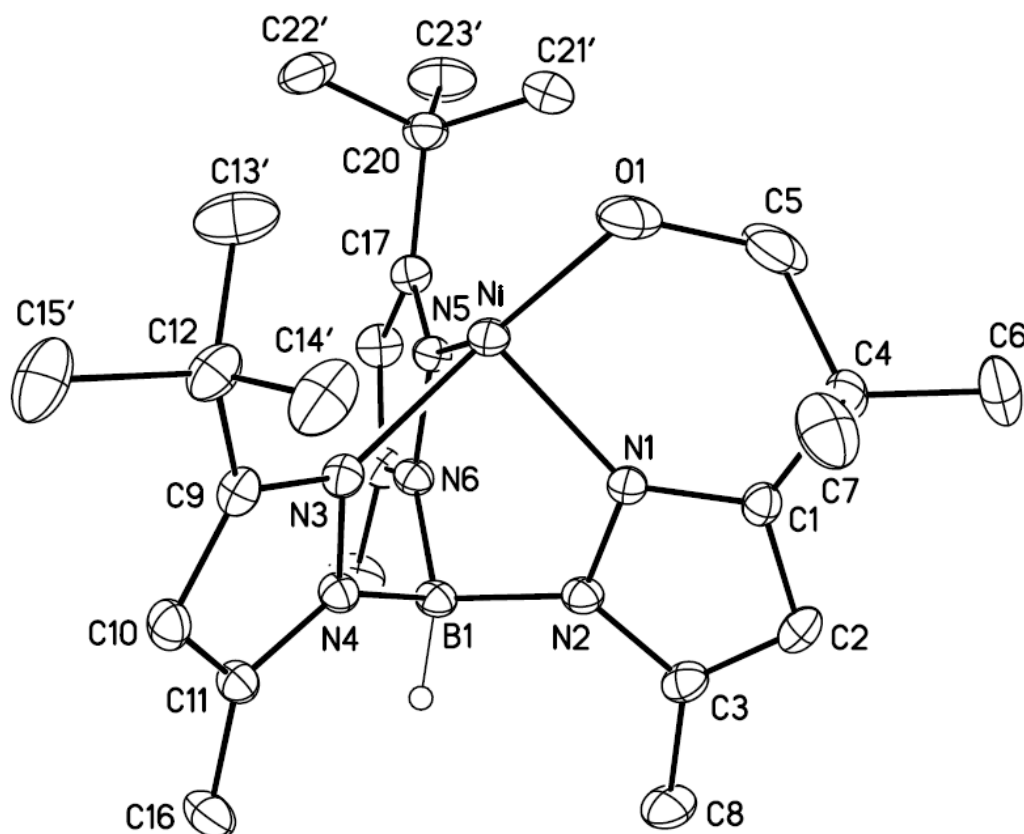


Figure 5.8 Thermal ellipsoid diagram of metallacycle with atom labeling. Thermal ellipsoids are drawn to 30% probability. Hydrogen atoms are omitted for clarity with the exception of B–H. The *tert*-butyl groups were located disordered in two positions and treated to restraints based on non-crystallographic symmetry.

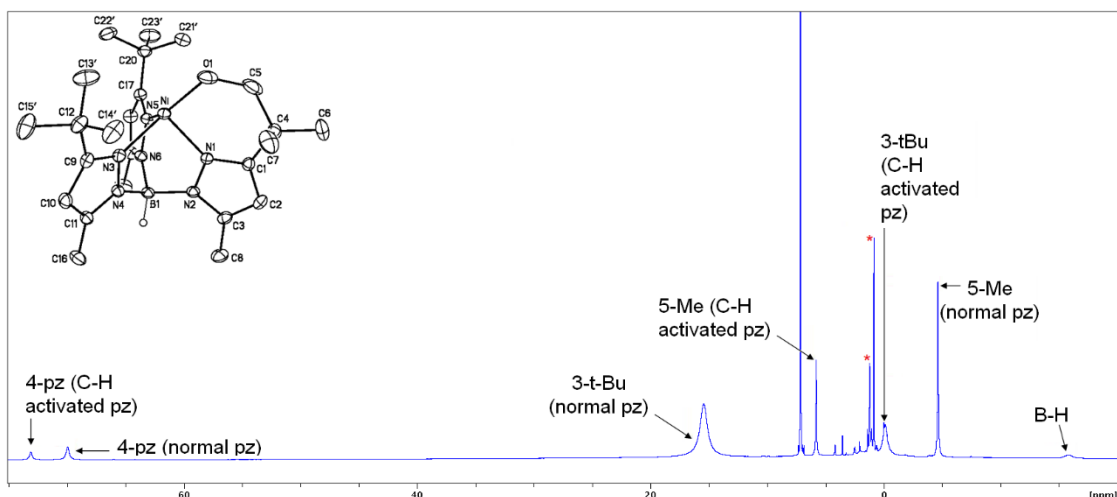


Figure 5.9 ^1H NMR spectrum of independently prepared metallacycle with activated and unactivated *tert*-butyl pyrazole features labeled. Molecular structure is inset for reference.

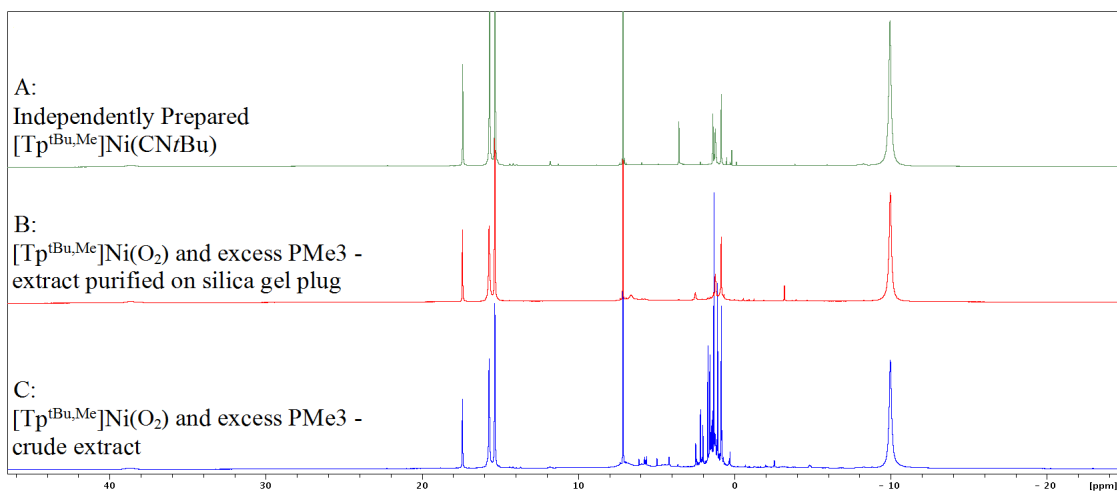


Figure 5.10 ^1H NMR spectral comparison of: A) Independently prepared $[\text{Tp}^{\text{tBu,Me}}]\text{Ni}(\text{CN}/\text{tBu})$. B) Pentane extract of residue from reaction of $[\text{Tp}^{\text{tBu,Me}}]\text{Ni}(\text{O}_2)$ with PMe_3 in the presence of *t*BuCN purified via silica gel plug chromatography. C. Crude reaction residue.

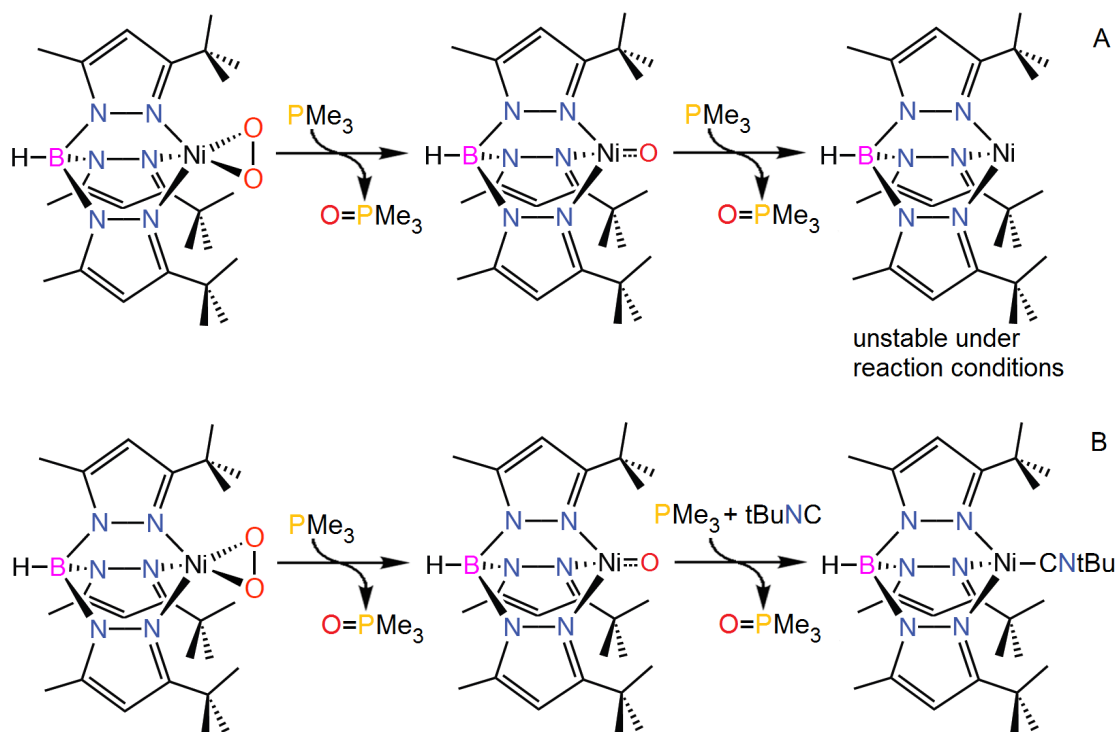


Figure 5.11 Proposed mechanism for sequential O-atom transfer in reaction of $[\text{Tp}^{\text{tBu,Me}}]\text{Ni}(\text{O}_2)$ and excess PMe_3 with and without tBuNC as a trapping agent.

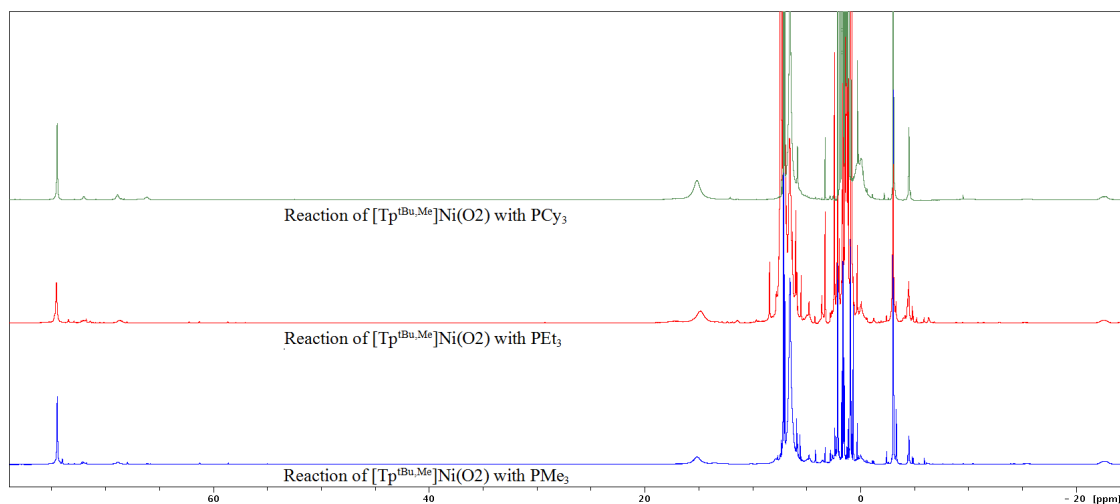


Figure 5.12 ^1H NMR spectral comparison of nickel products resulting from reaction of $[\text{Tp}^{\text{tBu,Me}}]\text{Ni}(\text{O}_2)$ with PMe_3 (top, red), PEt_3 and PCy_3 . The ratio of metallacycle to $[\text{Tp}^{\text{tBu,Me}}]\text{Ni}(\text{OH})$ increases with the increasing steric bulk of the phosphine.

5.2.4 Reaction of $[\text{Tp}^{\text{tBu,Me}}]\text{Ni}(\text{O}_2)$ with NO

The study of nitric oxide (NO) has become prominent in recent years due to its implication in a number of essential biological processes including vasodilation, immune response and neurotransmission.⁸⁰⁻⁸¹ The interaction of NO with the superoxide moiety in various metalloenzymes, such as superoxide dismutase (SOD) and hemoglobin, is of particular importance to the bioinorganic community due to their vital biological roles and, in the case of SOD, its near ubiquitous presence in organisms exposed to dioxygen.⁸²⁻⁸³⁻⁸⁴ Given the level of interest in the interactions between nitric oxide and metal-dioxygen species, the reaction of $[\text{Tp}^{\text{tBu,Me}}]\text{Ni}(\text{O}_2)$ and NO was chosen for study.

A degassed toluene solution of $[\text{Tp}^{\text{tBu,Me}}]\text{Ni}(\text{O}_2)$ was treated with a modest excess of NO and the reaction stirred for 24 hours at room temperature. As the reaction progressed, a color change from red-brown to green was observed. After

completion, the solvent was removed under vacuum and the residue subjected to analysis by ^1H NMR spectral analysis. The major products of the reaction were $[\text{Tp}^{\text{tBu,Me}}]\text{Ni}(\text{NO}_2)$ and $[\text{Tp}^{\text{tBu,Me}}]\text{Ni}(\text{NO}_3)$, which were produced in a $\sim 1:2$ ratio. As with phosphine oxidation, nickel product identification was based on NMR spectral comparison of the crude reaction material to independently prepared samples, Figure 5.14 In the case of $[\text{Tp}^{\text{tBu,Me}}]\text{Ni}(\text{NO}_3)$, independent preparation was accomplished via metalation of $\text{KTp}^{\text{tBu,Me}}$ with $\text{Ni}(\text{NO}_3)_2$ in methanol. For $[\text{Tp}^{\text{tBu,Me}}]\text{Ni}(\text{NO}_2)$, $[\text{Tp}^{\text{tBu,Me}}]\text{NiBr}$ in THF was treated with NaNO_2 in methanol, affording the nitrite complex. In addition to the aforementioned major products, smaller quantities of several unidentified species were also observed. Of these, at least one appears to be of the $[\text{Tp}^{\text{tBu,Me}}]\text{Ni}(\text{X})$ type with clearly distinguished pyrazole and methyl proton resonances in the area of the ^1H NMR spectrum commonly associated with these features.

The products observed in the reaction are similar to those reported for another monomeric superoxide adduct, $[\text{PhTt}^{\text{Ad}}]\text{Ni}(\text{O}_2)$, also prepared in the Riordan laboratory. In both cases the nitrate complex constitutes the major species with the nitrite complex making up a smaller fraction of the product distribution. One possible explanation for the presence of both nitrate and nitrite species in the final product mixture is the formation and subsequent decomposition of a nickel-peroxynitrite intermediate, Figure 5.15. A structurally analogous intermediate has been proposed by Theopold *et al.* for the reaction of $[\text{Tp}^{\text{tBu,Me}}]\text{Co}(\text{O}_2)$ with NO .⁸⁵ Other relevant examples include two spectroscopically characterized and DFT modeled copper peroxynitrite complexes, $[(\text{TMG}_3\text{tren})\text{Cu}^{\text{II}}(\text{OON}=\text{O})]^+$ and $[\text{Cu}^{\text{II}}(3,3'\text{-iminobis}(N,N'\text{-dimethylpropylamine}))(\text{ONOO}^-)]^+$ reported by Karlin and coworkers.^{86,87} The

former of these complexes, $[(\text{TMG}_3\text{tren})\text{Cu}^{\text{II}}(\text{OON}=\text{O})]$, was derived directly from a copper dioxygen adduct reacted with NO. The latter complex, while starting with a copper–nitrosyl complex, is also proposed to derive from a copper-dioxygen adduct formed via initial displacement of and subsequent reaction with the NO moiety.

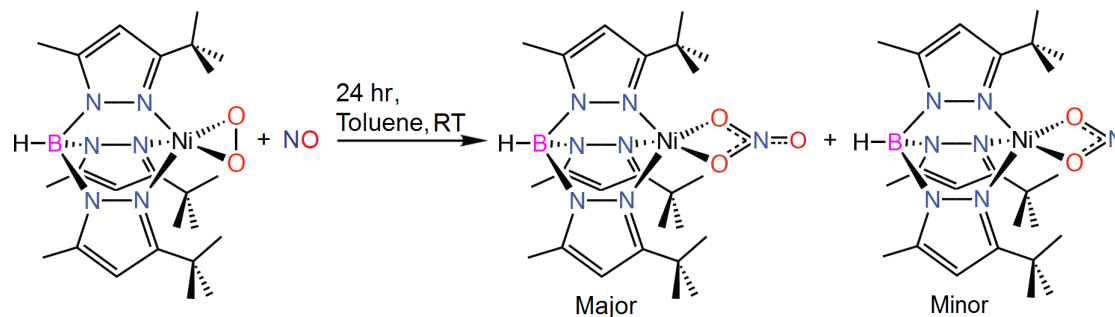


Figure 5.13 Reaction of $[\text{Tp}^{\text{tBu,Me}}\text{Ni}(\text{O}_2)]$ with NO.

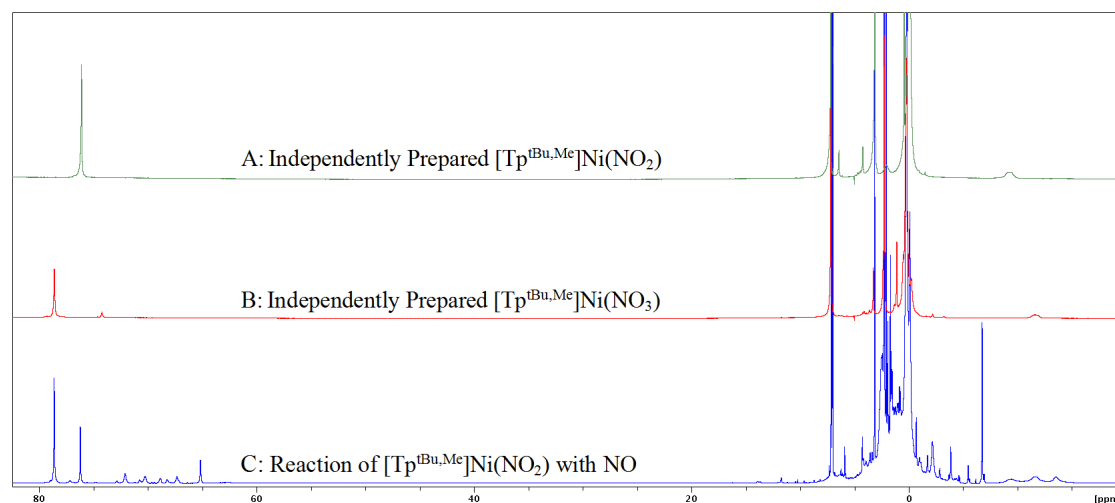


Figure 5.14 ^1H NMR spectral comparison of: A) Independently prepared $[\text{Tp}^{\text{tBu,Me}}\text{Ni}(\text{NO}_2)]$. B) Independently prepared $[\text{Tp}^{\text{tBu,Me}}\text{Ni}(\text{NO}_3)]$. C) Residue from reaction of $[\text{Tp}^{\text{tBu,Me}}\text{Ni}(\text{O}_2)]$ with NO.

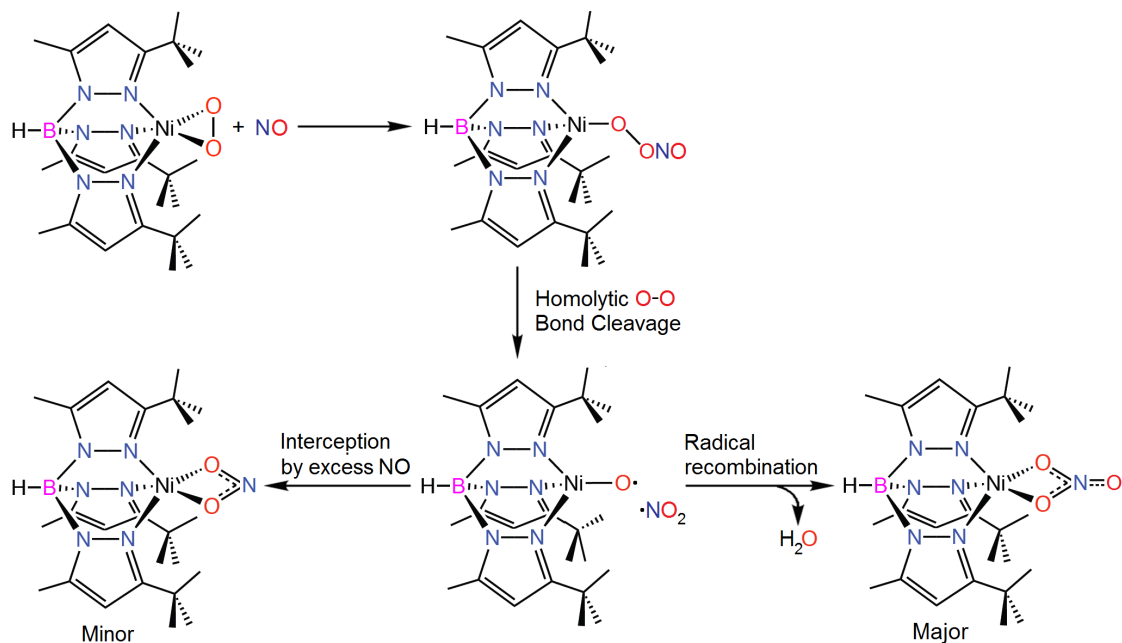


Figure 5.15 Possible mechanism for formation of $[\text{Tp}^{\text{tBu,Me}}]\text{Ni}(\text{NO}_2)$ and $[\text{Tp}^{\text{tBu,Me}}]\text{Ni}(\text{NO}_3)$ in the reaction of $[\text{Tp}^{\text{tBu,Me}}]\text{Ni}(\text{O}_2)$ with NO.

5.3 C-H Activation by $[\text{Tp}^{\text{tBu,Me}}]\text{Ni}(\text{O}_2)$

5.3.1 Reaction of $[\text{Tp}^{\text{tBu,Me}}]\text{Ni}(\text{O}_2)$ with 1,4-cyclohexadiene (CHD)

As a substrate with a relatively weak C–H bond (bond dissociation enthalpy (BDE) = 76.8 kcal/mol)⁸⁸, 1,4-cyclohexadiene (CHD) represents an attractive substrate for C-H activation by transition metal complexes.^{89,90,91} Driven by the thermodynamically favorable transformation to benzene, CHD is an excellent candidate for assessing the C-H activation potential of $[\text{Tp}^{\text{tBu,Me}}]\text{Ni}(\text{O}_2)$.

A solution of CHD and hexamethylbenzene (internal standard) in *d*₈-toluene was treated with two equivalents of $[\text{Tp}^{\text{tBu,Me}}]\text{Ni}(\text{O}_2)$ and stirred for approximately 24 hours at 60 °C, during which time a color change from red-brown to red-orange was observed. ¹H NMR spectral analysis of the reaction solution before and after reaction

with the superoxo complex indicated the formation of benzene in 65% yield based on comparison to the internal standard, Figure 5.16. The paramagnetic ^1H NMR spectrum confirmed the complete consumption of the $[\text{Tp}^{\text{tBu,Me}}]\text{Ni}(\text{O}_2)$ and the formation of two nickel containing products, $[\text{Tp}^{\text{tBu,Me}}]\text{Ni}(\text{OH})$ and the metallacycle, which were identified by ^1H NMR comparison to the independently prepared compounds, Figure 5.17. The nickel product distribution was heavily weighted toward the metallacycle with a $[\text{Tp}^{\text{tBu,Me}}]\text{Ni}(\text{OH})$: metallacycle ratio of 1:6. This was the first observed instance of a reaction involving $[\text{Tp}^{\text{tBu,Me}}]\text{Ni}(\text{O}_2)$ in which the metallacycle constituted the majority of the nickel products.

Mechanistically, the most straightforward pathway begins with initial C–H activation of CHD to give a hydroperoxo species, $[\text{Tp}^{\text{tBu,Me}}]\text{Ni}(\text{OOH})$, and the cyclohexadienyl radical, Figure 5.19. This newly formed hydroperoxo complex possesses a fairly weak O–O bond which can undergo homolytic cleavage generating an oxonickel species and hydroxyl radical. From this point, one can envision two possible scenarios. In the first, the highly reactive hydroxyl radical abstracts a H-atom from one of the proximal 3-*tert*-butyl groups on the ligand producing water. The newly generated ligand-based radical could then react with the oxonickel, itself possessing significant radical character, yielding the metallacycle. Alternatively, should the hydroxyl radical escape the coordination sphere, the oxonickel moiety obtains a H-atom, either from the Tp ligand, the solvent or the remaining CHD. This latter course results in the generation of $[\text{Tp}^{\text{tBu,Me}}]\text{Ni}(\text{OH})$. The observed product mixture, which contains both metallacycle and $[\text{Tp}^{\text{tBu,Me}}]\text{Ni}(\text{OH})$, suggests that both pathways occur with hydroxyl radical attack on the ligand occurring more often than escape under the reaction conditions. Regardless of the mechanism, the newly

generated cyclohexadienyl radical reacts with another equivalent of $[\text{Tp}^{\text{tBu,Me}}]\text{Ni}(\text{O}_2)$ to generate benzene and a second unit of $[\text{Tp}^{\text{tBu,Me}}]\text{Ni}(\text{OOH})$. The subsequent decomposition of the latter produces either metallacycle or $[\text{Tp}^{\text{tBu,Me}}]\text{Ni}(\text{OH})$ depending on the fate of the hydroxyl radical. The last step presumably occurs in the same mechanistic fashion as the initial reaction of $[\text{Tp}^{\text{tBu,Me}}]\text{Ni}(\text{O}_2)$ with CHD.

An alternative to discrete O–O bond homolysis and hydroxyl radical formation is possible if O–O and C–H bond breaking are concerted with O–H bond making in the decomposition of $[\text{Tp}^{\text{tBu,Me}}]\text{Ni}(\text{OOH})$. Such a scenario would avoid formation of the high energy hydroxyl radical. If this is indeed the pathway, the transition state might take the form of an extended ring structure, Figure 5.20. If one assumes that this latter mechanistic view occurs exclusively, it implies that the only nickel-containing product would be the metallacycle, an implication made problematic by the production of $[\text{Tp}^{\text{tBu,Me}}]\text{Ni}(\text{OH})$.

Lastly, it is also possible that the concerted and non-concerted decomposition routes are sufficiently close in energy, allowing some level of competition between the two, with both pathways contributing to the final product distribution. In this latter scenario, to explain the large amount of metallacycle produced relative to $[\text{Tp}^{\text{tBu,Me}}]\text{Ni}(\text{OH})$, the concerted pathway must be somewhat preferred and/or the non-concerted pathway highly weighted toward ligand C–H activation over hydroxyl radical escape. A follow-up DFT study exploring the energies of the associated transition states in each mechanistic scenario would be useful in determining the likely contributor(s). Such a study may also help explain the divergence in product type between CHD and 9,10-dihydroanthracene (*vide infra*).

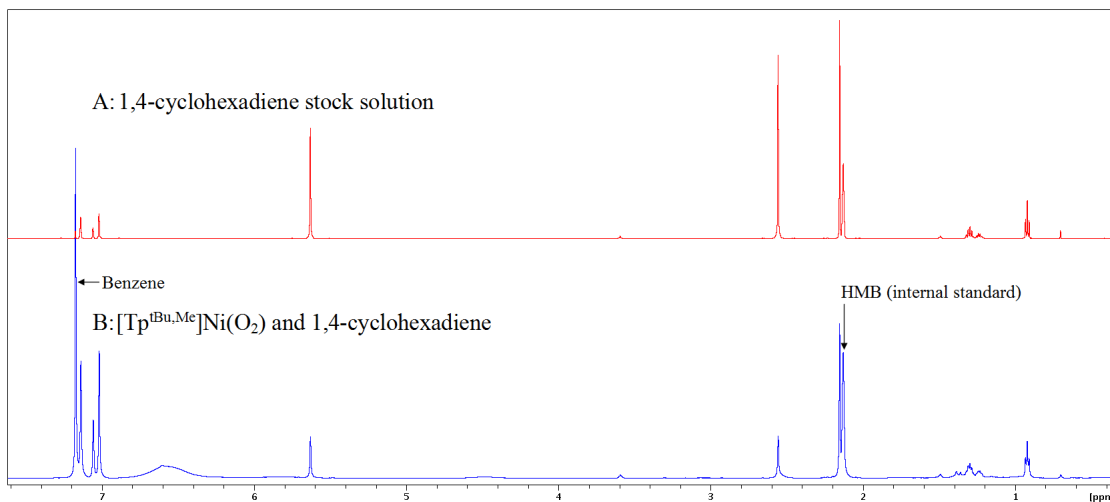


Figure 5.16 ¹H NMR spectral comparison of: A) 1,4-cyclohexadiene solution before addition of [Tp^{tBu,Me}]Ni(O₂). B) 1,4-cyclohexadiene solution after reaction.

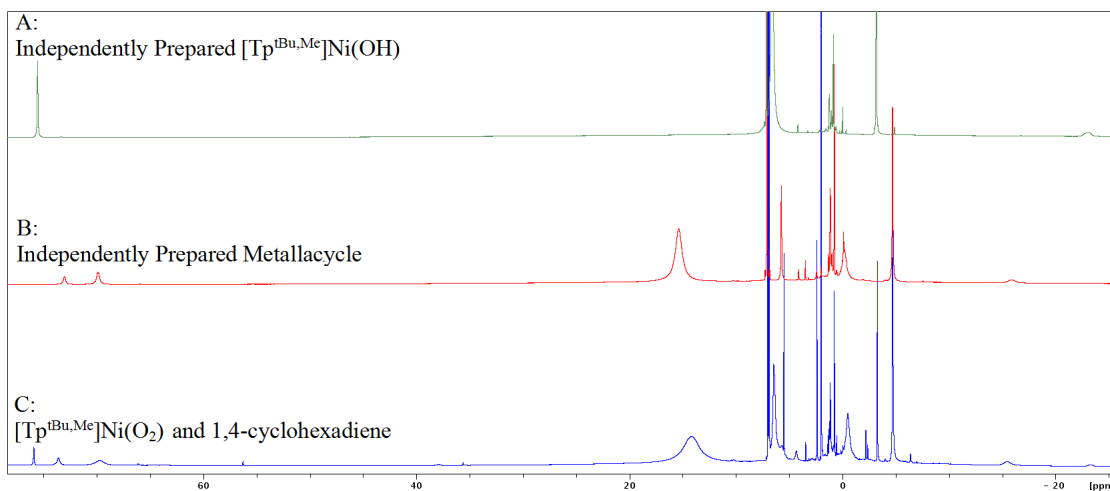


Figure 5.17 ¹H NMR spectral comparison of: A) Independently prepared [Tp^{tBu,Me}]Ni(OH). B) Independently prepared metallacycle. C) Crude residue from reaction of [Tp^{tBu,Me}]Ni(O₂) and 1,4-cyclohexadiene.

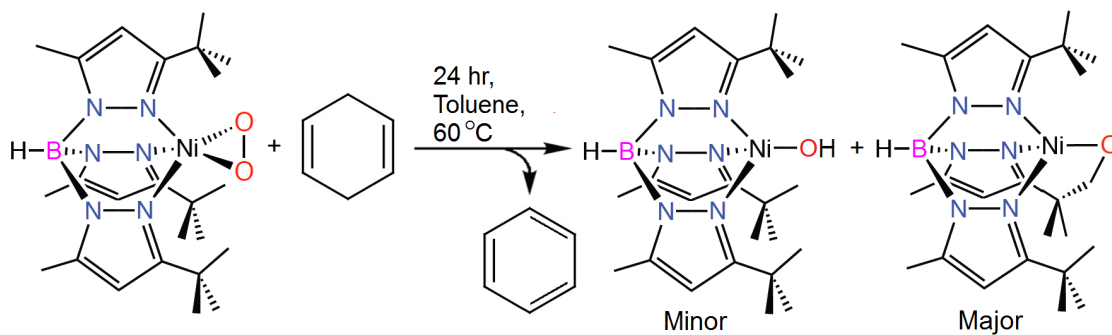


Figure 5.18 Reaction of $[\text{Tp}^{\text{tBu,Me}}]\text{Ni}(\text{O}_2)$ with 1,4-cyclohexadiene.

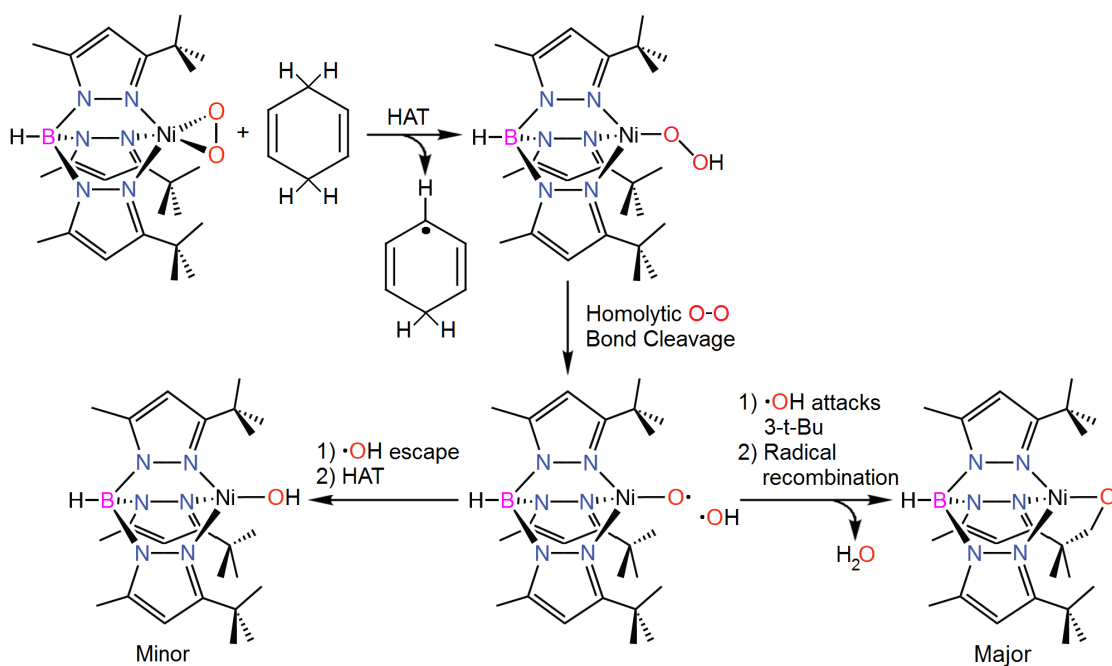


Figure 5.19 Proposed mechanism for the reaction of $[\text{Tp}^{\text{tBu,Me}}]\text{Ni}(\text{O}_2)$ with 1,4-cyclohexadiene. Abstraction of an H atom from the ligand t-Bu group by hydroxyl radical results in the formation of the major product, metallacycle. Hydroxyl radical escape generates the minor product, $[\text{Tp}^{\text{tBu,Me}}]\text{Ni}(\text{OH})$.

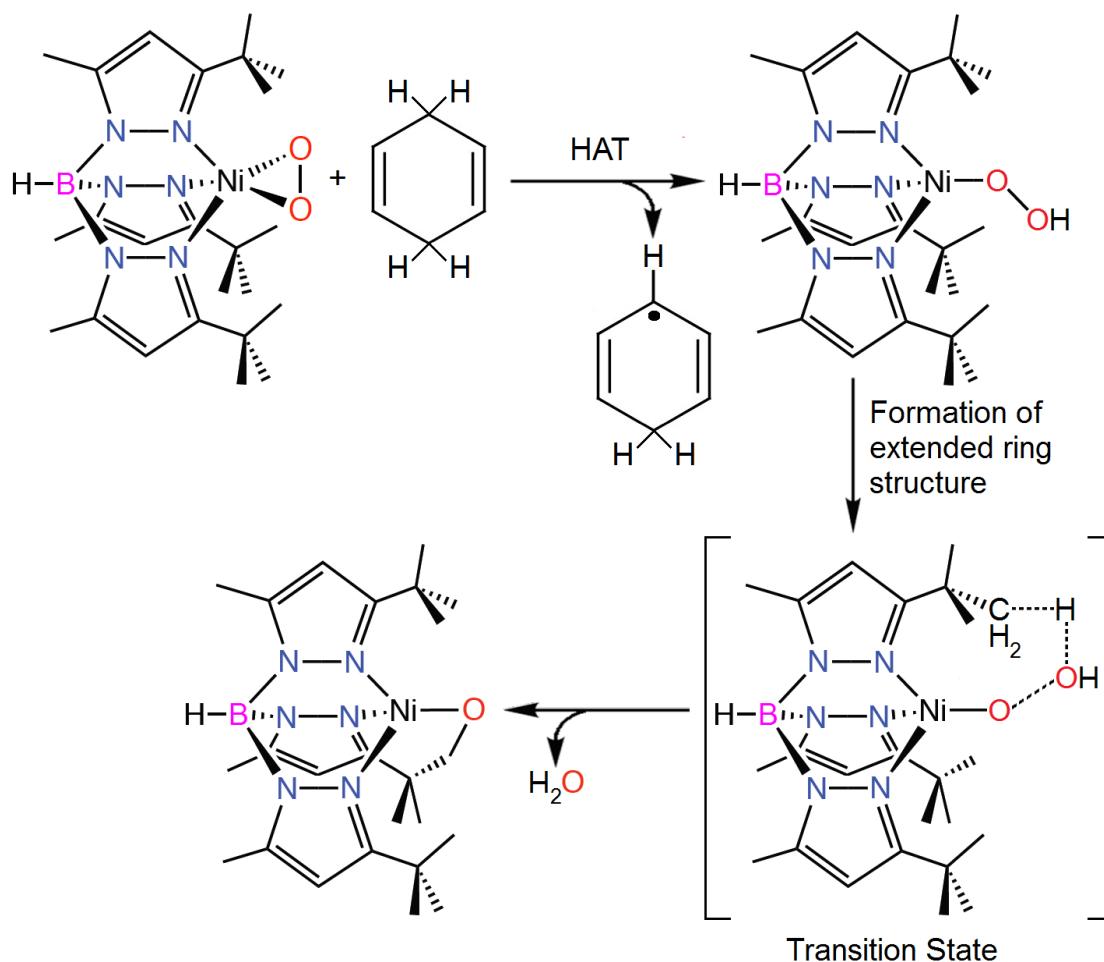


Figure 5.20 Alternative mechanism for the reaction of [Tp^{tBu,Me}]Ni(O₂) with 1,4-cyclohexadiene. Decomposition of [Tp^{tBu,Me}]Ni(OOH) proceeds through a transition state consisting of an extended ring structure. O–O and C–H bond breaking are concerted with O–H bond formation.

5.3.2 Independent Preparation of [Tp^{tBu,Me}]Ni(OOH)

Hydroperoxo-nickel species are exceedingly rare in the literature. Only recently has an example of such a species been fully characterized, in a groundbreaking report by Rettenmeier et al.⁹² This thermally unstable complex, supported by the bis(oxazolinyl)methylidenylpyrrolidinato ligand system, represents the only structurally characterized hydroperoxonickel. The rarity and potential

oxidative power of this type of nickel complex makes such species targets of significant value. In the present work, the presence of a hydroperoxo-nickel complex, $[\text{Tp}^{\text{tBu,Me}}]\text{Ni}(\text{OOH})$, is implicated by the observed nickel products in C–H activation reactions involving $[\text{Tp}^{\text{tBu,Me}}]\text{Ni}(\text{O}_2)$. This fact, combined with the general interest in such species, made the direct detection of $[\text{Tp}^{\text{tBu,Me}}]\text{Ni}(\text{OOH})$ a high priority. To this end, efforts have been made to independently prepare and characterize this species.

Perhaps the earliest implication of $[\text{Tp}^{\text{tBu,Me}}]\text{Ni}(\text{OOH})$ was the observation that the treatment of $[\text{Tp}^{\text{tBu,Me}}]\text{Ni}(\text{OH})$ with a slight excess of hydrogen peroxide at room temperature results in the exclusive generation of the metallacycle. As mentioned in Section 5.2, the structure of this species is analogous to that of a cobalt complex reported by Theopold and coworkers,⁷⁹ which was proposed to be derived from a hydroperoxo-cobalt intermediate, $[\text{Tp}^{\text{tBu,Me}}]\text{Co}(\text{OOH})$, identified spectroscopically at low temperature. It was speculated by Theopold that the formation of this intermediate was followed by C–H activation of the ligand generating the observed metallacycle. Extending this scenario to the nickel analog, treatment of $[\text{Tp}^{\text{tBu,Me}}]\text{Ni}(\text{OH})$ with aqueous hydrogen peroxide results in protonation of the ancillary hydroxyl group to generate water. The labile H_2O ligand is easily displaced by the newly generated hydroperoxy anion giving the intermediate, $[\text{Tp}^{\text{tBu,Me}}]\text{Ni}(\text{OOH})$. As with the cobalt analog, this species is unstable at room temperature, rapidly decomposing to the metallacycle as described in Section 5.3.1. Reasoning that the hydroperoxo-nickel might be persistent at lower temperatures, attempts were made to observe this species spectroscopically via variable temperature UV-vis and ^1H NMR spectroscopies. Matthew White, an undergraduate in the Riordan laboratory at the time, performed low temperature spectroscopic measurements on samples of $[\text{Tp}^{\text{tBu,Me}}]\text{Ni}(\text{OH})$ treated

with excess H₂O₂ as part of his senior thesis work.⁹³ Electronic absorption spectral analysis of the reaction at -55 °C, Figure 5.21, indicated the formation of a distinct intermediate upon H₂O₂ addition. This species remained stable at temperatures up to -28 °C, above which the spectrum decays to that of the metallacycle. In addition, investigation of the reaction using ¹H NMR spectroscopy at -60 °C revealed complete conversion of [Tp^{tBu,Me}]Ni(OH) to a species with spectral features consistent with that of an unknown [Tp^{tBu,Me}]NiX type complex, Figure 5.22. After warming the sample to room temperature and cooling back to -60 °C the intermediate species disappeared and was replaced by the spectral features of the metallacycle. Attempts at crystallizing this intermediate at low temperature have, as yet, been unsuccessful. However, the spectroscopic data provide compelling evidence for the formation of a thermally sensitive Ni(II) complex whose identity is ascribed as a hydroperoxo-nickel species.

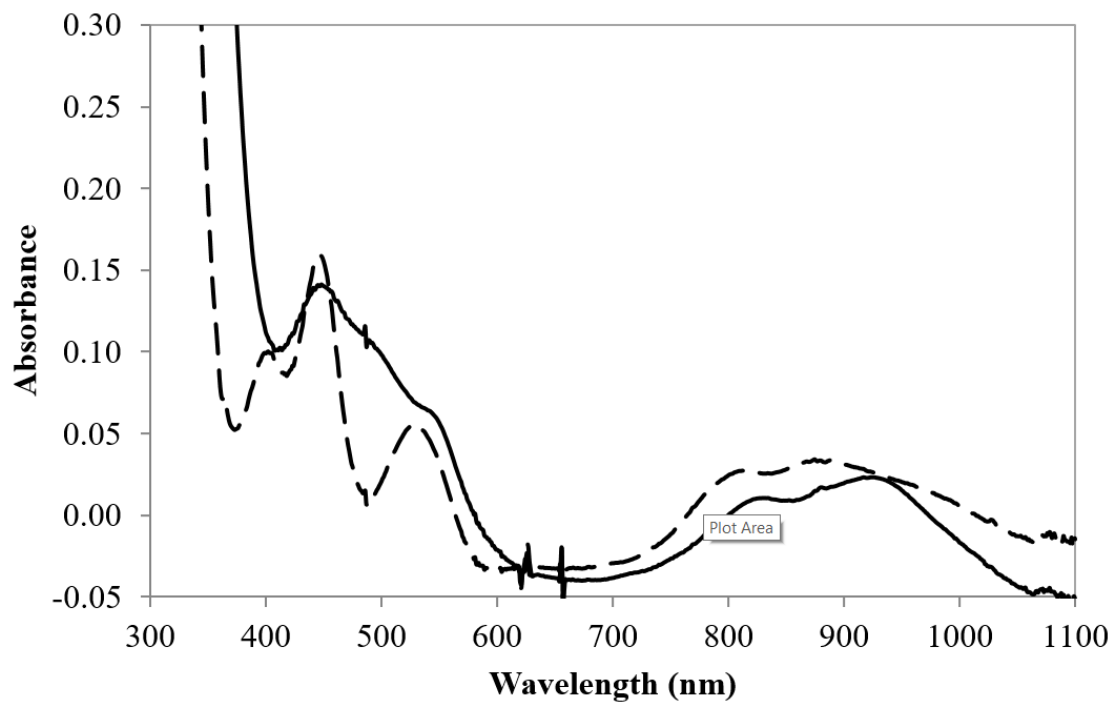


Figure 5.21 UV-Vis absorption analysis of the reaction $[\text{Tp}^{\text{tBu,Me}}]\text{Ni}(\text{OH})$ and H_2O_2 . Solid line: Intermediate produced upon addition of H_2O_2 to a solution of $[\text{Tp}^{\text{tBu,Me}}]\text{Ni}(\text{OH})$ in CH_2Cl_2 at $-55\text{ }^\circ\text{C}$ H_2O_2 . Dashed line: spectrum of solution after decomposition at room temperature. UV-Vis measurements and figure prepared by M. White.⁹³

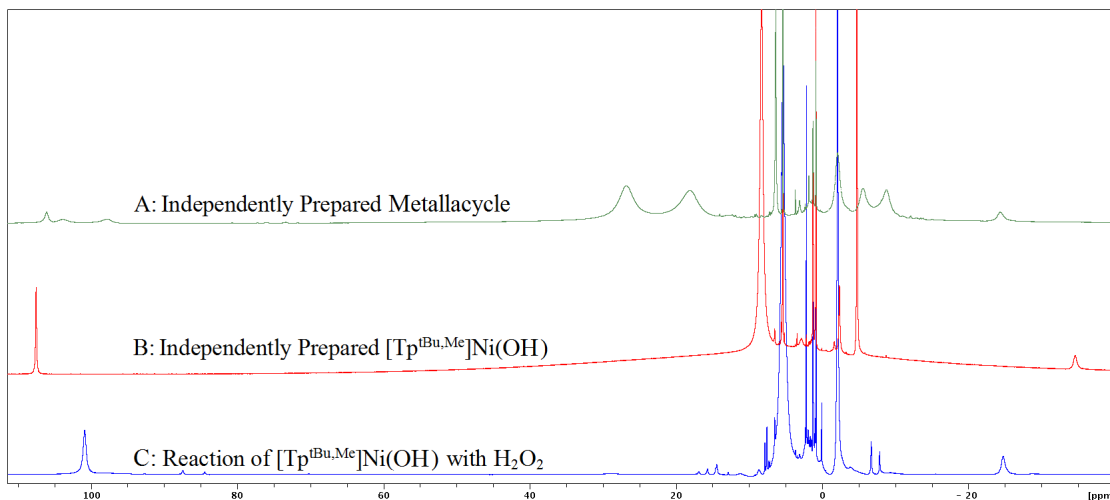


Figure 5.22 ^1H NMR spectral comparison of: A) Independently prepared metallacycle. B) Independently prepared $[\text{Tp}^{\text{tBu,Me}}]\text{Ni}(\text{OH})$. C) Intermediate species produced upon treatment of $[\text{Tp}^{\text{tBu,Me}}]\text{Ni}(\text{OH})$ with H_2O_2 . For consistency, all spectra were collected at $-60\text{ }^\circ\text{C}$. Spectroscopic measurements performed by M. White under the supervision of W. Green. Figure prepared by W. Green.

5.3.3 Preparation and Thermal Decomposition of $[\text{Tp}^{\text{tBu,Me}}]\text{Ni}(\text{OO}^t\text{Bu})$

Due to the challenges associated with obtaining crystals of $[\text{Tp}^{\text{tBu,Me}}]\text{Ni}(\text{OOH})$ suitable for X-ray analysis, it was reasoned that the synthesis of an alkylperoxo complex, which should be more stable, might be beneficial. Previous work from the Hikichi lab, utilizing the Tp^{iPr_2} ligand, demonstrated that an alkylperoxo species could be generated via treatment of a Ni(II) hydroxo precursor with *tert*-butylhydroperoxide.⁴⁴ While not stable at room temperature, the complex was nonetheless sufficiently robust to allow for crystallization and structural analysis by XRD. With this in mind, the alkylperoxo species, $[\text{Tp}^{\text{tBu,Me}}]\text{Ni}(\text{OO}^t\text{Bu})$, was targeted for preparation with the expectation that it would provide a more thermally stable analog of $[\text{Tp}^{\text{tBu,Me}}]\text{Ni}(\text{OOH})$, and thereby allow for structural analysis of the alkylperoxo-nickel core. Treatment of $[\text{Tp}^{\text{tBu,Me}}]\text{Ni}(\text{OH})$ in toluene with *tert*-butyl

hydroperoxide (*tBuOOH*, ~5.5 M in decane) resulted in a rapid color change from red-brown to a dark red-orange. Following solvent removal and a pentane wash, $[\text{Tp}^{\text{tBu,Me}}]\text{Ni}(\text{OO}t\text{Bu})$ was isolated as a red-brown powder in 86% yield, Figure 5.23. ^1H NMR spectra of samples of the complex obtained over multiple weeks demonstrated its room temperature stability in both the solid state and solution.

Structural analysis of $[\text{Tp}^{\text{tBu,Me}}]\text{Ni}(\text{OO}t\text{Bu})$ via single crystal XRD, Figure 5.26, revealed a heavily distorted trigonal pyramidal geometry with a τ_4 value of 0.67. From a structural perspective, this value makes $[\text{Tp}^{\text{tBu,Me}}]\text{Ni}(\text{OO}t\text{Bu})$ unique among the complexes reported in the current work as all other 4-coordinate complexes herein have a geometry closer to a tetrahedron ($\tau_4 < 0.5$). The alkylperoxo moiety is bound to the nickel in a η^1 fashion with a Ni–O_{proximal} distance of 1.872(5) Å. The O–O distance of 1.446(8) Å is nearly identical to that reported for $[\text{Tp}^{\text{iPr}_2}]\text{Ni}(\text{OO}t\text{Bu})$ (1.440(7) Å) and unambiguously places the molecule in the peroxo regime. Both the O(2)–O(1)–Ni(1) bond angle of 105.2(4)° and the Ni–O_{distal} distance of 2.648(10) Å are larger than in the smaller, Tp^{iPr_2} supported system, 96.2(4)° and 2.467(7) Å, respectively.

While $[\text{Tp}^{\text{tBu,Me}}]\text{Ni}(\text{OO}t\text{Bu})$ is stable indefinitely at room temperature, thermal decomposition occurs upon heating in solution at 60° C. Thermolysis was studied via ^1H NMR spectroscopy, Figure 5.27. It is a reflection of the additional stability imparted by the *tert*-butyl groups that while $[\text{Tp}^{\text{iPr}_2}]\text{Ni}(\text{OO}t\text{Bu})$ is unstable at ambient temperature, $[\text{Tp}^{\text{tBu,Me}}]\text{Ni}(\text{OO}t\text{Bu})$ in C_6D_6 was still not fully decomposed even after heating for 48 hours at 60° C. Decomposition was accelerated by increasing the temperature to 80° C. The nickel products were determined to be $[\text{Tp}^{\text{tBu,Me}}]\text{Ni}(\text{OH})$ and metallacycle, forming in a 5:2 ratio, respectively. If one assumes that the decomposition occurs via a mechanism similar to that postulated for the hydroperoxo

complex, $[\text{Tp}^{\text{tBu,Me}}]\text{Ni}(\text{OOH})$, the process likely begins with homolytic scission of the O–O bond generating an oxonickel intermediate and *tert*-butoxy radical, Figure 5.24. The difference in the product distribution between the decomposition of $[\text{Tp}^{\text{tBu,Me}}]\text{Ni}(\text{OOtBu})$ and $[\text{Tp}^{\text{tBu,Me}}]\text{Ni}(\text{OOH})$ may be due to the *tert*-butoxy radical being a less potent oxidant (O–H BDE of *tert*-butanol and H_2O : 105 kcal/mol and 119 kcal/mol, respectively),^{94,95} and hence less likely to abstract a H-atom from the ligand than hydroxyl radical.

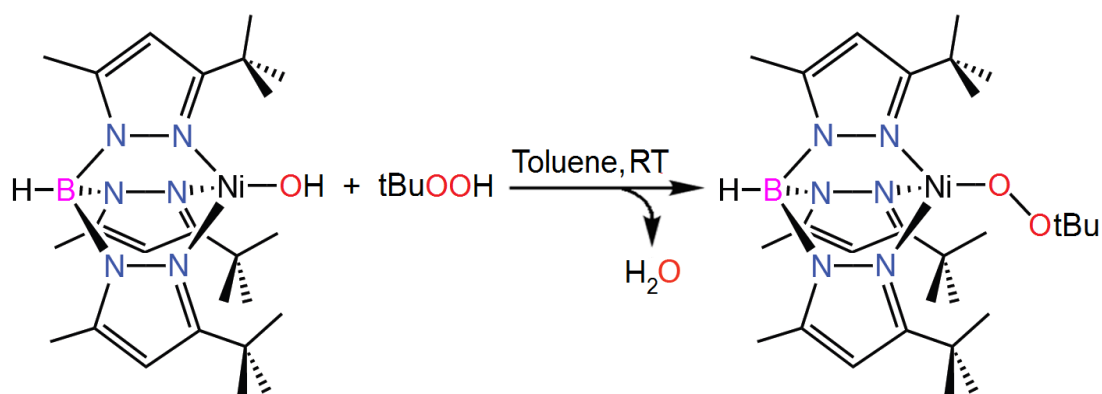


Figure 5.23 Preparation of $[\text{Tp}^{\text{tBu,Me}}]\text{Ni}(\text{OOtBu})$.

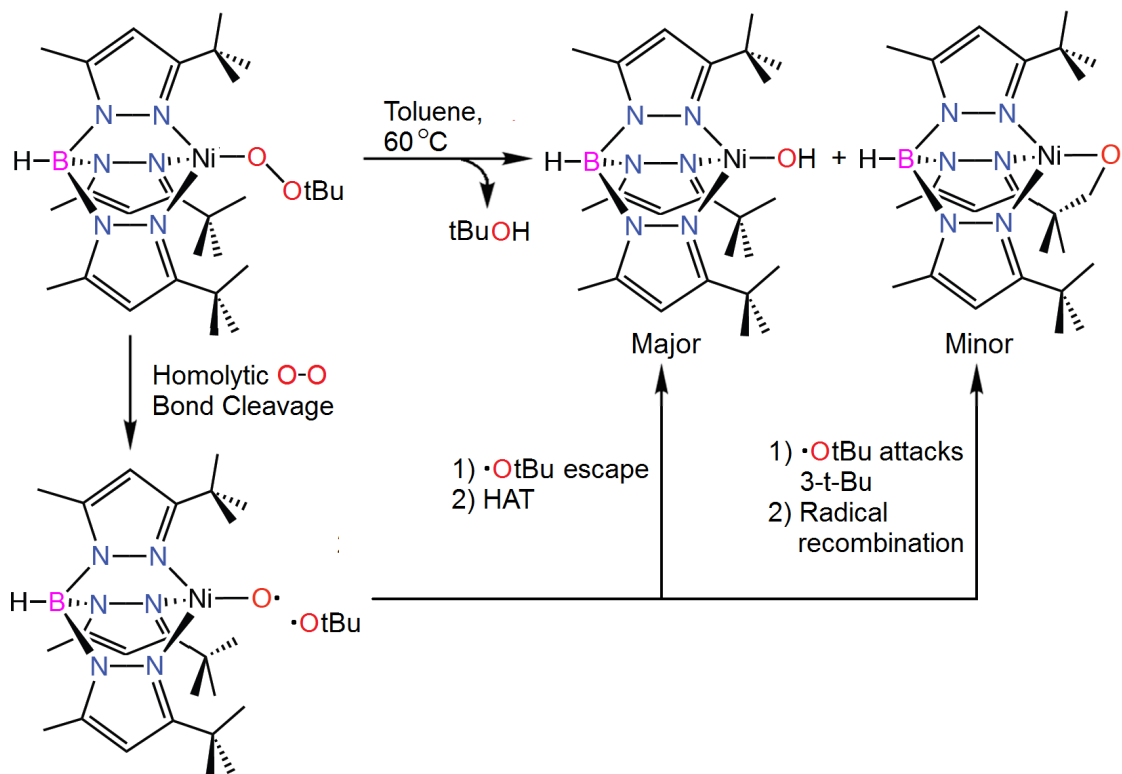


Figure 5.24 Mechanism for the thermal decomposition of $\text{Tp}^{\text{tBu,Me}}\text{Ni}(\text{OOtBu})$.

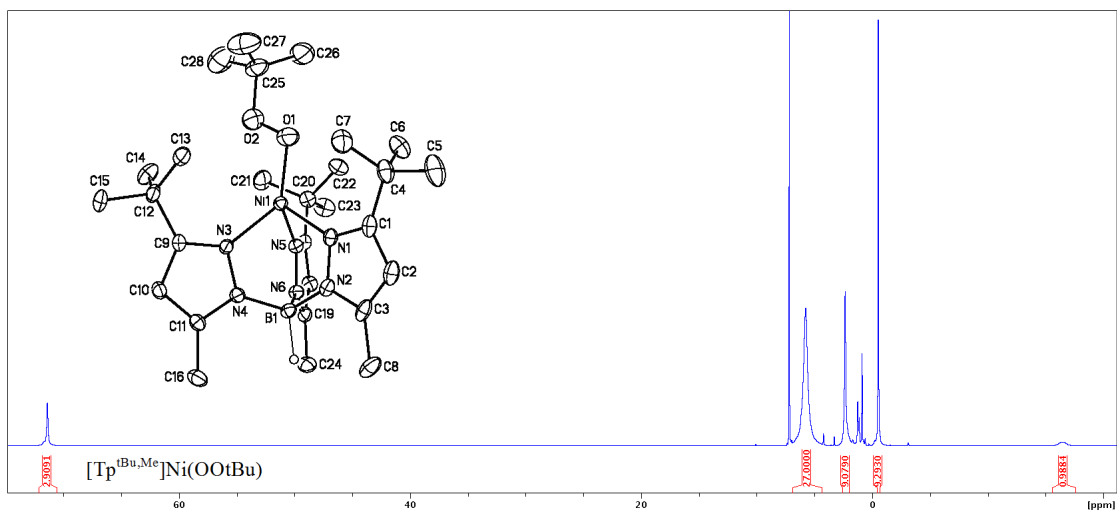


Figure 5.25 ^1H NMR spectrum of $[\text{Tp}^{\text{tBu,Me}}]\text{Ni}(\text{OOtBu})$. Crystal structure is inset for reference.

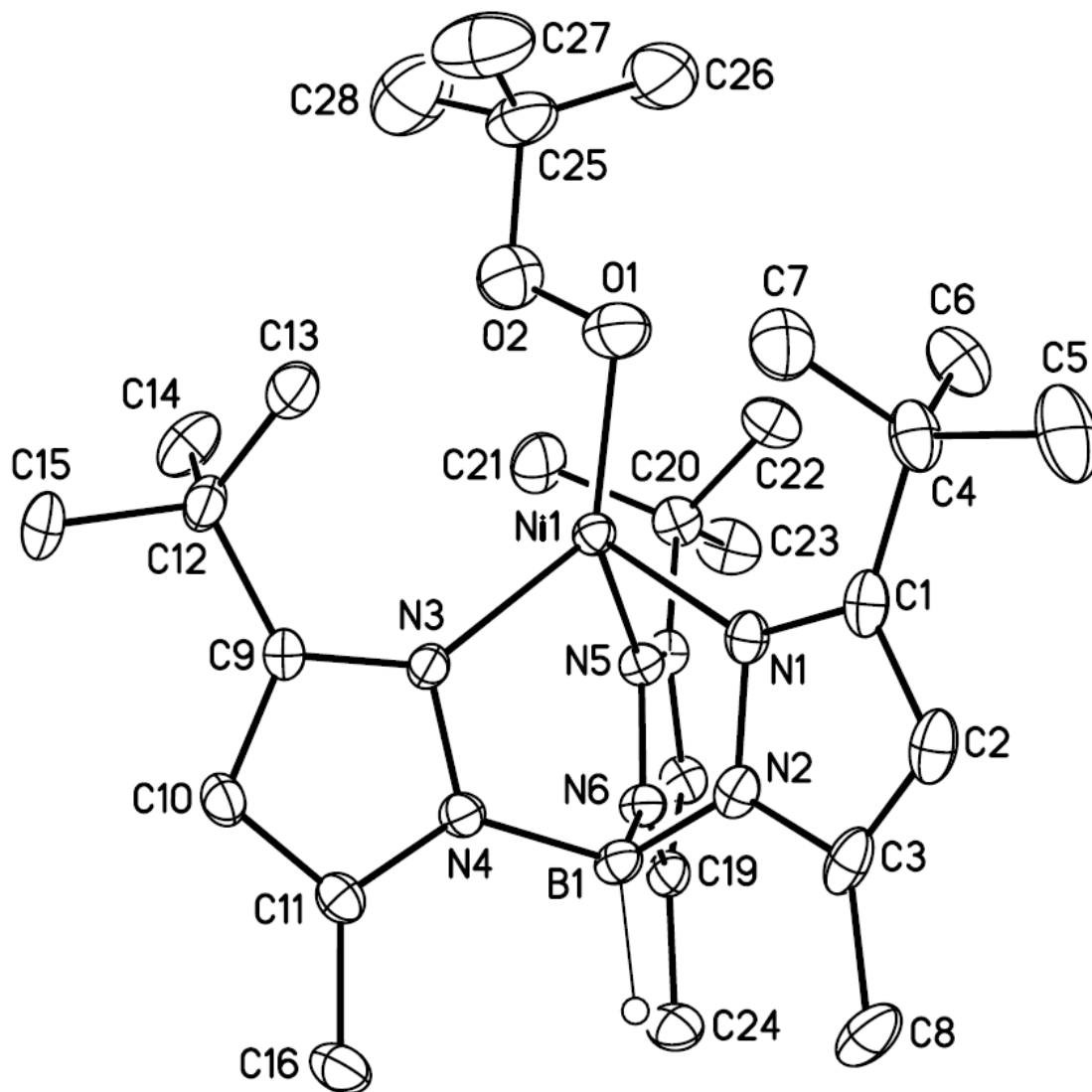


Figure 5.26 Thermal ellipsoid diagram of $[\text{Tp}^{\text{tBu,Me}}]\text{Ni}(\text{OOtBu})$ with atom labeling. Thermal ellipsoids are drawn to 30% probability. Hydrogen atoms are omitted for clarity with the exception of B–H.

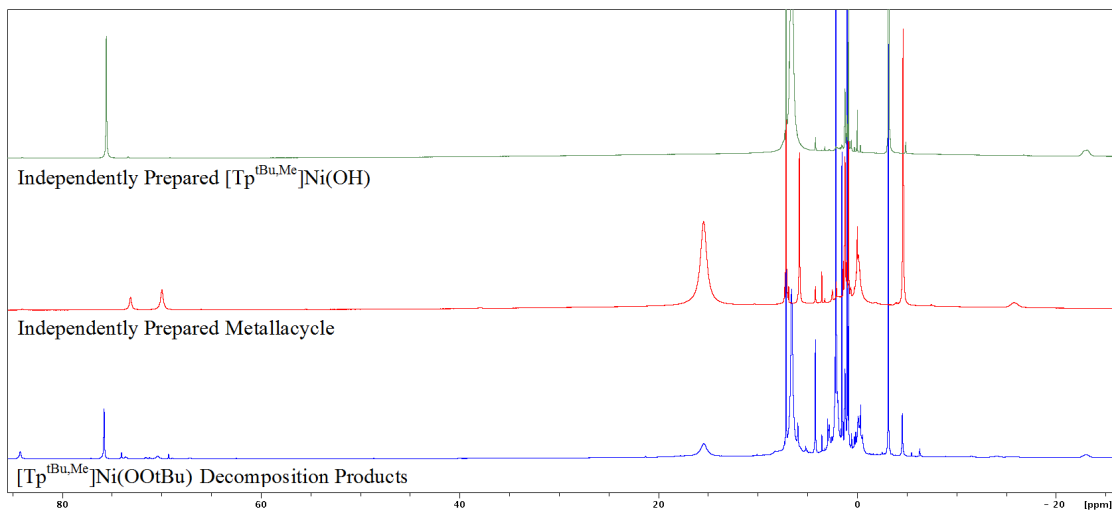


Figure 5.27 ¹H NMR spectral analysis of the thermal decomposition of [Tp^{tBu,Me}]Ni(OOtBu) with comparison to independently prepared products.

5.3.4 Reaction of [Tp^{tBu,Me}]NiO₂ with DHA

With a C–H BDE of 78 kcal/mol⁹⁶, 9,10-dihydroanthracene (DHA) is in many ways a larger analog of 1,4-cyclohexadiene, with a slightly stronger C–H bond. As with its smaller analog, C–H activation of this molecule has been explored with a variety of transition metal complexes.^{97,98,99} The driving force to form the fully aromatic anthracene is akin to the transition from CHD to benzene. These characteristics, along with its greater steric demands, made DHA an interesting target for C–H activation by [Tp^{tBu,Me}]Ni(O₂). Surprisingly, the reaction of DHA with [Tp^{tBu,Me}]Ni(O₂) resulted in an unanticipated oxidation to 9,10-anthraquinone without formation of anthracene.

To a stock solution of DHA and hexamethylbenzene (internal standard) in benzene was added two equivalents of [Tp^{tBu,Me}]Ni(O₂). The reaction mixture was stirred at room temperature until all [Tp^{tBu,Me}]Ni(O₂) was dissolved. Unlike the

reaction with CHD, the stoichiometric reaction between DHA and $[\text{Tp}^{\text{tBu,Me}}]\text{Ni}(\text{O}_2)$ is exceedingly slow at room temperature, requiring weeks to completely consume the $[\text{Tp}^{\text{tBu,Me}}]\text{Ni}(\text{O}_2)$. Therefore, with DHA, the initial ^1H NMR spectral measurement can be performed well after all reactants have been mixed, whereas with CHD, the measurement must be made prior to the addition of $[\text{Tp}^{\text{tBu,Me}}]\text{Ni}(\text{O}_2)$ due to the non-negligible progression of that reaction at room temperature. Following the initial ^1H NMR spectral analysis, the reaction solution was heated to 40 °C for 72 hours, during which time a color change from red-brown to red-orange was observed. After the initial heating, the temperature was increased to 60 °C for 48 hours to drive the reaction to completion. Following the second heating period, an aliquot was removed from the reaction solution and its proton spectrum compared with that of the initial, unheated solution. This reaction was repeated with $[\text{Tp}^{\text{tBu,Me}}]\text{Ni}(\text{O}_2)$:DHA ratios of 4:1 and 6:1.

Instead of the expected anthracene, the spectral comparison revealed the organic product to be 9,10-anthraquinone in addition to significant amounts of unreacted DHA. These results were confirmed by ^1H NMR spectral comparison to authentic materials, Figure 5.28. ^1H NMR spectral analysis also indicated full consumption of the $[\text{Tp}^{\text{tBu,Me}}]\text{Ni}(\text{O}_2)$ starting material and the formation of two nickel-containing products, $[\text{Tp}^{\text{tBu,Me}}]\text{Ni}(\text{OH})$ and the metallacycle, Figure 5.29. In contrast to reactions with CHD, where the product distribution was heavily weighted toward the metallacycle, in this case the reaction produced approximately equal amounts of the two nickel species. The low conversion of DHA to anthraquinone led to the reaction being run at higher $[\text{Tp}^{\text{tBu,Me}}]\text{Ni}(\text{O}_2)$:DHA ratios, 4:1, and 6:1, with the reaction optimizing at the 4:1 stoichiometry. The average organic product yields resulting from

all experimental runs are contained in Table 5.1. Though the yield of anthraquinone increases with greater amounts of $[\text{Tp}^{\text{tBu,Me}}]\text{Ni}(\text{O}_2)$, the nickel product distribution remains essentially unchanged with average yields of 46% $[\text{Tp}^{\text{tBu,Me}}]\text{Ni}(\text{OH})$ and 47% metallacycle at the optimal stoichiometry.

Table 5.1 DHA yield versus reaction stoichiometry.[#]

Ratio of $[\text{Tp}^{\text{tBu,Me}}]\text{Ni}(\text{O}_2)$ to DHA	Yield of AQ (%)	Amount of $[\text{Tp}^{\text{tBu,Me}}]\text{Ni}(\text{O}_2)$ Remaining After Reaction (%)
2	43	0
4	75	0
6	95	22

[#]Average of triplicate runs.

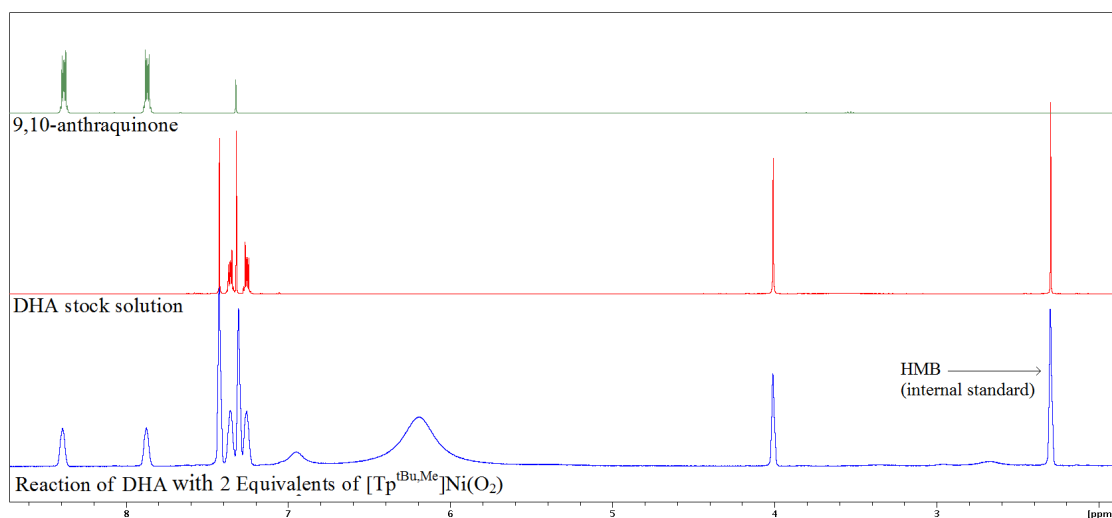


Figure 5.28 ^1H NMR spectral analysis of organic products in the reaction of DHA with 2 equivalents of $[\text{Tp}^{\text{tBu,Me}}]\text{Ni}(\text{O}_2)$.

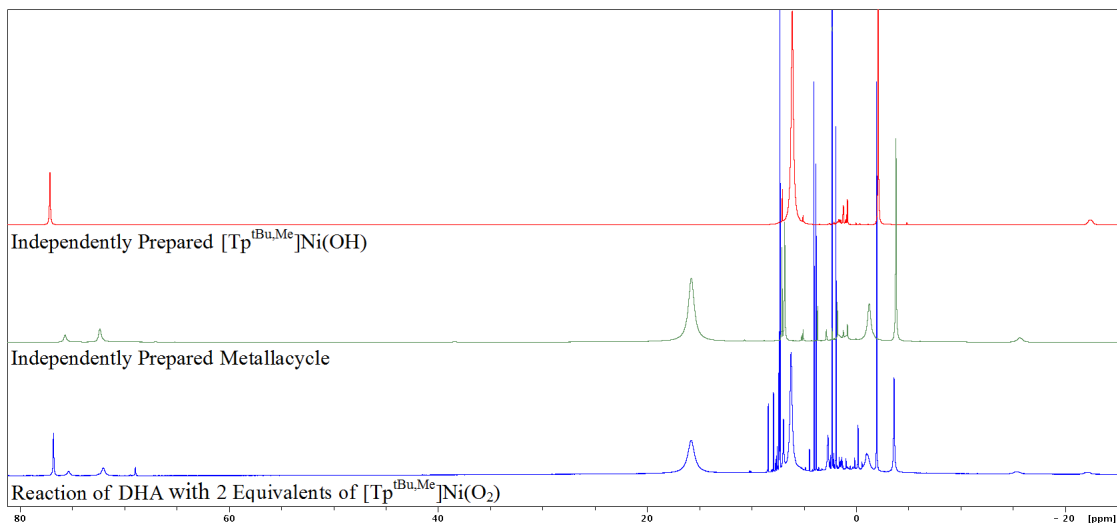


Figure 5.29 ^1H NMR spectral analysis of nickel products in the reaction of DHA with 2 equivalents of $[\text{Tp}^{\text{tBu,Me}}]\text{Ni}(\text{O}_2)$.

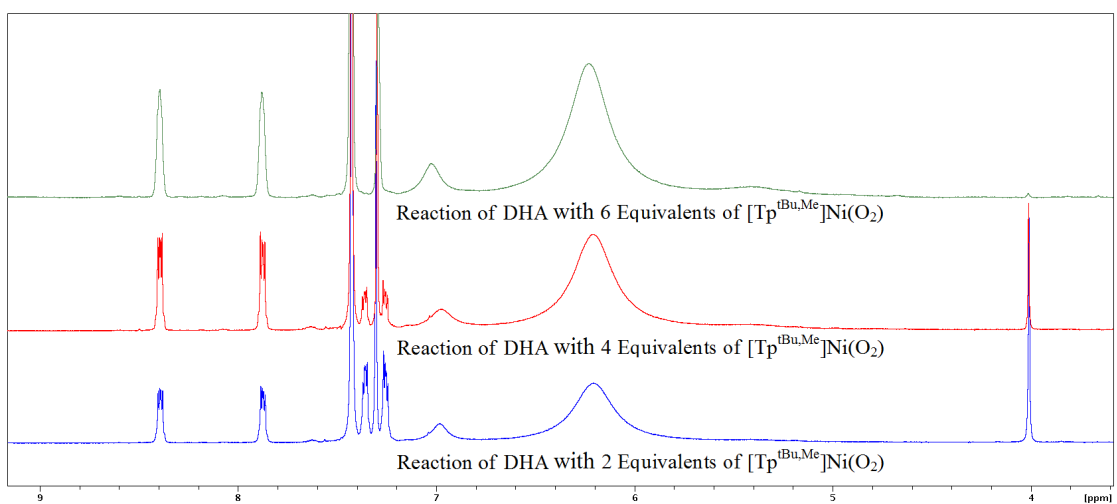


Figure 5.30 ^1H NMR spectral comparison of organic products in the reaction of DHA with 2, 4 and 6 equivalents of $[\text{Tp}^{\text{tBu,Me}}]\text{Ni}(\text{O}_2)$.

5.3.4.1 Mechanistic Insights into the Reaction of $[\text{Tp}^{\text{tBu,Me}}]\text{NiO}_2$ with DHA

The conversion of DHA to 9,10-anthraquinone, while not common, has been observed for certain transition metal complexes.¹⁰⁰⁻¹⁰¹⁻¹⁰² The bulk of these

transformations, however, are promoted by high potential oxometal complexes. To the best of the author's knowledge, no precedent exists for the facilitation of this transformation by a nickel complex, nor by any transition metal complex possessing a superoxide ligand. This result is therefore quite interesting as it represents a rare example of an Earth abundant, first row transition metal species affecting this conversion. This, in turn, makes the mechanistic interrogation of this reaction an inquiry of significance.

As the C–H activation of DHA was the original goal of this experiment, it seems reasonable to invoke H-atom abstraction as the initial step in the pathway leading to anthraquinone production. By analogy to the mechanism of CHD activation by $[\text{Tp}^{\text{tBu,Me}}]\text{Ni}(\text{O}_2)$, this initial abstraction generates a radical on the DHA substrate as well as a hydroperoxonickel intermediate, the latter of which is unstable under the reaction conditions, *vide supra*. If decomposition of the hydroperoxo species occurs via homolytic cleavage of the O–O bond, the resulting hydroxyl radical can undergo rebound to the activated substrate to incorporate the first of two oxygen atoms, Figure 5.31. The remaining oxonickel fragment abstracts a second H-atom from the oxidized substrate generating the hydroxide complex. A second equivalent of $[\text{Tp}^{\text{tBu,Me}}]\text{Ni}(\text{O}_2)$ then removes the last remaining H-atom on the activated side of the substrate to generate anthrone and another equivalent of the hydroperoxonickel complex. Without a viable site for hydroxyl radical rebound, this newly generated hydroperoxo complex decomposes to the metallacycle via the previously described route. A further two equivalents of $[\text{Tp}^{\text{tBu,Me}}]\text{Ni}(\text{O}_2)$ complete the conversion to anthraquinone by effecting an identical series of reactions on the opposite side of the substrate. The proposed mechanism accounts for the observed optimal stoichiometry of 4:1,

$[\text{Tp}^{\text{tBu,Me}}]\text{Ni}(\text{O}_2):\text{DHA}$, as well as the formation of virtually equal amounts of the metallacycle and hydroxonickel complexes.

No trace of the likely organic intermediates, i.e. anthrone or its alcohol precursor, etc., was detected in the ^1H NMR spectra of the reaction mixtures. This was the case even at the lowest stoichiometry (2:1, $[\text{Tp}^{\text{tBu,Me}}]\text{Ni}(\text{O}_2):\text{DHA}$), where more than half of the DHA remained unreacted. If the aforementioned mechanistic scheme is operable, this suggests that the initial hydrogen atom abstraction from DHA is rate limiting. To test this, the hydroquinone compound 9,10-dihydroxy-9,10-dihydroanthracene was prepared as a substrate for reaction with $[\text{Tp}^{\text{tBu,Me}}]\text{Ni}(\text{O}_2)$. This species was used as an analog for the mono-alcohol, 9-hydroxy-10-dihydroanthracene, proposed as an intermediate in the transformation to anthraquinone. Via the above rationale, one might expect this reaction to proceed faster, and under more mild condition than that observed in the case of DHA to AQ conversion. Indeed, reaction of $[\text{Tp}^{\text{tBu,Me}}]\text{Ni}(\text{O}_2)$ with the hydroquinone is efficient at room temperature with the 2:1 stoichiometry running to completion in less than 24 hr. As anticipated, the sole organic product of the reaction is anthraquinone, generated in a yield of 48%, Figure 5.32. Perhaps more significantly, the nickel product of the reaction is almost exclusively the metallacycle with a trace of hydroxo complex (~2%), Figure 5.33. This, too is in accord with the proposed DHA to AQ conversion mechanism, where the oxidation of the alcohol to the ketone is the step responsible for the production of metallacycle. Lastly, the yield of this reaction at the $2[\text{Tp}^{\text{tBu,Me}}]\text{Ni}(\text{O}_2):\text{DHA}$ stoichiometry, which consistently approaches but never exceeds 50%, suggests that four equivalents of $[\text{Tp}^{\text{tBu,Me}}]\text{Ni}(\text{O}_2)$ rather than two is the optimal stoichiometry. At first glance, this last observation would seem to contradict the empirical evidence suggesting a 4:1

optimization in the case of reactions of $[\text{Tp}^{\text{tBu,Me}}]\text{Ni}(\text{O}_2)$ with DHA, instead suggesting a 6:1 ratio should be optimum. However, this apparent discrepancy can be reconciled if one considers the source of the H-atom abstracted by the proposed oxonickel intermediate (*vide supra*). If this species (presumably produced as a result of the O–O bond scission in the hydroperoxo intermediate, following the initial C–H activation of DHA) abstracts a second H-atom (adjacent to the newly installed hydroxyl group) post rebound, then only one additional equivalent of $[\text{Tp}^{\text{tBu,Me}}]\text{Ni}(\text{O}_2)$ is required to oxidize to the ketone. On the other hand, if the oxonickel intermediate removes a H atom from *anywhere* else, then two equivalents of $[\text{Tp}^{\text{tBu,Me}}]\text{Ni}(\text{O}_2)$ would be necessary to fully oxidize *each* O-H functional group. The latter scenario also fits the nature of the independent reaction between $[\text{Tp}^{\text{tBu,Me}}]\text{Ni}(\text{O}_2)$ and 9,10-dihydroxy-9,10-dihydroanthracene, Figure 5.34, where two H atoms must be removed from each side of the substrate to effect conversion to anthraquinone (hence the discrepancy in the apparent optimal stoichiometry between the two experiments). Of course, a species as reactive as the proposed oxonickel cannot be expected to remove an H atom from the post rebound substrate with perfect fidelity. Thus, where the yield of AQ from the reaction of 9,10-dihydroxy-9,10-dihydroanthracene with $[\text{Tp}^{\text{tBu,Me}}]\text{Ni}(\text{O}_2)$ is nearly quantitative, the yield of AQ derived from DHA is significantly lower (75% at the optimal stoichiometry).

The reactions of $[\text{Tp}^{\text{tBu,Me}}]\text{Ni}(\text{O}_2)$ with DHA and CHD, respectively, lead to distinctly different outcomes, both in the manner of substrate oxidation as well as in the ratio of the derivative nickel complexes. The significant divergence in the nature of substrate reactivity (despite very similar bond dissociation enthalpies) poses a number of interesting questions. Perhaps the most significant of these is why hydroxyl

rebound occurs in DHA but not in CHD. While the scope of the present work does not provide a definitive answer to this question, a reasonable potential explanation lies in the relative stability of the organic, radical intermediates generated immediately after initial hydrogen atom abstraction by $[\text{Tp}^{\text{tBu,Me}}]\text{Ni}(\text{O}_2)$. The thermodynamic drive toward aromatization is greater for CHD than for DHA. This is indicated by the slightly lower BDE of the former, as well as by the higher resonance stabilization energy of its aromatized derivative, benzene (on a per ring basis).¹⁰³ In addition, the stability of the radical generated by H-atom abstraction is greater for DHA than for CHD, due to the larger number of resonance structures available in the former.^{104,105} While the lifetime of these radicals under the present reaction conditions is unknown, the aforementioned considerations suggest that the radical intermediate derived from DHA will persist longer than that derived from CHD. If true, this would provide a greater temporal window for rebound in the case of DHA. Given that the decomposition of the putative hydroperoxo nickel derivative is not instantaneous (*vide supra*), it is entirely possible that the cyclohexadienyl radical decomposes before a hydroxyl radical is available for rebound. Such a scenario would simultaneously explain why no O-atom addition products were detected in the oxidation of CHD, as well as why the nickel product distribution so heavily favors metallacycle over hydroxo in that reaction.

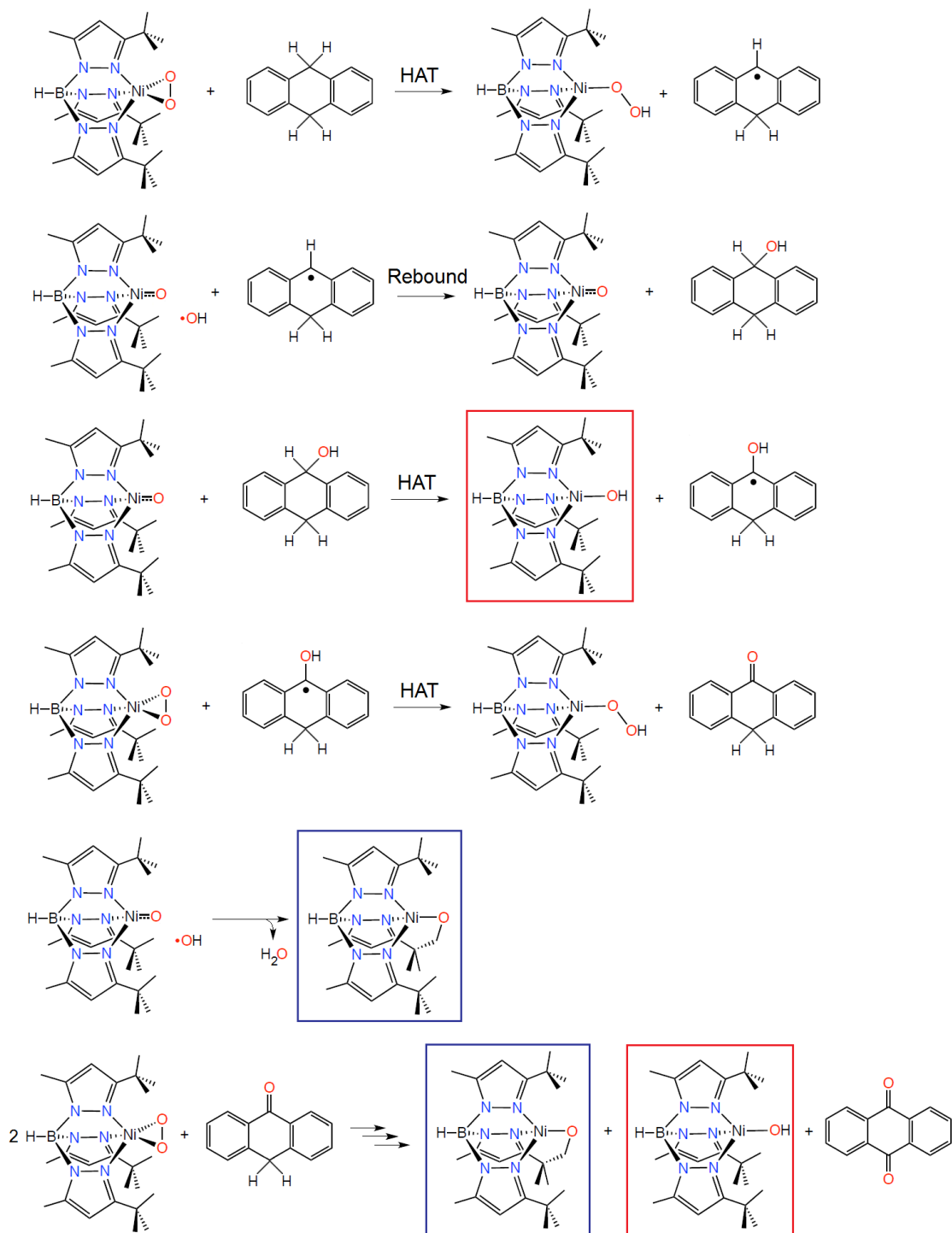


Figure 5.31 Proposed mechanism for the formation of 9,10-anthraquinone in the reaction of [Tp^{tBu,Me}]Ni(O₂) with 9,10-dihydroanthracene.

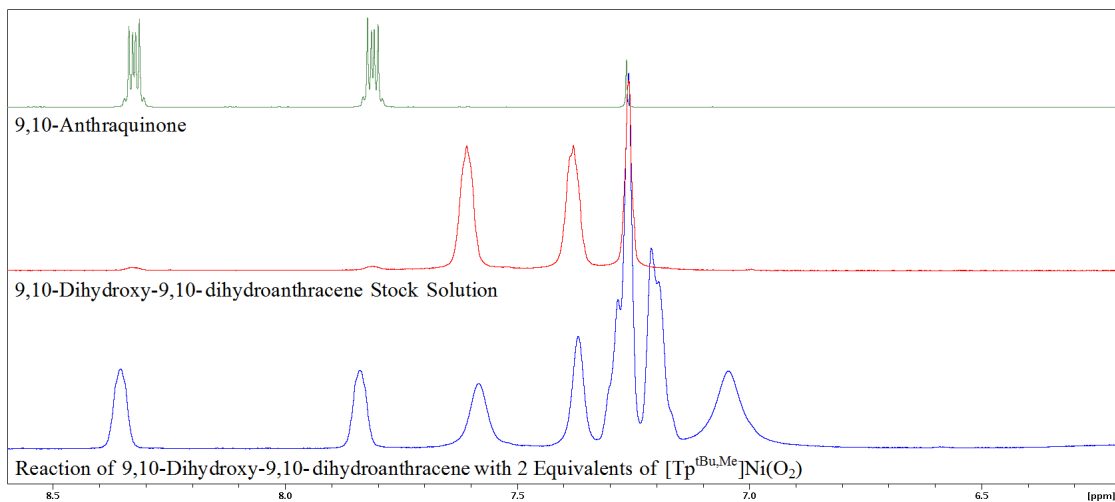


Figure 5.32 ^1H NMR spectral analysis of organic products in the reaction of 9,10-dihydroxy-9,10-dihydroanthracene with 2 equivalents of $[\text{Tp}^{\text{tBu,Me}}]\text{Ni}(\text{O}_2)$.

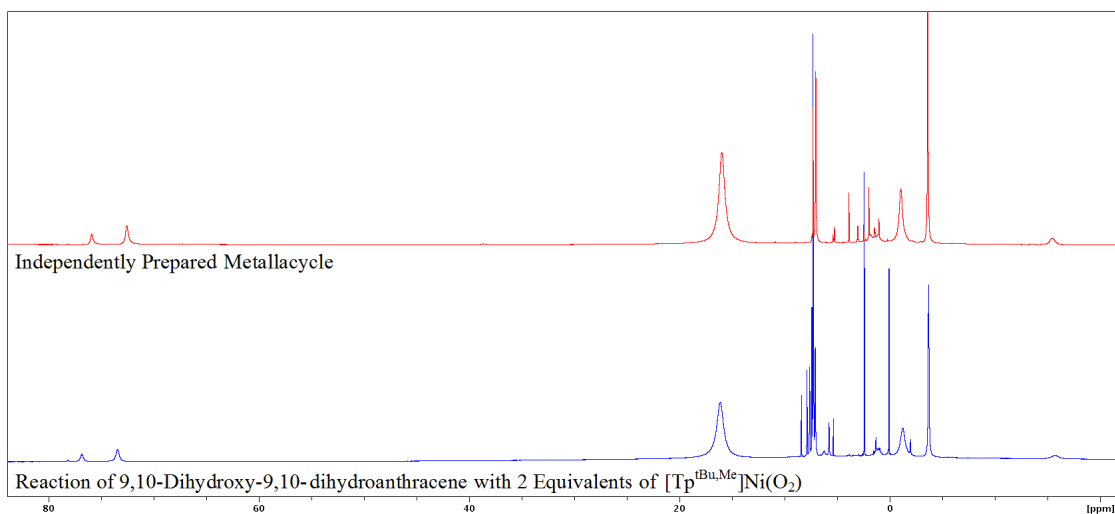


Figure 5.33 ^1H NMR spectral analysis of nickel products in the reaction of 9,10-dihydroanthracene with 2 equivalents of $[\text{Tp}^{\text{tBu,Me}}]\text{Ni}(\text{O}_2)$.

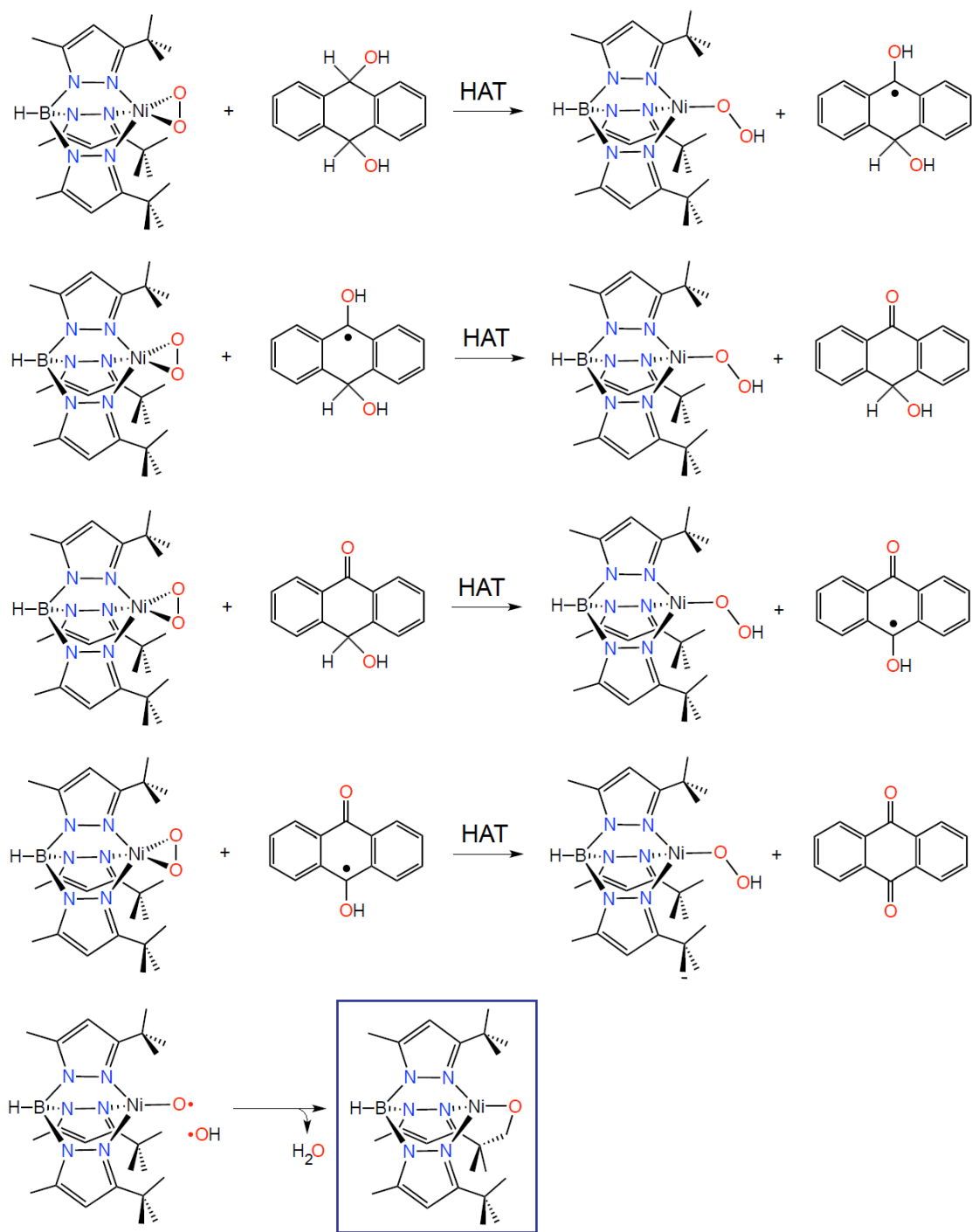


Figure 5.34 Proposed mechanism for the reaction of $[\text{Tp}^{\text{tBu,Me}}]\text{Ni}(\text{O}_2)$ with 9,10-dihydroxy-9,10-dihydroanthracene.

5.3.4.2 Kinetic Study of the Reaction of $[\text{Tp}^{\text{tBu,Me}}\text{Ni}(\text{O}_2)]$ with DHA

Given the complex and fascinating nature of the $[\text{Tp}^{\text{tBu,Me}}\text{Ni}(\text{O}_2)]/\text{DHA}$ reaction, a kinetic analysis seemed a prudent endeavor to shed light on the mechanism. This course of study was further encouraged by our failure to detect postulated organic intermediates, leading to the suspicion that the initial C–H bond activation is rate limiting (*vide supra*). If this is indeed the case, a significant primary hydrogen kinetic isotope effect (KIE) would be anticipated upon deuterium substitution at the 9 and 10 positions of DHA. A hydrogen/deuterium KIE can be derived by determining the ratio of the rate constants of the proteo substrate and its deuterium isotopomer ($k_{\text{H}}/k_{\text{D}}$) upon reaction with $[\text{Tp}^{\text{tBu,Me}}\text{Ni}(\text{O}_2)]$. Primary hydrogen/deuterium KIEs have a value significantly greater than 1 and are indicative of a bond to the labeled hydrogen being formed or broken in the rate-determining step of the reaction.¹⁰⁶ An evaluation of the KIE in the present case would therefore prove beneficial in providing evidence in support of the proposed mechanism.

The data for the kinetic analysis was obtained by tracking the decrease of the optical absorbance features of $[\text{Tp}^{\text{tBu,Me}}\text{Ni}(\text{O}_2)]$ at 505 nm under pseudo-first order conditions, Figure 5.35. In each kinetic run, DHA (or its deuterated isotopomer, d4-DHA) was present in at least 20-fold excess. Observed pseudo-first order rate constants (k_{obs} , s^{-1}) were determined via the initial rate method by plotting absorbance vs. time for the first 10% of the reaction using various concentrations of DHA. All kinetic runs exhibited pseudo first-order behavior with the values of k_{obs} varying linearly with DHA concentration. This result is indicative of a second order rate law ($\text{rate} = k[[\text{Tp}^{\text{tBu,Me}}\text{Ni}(\text{O}_2)][\text{DHA}]$).⁹⁷ The second order rate constant for the reaction with DHA was determined to be $2.2 \times 10^{-3} (1) \text{ M}^{-1} \text{ s}^{-1}$ and was derived from the slope/4

of the plot of k_{obs} vs [DHA], Figure 5.36. The factor of 4 is necessary to account for 4 reactive C–H bonds in each DHA molecule.

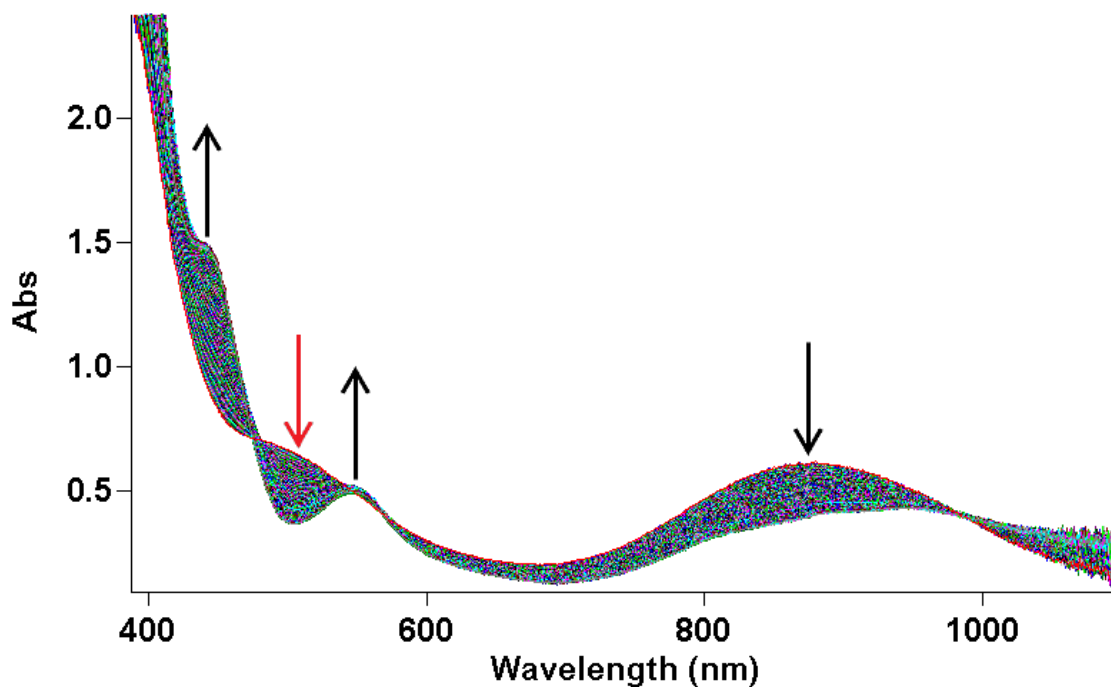


Figure 5.35 Example of a typical kinetic run. Arrows indicate major absorbance changes. Red arrow indicates change at 505 nm which was the wavelength chosen for analysis in the kinetic study. Conditions in this run: $[\text{Tp}^{\text{tBu,Me}}]\text{Ni}(\text{O}_2)$ at 2 mg/mL in toluene, 40 equivalents of DHA (156 mM), 45 °C.

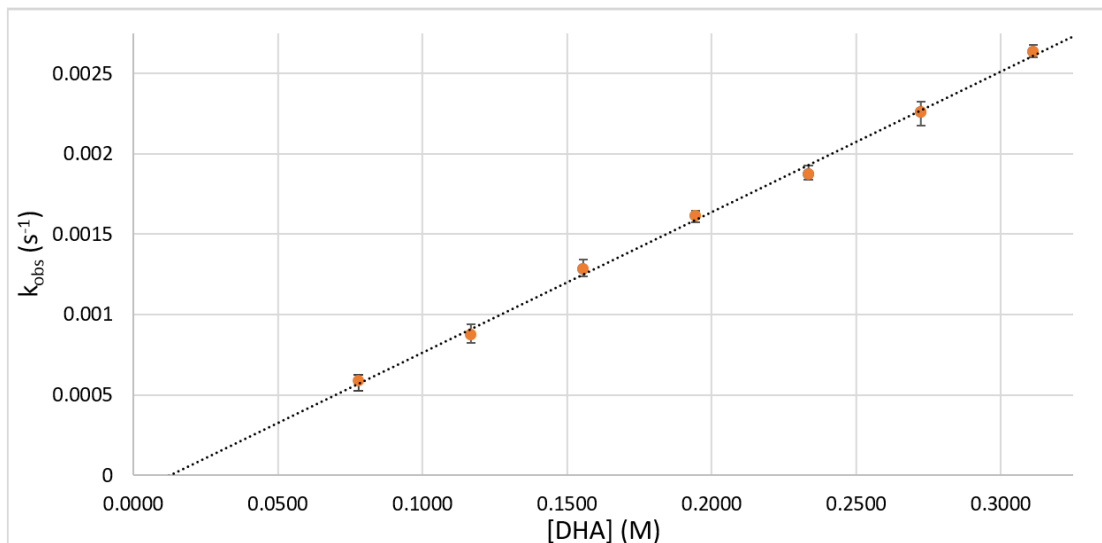


Figure 5.36 Plot of k_{obs} vs [DHA] at 60 °C for the reaction of $[\text{Tp}^{\text{tBu,Me}}\text{Ni}(\text{O}_2)]$ with DHA. DHA concentration was varied from 20 to 80 equivalents (78 – 311 mM) in 10 equivalent increments. The second order rate constant was derived from slope of the linear, least-squares fit of the data as indicated by the trend line. Data points shown are the average of triplicate kinetic runs. Error bars show the range of values obtained at each concentration.

In addition to examining the rate law, the temperature dependence of the rate constant was also investigated to determine the activation parameters associated the reaction. This was accomplished via an Eyring analysis, i.e. plotting $\ln(k/T)$ against $1/T$ over a 40 K temperature range. The plotted kinetic data displayed a linear relationship from which the activation parameters were extracted, Figure 5.37. The linear, least-squares fit of an Eyring plot affords a straight line with slope = $-\Delta H^\ddagger/R$ and an intercept = $\ln(k_B/h) + \Delta S^\ddagger/R$ where ΔH^\ddagger is the enthalpy of activation, ΔS^\ddagger is the entropy of activation, R is the molar gas constant, k_B is the Boltzman constant and h is Planck's constant.¹⁰⁷ The values of ΔH^\ddagger and ΔS^\ddagger were calculated using this relationship and are reported in Table 5.2.

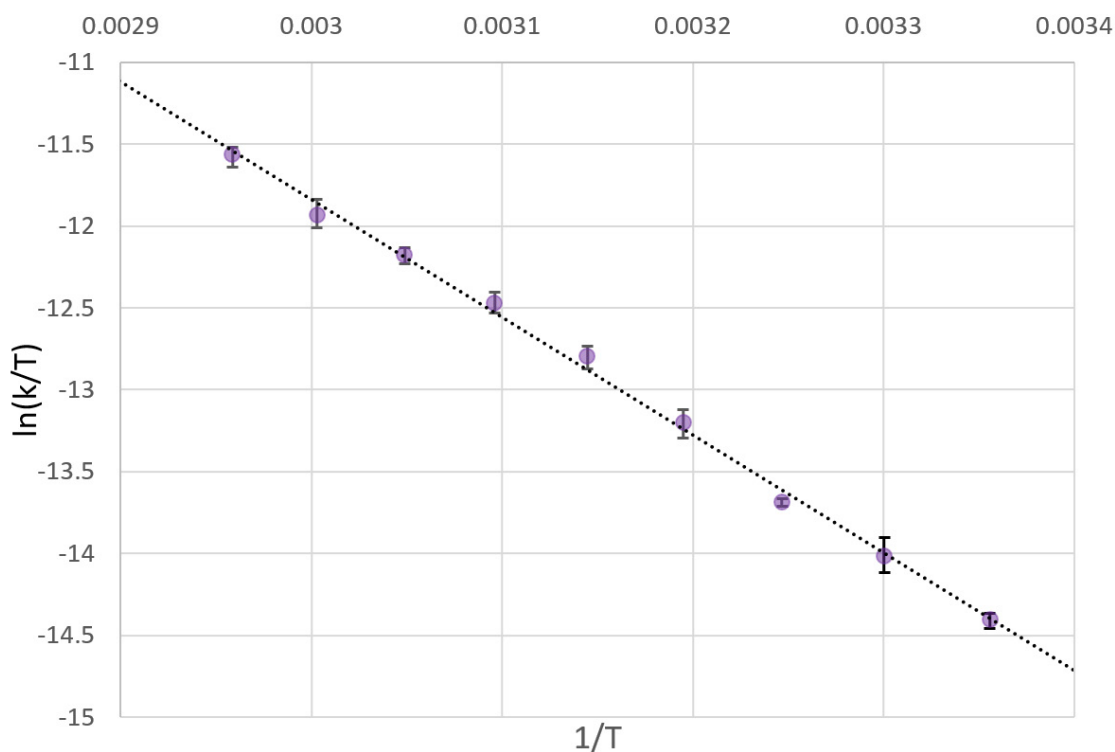


Figure 5.37 Eyring plot of $\ln(k/T)$ vs. $1/T$ for the reaction of $[\text{Tp}^{\text{tBu,Me}}]\text{Ni}(\text{O}_2)$ with DHA. All kinetics runs were conducted with an initial DHA concentration of 156 mM. Temperature was varied from 25 to 65 °C in 5 °C increments. Activation parameters, ΔH^\ddagger and ΔS^\ddagger , were derived from the slope and intercept, respectively, of the linear, least-squares fit of the data as indicated by the trend line. Data points shown are the average of triplicate kinetic runs. Error bars show the range of values obtained at each temperature.

Table 5.2 2nd order rate constant, kinetic isotope effect and Eyring parameters from the reaction of $[\text{Tp}^{\text{tBu,Me}}]\text{Ni}(\text{O}_2)$ with DHA

2 nd order rate constant (k , $\text{M}^{-1}\text{s}^{-1}$) ^a	KIE ($k_{\text{H}}/k_{\text{D}}$) ^a	Enthalpy of Activation (ΔH^\ddagger , kcal/mol) ^b	Entropy of Activation (ΔS^\ddagger , $\text{J mol}^{-1}\text{K}^{-1}$) ^b
$2.2 \times 10^{-3}(1)$	≥ 12	14(1)	-117(10)

^acalc. at 60 °C ^b calc. for range of $T = 25 - 65$ °C at 40 equiv. DHA (156 mM)

Unfortunately, due to what we presume to be competing side reactions, a full kinetic analysis of d4-DHA was not possible. However, comparison of the pseudo first-order rate constants obtained at 60 °C for both DHA and d4-DHA indicate a KIE value (k_H/k_D) of at least 12. A report by Karlin and coworkers investigating the reaction of the superoxo-copper complex, $[(\text{DMM-tmpa})\text{Cu}^{\text{II}}(\text{O}_2^{\cdot-})]^+$ (DMMtmpa = tris((4-methoxy-3,5-dimethylpyridin-2-yl)methyl)-amine), with *p*-OMe-DTBP revealed a KIE of 11.¹⁰⁸ The authors ascribe this value to a hydrogen atom transfer pathway. The fact that the substrate in that report, *p*-OMe-DTBP, has a BDE similar to that of DHA (79.6 vs 78 kcal/mol), increases the relevance to the present work. The KIE is also of similar magnitude to that reported by Bakac and coworkers in the oxidation of a water-soluble trisubstituted phenol by a chromium–superoxo complex.¹⁰⁹ That study also pointed to a hydrogen atom transfer event. A KIE of the magnitude found for the reaction of $[\text{Tp}^{\text{tBu,Me}}\text{Ni}(\text{O}_2)]$ with DHA is, therefore, consistent with C–H/C–D bond breaking in the transition state. This result strongly implicates initial H-atom abstraction from DHA as being rate limiting. This conclusion is in line with the second-order rate law and the observed Eyring parameters. An examination of potential quantum mechanical tunneling contributions to the rate determining step was beyond the scope of this study, however, the magnitude of the KIE leaves open the possibility that such contributions are a significant factor in the observed kinetic behavior. In order to strongly invoke tunneling in the present case, additional experimentation would be required in order to establish the temperature dependence of the KIE as well as the associated value for the Arrhenius prefactor ratio ($A_H:A_D$).

5.3.5 Reaction of $[\text{Tp}^{\text{tBu,Me}}]\text{Ni}(\text{O}_2)$ with Xanthene

To further probe the mechanism of DHA to AQ conversion promoted by $[\text{Tp}^{\text{tBu,Me}}]\text{Ni}(\text{O}_2)$, xanthene was examined as a substrate. Due to its similar structure to DHA and the relatively low bond dissociation energy of its target C–H bond (75.5 kcal/mol),¹¹⁰ xanthene essentially represents a half scale analog of DHA. Therefore, provided that its reactivity mirrors that of DHA, xanthene offers a chance to test the validity of the mechanistic inferences made in the former case.

The reaction of xanthene with $[\text{Tp}^{\text{tBu,Me}}]\text{Ni}(\text{O}_2)$ was conducted under similar conditions to those used for DHA. One equivalent of $[\text{Tp}^{\text{tBu,Me}}]\text{Ni}(\text{O}_2)$ was added to a stock solution of xanthene and hexamethylbenzene (internal standard) in benzene. The reaction mixture was stirred at room temperature until all $[\text{Tp}^{\text{tBu,Me}}]\text{Ni}(\text{O}_2)$ was dissolved. As with DHA, the reaction between xanthene and $[\text{Tp}^{\text{tBu,Me}}]\text{Ni}(\text{O}_2)$ is relatively slow at room temperature, which allowed for determination of the initial ratios of xanthene and $[\text{Tp}^{\text{tBu,Me}}]\text{Ni}(\text{O}_2)$ to the hexamethylbenzene internal standard via ^1H NMR spectral analysis. The reaction solution was then heated to 40 °C for 72 hours, during which time a color change from red-brown to red-orange was observed. After the heating period, a second aliquot was removed from the reaction solution for final ^1H NMR spectral acquisition. The reaction was repeated with $[\text{Tp}^{\text{tBu,Me}}]\text{Ni}(\text{O}_2)$:xanthene ratios of 2:1 and 3:1.

^1H NMR spectral analysis showed the organic product of the reaction to be xanthone accompanied by unreacted xanthene, Figure 5.38. The $[\text{Tp}^{\text{tBu,Me}}]\text{Ni}(\text{O}_2)$ was completely consumed with the nickel products consisting of a 1:1 mixture of $[\text{Tp}^{\text{tBu,Me}}]\text{Ni}(\text{OH})$ and the metallacycle, Figure 5.39. The reaction optimized at the 2:1 stoichiometry. The average organic product yields are contained in Table 5.2. As with AQ, the yield of xanthone increases with higher ratios of $[\text{Tp}^{\text{tBu,Me}}]\text{Ni}(\text{O}_2)$:xanthene,

whereas the nickel product distribution remains unchanged with yields of 44% $[\text{Tp}^{\text{tBu,Me}}]\text{Ni}(\text{OH})$ and 46% metallacycle at the optimal stoichiometry.

Table 5.3 Xanthone yield versus reaction stoichiometry.[#]

Ratio of $[\text{Tp}^{\text{tBu,Me}}]\text{NiO}_2$ to Xanthone	Yield of Xanthone (%)	Amount of $[\text{Tp}^{\text{tBu,Me}}]\text{NiO}_2$ Remaining After Reaction (%)
1	48	0
2	83	0
3	97	24

[#]Average of triplicate runs.

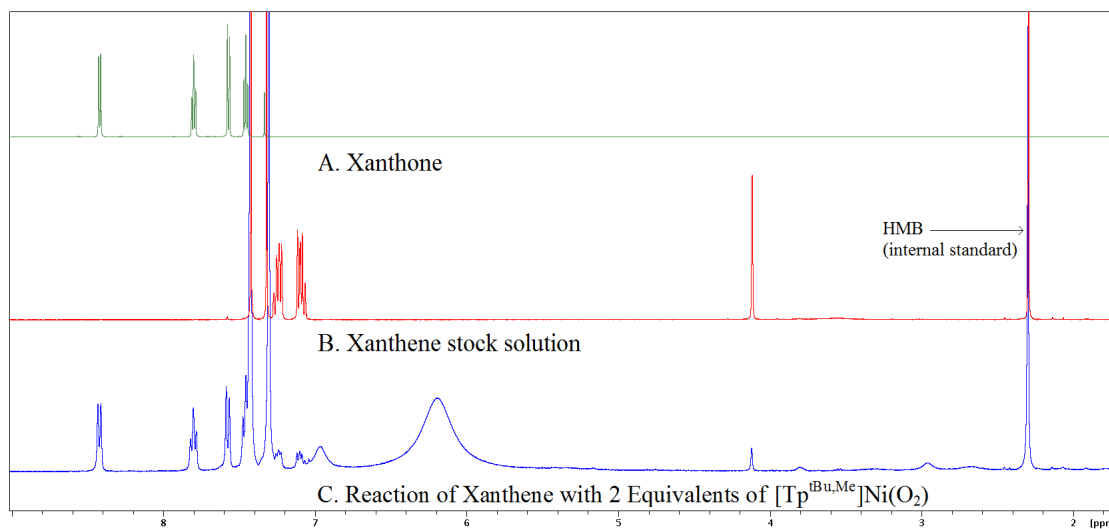


Figure 5.38 ¹H NMR spectral analysis of organic products in the reaction of xanthone with 2 equivalents of $[\text{Tp}^{\text{tBu,Me}}]\text{Ni}(\text{O}_2)$.

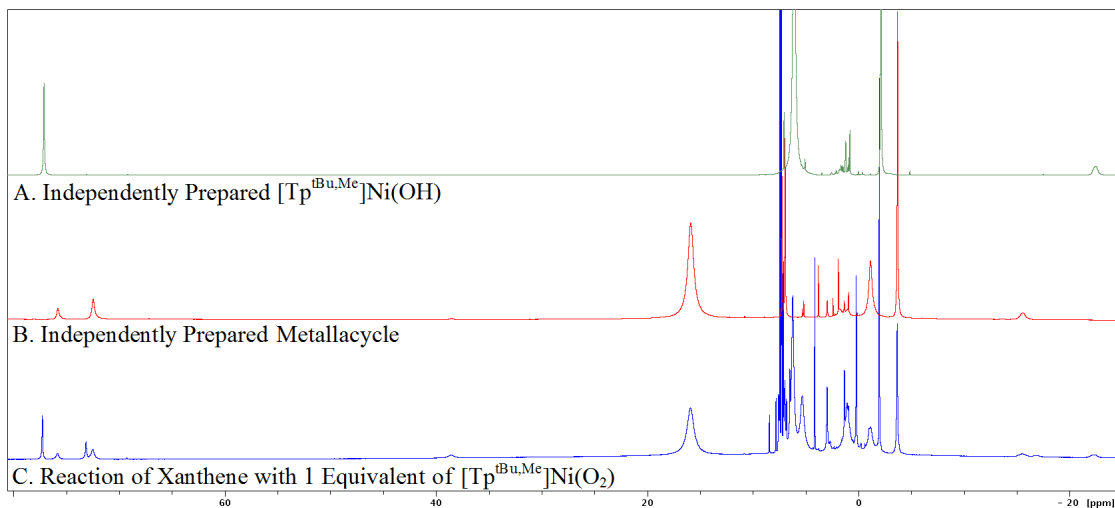


Figure 5.39 ^1H NMR spectral analysis of nickel products in the reaction of xanthene with 1 equivalent of $[\text{Tp}^{\text{tBu,Me}}]\text{Ni}(\text{O}_2)$.

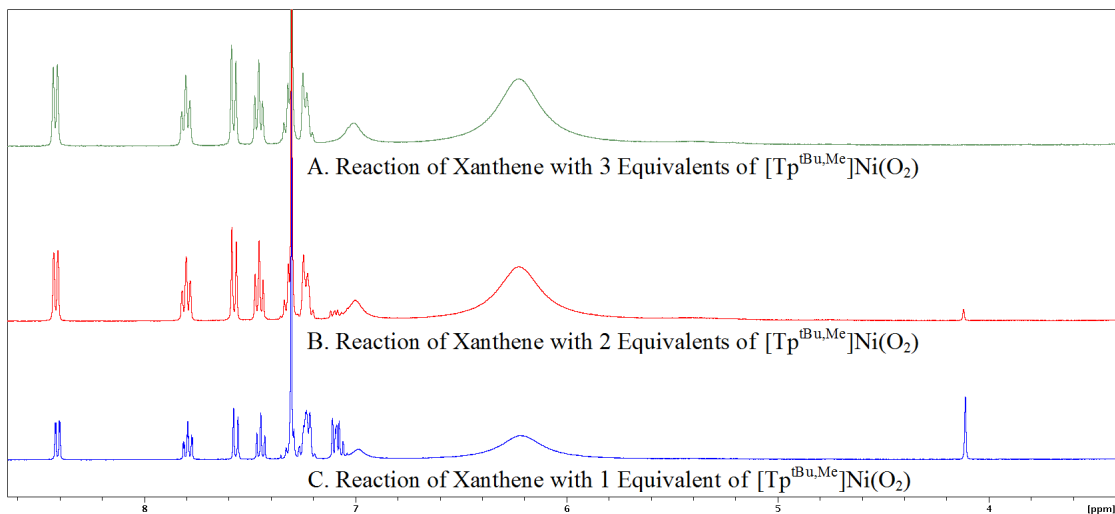


Figure 5.40 ^1H NMR spectral comparison of organic products in the reaction of xanthene with 1, 2 and 3 equivalents of $[\text{Tp}^{\text{tBu,Me}}]\text{Ni}(\text{O}_2)$.

5.3.5.1 Mechanistic Analysis and Comparisons to DHA

Given the similarities between DHA and xanthene, the most reasonable mechanism for the observed production of xanthone parallels that for production of

9,10-anthroquinone, Figure 5.43. An initial hydrogen atom abstraction by $[\text{Tp}^{\text{tBu,Me}}]\text{Ni}(\text{O}_2)$ results in the generation of the 9-xanthyl radical. The resulting nickel species, $[\text{Tp}^{\text{tBu,Me}}]\text{Ni}(\text{OOH})$, rapidly decomposes giving the oxonickel and hydroxyl radical. The latter species undergoes rebound with the organic radical forming 9-hydroxyxanthene, which is then attacked by the oxonickel in a second H-atom abstraction event. Thus, as is the case with DHA, the first equivalent of $[\text{Tp}^{\text{tBu,Me}}]\text{Ni}(\text{O}_2)$ is responsible for the abstraction two hydrogen atoms. The second abstraction results in production of both the 9-hydroxyxanthyl radical as well as the first of the two observed nickel products, $[\text{Tp}^{\text{tBu,Me}}]\text{Ni}(\text{OH})$. A second equivalent of $[\text{Tp}^{\text{tBu,Me}}]\text{Ni}(\text{O}_2)$ completes the conversion to xanthone by performing a third and final H-atom transfer. The resulting unstable hydroperoxo-nickel complex decomposes, but with no ability for rebound, the resulting hydroxyl radical attacks the proximal ligand *tert*-butyl group eliminating water and forming the nickel metallacycle.

As was noted earlier, xanthene was selected as a substrate due to its similarity to DHA. Accordingly, if xanthone is indeed formed according to the proposed mechanism, the reaction would be expected to require two equivalents of $[\text{Tp}^{\text{tBu,Me}}]\text{Ni}(\text{O}_2)$. The aforementioned experimental data provide empirical evidence to this effect. As shown in Table 5.2, the reaction optimizes at a 2:1 stoichiometry, which is consistent with the experimental results and mechanistic scenario proposed for DHA oxidation. In addition, the metallacycle: $[\text{Tp}^{\text{tBu,Me}}]\text{Ni}(\text{OH})$ ratio of 1:1 is consistent with the proposed mechanism. As with DHA, this ratio is independent of substrate stoichiometry.

As with DHA, the probable organic intermediate, 9-hydroxyxanthene, was not detected in ^1H NMR spectra of the completed reaction mixtures, suggesting that the

initial hydrogen atom abstraction from xanthene is rate limiting. As 9-hydroxyxanthene is commercially available, it was straightforward to assess the reactivity of the organic intermediate with $[\text{Tp}^{\text{tBu,Me}}]\text{Ni}(\text{O}_2)$ directly.

A 1:1 reaction of $[\text{Tp}^{\text{tBu,Me}}]\text{Ni}(\text{O}_2)$ with 9-hydroxyxanthene proceeds to completion at room temperature in less than 24 hr. The only organic product is xanthone, generated in 49% yield, Figure 5.41. The nickel product of the reaction is predominantly the metallacycle with only traces of $[\text{Tp}^{\text{tBu,Me}}]\text{Ni}(\text{OH})$, Figure 5.42. The reaction optimizes at the 2:1 stoichiometry with metallacycle remaining as the majority nickel product. Proceeding from the mechanistic implications discussed for DHA and 9,10-dihydroxy-9,10-dihydroanthracene, the 2:1 optimum ratio suggests that two H-atom abstractions occur in the conversion of 9-hydroxyxanthene to xanthone, with one equivalent of $[\text{Tp}^{\text{tBu,Me}}]\text{Ni}(\text{O}_2)$ being required for each HAT event, Figure 5.44. In the case of xanthene, the first of these H-atom abstractions could be performed by the oxonickel intermediate generated in the initial reaction. As this intermediate is not present at the initiation of the reaction with 9-hydroxyxanthene, a sacrificial equivalent of $[\text{Tp}^{\text{tBu,Me}}]\text{Ni}(\text{O}_2)$ is used in the transfer. Again, this behavior parallels that observed with 9,10-dihydroxy-9,10-dihydroanthracene where the optimal ratio of 4:1 required two equivalents of $[\text{Tp}^{\text{tBu,Me}}]\text{Ni}(\text{O}_2)$ in lieu of the oxonickel moiety.

The patterns of reactivity observed for DHA/9,10-dihydroxy-9,10-dihydroanthracene and xanthene/9-hydroxyxanthene make a strong case for the oxidation reactions proceeding by similar mechanisms. The mechanistic analysis put forth for these reactions fully explains the organic and inorganic products as well as their respective reaction stoichiometries and product yields. It also invokes

hydroperoxonickel and oxonickel complexes, with the latter being implicated in O-atom transfer reactions of $[\text{Tp}^{\text{tBu,Me}}]\text{Ni}(\text{O}_2)$.

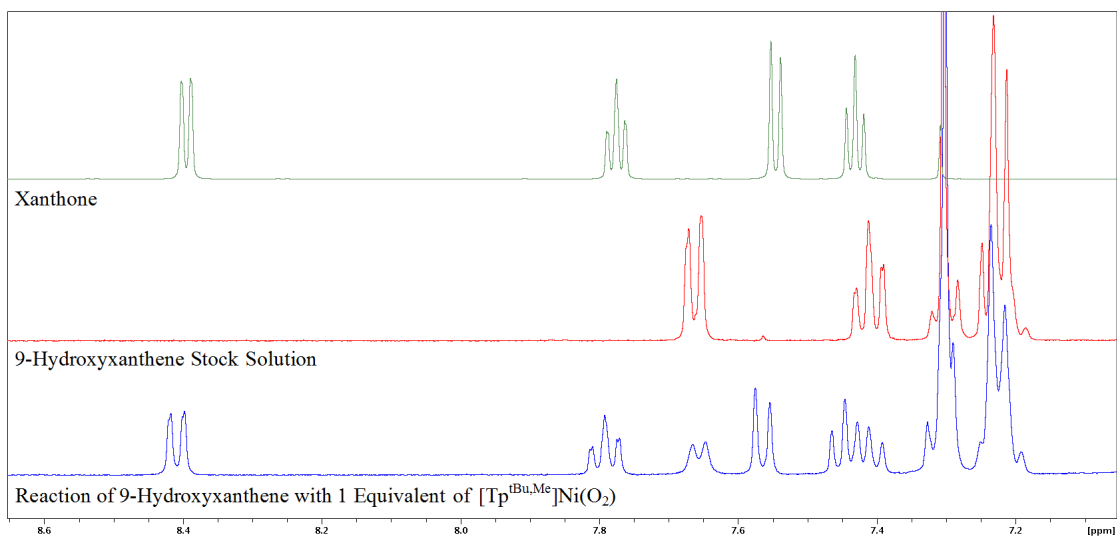


Figure 5.41 ^1H NMR spectral analysis of organic products in the reaction of 9-hydroxyxanthene with 1 equivalent of $[\text{Tp}^{\text{tBu,Me}}]\text{Ni}(\text{O}_2)$.

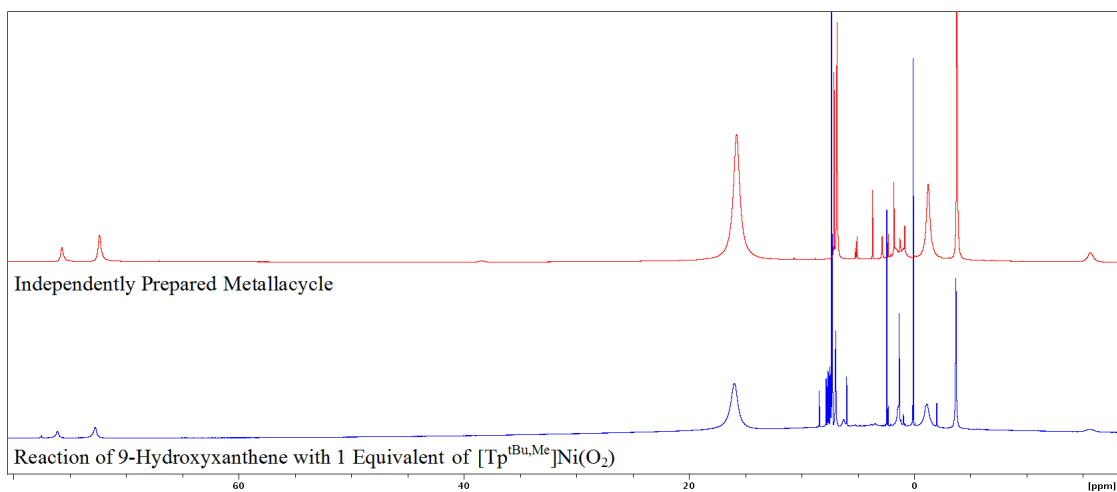


Figure 5.42 ^1H NMR spectral analysis of nickel products in the reaction of 9-hydroxyxanthene with 1 equivalent of $[\text{Tp}^{\text{tBu,Me}}]\text{Ni}(\text{O}_2)$.

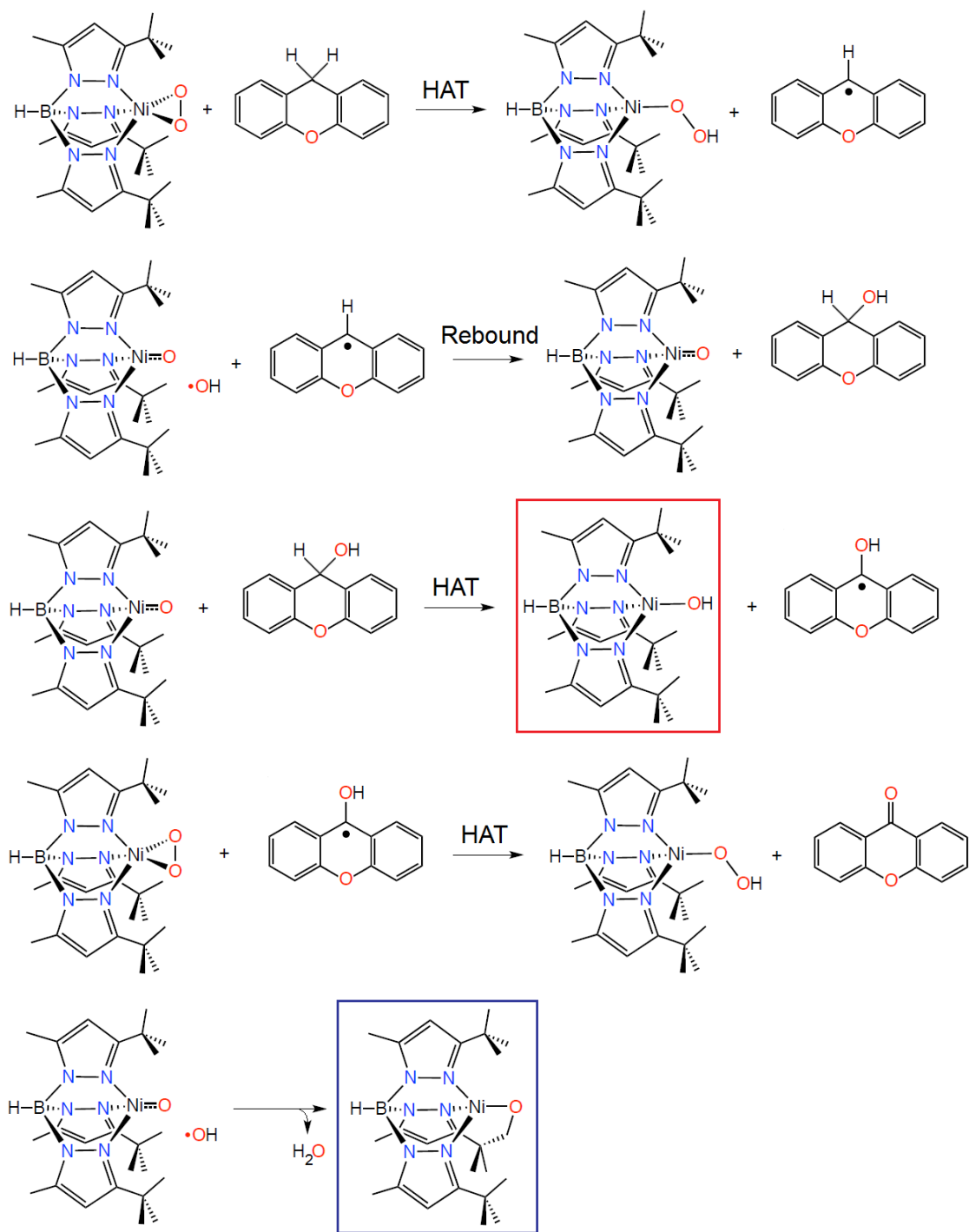


Figure 5.43 Proposed mechanism for the formation of xanthenone in the reaction of $[\text{Tp}^{\text{tBu,Me}}\text{Ni}(\text{O}_2)]$ with xanthene.

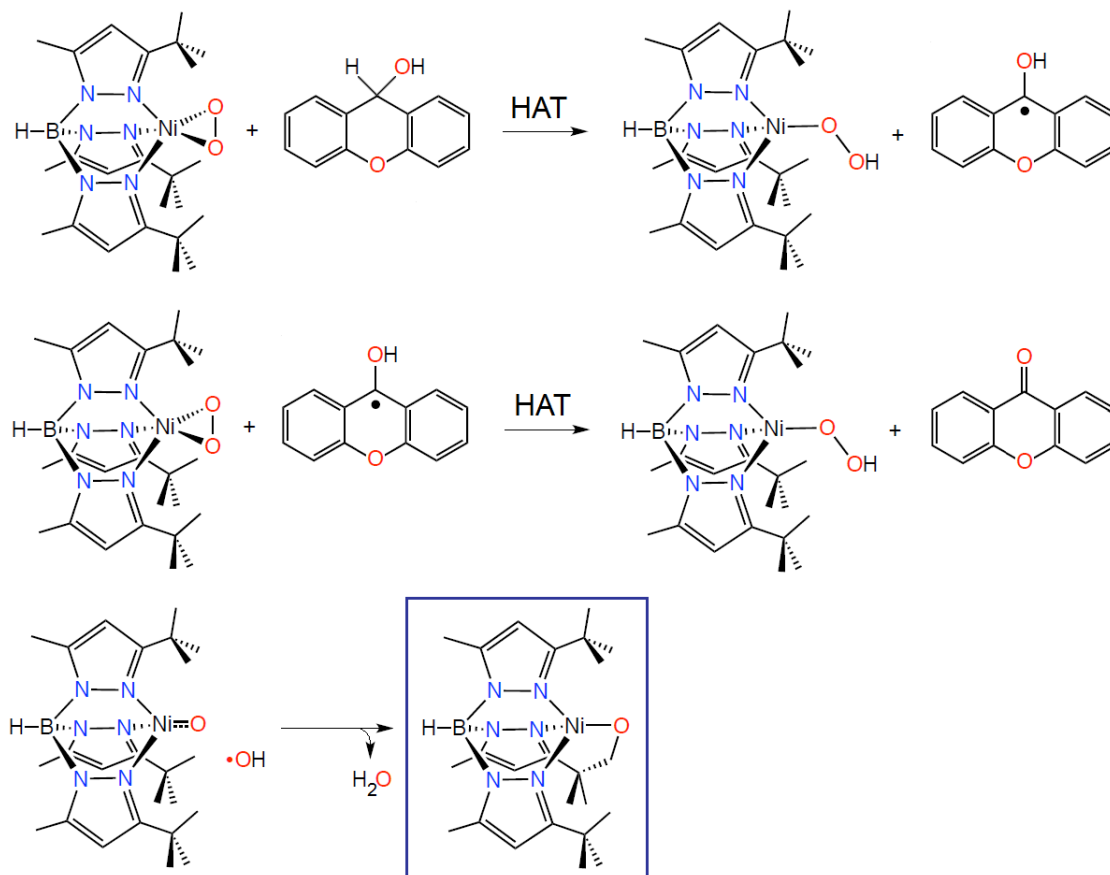


Figure 5.44 Proposed mechanism for the reaction of [Tp^{tBu,Me}]Ni(O₂) with 9-hydroxyxanthene. Note that the metallacycle is the only predicted nickel product.

5.4 Reaction of [Tp^{tBu,Me}]Ni(O₂) with 2-Phenylpropionaldehyde - Aldehyde Deformylation

Having uncovered a number of interesting patterns of reactivity of [Tp^{tBu,Me}]Ni(O₂) it seemed advantageous to explore other classes of substrate for further study. The selective removal of formyl groups from aldehydes is a transformation of considerable synthetic utility. Recent work by Nam and coworkers has shown that a Ni-O₂ moiety reacts with 2-phenylpropionaldehyde (2-PPA) producing acetophenone.²⁷ While the identity of the organic product is clear, the metal

product(s) and mechanism of the reaction remain unreported. Aldehyde deformylation is a hallmark reaction of nucleophilic metal peroxo complexes.^{111,112} Indeed, Nam used this reactivity, in part, to justify assignment of the complex, $[\text{Ni}^{\text{III}}(\text{13-TMC})(\text{O}_2)]^+$, as a Ni^{III} peroxo, despite structural considerations more in line with a Ni^{II} superoxo designation. Given the unequivocal assignment of $[\text{Tp}^{\text{tBu,Me}}]\text{Ni}(\text{O}_2)$ as a Ni^{II} superoxo species, as well as its propensity for producing stable metal products amenable to identification and characterization, the reaction of $[\text{Tp}^{\text{tBu,Me}}]\text{Ni}(\text{O}_2)$ with 2-PPA was studied with an eye toward shedding additional light on the nature of superoxo-nickel/formyl interactions.

Treatment of a toluene solution of $[\text{Tp}^{\text{tBu,Me}}]\text{Ni}(\text{O}_2)$ with 1 equiv. of 2-PPA resulted in a color change from red-brown to dark purple over the course of several hours. After 24 hours, the solution was analyzed by ^1H NMR spectroscopy (Figure 5.47), GC-MS (Figure 5.46), and LIFDI-MS (Figure 5.48) methods. The GC-MS spectrum established production of acetophenone, confirming that deformylation of the substrate occurred. ^1H NMR spectral analysis revealed the complete consumption of $[\text{Tp}^{\text{tBu,Me}}]\text{Ni}(\text{O}_2)$ as well as the formation of several nickel complexes of the $[\text{Tp}^{\text{tBu,Me}}]\text{NiX}$ type. Of these products only one, $[\text{Tp}^{\text{tBu,Me}}]\text{Ni}(\text{OH})$, was immediately identifiable by ^1H NMR spectral comparison to previously known complexes. The LIFDI-MS spectrum shed additional light on the identity of the other nickel derivatives. The features centered on the m/z values of 496.26 and 526.27 indicated the presence of the metallacycle and $[\text{Tp}^{\text{tBu,Me}}]\text{Ni}(\text{O}_2\text{CH})$ complexes, respectively. A feature at 614.34 m/z is consistent with the mass of a deprotonated 2-PPA ligand bound to nickel, i.e. $[\text{Tp}^{\text{tBu,Me}}]\text{Ni}(\text{C}(\text{O})\text{R})$. The identity of the formate complex, $[\text{Tp}^{\text{tBu,Me}}]\text{Ni}(\text{O}_2\text{CH})$, was subsequently confirmed by ^1H NMR spectral comparison to

independently prepared material. Synthesis of $[\text{Tp}^{\text{tBu,Me}}]\text{Ni}(\text{O}_2\text{CH})$ was achieved via the treatment of $[\text{Tp}^{\text{tBu,Me}}]\text{Ni}(\text{OH})$ with an equivalent of formic acid. The ^1H NMR spectral comparison of pure metallacycle to the reaction residue does not indicate an exact match, however, this may be due to the metallacycle having either 2-PPA or acetophenone bound as an ancillary ligand. An attempt was made to prepare the putative deprotonated 2-PPA complex, $[\text{Tp}^{\text{tBu,Me}}]\text{Ni}(2\text{-PPA})$ by stirring a solution of $[\text{Tp}^{\text{tBu,Me}}]\text{NiBr}$ with NaH and 2-PPA. The reaction did not proceed to completion even after 1 week. However, ^1H NMR spectral comparison of this reaction mixture to that of the reaction between $[\text{Tp}^{\text{tBu,Me}}]\text{Ni}(\text{O}_2)$ and 2-PPA indicates a likely product match as indicated in Figure 5.47.

The preparation of a well defined mechanistic scheme for the reaction is complicated for several reasons. The large number and incomplete identification of nickel products makes a comprehensive examination of possible intermediates difficult. Furthermore, the apparent binding of both the substrate and organic products to nickel derivatives precludes a truly quantitative evaluation of 2-PPA consumption and acetophenone yield. Nevertheless, the known and suspected products provide some clues as to possible mechanistic steps. In addition, there are parallels which can be drawn from similar deformylations performed by iron and manganese O_2 adducts.^{113,114} Using what data is available, one possible mechanistic pathway is illustrated in Figure 5.49. In this scheme, deformylation is initiated via nucleophilic attack by the superoxo moiety on the aldehyde carbon to give a nickel peroxohemiacetal intermediate. Subsequent homolytic bond scission generates an oxyl-nickel complex as well as an organic radical anion species. The former can abstract a hydrogen atom from any number of sources to form the hydroxo complex.

The radical anion undergoes spontaneous decomposition to eliminate formate and leave behind a secondary radical site on the remaining portion of the substrate. The reaction of this radical fragment with a second equivalent of the superoxo complex results in the production of a transient alkylperoxonickel species. Subsequent decomposition of this complex (via homolysis of the peroxo moiety) is followed by hydrogen atom abstraction from the organic fragment by the concomitantly generated oxyl-nickel unit to give acetophenone. Such a mechanistic scenario explains the presence of both the hydroxo and formate complexes. The former is produced directly while the latter is generated via either ligand substitution or by reaction of the hydroxo complex with formic acid (derived from the reprotonated formate). Other nickel derivatives, including the metallacycle and the putative, nickel-bound 2-PPA complex, are harder to justify from this scheme. This may indicate competitive or alternative pathways including direct hydrogen atom abstraction from 2-PPA by the superoxo complex.

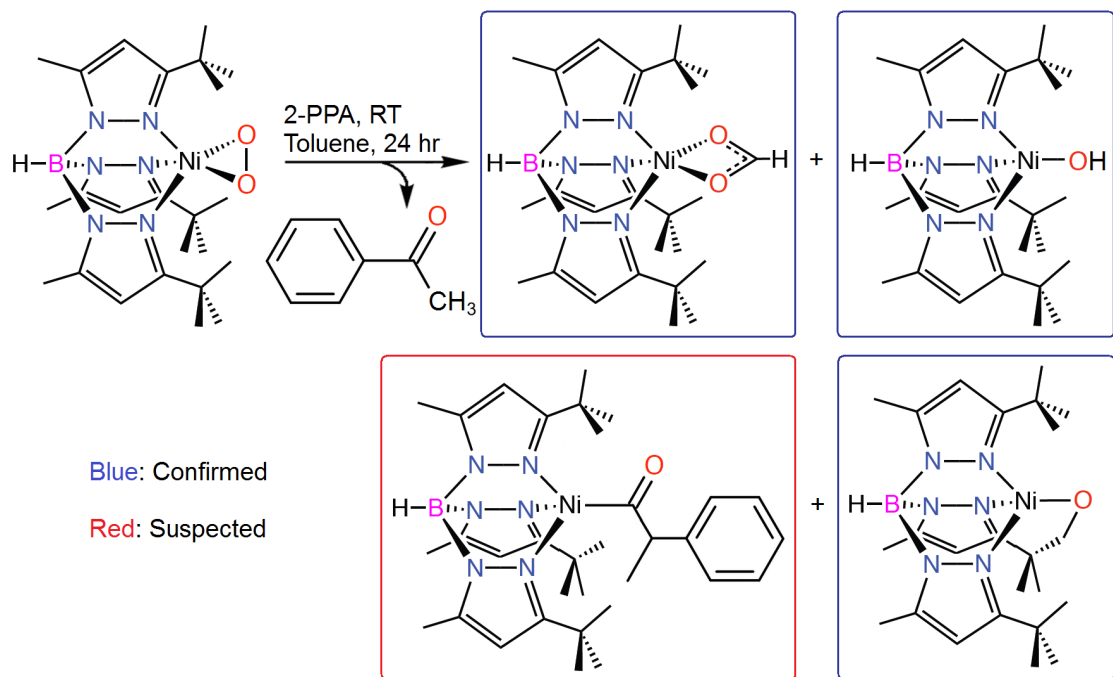


Figure 5.45 Reaction of $[\text{Tp}^{\text{tBu,Me}}\text{Ni}(\text{O}_2)]$ with 2-PPA. Products boxed in blue have been confirmed. Product in red is suspected.

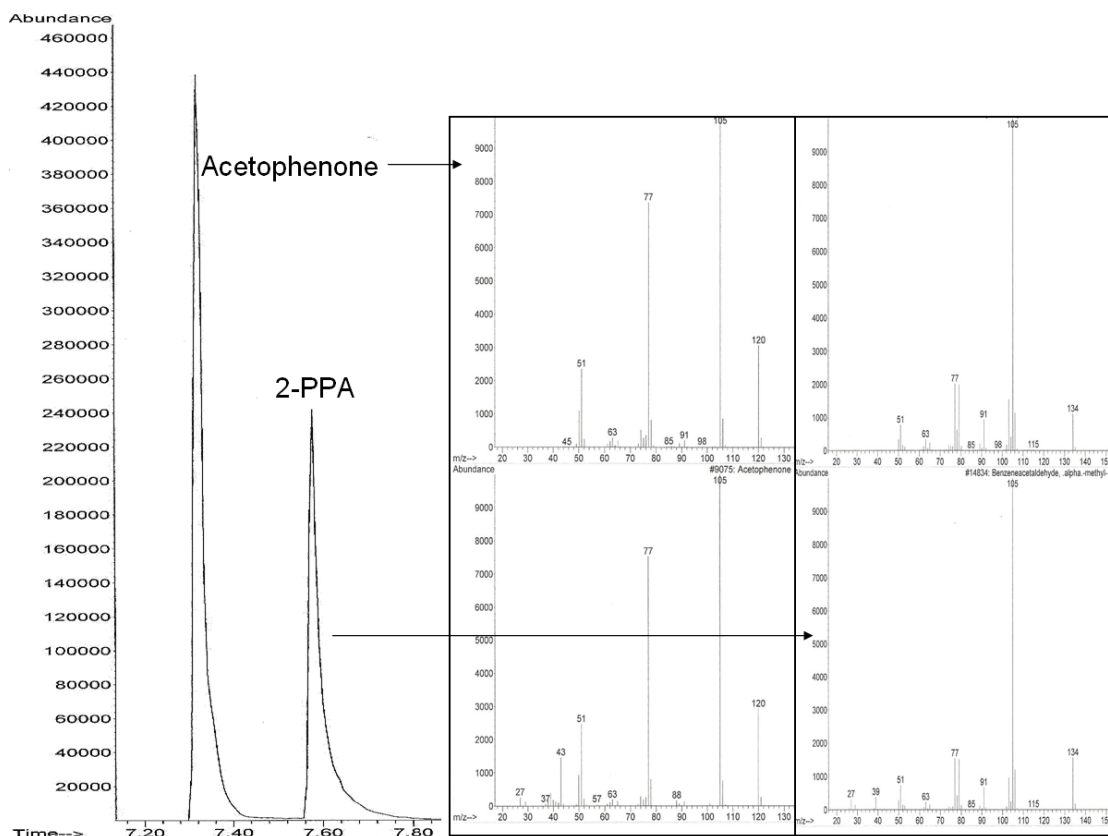


Figure 5.46 Excerpt from GC-MS spectrum of the reaction of $[\text{Tp}^{\text{tBu,Me}}\text{Ni}(\text{O}_2)]$ and 2-PPA showing production of acetophenone as well as residual 2-PPA. Peak identity was determined by spectral comparison to known compounds (see inset, right).

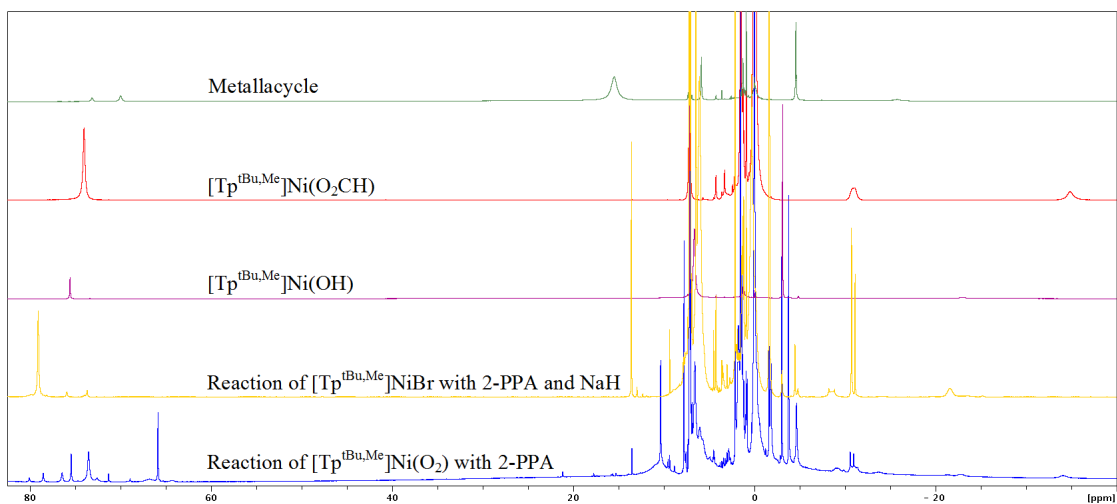


Figure 5.47 ^1H NMR spectral analysis of nickel products in the reaction of $[\text{Tp}^{\text{tBu,Me}}]\text{Ni}(\text{O}_2)$ and 2-PPA.

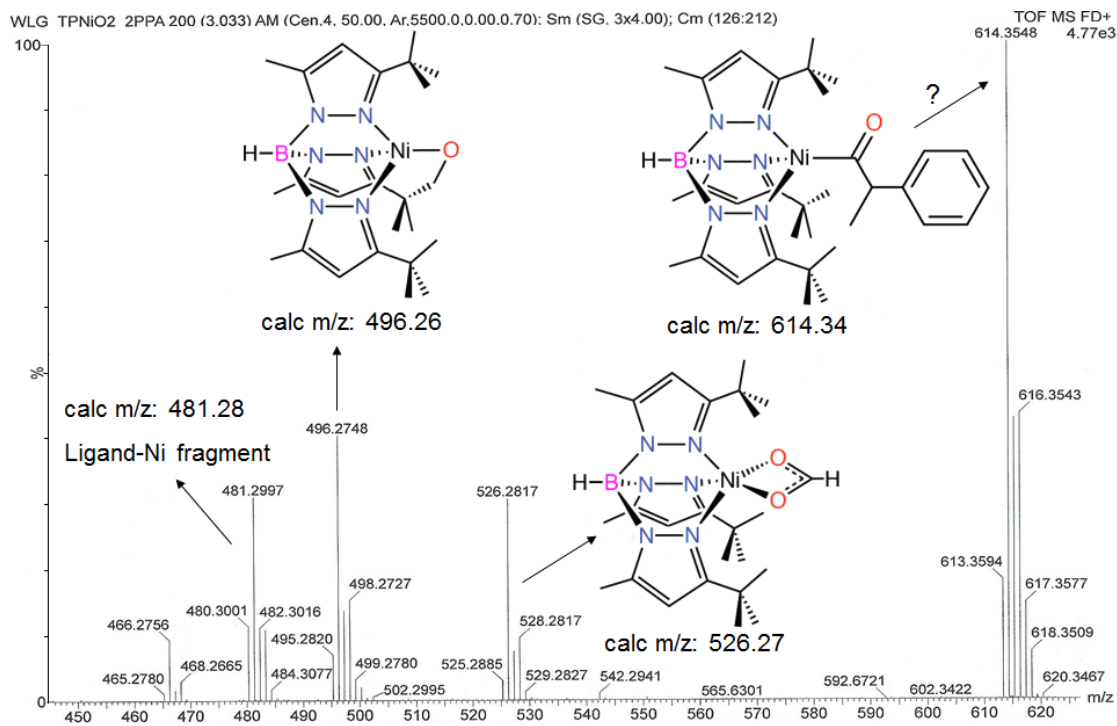


Figure 5.48 LIFDI-MS spectrum of the reaction of $[\text{Tp}^{\text{tBu,Me}}]\text{Ni}(\text{O}_2)$ and 2-PPA. Possible identities for major mass fragments are inset.

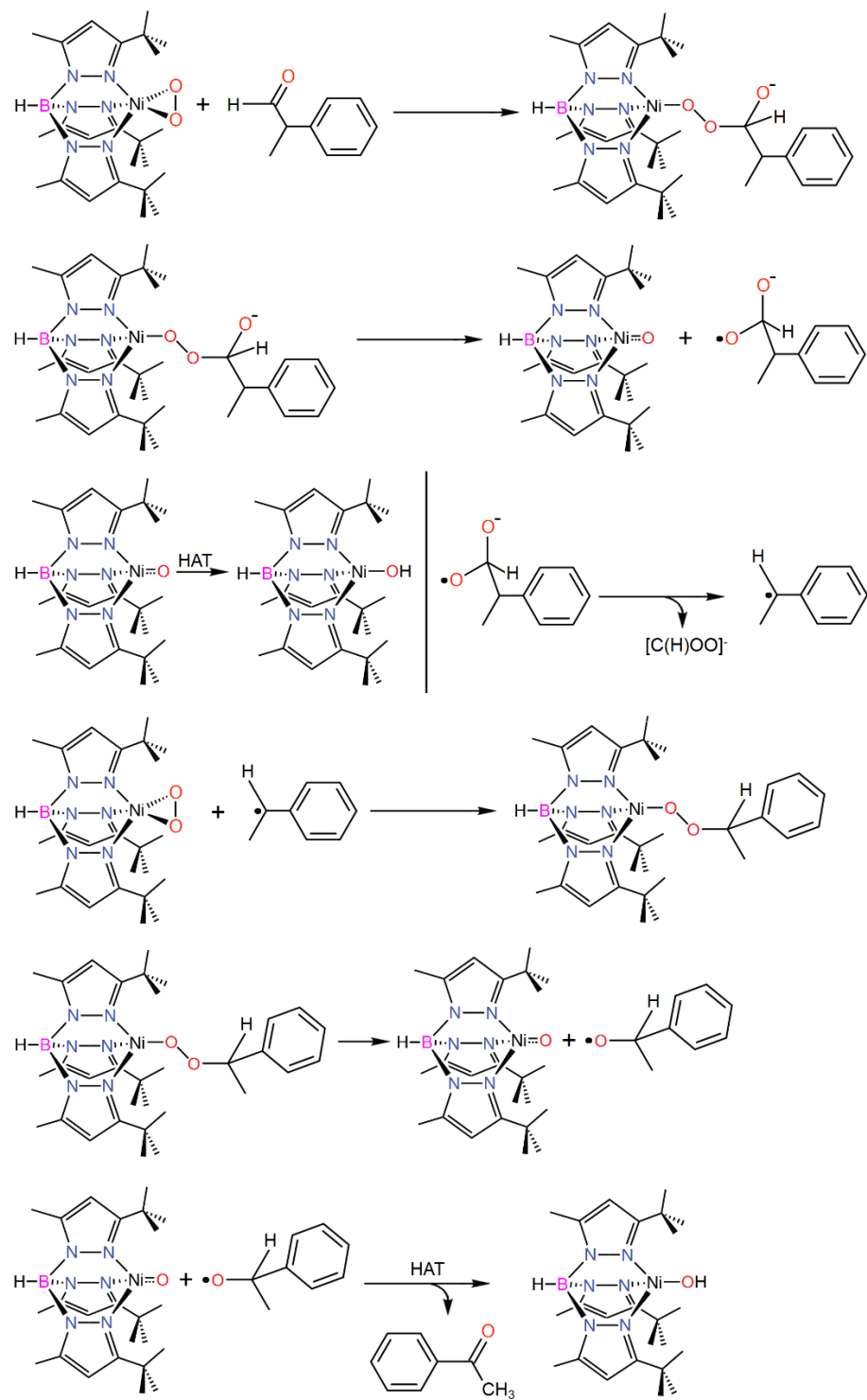


Figure 5.49 Possible mechanism for the deformylation of 2-phenylpropionaldehyde by $[\text{Tp}^{\text{tBu,Me}}\text{Ni}(\text{O}_2)]$.

5.5 Summary

The purpose of this study was to explore the reactivity of the superoxo-nickel complex, $[\text{Tp}^{\text{tBu,Me}}]\text{Ni}(\text{O}_2)$, whose preparation and characterization were described in the previous chapter. To this end, a diverse range of substrates were employed to determine the ability of $[\text{Tp}^{\text{tBu,Me}}]\text{Ni}(\text{O}_2)$ to facilitate transformations such as oxygen atom transfer, C-H activation, and aldehyde deformylation. Significant efforts were made to identify the both the organic products and nickel derivatives of these reactions and, where possible, to interrogate the mechanism leading to their formation.

$[\text{Tp}^{\text{tBu,Me}}]\text{Ni}(\text{O}_2)$ was found to be a competent O-atom transfer agent to both alkyl phosphines and nitric oxide. In the former case, it was found that $[\text{Tp}^{\text{tBu,Me}}]\text{Ni}(\text{O}_2)$ will not oxidize aryl phosphines but will transfer oxygen atoms to alkylphosphines including trimethylphosphine, triethylphosphine and tricyclohexylphosphine. In each the case the phosphine is converted to the phosphine oxide in high yield with the dominant nickel product identified as a monomeric nickel hydroxide complex, $[\text{Tp}^{\text{tBu,Me}}]\text{Ni}(\text{OH})$. A second nickel complex, a metallacycle resulting from C-H activation of the ligand, was identified as a minor product. In the case of reactions involving excess PMe_3 , it was discovered that $[\text{Tp}^{\text{tBu,Me}}]\text{Ni}(\text{O}_2)$ is capable of transferring both oxygen atoms from the bound O_2 ligand. This transfer is catalytic in the presence of excess O_2 with evidence implicating both oxo-nickel and monovalent nickel species as intermediates in the catalytic cycle. $[\text{Tp}^{\text{tBu,Me}}]\text{Ni}(\text{O}_2)$ was also found to facilitate the oxidation of nitric oxide. Treatment of $[\text{Tp}^{\text{tBu,Me}}]\text{Ni}(\text{O}_2)$ with a modest excess of NO results in the generation of both nickel-nitrate and nitrite complexes. The nickel products are formed in a 2:1 ratio for the nickel nitrate and nitrite respectively with a small amount of an unidentified complex of the $[\text{Tp}^{\text{tBu,Me}}]\text{Ni}(\text{X})$ type.

In addition to O-atom transfer reactions, $[\text{Tp}^{\text{tBu,Me}}]\text{Ni}(\text{O}_2)$ has also shown itself capable of performing C-H activation in the case of 1,4-cyclohexadiene (CHD), 9,10-dihydroanthracene (DHA), and xanthene. The reaction of two equivalents of $[\text{Tp}^{\text{tBu,Me}}]\text{Ni}(\text{O}_2)$ with a single equivalent of CHD results in the production of benzene (65%). The nickel products in this reaction were identified as $[\text{Tp}^{\text{tBu,Me}}]\text{Ni}(\text{O}_2)$ and the metallacycle, occurring in a 1:6 ratio. A hydroperoxo-nickel species, formed by H-atom abstraction from CHD, is postulated as the intermediate resulting in metallacycle formation. Independent attempts at preparation of the intermediate at low temperatures have produced strong spectroscopic evidence of its existence. An alkylperoxo analog, $[\text{Tp}^{\text{tBu,Me}}]\text{Ni}(\text{OO}t\text{Bu})$, has also been prepared. This complex is thermally stable under ambient conditions and has been both structurally and spectroscopically characterized. The reaction of $[\text{Tp}^{\text{tBu,Me}}]\text{Ni}(\text{O}_2)$ with DHA results in the production of 9,10-anthraquinone. The metal products have been identified as the hydroxo complex and metallacycle with the two complexes occurring in nearly equal amounts. The reaction optimizes at a $[\text{Tp}^{\text{tBu,Me}}]\text{Ni}(\text{O}_2)$:DHA ratio of 4:1 and is proposed to occur via a multistep mechanistic pathway involving both oxo-nickel and hydroperoxo-nickel intermediates. A kinetic analysis of the reaction reveals a KIE (kH/kD) of at least 12. Activation parameters, $\Delta H^\ddagger = 14(1)$ kcal/mol and $\Delta S^\ddagger = -117(10)$ J mol⁻¹K⁻¹, were determined from an Eyring analysis. The reaction of $[\text{Tp}^{\text{tBu,Me}}]\text{Ni}(\text{O}_2)$ with xanthene results in the production of xanthone. The reaction bears very strong similarities to that of reaction with DHA with the two processes sharing common product distributions, relative optimal stoichiometries and proposed reaction mechanisms.

Lastly, $[\text{Tp}^{\text{tBu,Me}}]\text{Ni}(\text{O}_2)$ was evaluated with regard to its ability to perform aldehyde deformylation. Treatment of $[\text{Tp}^{\text{tBu,Me}}]\text{Ni}(\text{O}_2)$ with 2-phenylpropionaldehyde

(2-PPA) demonstrated that deformylation does occur, with GC-MS analysis indicating the production of acetophenone. The reaction results in the production of a number of different nickel derivatives, not all of which have been positively identified. LIFDI-MS and ^1H NMR analysis have positively identified three products including the hydroxo, metallacycle and formate complexes. The formation of an additional complex consisting of nickel-bound 2-PPA is considered likely but has not been definitively confirmed. A speculative mechanistic scenario for the reaction has been proposed.

REFERENCES

- 1 Sigel, A.; Sigel, H.; Sigel, R. K. O. *Nickel and Its Surprising Impact in Nature, Metal Ions in the Life Sciences, Volume 2*. John Wiley and Sons (Chichester, UK). **2007**
- 2 Volbeda, A.; Charon, M. H.; Piras, C.; Hatchikian, E. C.; Frey, M.; Fontecilla-Camps, J. C.; *Nature*. **1995**, *373*, 580
- 3 Greig, N.; Wyllie, S.; Vickers, T. J.; Fairlamb, A. H. *Biochemical Journal*. **2006**, *400*, 217
- 4 Thauer, R. K. *Microbiology*. **1998**, *144*, 2377
- 5 Karplus, P. A.; Pearson, M. A.; Hausinger, R. P. *Accounts of Chemical Research*. **1997**, *30*, 330
- 6 Dai, Y.; Wensink, P. C.; Abeles, R. H. *J. Biol. Chem.* **1999**, *274*, 1193
- 7 Szajna-Fuller, E.; Rudzka, K.; Arif, A. M.; Berreau, L. M. *Inorg. Chem.* **2007**, *46*, 5499
- 8 Gale, E. M.; Cowart, D. M.; Scott, R. A.; Harrop, T. C. *Inorg. Chem.*, **2011**, *50*, 10460
- 9 Krause, M. E.; Glass, A. M.; Jackson, T. A.; Laurence, J. S. *Inorg. Chem.*, **2010**, *49*, 362
- 10 Pochapsky, T. C.; Pochapsky, S. S.; Ju, T.; Mo, H.; Al-Mjeni, F.; Maroney, M. J. *Nature Structural Biology*. **2002**, *9*, 966
- 11 Ragsdale, S. W. *The Journal of Biological Chemistry*. **2009**, *284*, 18571
- 12 Jeoung, J.-H.; Nianios, D.; Fetzner, S.; Dobbek, H. *Angew. Chem. Int. Ed.* **2016**, *55*, 3281

-
- 13 Richardson, J.; Thomas, K. A.; Rubin, B. H.; Richardson, D. C. *PNAS*. **1975**, *72*, 1349
- 14 Tainer, J. A.; Getzoff, E. D.; Richardson, J. S.; Richardson, D. C. *Nature*. **1983**, *306*, 284
- 15 Abreu, I. A.; Cabelli, D. E. *Biochimica et Biophysica Acta*. **2010**, *1804*, 263
- 16 Fiedler, A. T.; Bryngelson, P. A.; Maroney, M. J.; Brunold, T. C. *J. Am. Chem. Soc.* **2005**, *127*, 5449
- 17 Maroney, M. J. *Current Opinion in Chemical Biology*. **1999**, *3*, 188
- 18 Sheldon, R. A.; Kochi, J. K. *Metal Catalyzed Oxidations of Organic Compounds*; Academic Press: New York (USA), **1981**
- 19 Bullock, M. R. *Catalysis without Precious Metals*; John Wiley & Sons, Weinheim (Germany), **2011**
- 20 Koola, J. D.; Kochi, J. K.; *Inorganic Chemistry*, **1986**, *26*, 908
- 21 Mack, D. P.; Iverson, B. L.; Dervan, P. B. *J. Am. Chem. Soc.* **1988**, *110*, 7572
- 22 Mack, D. P.; Dervan, P. B. *J. Am. Chem. Soc.*, **1990**, *112*, 4604
- 23 Morrow, J. R.; Kolasa, K. A. *Inorg. Chim. Acta*, **1992**, *195*, 245
- 24 Hikichi, S.; Yoshizawa, M.; Sasakura, Y.; Akita, M.; Moro-oka, Y. *J. Am. Chem. Soc.* **1998**, *120*, 10567
- 25 Shiren, K.; Ogo, S.; Fujinami, S.; Hayashi, H.; Suzuki, M.; Uehara, A.; Watanabe, Y.; Moro-oka, Y. *J. Am. Chem. Soc.* **2000**, *122*, 254
- 26 Cho, J.; Sarangi, R.; Annaraj, J.; Kim, S. Y.; Kubo, M.; Ogura, T.; Solomon, E. I.; Nam, W.; *Nature Chemistry*. **2009**, *1*, 568
- 27 Cho, J.; Kang, Y. H.; Liu, L. V.; Sarangi, R.; Solomon, I. E.; Nam, W.; *Chem. Sci.* **2013**, *4*, 1502

-
- 28 Otsuka, S.; Nakamura, A.; Tatsuno, Y. *J. Am. Chem. Soc.* **1969**, *91*, 6994.
- 29 Mandimutsira, B. S.; Yamarik, J. L.; Brunold, T. C.; Gu, W.; Cramer S. P.; Riordan, C. G. *J. Am. Chem. Soc.* **2001**, *123*, 9194
- 30 Fujita, K.; Schenker, R.; Gu, W.; Brunold, T. C.; Cramer, S. P.; Riordan, C. G. *Inorg. Chem.* **2004**, *43*, 3324
- 31 Kieber-Emmons, M. T.; Annaraj, J.; Seo, S. M.; Van Heuvelen, K. M.; Tosha, T.; Kitagawa, T.; Brunold, T. C.; Nam, W.; Riordan, C. G. *J. Am. Chem. Soc.* **2006**, *128*, 14230
- 32 Bai, G.; Wei, P.; Stephan, D. W. *Organometallics*. **2005**, *24*, 5901
- 33 a) Shreedhara Murthy, R. S.; Leyden, D. E. *Anal. Chem.* **1986**, *58*, 1228; b) Caravajal, G. S.; Leyden, D. E.; Quinting, G. R.; Maciel, G. E. *Anal. Chem.* **1988**, *60*, 1776.
- 34 Le, H. V.; Ganem, B. *Org. Lett.* **2011**, *13*(10), 2584
- 35 Trofimenko, S.; Calabrese, J. C.; Kochi, J. K.; Wolowiec, S.; Hulsbergen, F. B.; Reedijk, J. *Inorg. Chem.* **1992**, *31*(19), 3943
- 36 Santi, R.; Romano, A. M.; Sommazzi, A.; Grande, M.; Bianchini, C.; Mantovani, G. *J. Mol. Catal. A: Chem.* **2005**, *229*(1-2), 191.
- 37 Desrochers, P. J.; Cutts, R. W.; Rice, P. K.; Golden, M. L. *Inorg. Chem.*, **1999**, *38* (25), 5690
- 38 Criswell, T. R.; Klanderman, B. H. *J. Org. Chem.* **1974**, *39*(6), 770
- 39 Goldsmith, C. R.; Jonas, R. T.; Stack, T. D. P. *J. Am. Chem. Soc.* **2002**, *124*, 83
- 40 a) Evans, D. F. *J. Chem. Soc.* **1959**, 2003; b) Live, D. H.; Chan, S. I. *Anal. Chem.* **1970**, *42*, 791.
- 41 a) Linden, H. B. *Eur. J. Mass Spectrom.* **2004**, *10*, 459; b) Gross, J. H.; Nieth, N.; Linden, H. B.; Blumbach, U.; Richter, F. J.; Tauchert, M. E.; Tompers, R.; Hofmann, P. *Anal. Bioanal. Chem.* **2006**, 386, 52.

-
- 42 Collins, T.J.; Brooker, S.; Croucher, P.D.; Wang, K.; Stiefel, E.I.; Cramer, S.P. *J. Am. Chem. Soc.* **2000**, *122*, 10544.
- 43 Tsuda, K.; Miyata, K.; Okuno, T.; Yoshimura, M.; Tanaka, S.; Kitamura, M. *Tetrahedron Letters*, **2008**, *49*, 2990
- 44 Hikichi, S.; Okuda, H.; Ohzu, Y.; Akita, M. *Angew. Chem. Int. Ed.*, **2009**, *48*, 188
- 45 a) Sheldrick, G.M. *Acta Cryst.* **2008**, *A64*, 112; b) Sheldrick, G. M. *SHELXTL 6.12 program library*, Bruker-AXS, Inc., Madison, WI, **2001**
- 46 Yao, S.; Eckhard, B.; Milsman, C.; Wieghardt, K.; Driess, M. *Angew. Chem. Int. Ed.* **2008**, *47*, 7110
- 47 Porri, L.; Gallazzi, M. C.; Vitulli, G. *Chem. Commun.* **1967**, 228
- 48 Olson, D. C.; Vasilevskis, J. *Inorg. Chem.* **1969**, *8* (8), 1611
- 49 Barefield, K. E.; Freeman, M.; Van Derveer, D. G. *Inorg. Chem.*, **1986**, *25* (4), 552
- 50 Becker, J. Y.; Kerr, J. B.; Pletcher, D.; Rosas, R. *J. Electroanal. Chem.* **1981**, *117*, 87
- 51 Mindiola, D. J.; Waterman, R.; Jenkins, D. M.; Hillhouse, G. L. *Inorg. Chim. Acta.* **2003**, *345*, 299
- 52 Egan, J. W. Jr.; Haggerty, B. S.; Rheingold, A.; Sendlinger, S. C.; Theopold, K. T. *J. Am. Chem. Soc.* **1990**, *112* (6), 2445
- 53 Fujisawa, K.; Tanaka, M.; Moro-oka, M.; Kitajima, N.; *J. Am. Chem. Soc.* **1994**, *116* (26), 12079
- 54 Parkin, G.; *Advances in Inorganic Chemistry.* **1995**. *42*, 303
- 55 K. Fujita, G. P. A. Yap, C. G. Riordan, unpublished results
- 56 Imai, S.; Fujisawa, K.; Kobayashi, T.; Shirasawa, N.; Fujii, H.; Yoshimura, T.; Kitajima, N.; Moro-oka, Y. *Inorg. Chem.*, **1998**, *37* (12), 3066

-
- 57 Zhou, M.; Andrews, L.; Bauschlicher, C. W. Jr. *Chem Rev.* **2001**, *101*(7), 1931
- 58 DuPont, J. A.; Coxey, M. B.; Schebler, P. J.; Incarvito, C. D.; Dougherty, W. G.; Yap, G. P. A.; Rheingold, A. L.; Riordan, C. G. *Organometallics*. **2007**, *26* (4), 971
- 59 Krishnan, R.; Voo, J. K.; Riordan, C. G.; Zahkarov, L.; Rheingold, A. L. *J. Am. Chem. Soc.* **2003**, *125*(15), 4422
- 60 Ito, H.; Ito, T. *Bull. Chem. Soc. Jpn.* **1985**, *58*, 1755
- 61 Niu, D. F.; Zhang, L.; Xiao, L. P.; Luo, Y. W.; Lu, J. X. *Appl. Organometal. Chem.* **2007**, *21*, 941
- 62 Zhang, C.; Liu, R.; Zhang, J.; Chen, Z.; Zhou, X. *Inorg. Chem.*, **2006**, *45*(15), 5867
- 63 Trofimenko, S. *Scorpionates: The Coordination Chemistry of Polypyrazolylborate Ligands*. 1st Ed. Imperial College Press (London, UK). **1999**
- 64 Pettinari, C. *Scorpionates II: Chelating Borate Ligands*. 1st Ed. Imperial College Press (London, UK). **2008**
- 65 Pettinari, C.; Santini, C. *Comprehensive Coordination Chemistry II*. **2003**, *1*, 159
- 66 Calabrese, J. C.; Domaille, P. J.; Trofimenko, S.; Long, G. J. *Inorg. Chem.* **1991**, *30*(13), 2795
- 67 Deb, T.; Anderson, C. M.; Ma, H.; Petersen, J. L.; Young Jr, V G.; Michael P. Jensen, M. P. *Eur. J. Inorg. Chem.* **2015**, 458
- 68 Green, W. L.; Sirianni, E. R.; Yap, G. P. A.; Riordan, C. G. *Acta Cryst. C72*, **2016**, Article in Press, doi:10.1107/S2053229616001789
- 69 Rheingold, A. L.; Ostrander, R. L.; Haggerty, B. S.; Trofimenko, S. *Inorg. Chem.*, **1994**, *33* (17), 3666
- 70 Kitajima, N.; Tolman, W. B. *Prog. Inorg. Chem.*, **1995**, *43*, 419
- 71 Koehler, J.; Meiler, J. *Prog Nucl Magn Reson Spectrosc.* **2011**, *59*(4), 360

-
- 72 Ploskonka, A. *Synthesis of Trispyrrolylborate-Supported Nickel Complexes for Small Molecule Activation*. MS Thesis. University of Delaware. **2015**.
- 73 Cramer, C. J.; Tolman, W. B.; Theopold, K. T.; Rheingold, A. L. *Proc. Nat. Acad. Sci.* **2003**, *100*, 3635.
- 74 Westre, T. E.; Kennepohl, P.; DeWitt, J. G.; Hedman, B.; Hodgson, K. O.; Solomon, E. I. *J. Am. Chem. Soc.* **1997**, *119*(27), 6297
- 75 Cramer, S. P.; DeGroot, F. M. F.; Ma, Y.; Chen, C. T.; Sette, F.; Kipke, C. A.; Eichhorn, D. M.; Chan, M. K.; Armstrong, W. H. *J. Am. Chem. Soc.* **1991**, *113*(21), 7937
- 76 Reinaud, O. M.; Theopold, K. H. *J. Am. Chem. Soc.* **1994**, *116*(15), 6979
- 77 Schenker, R.; Riordan, C. G.; Brunold, T. C. *J. Am. Chem. Soc.* **2002**, *124*(46), 13842
- 78 Hikichi et al, *Chemistry - A European Journal*. **2001**, *7*(23), 5011
- 79 Thyagarajan, S.; Incarvito, C. D.; Rheingold, A. L.; Theopold, K. H. *Chem. Commun.*, **2001**, 2198
- 80 Yoon, Y.; Song, U.; Hong, S.H.; Kim, J.Q. *Clinic. Chem.* **2000**, *46*(10), 1626
- 81 Hopper, R. A.; Garthwaite, J. *Journal of Neuroscience*. **2006**, *26*(45), 11513
- 82 Beckman, J. S.; Ischiropoulos, H.; Zhu, L.; van der Woerd, M.; Smith, C.; Chen, J.; Harrison, J.; Martin, J. C.; Tsai, M.. *Archives of Biochemistry and Biophysics*. **1992**, *298*(2), 438
- 83 Harold, S.. *FEBS Letters*. **1998**, *439*, 85
- 84 Doyle, M. P.; Hoekstra, J. W.. *Inorg. Biochem.* **1981**, *14*, 351
- 85 Thyagarajan, S.; Incarvito, C.; Rheingold, A. L.; Theopold, K. H. *Inorganica Chimica Acta*. **2003**, *345*, 333

-
- 86 Maiti, D.; Lee, D. H.; Narducci Sarjeant, A. A.; Pau, M. Y. M.; Solomon, E. I.; Gaoutchenova, K.; Sundermeyer, J.; Karlin, K. D. *J. Am. Chem. Soc.*, **2008**, *130* (21), 6700
- 87 Park, G. Y.; Deepalatha, S.; Puiiu, S. C.; Lee, D. H.; Mondal, B.; Narducci Sarjeant, A. A.; del Rio, D.; Pau, M. Y. M.; Solomon, E. I.; Karlin, K. D. *J Biol Inorg Chem.* **2009**. *14*(8), 1301
- 88 Gao, Y.; DeYonker, N. J.; Garrett, E. C.; Wilson, A. K.; Cundari, T. R.; Marshall, P. J.. *Phys.Chem.A.* **2009**, *113*, 6955
- 89 England, J.; Martinho, M.; Farquhar, E. R.; Frisch, J. R.; Bominaar, E. L.; Münck, E.; Que, L.; *Angew. Chem. Int. Ed.* **2009**, *48*, 3622
- 90 Summerscales, O. T.; Fettinger, J. C.; Power, P. P. *J. Am. Chem. Soc.*, **2011**, *133* (31), 11960
- 91 Yu, J. Q.; Shi, Z. *Topics in Current Chemistry - C-H Activation*, **2010**, 292, 322
- 92 Rettenmeier, C. A.; Wadepohl, H.; Gade, L. H. *Angew. Chem. Int. Ed.*, **2015**, *54*, 4880
- 93 White, M. *Exploring Kinetics and Reactivity of Nickel Tris(pyrazolyl)borate Complexes*. Senior Thesis. University of Delaware. **2013**.
- 94 DeTuri, V. F.; Ervin, K. M. *J. Phys. Chem. A*, **1999**, *103*, 6911
- 95 Ruscic, B.; Feller, D.; Dixon, D. A.; Peterson, K. A.; Harding, L. B.; Asher, R. L.; Wagner, A. F.. *J. Phys. Chem. A*, **2001**, *105*, 1
- 96 Bordwell, F. G.; Cheng, J. P.; Ji, G. Z.; Satish, A.V.; Zhang, X. M. *J. Am. Chem. Soc.* **1991**, *113*, 9790
- 97 Parsell, T. H.; Yang, M. Y.; Borovik, A. S. *J. Am. Chem. Soc.*, **2009**, *131*, 2762
- 98 Donoghue, P. J.; Tehranchi, J.; Cramer, C. J.; Sarangi, R.; Solomon, E. I.; Tolman, W. B.. *J. Am. Chem. Soc.*, **2011**, *133* (44), 17602
- 99 Cho, K.; Kang, H.; Woo, J; Park, Y. J.; Seo, M. S.; Cho, J.; Nam, W. *Inorg. Chem.*, **2014**, *53* (1), 645

-
- 100 Shi, S.; Wang, Y.; Xu, A.; Wang, H.; Zhu, D.; Roy, S. B.; Jackson, T. A.; Busch, D. H.; Yin, G. *Angew. Chem. Int. Ed.* **2011**, *50*, 7321
- 101 Mihailović, M. L.; Čeković, Z.; Lorenc, L. *Chapter 14: Oxidations with Lead Tetraacetate*. Mijs, W. J.; de Jonge, C. R. H. I. *Organic Synthesis by Oxidation with Metal Compounds*, 1st Ed. Plenum Press (New York, NY). **1986**
- 102 Bryant, J. R.; Mayer, J. M.; *J. Am. Chem. Soc.*, **2003**, *125*(34), 10351
- 103 Carey, F. A.; Giuliano, R. M. *Organic Chemistry*. 9th Ed. McGraw-Hill (New York, NY). **2013**
- 104 Stein, S. E.; Golden, D. M. *J. Org. Chem.* **1977**, *42*(5), 839
- 105 Tsang, W. *J. Phys. Chem.* **1986**, *90*, 1152
- 106 Westheimer, F. H. *Chem. Rev.* **1961**, *61*(3), 265
- 107 Drago, R.S. *Physical Methods for Chemists*, 2nd Ed. Saunders College Publishing (Ft. Worth, TX). **1992**.
- 108 Lee, J. Y.; Peterson, R. L.; Ohkubo, K.; Garcia-Bosch, I.; Himes, R. A.; Woertink, J.; Moore, C. D.; Solomon, E. I.; Fukuzumi, S.; Karlin, K. D. *J. Am. Chem. Soc.*, **2014**, *136*(28), 9925
- 109 Nemes, A.; Bakac, A. *Inorg. Chem.* **2001**, *40*(4), 746
- 110 Burkey T. J.; Majewski M.; Griller D.. *J Am Chem Soc.*, **1986**, *108* (9), 2218
- 111 Cho, J.; Sarangi, R.; Kang, H. Y.; Lee, J. Y.; Kubo, M.; Ogura, T.; Solomon, E. I.; Nam, W. *J. Am. Chem. Soc.*, **2010**, *132* (47), 16977
- 112 Annaraj, J.; Suh, Y.; Seo, M. S.; Kim, S. O.; Nam, W. *Chem. Commun.* **2005**, 4529
- 113 Wertz, D. L.; Valentine, J. S. *Structure and Bonding.* **2001**, *97*, 37
- 114 Cho, J.; Sarangi, R.; Nam, W. *Acc. Chem. Res.*, **2012**, *45*, 1321

Alert level A

PLAT073 ALERT 1 A H-atoms ref, but _hydrogen_treatment reported as constr

Alert level B

SYMMS02 ALERT 1 B The unit-cell lengths a and c should be equal for a rhombohedral cell

Cell	15.9240	15.9240	9.5760
Angles	90.0000	90.0000	120.0000

SYMMS02 ALERT 1 B Cell angles alpha and gamma should be equal for a rhombohedral cell

Cell	15.9240	15.9240	9.5760
Angles	90.0000	90.0000	120.0000

SYMMS02 ALERT 1 B All angles should not be 90 for a rhombohedral cell

Cell	15.9240	15.9240	9.5760
Angles	90.0000	90.0000	120.0000

Alert level C

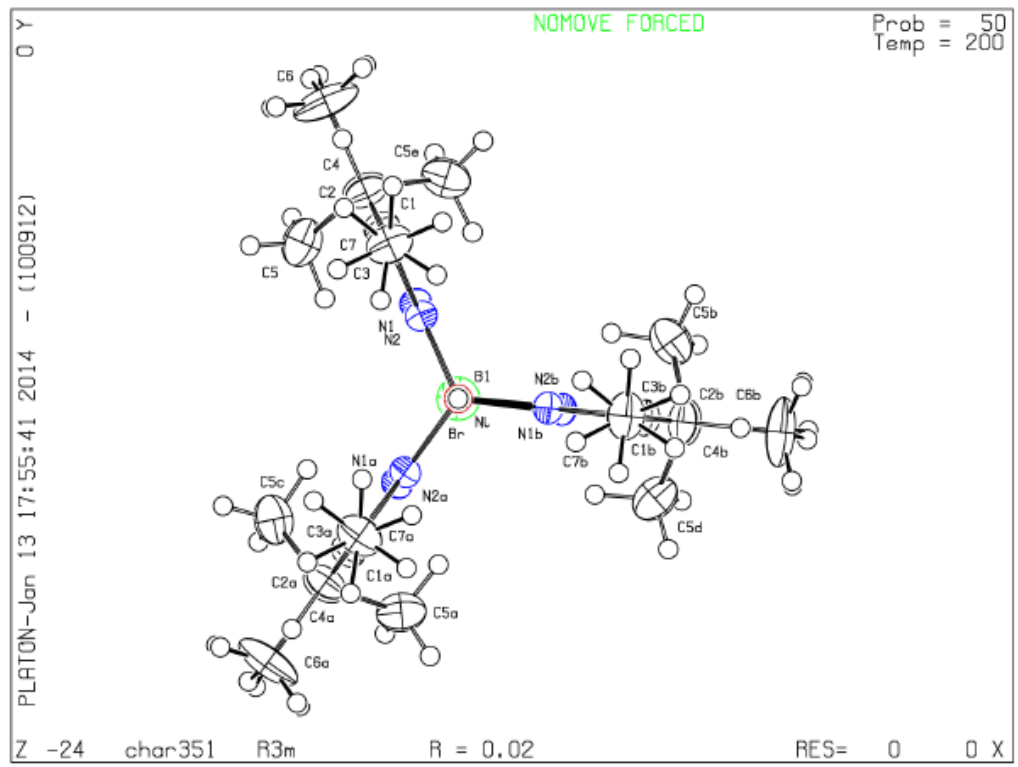
PLAT090 ALERT 3 C Poor Data / Parameter Ratio (Zmax > 18) 9.04

Alert level G

PLAT005 ALERT 5 G	No _iucr_refine_instructions_details in the CIF	Please Do !
PLAT104 ALERT 1 G	The Reported Crystal System is Inconsistent with	R3m Check
PLAT152 ALERT 1 G	The Supplied and Calc. Volume s.u. Differ by ...	2 Units
PLAT301 ALERT 3 G	Main Residue Disorder Percentage =	10 Note
PLAT764 ALERT 4 G	Overcomplete CIF Bond List Detected (Rep/Expd) .	1.13 Ratio

- 1 ALERT level A = Most likely a serious problem - resolve or explain
- 3 ALERT level B = A potentially serious problem, consider carefully
- 1 ALERT level C = Check. Ensure it is not caused by an omission or oversight
- 5 ALERT level G = General information/check it is not something unexpected

- 6 ALERT type 1 CIF construction/syntax error, inconsistent or missing data
- 0 ALERT type 2 Indicator that the structure model may be wrong or deficient
- 2 ALERT type 3 Indicator that the structure quality may be low
- 1 ALERT type 4 Improvement, methodology, query or suggestion
- 1 ALERT type 5 Informative message, check



2. [Tp^{tBu,Ph}]Ni(Br)

checkCIF/PLATON report

You have not supplied any structure factors. As a result the full set of tests cannot be run.

THIS REPORT IS FOR GUIDANCE ONLY. IF USED AS PART OF A REVIEW PROCEDURE FOR PUBLICATION, IT SHOULD NOT REPLACE THE EXPERTISE OF AN EXPERIENCED CRYSTALLOGRAPHIC REFEREE.

No syntax errors found. [CIF dictionary](#) [Interpreting this report](#)

Datablock: char429

Bond precision: C-C = 0.0049 A Wavelength=0.71073

Cell: a=44.049(2) b=9.6989(5) c=24.3038(13)
 alpha=90 beta=123.288(1) gamma=90

Temperature: 200 K

	Calculated	Reported
Volume	8679.6(8)	8679.7(8)
Space group	C 2/c	C2/c
Hall group	-C 2yc	?
Moiety formula	C39 H46 B Br N6 Ni, C5 H12 ?	
Sum formula	C44 H58 B Br N6 Ni	C44 H58 B Br N6 Ni
Mr	820.36	820.39
Dx, g cm-3	1.256	1.256
Z	8	8
Mu (mm-1)	1.404	1.404
F000	3456.0	3456.0
F000'	3457.25	
h,k,lmax	61,13,33	61,13,33
Nref	12281	12208
Tmin,Tmax	0.709,0.810	0.644,0.817
Tmin'	0.614	

Correction method= MULTI-SCAN

Data completeness= 0.994 Theta(max)= 29.650

R(reflections)= 0.0549(10062) wR2(reflections)= 0.1823(12208)

S = 1.010 Npar= 455

● Alert level C

PLAT411 ALERT 2 C Short Inter H...H Contact H21 .. H46B .. 2.06 Ang.

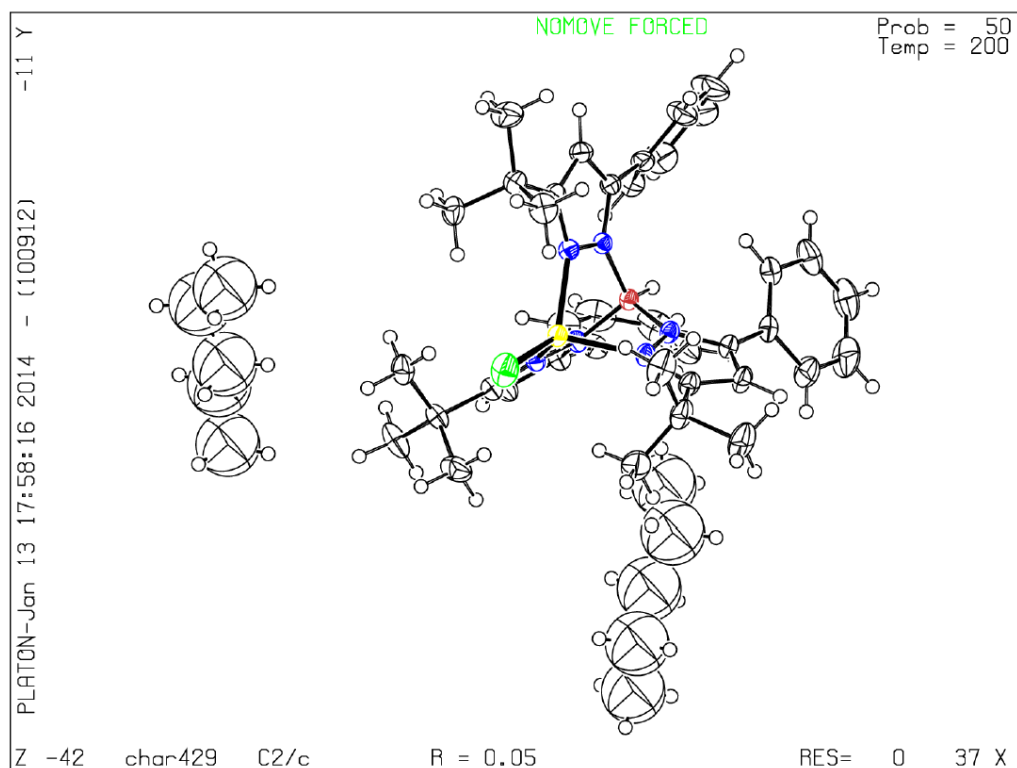
● Alert level G

PLAT005 ALERT 5 G	No _iucr_refine_instructions_details in the CIF	Please Do !
PLAT072 ALERT 2 G	SHELXL First Parameter in WGHT Unusually Large.	0.12
PLAT083 ALERT 2 G	SHELXL Second Parameter in WGHT Unusually Large.	17.98
PLAT128 ALERT 4 G	Alternate Setting for Input Space-Group C2/c	I2/a Note
PLAT232 ALERT 2 G	Hirshfeld Test Diff (M-X) Br -- Ni ..	44.5 su
PLAT302 ALERT 4 G	Anion/Solvent Disorder Percentage =	100 Note
PLAT790 ALERT 4 G	Centre of Gravity not Within Unit Cell: Resd. #	2

C5 H12

0 ALERT level A = Most likely a serious problem - resolve or explain
0 ALERT level B = A potentially serious problem, consider carefully
1 ALERT level C = Check. Ensure it is not caused by an omission or oversight
7 ALERT level G = General information/check it is not something unexpected

0 ALERT type 1 CIF construction/syntax error, inconsistent or missing data
4 ALERT type 2 Indicator that the structure model may be wrong or deficient
0 ALERT type 3 Indicator that the structure quality may be low
3 ALERT type 4 Improvement, methodology, query or suggestion
1 ALERT type 5 Informative message, check



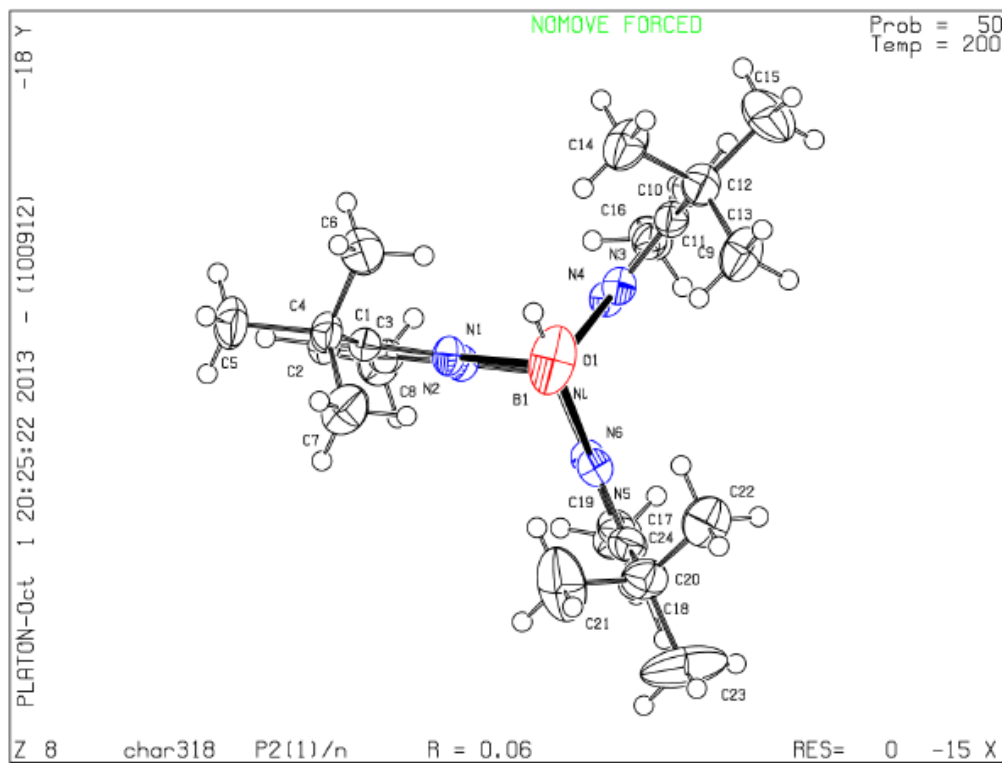
Alert level B
PLAT420 ALERT 2 B D-H Without Acceptor 01 - H1A ... Please Check

Author Response: Assignment of OH group consistent with Ni-O distance and noncrystallographic spectroscopy.

Alert level C
PLAT220 ALERT 2 C Large Non-Solvent C Ueq(max)/Ueq(min) ... 3.4 Ratio
PLAT222 ALERT 3 C Large Non-Solvent H Uiso(max)/Uiso(min) .. 4.3 Ratio
PLAT242 ALERT 2 C Low Ueq as Compared to Neighbors for C20 Check

Alert level G
PLAT005 ALERT 5 G No _iucr_refine_instructions_details in the CIF Please Do !
PLAT007 ALERT 5 G Number of Unrefined Donor-H Atoms 1 Why ?

-
- 0 **ALERT level A** = Most likely a serious problem - resolve or explain
 - 1 **ALERT level B** = A potentially serious problem, consider carefully
 - 3 **ALERT level C** = Check. Ensure it is not caused by an omission or oversight
 - 2 **ALERT level G** = General information/check it is not something unexpected
-
- 0 ALERT type 1 CIF construction/syntax error, inconsistent or missing data
 - 3 ALERT type 2 Indicator that the structure model may be wrong or deficient
 - 1 ALERT type 3 Indicator that the structure quality may be low
 - 0 ALERT type 4 Improvement, methodology, query or suggestion
 - 2 ALERT type 5 Informative message, check



Alert level A

PLAT601 ALERT 2 A Structure Contains Solvent Accessible VOIDS of . 420 Ang3

Author Response: Nothing chemically reasonable could be modeled in these spaces because of the low electron density (199 electrons per void). It is possible that these spaces are truly empty. The data presented have not been treated with Squeeze.

Alert level C

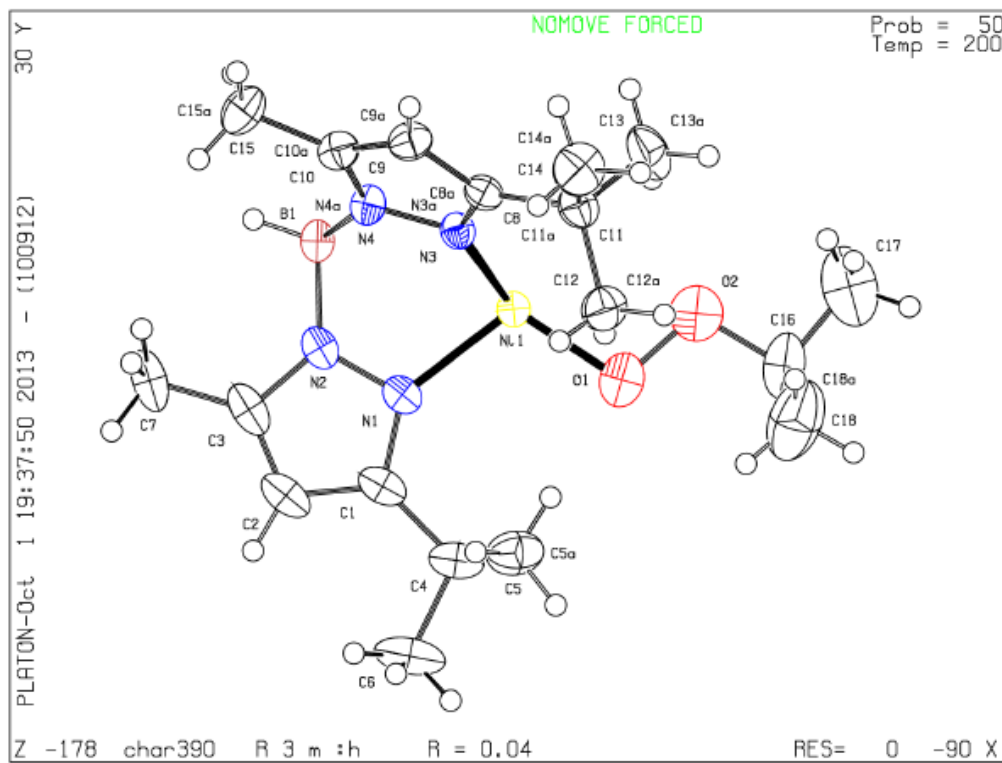
PLAT094 ALERT 2 C	Ratio of Maximum / Minimum Residual Density	2.23
PLAT220 ALERT 2 C	Large Non-Solvent C Ueq(max)/Ueq(min) ...	3.6 Ratio
PLAT222 ALERT 3 C	Large Non-Solvent H Uiso(max)/Uiso(min) ..	4.4 Ratio
PLAT242 ALERT 2 C	Low Ueq as Compared to Neighbors for	C16 Check
PLAT341 ALERT 3 C	Low Bond Precision on C-C Bonds	0.0079 Ang.

Alert level G

PLAT083 ALERT 2 G	SHELXL Second Parameter in WGHT Unusually Large.	5.32
PLAT232 ALERT 2 G	Hirshfeld Test Diff (M-X) Nil -- O1 ..	6.3 su

1 **ALERT level A** = Most likely a serious problem - resolve or explain
0 **ALERT level B** = A potentially serious problem, consider carefully
5 **ALERT level C** = Check. Ensure it is not caused by an omission or oversight
2 **ALERT level G** = General information/check it is not something unexpected

0 ALERT type 1 CIF construction/syntax error, inconsistent or missing data
6 ALERT type 2 Indicator that the structure model may be wrong or deficient
2 ALERT type 3 Indicator that the structure quality may be low
0 ALERT type 4 Improvement, methodology, query or suggestion
0 ALERT type 5 Informative message, check



5. Metallacycle checkCIF/PLATON report

You have not supplied any structure factors. As a result the full set of tests cannot be run.

THIS REPORT IS FOR GUIDANCE ONLY. IF USED AS PART OF A REVIEW PROCEDURE FOR PUBLICATION, IT SHOULD NOT REPLACE THE EXPERTISE OF AN EXPERIENCED CRYSTALLOGRAPHIC REFEREE.

No syntax errors found. [CIF dictionary](#) [Interpreting this report](#)

Datablock: char387

Bond precision: C-C = 0.0052 A Wavelength=0.71073

Cell: a=9.3513 (16) b=30.260 (5) c=9.5648 (16)
 alpha=90 beta=102.279 (3) gamma=90

Temperature: 200 K

	Calculated	Reported
Volume	2644.6 (8)	2644.6 (8)
Space group	P 21/n	P2 (1) /n
Hall group	-P 2yn	?
Moiety formula	C24 H39 B N6 Ni O	?
Sum formula	C24 H39 B N6 Ni O	C24 H39 B N6 Ni O
Mr	497.22	497.13
Dx, g cm-3	1.249	1.249
Z	4	4
Mu (mm-1)	0.760	0.760
F000	1064.2	1064.0
F000'	1065.80	
h,k,lmax	12,40,12	12,40,12
Nref	6579	6567
Tmin,Tmax	0.934,0.970	0.933,0.968
Tmin'	0.934	

Correction method= MULTI-SCAN

Data completeness= 0.998 Theta(max) = 28.300

R(reflections)= 0.0664 (4726) wR2(reflections)= 0.1971 (6567)

S = 1.008 Npar= 355

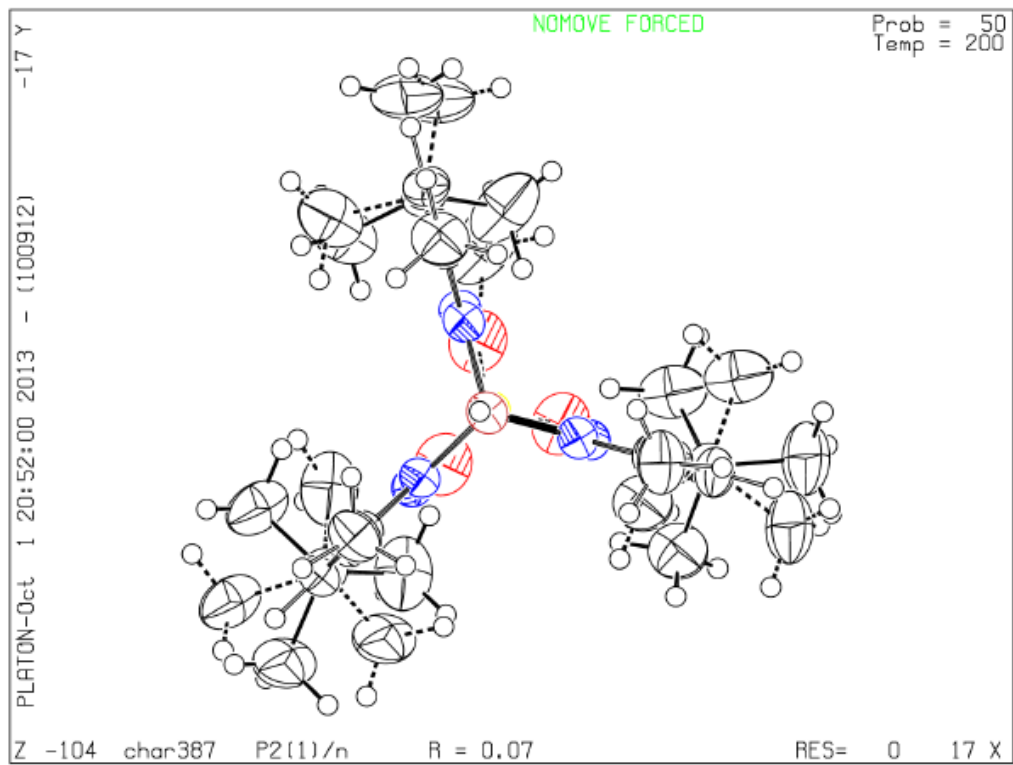
● **Alert level C**

PLAT068 ALERT 1 C	Reported F000 Differs from Calcd (or Missing)...	Please Check
PLAT234 ALERT 4 C	Large Hirshfeld Difference C4 -- C7 ...	0.16 Ang.
PLAT242 ALERT 2 C	Low Ueq as Compared to Neighbors for	C4 Check
PLAT242 ALERT 2 C	Low Ueq as Compared to Neighbors for	C12 Check
PLAT242 ALERT 2 C	Low Ueq as Compared to Neighbors for	C20 Check

● **Alert level G**

CELLZ01 ALERT 1 G	Difference between formula and atom_site contents detected.	
CELLZ01 ALERT 1 G	ALERT: check formula stoichiometry or atom site occupancies.	
	From the CIF: _cell_formula_units_Z 4	
	From the CIF: _chemical_formula_sum C24 H39 B N6 Ni O	
	TEST: Compare cell contents of formula and atom_site data	
	atom Z*formula cif sites diff	
	C 96.00 96.00 0.00	
	H 156.00 155.97 0.03	
	B 4.00 4.00 0.00	
	N 24.00 24.00 0.00	
	Ni 4.00 4.00 0.00	
	O 4.00 4.03 -0.03	
PLAT002 ALERT 2 G	Number of Distance or Angle Restraints on AtSite	25 Note
PLAT003 ALERT 2 G	Number of Uiso or Uij Restrained non-H Atoms ...	44
PLAT005 ALERT 5 G	No _iucr_refine_instructions_details in the CIF	Please Do !
PLAT230 ALERT 2 G	Hirshfeld Test Diff for C12 -- C13 ..	16.2 su
PLAT230 ALERT 2 G	Hirshfeld Test Diff for C12 -- C14 ..	12.5 su
PLAT230 ALERT 2 G	Hirshfeld Test Diff for C12 -- C15 ..	10.8 su
PLAT230 ALERT 2 G	Hirshfeld Test Diff for C20 -- C22 ..	7.7 su
PLAT230 ALERT 2 G	Hirshfeld Test Diff for C20 -- C23 ..	6.4 su
PLAT232 ALERT 2 G	Hirshfeld Test Diff (M-X) Ni -- O1 ..	6.7 su
PLAT232 ALERT 2 G	Hirshfeld Test Diff (M-X) Ni -- O2 ..	9.0 su
PLAT301 ALERT 3 G	Main Residue Disorder Percentage =	30 Note
PLAT720 ALERT 4 G	Number of Unusual/Non-Standard Labels	9
PLAT779 ALERT 4 G	Suspect or Irrelevant (Bond) Angle in CIF #	59
	C7' -C4 -C7 1.555 1.555 1.555	16.20 Deg.
PLAT779 ALERT 4 G	Suspect or Irrelevant (Bond) Angle in CIF #	60
	C6 -C4 -C6' 1.555 1.555 1.555	21.50 Deg.
PLAT779 ALERT 4 G	Suspect or Irrelevant (Bond) Angle in CIF #	67
	C5' -C4 -C5 1.555 1.555 1.555	27.40 Deg.
PLAT779 ALERT 4 G	Suspect or Irrelevant (Bond) Angle in CIF #	85
	C15 -C12 -C13' 1.555 1.555 1.555	42.20 Deg.
PLAT779 ALERT 4 G	Suspect or Irrelevant (Bond) Angle in CIF #	115
	C22 -C20 -C22' 1.555 1.555 1.555	37.30 Deg.
PLAT779 ALERT 4 G	Suspect or Irrelevant (Bond) Angle in CIF #	116
	C23' -C20 -C23 1.555 1.555 1.555	41.80 Deg.
PLAT779 ALERT 4 G	Suspect or Irrelevant (Bond) Angle in CIF #	122
	C21 -C20 -C21' 1.555 1.555 1.555	43.90 Deg.
PLAT811 ALERT 5 G	No ADDSYM Analysis: Too Many Excluded Atoms	! Info
PLAT860 ALERT 3 G	Number of Least-Squares Restraints	571 Note

0 **ALERT level A** = Most likely a serious problem - resolve or explain
0 **ALERT level B** = A potentially serious problem, consider carefully
5 **ALERT level C** = Check. Ensure it is not caused by an omission or oversight
23 **ALERT level G** = General information/check it is not something unexpected



Alert level B

PLAT220 ALERT 2 B Large Non-Solvent C Ueq(max)/Ueq(min) ... 4.2 Ratio

Author Response: Slight unresolvable disorder at the t-butyl groups cause a large range in C Ueq.

Alert level C

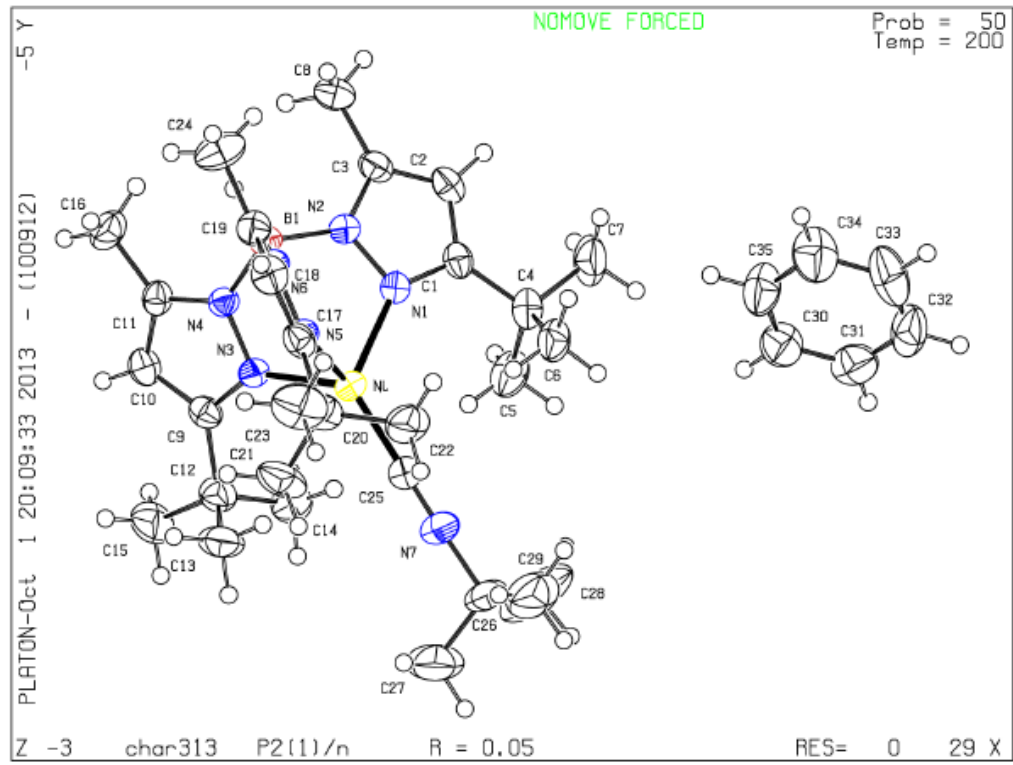
PLAT094 ALERT 2 C Ratio of Maximum / Minimum Residual Density ... 2.89
PLAT222 ALERT 3 C Large Non-Solvent H Uiso(max)/Uiso(min) .. 5.7 Ratio
PLAT242 ALERT 2 C Low Ueq as Compared to Neighbors for C26 Check
PLAT331 ALERT 2 C Small Average Phenyl C-C Dist. C30 -C35 1.37 Ang.

Alert level G

PLAT005 ALERT 5 G No _iucr_refine_instructions_details in the CIF Please Do !
PLAT232 ALERT 2 G Hirshfeld Test Diff (M-X) Ni -- C25 .. 6.9 su
PLAT710 ALERT 4 G Delete 1-2-3 or 2-3-4 Linear Torsion Angle ... # 97 Do !
C26 -N7 -C25 -NI 81.00 61.00 1.555 1.555 1.555 1.555
PLAT710 ALERT 4 G Delete 1-2-3 or 2-3-4 Linear Torsion Angle ... # 98 Do !
N3 -NI -C25 -N7 21.00 61.00 1.555 1.555 1.555 1.555
PLAT710 ALERT 4 G Delete 1-2-3 or 2-3-4 Linear Torsion Angle ... # 99 Do !
N1 -NI -C25 -N7 -98.00 61.00 1.555 1.555 1.555 1.555
PLAT710 ALERT 4 G Delete 1-2-3 or 2-3-4 Linear Torsion Angle ... # 100 Do !
N5 -NI -C25 -N7 14.00 0.00 1.555 1.555 1.555 1.555
PLAT710 ALERT 4 G Delete 1-2-3 or 2-3-4 Linear Torsion Angle ... # 101 Do !
C25 -N7 -C26 -C27 -138.00 5.00 1.555 1.555 1.555 1.555
PLAT710 ALERT 4 G Delete 1-2-3 or 2-3-4 Linear Torsion Angle ... # 102 Do !
C25 -N7 -C26 -C29 102.00 5.00 1.555 1.555 1.555 1.555
PLAT710 ALERT 4 G Delete 1-2-3 or 2-3-4 Linear Torsion Angle ... # 103 Do !
C25 -N7 -C26 -C28 -17.00 5.00 1.555 1.555 1.555 1.555

0 ALERT level A = Most likely a serious problem - resolve or explain
1 ALERT level B = A potentially serious problem, consider carefully
4 ALERT level C = Check. Ensure it is not caused by an omission or oversight
9 ALERT level G = General information/check it is not something unexpected

0 ALERT type 1 CIF construction/syntax error, inconsistent or missing data
5 ALERT type 2 Indicator that the structure model may be wrong or deficient
1 ALERT type 3 Indicator that the structure quality may be low
7 ALERT type 4 Improvement, methodology, query or suggestion
1 ALERT type 5 Informative message, check



Alert level A

PLAT241	ALERT 2 A	High	'MainMol' Ueq as Compared to Neighbors of	O4	Check
---------	-----------	------	-------------------------------------------	----	-------

Alert level B

PLAT230	ALERT 2 B	Hirshfeld Test Diff for	O3 -- N10 ..	24.5	s.u.
PLAT242	ALERT 2 B	Low	'MainMol' Ueq as Compared to Neighbors of	Ni2	Check

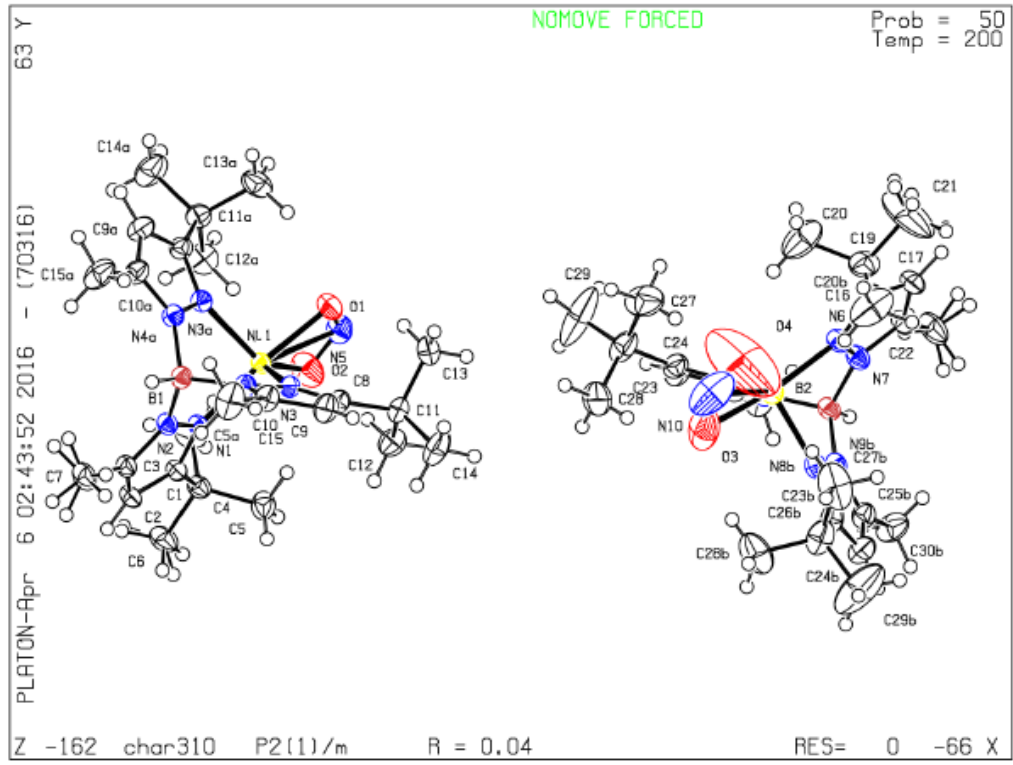
Alert level C

PLAT213	ALERT 2 C	Atom O4	has ADP max/min Ratio	3.7	prolat
PLAT213	ALERT 2 C	Atom C21	has ADP max/min Ratio	3.4	prolat
PLAT220	ALERT 2 C	Non-Solvent Resd 2	C Ueq(max)/Ueq(min) Range	4.0	Ratio
PLAT220	ALERT 2 C	Non-Solvent Resd 2	N Ueq(max)/Ueq(min) Range	3.1	Ratio
PLAT222	ALERT 3 C	Non-Solvent Resd 2	H Uiso(max)/Uiso(min) Range	6.0	Ratio
PLAT230	ALERT 2 C	Hirshfeld Test Diff for	O1 -- N5 ..	5.9	s.u.
PLAT234	ALERT 4 C	Large Hirshfeld Difference	O4 -- N10 ..	0.16	Ang.
PLAT241	ALERT 2 C	High	'MainMol' Ueq as Compared to Neighbors of	O2	Check
PLAT241	ALERT 2 C	High	'MainMol' Ueq as Compared to Neighbors of	O3	Check
PLAT242	ALERT 2 C	Low	'MainMol' Ueq as Compared to Neighbors of	N10	Check
PLAT242	ALERT 2 C	Low	'MainMol' Ueq as Compared to Neighbors of	C19	Check
PLAT242	ALERT 2 C	Low	'MainMol' Ueq as Compared to Neighbors of	C26	Check

Alert level G

PLAT005	ALERT 5 G	No Embedded Refinement Details found in the CIF	Please Do !
PLAT066	ALERT 1 G	Predicted and Reported Tmin&Tmax Range Identical	? Check
PLAT232	ALERT 2 G	Hirshfeld Test Diff (M-X) Ni1 -- O1 ..	8.1 s.u.
PLAT232	ALERT 2 G	Hirshfeld Test Diff (M-X) Ni1 -- O2 ..	7.5 s.u.
PLAT232	ALERT 2 G	Hirshfeld Test Diff (M-X) Ni1 -- N5 ..	6.4 s.u.
PLAT232	ALERT 2 G	Hirshfeld Test Diff (M-X) Ni2 -- O3 ..	5.7 s.u.
PLAT232	ALERT 2 G	Hirshfeld Test Diff (M-X) Ni2 -- O4 ..	5.7 s.u.
PLAT232	ALERT 2 G	Hirshfeld Test Diff (M-X) Ni2 -- N10 ..	12.7 s.u.
PLAT300	ALERT 4 G	Atom Site Occupancy of *H6A is Constrained at	0.5 Check
PLAT300	ALERT 4 G	Atom Site Occupancy of *H6B is Constrained at	0.5 Check
PLAT300	ALERT 4 G	Atom Site Occupancy of *H6C is Constrained at	0.5 Check
PLAT300	ALERT 4 G	Atom Site Occupancy of *H7A is Constrained at	0.5 Check
PLAT300	ALERT 4 G	Atom Site Occupancy of *H7B is Constrained at	0.5 Check
PLAT300	ALERT 4 G	Atom Site Occupancy of *H7C is Constrained at	0.5 Check
PLAT300	ALERT 4 G	Atom Site Occupancy of *H21A is Constrained at	0.5 Check
PLAT300	ALERT 4 G	Atom Site Occupancy of *H21B is Constrained at	0.5 Check
PLAT300	ALERT 4 G	Atom Site Occupancy of *H21C is Constrained at	0.5 Check
PLAT300	ALERT 4 G	Atom Site Occupancy of *H22A is Constrained at	0.5 Check
PLAT300	ALERT 4 G	Atom Site Occupancy of *H22B is Constrained at	0.5 Check
PLAT300	ALERT 4 G	Atom Site Occupancy of *H22C is Constrained at	0.5 Check
PLAT367	ALERT 2 G	Long? C(sp?)-C(sp?) Bond C3 - C7 ..	1.50 Ang.
PLAT367	ALERT 2 G	Long? C(sp?)-C(sp?) Bond C4 - C6 ..	1.53 Ang.
PLAT367	ALERT 2 G	Long? C(sp?)-C(sp?) Bond C19 - C21 ..	1.51 Ang.
PLAT899	ALERT 4 G	SHELXL97 is Deprecated and Succeeded by SHELXL	2014 Note

- 1 **ALERT level A** = Most likely a serious problem - resolve or explain
 2 **ALERT level B** = A potentially serious problem, consider carefully
 12 **ALERT level C** = Check. Ensure it is not caused by an omission or oversight
 24 **ALERT level G** = General information/check it is not something unexpected



Alert level B

PLAT094 ALERT 2 B	Ratio of Maximum / Minimum Residual Density ...	6.90	Report
PLAT241 ALERT 2 B	High 'MainMol' Ueq as Compared to Neighbors of	05	Check

Alert level C

STRVA01 ALERT 4 C Flack test results are ambiguous.
From the CIF: _refine_ls_abs_structure_Flack 0.370
From the CIF: _refine_ls_abs_structure_Flack_su 0.011

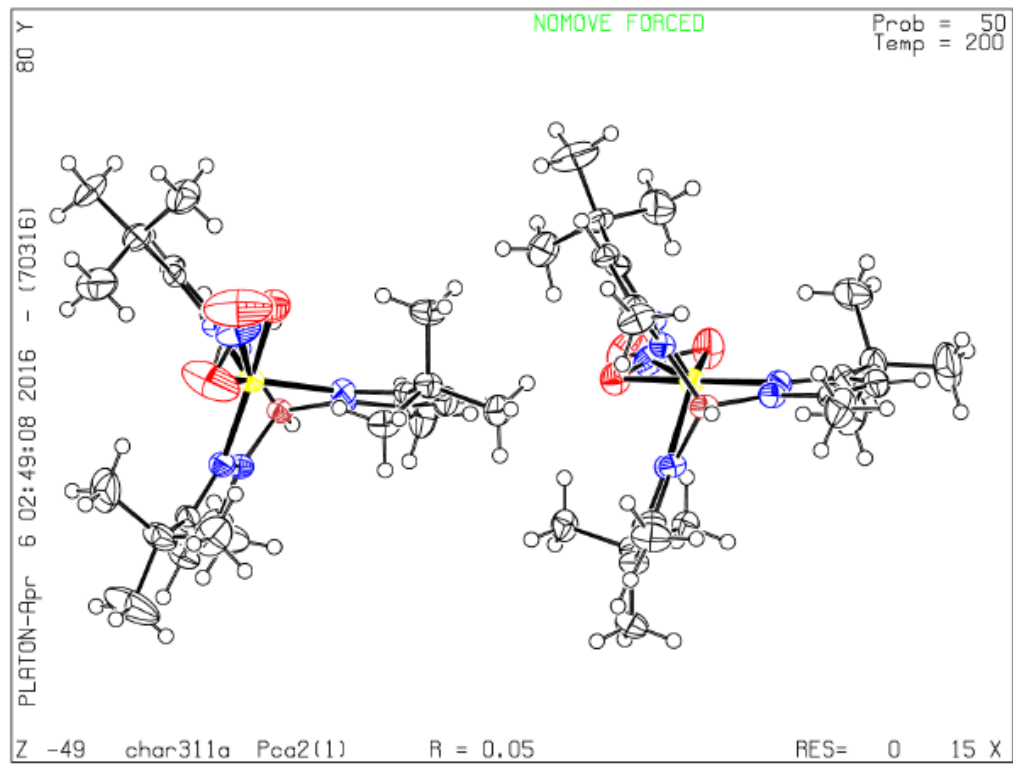
PLAT220 ALERT 2 C	Non-Solvent Resd 2 C Ueq(max)/Ueq(min) Range	3.9	Ratio
PLAT222 ALERT 3 C	Non-Solvent Resd 2 H Uiso(max)/Uiso(min) Range	4.6	Ratio
PLAT241 ALERT 2 C	High 'MainMol' Ueq as Compared to Neighbors of	01	Check
PLAT242 ALERT 2 C	Low 'MainMol' Ueq as Compared to Neighbors of	Ni2	Check
PLAT242 ALERT 2 C	Low 'MainMol' Ueq as Compared to Neighbors of	C37	Check

Alert level G

PLAT005 ALERT 5 G	No Embedded Refinement Details found in the CIF	Please Do !
PLAT066 ALERT 1 G	Predicted and Reported Tmin&Tmax Range Identical	? Check
PLAT232 ALERT 2 G	Hirshfeld Test Diff (M-X) Nil -- O1 ..	9.1 s.u.
PLAT232 ALERT 2 G	Hirshfeld Test Diff (M-X) Nil -- O3 ..	6.7 s.u.
PLAT232 ALERT 2 G	Hirshfeld Test Diff (M-X) Ni2 -- O4 ..	9.0 s.u.
PLAT899 ALERT 4 G	SHELXL97 is Deprecated and Succeeded by SHELXL	2014 Note

0 ALERT level A = Most likely a serious problem - resolve or explain
2 ALERT level B = A potentially serious problem, consider carefully
6 ALERT level C = Check. Ensure it is not caused by an omission or oversight
6 ALERT level G = General information/check it is not something unexpected

1 ALERT type 1 CIF construction/syntax error, inconsistent or missing data
9 ALERT type 2 Indicator that the structure model may be wrong or deficient
1 ALERT type 3 Indicator that the structure quality may be low
2 ALERT type 4 Improvement, methodology, query or suggestion
1 ALERT type 5 Informative message, check



9. [Tp^{tBu,Ph}]Ni(CNtBu)
checkCIF/PLATON report

You have not supplied any structure factors. As a result the full set of tests cannot be run.

THIS REPORT IS FOR GUIDANCE ONLY. IF USED AS PART OF A REVIEW PROCEDURE FOR PUBLICATION, IT SHOULD NOT REPLACE THE EXPERTISE OF AN EXPERIENCED CRYSTALLOGRAPHIC REFEREE.

No syntax errors found. [CIF dictionary](#) [Interpreting this report](#)

Datablock: char457

Bond precision: C-C = 0.0038 A Wavelength=0.71073

Cell: a=9.7125 (7) b=28.446 (2) c=17.9486 (13)
 alpha=90 beta=100.168 (1) gamma=90

Temperature: 200 K

	Calculated	Reported
Volume	4881.0 (6)	4880.9 (6)
Space group	P 21/c	P2 (1) /c
Hall group	-P 2ybc	?
Moiety formula	C44 H55 B N7 Ni, C5 H12	?
Sum formula	C49 H67 B N7 Ni	C49 H67 B N7 Ni
Mr	823.60	823.62
Dx, g cm-3	1.121	1.121
Z	4	4
Mu (mm-1)	0.436	0.436
F000	1772.0	1772.0
F000'	1773.81	
h,k,lmax	12,37,23	12,36,23
Nref	11283	11257
Tmin,Tmax	0.877,0.945	0.879,0.946
Tmin'	0.877	

Correction method= MULTI-SCAN

Data completeness= 0.998 Theta(max)= 27.550

R(reflections)= 0.0455 (8536) wR2(reflections)= 0.1280 (11257)

S = 1.043 Npar= 523

Alert level B

PLAT220 ALERT 2 B Large Non-Solvent C Ueq(max)/Ueq(min) ... 4.1 Ratio

Author Response: Unresolvable slight disorder in the t-butyl groups lead to wider range of C Ueq.

Alert level C

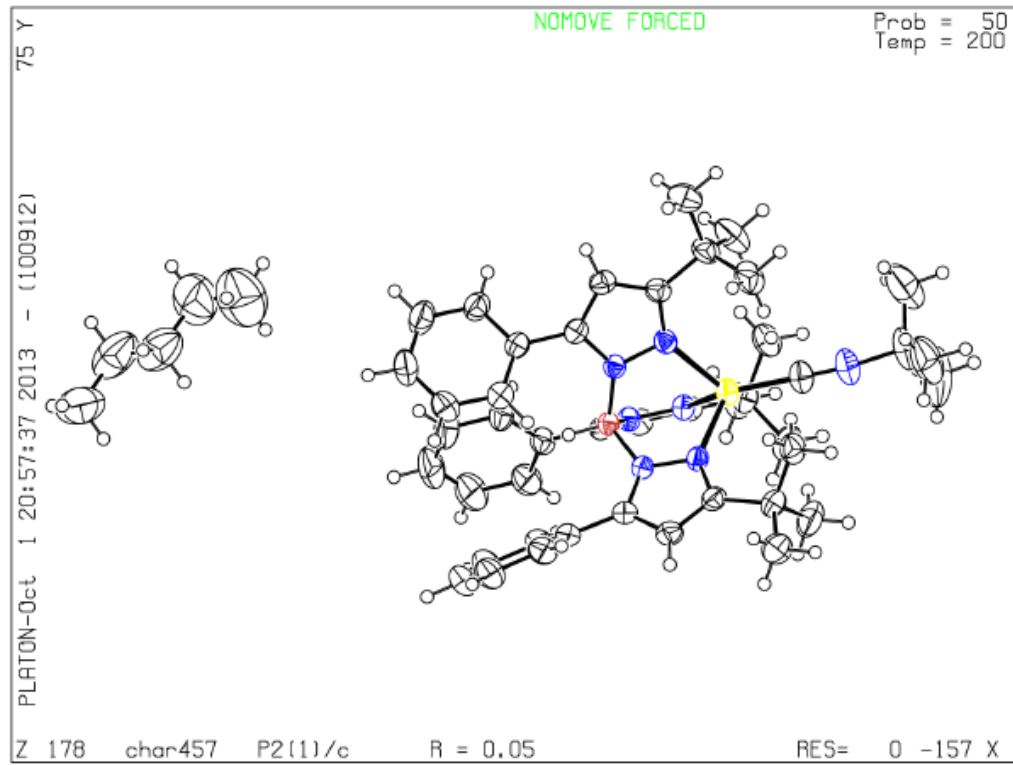
PLAT222 ALERT 3 C Large Non-Solvent H Uiso(max)/Uiso(min) .. 5.6 Ratio
PLAT242 ALERT 2 C Low Ueq as Compared to Neighbors for C45 Check
PLAT244 ALERT 4 C Low 'Solvent' Ueq as Compared to Neighbors of C48 Check

Alert level G

PLAT005 ALERT 5 G No _iucr_refine_instructions_details in the CIF Please Do !
PLAT232 ALERT 2 G Hirshfeld Test Diff (M-X) Ni -- C41 .. 5.1 su
PLAT710 ALERT 4 G Delete 1-2-3 or 2-3-4 Linear Torsion Angle ... # 133 Do !
C45 -N7 -C41 -NI -53.00 7.00 1.555 1.555 1.555 1.555
PLAT710 ALERT 4 G Delete 1-2-3 or 2-3-4 Linear Torsion Angle ... # 134 Do !
N1 -NI -C41 -N7 161.00 6.00 1.555 1.555 1.555 1.555
PLAT710 ALERT 4 G Delete 1-2-3 or 2-3-4 Linear Torsion Angle ... # 135 Do !
N3 -NI -C41 -N7 -79.00 6.00 1.555 1.555 1.555 1.555
PLAT710 ALERT 4 G Delete 1-2-3 or 2-3-4 Linear Torsion Angle ... # 136 Do !
N5 -NI -C41 -N7 40.00 6.00 1.555 1.555 1.555 1.555
PLAT710 ALERT 4 G Delete 1-2-3 or 2-3-4 Linear Torsion Angle ... # 137 Do !
C41 -N7 -C45 -C44 -140.00 2.00 1.555 1.555 1.555 1.555
PLAT710 ALERT 4 G Delete 1-2-3 or 2-3-4 Linear Torsion Angle ... # 138 Do !
C41 -N7 -C45 -C42 96.00 2.00 1.555 1.555 1.555 1.555
PLAT710 ALERT 4 G Delete 1-2-3 or 2-3-4 Linear Torsion Angle ... # 139 Do !
C41 -N7 -C45 -C43 -24.00 2.00 1.555 1.555 1.555 1.555

0 ALERT level A = Most likely a serious problem - resolve or explain
1 ALERT level B = A potentially serious problem, consider carefully
3 ALERT level C = Check. Ensure it is not caused by an omission or oversight
9 ALERT level G = General information/check it is not something unexpected

0 ALERT type 1 CIF construction/syntax error, inconsistent or missing data
3 ALERT type 2 Indicator that the structure model may be wrong or deficient
1 ALERT type 3 Indicator that the structure quality may be low
8 ALERT type 4 Improvement, methodology, query or suggestion
1 ALERT type 5 Informative message, check



● **Alert level C**

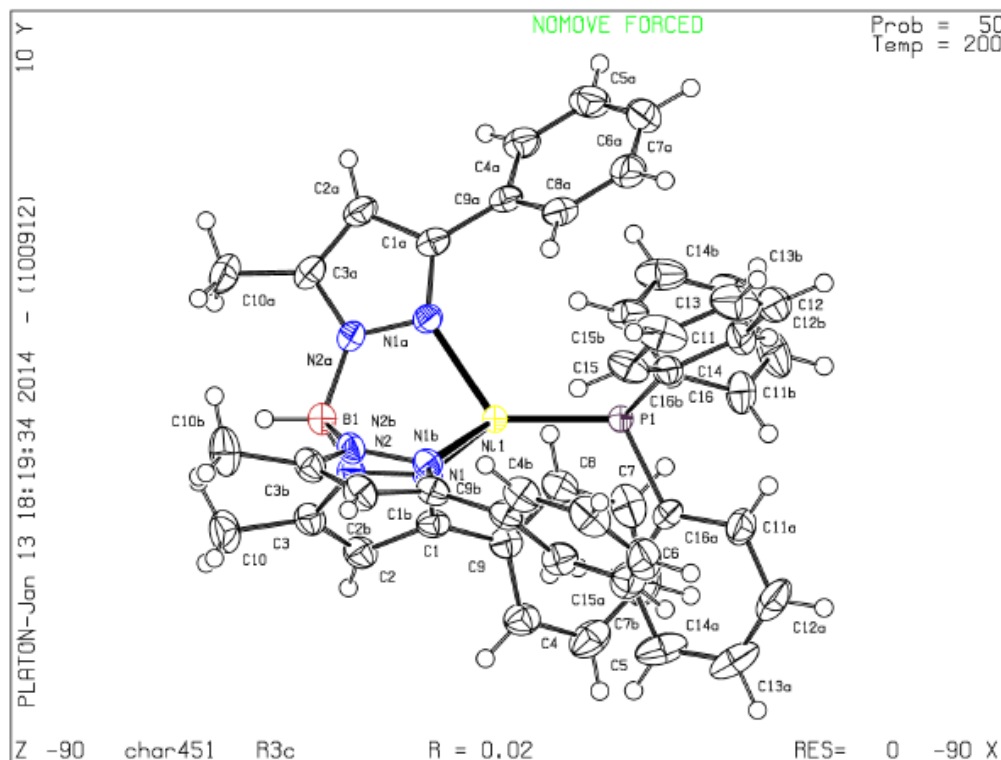
PLAT090 ALERT 3 C	Poor Data / Parameter Ratio (Zmax > 18)	9.18
PLAT094 ALERT 2 C	Ratio of Maximum / Minimum Residual Density	2.32

● **Alert level G**

PLAT003 ALERT 2 G	Number of Uiso or Uij Restrained non-H Atoms ...	21
PLAT005 ALERT 5 G	No _iucr_refine_instructions_details in the CIF	Please Do !
PLAT152 ALERT 1 G	The Supplied and Calc. Volume s.u. Differ by ...	5 Units
PLAT860 ALERT 3 G	Number of Least-Squares Restraints	55 Note

- 0 **ALERT level A** = Most likely a serious problem - resolve or explain
0 **ALERT level B** = A potentially serious problem, consider carefully
2 **ALERT level C** = Check. Ensure it is not caused by an omission or oversight
4 **ALERT level G** = General information/check it is not something unexpected

- 1 ALERT type 1 CIF construction/syntax error, inconsistent or missing data
2 ALERT type 2 Indicator that the structure model may be wrong or deficient
2 ALERT type 3 Indicator that the structure quality may be low
0 ALERT type 4 Improvement, methodology, query or suggestion
1 ALERT type 5 Informative message, check

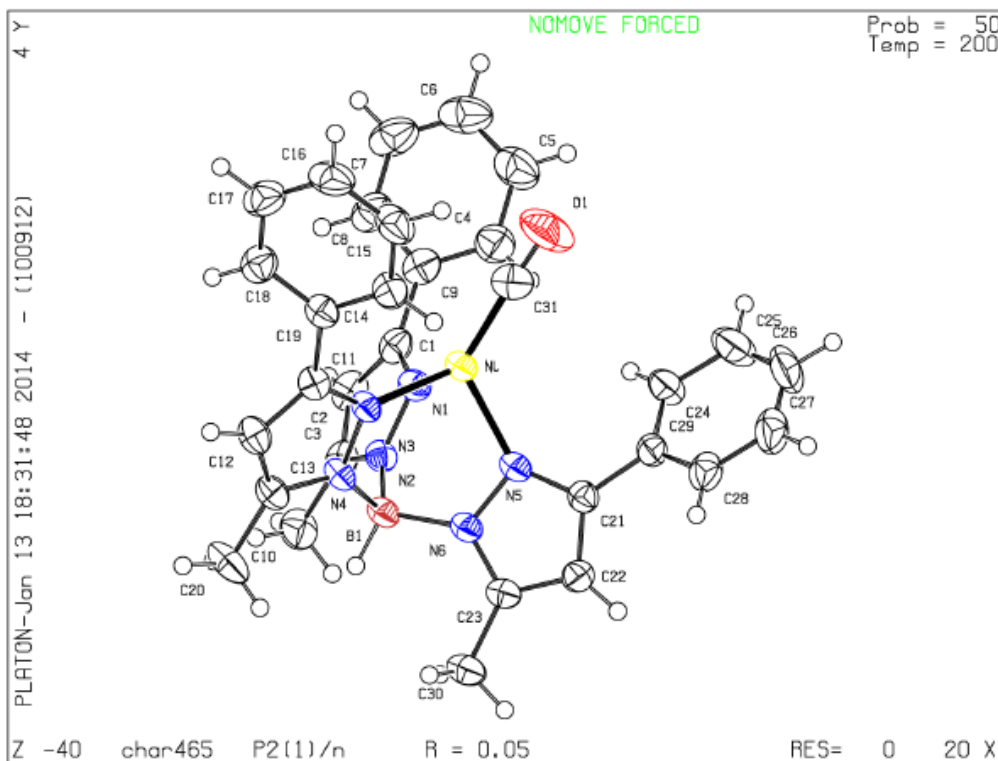


Alert level G

PLAT003 ALERT 2 G	Number of Uiso or Uij Restrained non-H Atoms ...	40
PLAT005 ALERT 5 G	No _iucr_refine_instructions_details in the CIF	Please Do !
PLAT083 ALERT 2 G	SHELXL Second Parameter in WGHT Unusually Large.	5.20
PLAT232 ALERT 2 G	Hirshfeld Test Diff (M-X) Ni -- C31 ..	10.3 su
PLAT710 ALERT 4 G	Delete 1-2-3 or 2-3-4 Linear Torsion Angle ... #	115 Do !
	N5 -NI -C31 -O1 61.00 5.00 1.555 1.555 1.555	1.555
PLAT710 ALERT 4 G	Delete 1-2-3 or 2-3-4 Linear Torsion Angle ... #	116 Do !
	N1 -NI -C31 -O1 -51.00 5.00 1.555 1.555 1.555	1.555
PLAT710 ALERT 4 G	Delete 1-2-3 or 2-3-4 Linear Torsion Angle ... #	117 Do !
	N3 -NI -C31 -O1 -173.00 5.00 1.555 1.555 1.555	1.555
PLAT860 ALERT 3 G	Number of Least-Squares Restraints	120 Note

0 ALERT level A = Most likely a serious problem - resolve or explain
 0 ALERT level B = A potentially serious problem, consider carefully
 0 ALERT level C = Check. Ensure it is not caused by an omission or oversight
 8 ALERT level G = General information/check it is not something unexpected

0 ALERT type 1 CIF construction/syntax error, inconsistent or missing data
 3 ALERT type 2 Indicator that the structure model may be wrong or deficient
 1 ALERT type 3 Indicator that the structure quality may be low
 3 ALERT type 4 Improvement, methodology, query or suggestion
 1 ALERT type 5 Informative message, check



● **Alert level C**

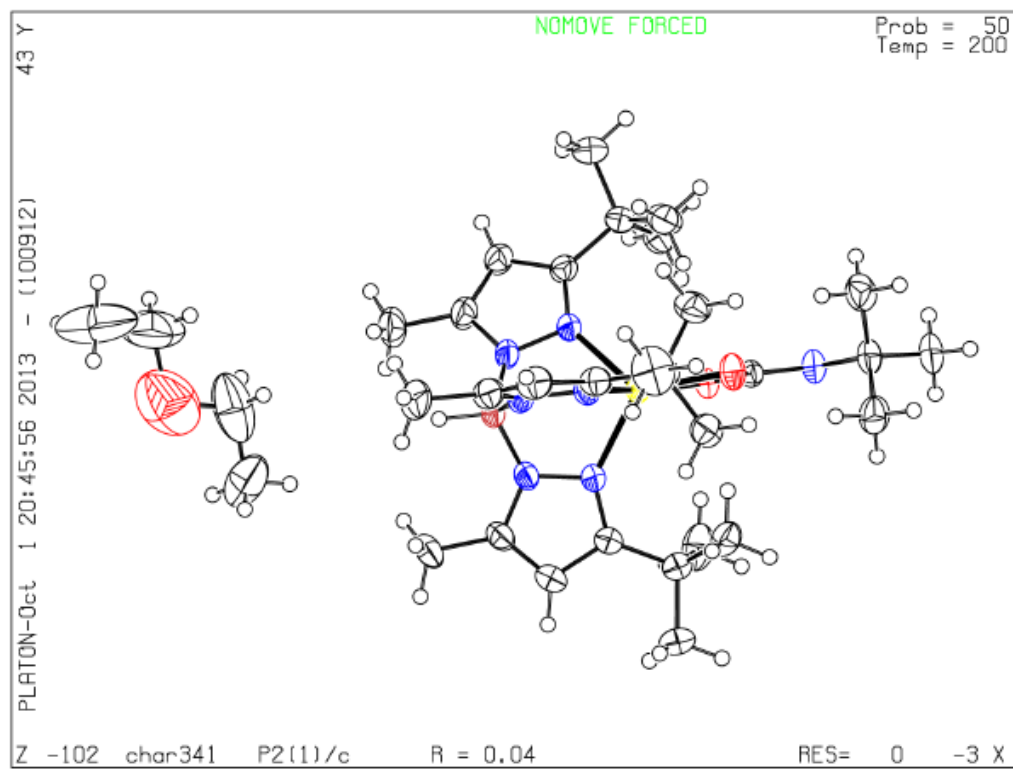
PLAT242 ALERT 2 C	Low	Ueq as Compared to Neighbors for	C12	Check
PLAT243 ALERT 4 C	High	'Solvent' Ueq as Compared to Neighbors of	O3	Check
PLAT360 ALERT 2 C	Short	C(sp3)-C(sp3) Bond C32 - C33 ...	1.37	Ang.
PLAT601 ALERT 2 C		Structure Contains Solvent Accessible VOIDS of .	51	Ang3

● **Alert level G**

PLAT005 ALERT 5 G	No	_iucr_refine_instructions_details	in the CIF	Please	Do !
PLAT232 ALERT 2 G	Hirshfeld	Test Diff (M-X)	Ni -- O1 ..	8.3	su
PLAT232 ALERT 2 G	Hirshfeld	Test Diff (M-X)	Ni -- O2 ..	5.6	su
PLAT380 ALERT 4 G	Incorrectly?	Oriented X(sp2)-Methyl	Moiety	C8	Check
PLAT710 ALERT 4 G	Delete 1-2-3	or 2-3-4	Linear Torsion Angle ... #	123	Do !
	C26 -N7	-C25 -NI	-53.00 4.00 1.555 1.555 1.555	1.555	
PLAT710 ALERT 4 G	Delete 1-2-3	or 2-3-4	Linear Torsion Angle ... #	132	Do !
	O1 -NI	-C25 -N7	55.00 4.00 1.555 1.555 1.555	1.555	
PLAT710 ALERT 4 G	Delete 1-2-3	or 2-3-4	Linear Torsion Angle ... #	133	Do !
	N1 -NI	-C25 -N7	18.00 0.00 1.555 1.555 1.555	1.555	
PLAT710 ALERT 4 G	Delete 1-2-3	or 2-3-4	Linear Torsion Angle ... #	134	Do !
	N3 -NI	-C25 -N7	-65.00 4.00 1.555 1.555 1.555	1.555	
PLAT710 ALERT 4 G	Delete 1-2-3	or 2-3-4	Linear Torsion Angle ... #	135	Do !
	N5 -NI	-C25 -N7	56.00 4.00 1.555 1.555 1.555	1.555	
PLAT710 ALERT 4 G	Delete 1-2-3	or 2-3-4	Linear Torsion Angle ... #	136	Do !
	O2 -NI	-C25 -N7	-126.00 4.00 1.555 1.555 1.555	1.555	

0 **ALERT level A** = Most likely a serious problem - resolve or explain
0 **ALERT level B** = A potentially serious problem, consider carefully
4 **ALERT level C** = Check. Ensure it is not caused by an omission or oversight
10 **ALERT level G** = General information/check it is not something unexpected

0 ALERT type 1 CIF construction/syntax error, inconsistent or missing data
5 ALERT type 2 Indicator that the structure model may be wrong or deficient
0 ALERT type 3 Indicator that the structure quality may be low
8 ALERT type 4 Improvement, methodology, query or suggestion
1 ALERT type 5 Informative message, check



13. [Tp^{tBu,Me}]Ni(O₂CN(H)Cy)
checkCIF/PLATON report

You have not supplied any structure factors. As a result the full set of tests cannot be run.

THIS REPORT IS FOR GUIDANCE ONLY. IF USED AS PART OF A REVIEW PROCEDURE FOR PUBLICATION, IT SHOULD NOT REPLACE THE EXPERTISE OF AN EXPERIENCED CRYSTALLOGRAPHIC REFEREE.

No syntax errors found. [CIF dictionary](#) [Interpreting this report](#)

Datablock: char329

Bond precision: C-C = 0.0053 A Wavelength=0.71073
Cell: a=21.892 (8) b=12.062 (4) c=26.556 (10)
 alpha=90 beta=105.327 (7) gamma=90
Temperature: 200 K

	Calculated	Reported
Volume	6763 (4)	6763 (4)
Space group	P 21/c	P2 (1) /c
Hall group	-P 2ybc	?
Moiety formula	C31 H52 B N7 Ni O2	?
Sum formula	C31 H52 B N7 Ni O2	C31 H52 B N7 Ni O2
Mr	624.30	624.32
Dx, g cm-3	1.226	1.226
Z	8	8
Mu (mm-1)	0.611	0.611
F000	2688.0	2688.0
F000'	2691.43	
h,k,lmax	29,16,35	29,16,35
Nref	16841	16796
Tmin,Tmax	0.783,0.822	0.792,0.829
Tmin'	0.783	

Correction method= MULTI-SCAN

Data completeness= 0.997 Theta(max)= 28.320

R(reflections)= 0.0656 (10242) wR2(reflections)= 0.1930 (16796)

S = 1.013 Npar= 793

Alert level B

PLAT094 ALERT 2 B Ratio of Maximum / Minimum Residual Density ... 5.60

Author Response: Peaks are located less than 1 Ang from the nickel atom sites and were ignored as artefactual.

PLAT220 ALERT 2 B Large Non-Solvent C Ueq(max)/Ueq(min) ... 4.2 Ratio

Author Response: Slight unresolvable disorder in the cyclohexyl rings cause wider range of C Ueq.

PLAT230 ALERT 2 B Hirshfeld Test Diff for C28 -- C29 .. 8.5 su

Author Response: The carbon atom identities assigned are consistent with synthesis.

Alert level C

DIFMX01 ALERT 2 C The maximum difference density is > 0.1*ZMAX*0.75
_refine_diff_density_max given = 2.365
Test value = 2.100

DIFMX02 ALERT 1 C The maximum difference density is > 0.1*ZMAX*0.75
The relevant atom site should be identified.

PLAT097 ALERT 2 C Large Reported Max. (Positive) Residual Density 2.37 eA-3

PLAT220 ALERT 2 C Large Non-Solvent C Ueq(max)/Ueq(min) ... 3.3 Ratio

Author Response: Slight unresolvable disorder in the cyclohexyl rings cause wider range of C Ueq.

PLAT222 ALERT 3 C Large Non-Solvent H Uiso(max)/Uiso(min) .. 4.5 Ratio

PLAT222 ALERT 3 C Large Non-Solvent H Uiso(max)/Uiso(min) .. 4.1 Ratio

PLAT234 ALERT 4 C Large Hirshfeld Difference C29 -- C30 .. 0.17 Ang.

PLAT241 ALERT 2 C High Ueq as Compared to Neighbors for C29 Check

PLAT241 ALERT 2 C High Ueq as Compared to Neighbors for C60 Check

PLAT242 ALERT 2 C Low Ueq as Compared to Neighbors for C43 Check

PLAT242 ALERT 2 C Low Ueq as Compared to Neighbors for C59 Check

PLAT242 ALERT 2 C Low Ueq as Compared to Neighbors for C62 Check

PLAT790 ALERT 4 C Centre of Gravity not Within Unit Cell: Resd. # 1
C31 H52 B N7 N1 O2

Alert level G

PLAT005 ALERT 5 G No _iucr_refine_instructions_details in the CIF Please Do !

PLAT072 ALERT 2 G SHELXL First Parameter in WGHT Unusually Large. 0.11

PLAT232 ALERT 2 G Hirshfeld Test Diff (M-X) N11 -- O1 .. 6.5 su

PLAT380 ALERT 4 G Incorrectly? Oriented X(sp2)-Methyl Moiety C8 Check

PLAT380 ALERT 4 G Incorrectly? Oriented X(sp2)-Methyl Moiety C47 Check

PLAT710 ALERT 4 G Delete 1-2-3 or 2-3-4 Linear Torsion Angle ... # 5 Do !

N3 -N11 -O2 -C25 -1.20 0.90 1.555 1.555 1.555 1.555

PLAT710 ALERT 4 G Delete 1-2-3 or 2-3-4 Linear Torsion Angle ... # 10 Do !

N12 -N12 -O3 -C56 -3.00 0.80 1.555 1.555 1.555 1.555

PLAT710 ALERT 4 G Delete 1-2-3 or 2-3-4 Linear Torsion Angle ... # 59 Do !

O2 -N11 -C25 -N7 -20.00 8.00 1.555 1.555 1.555 1.555

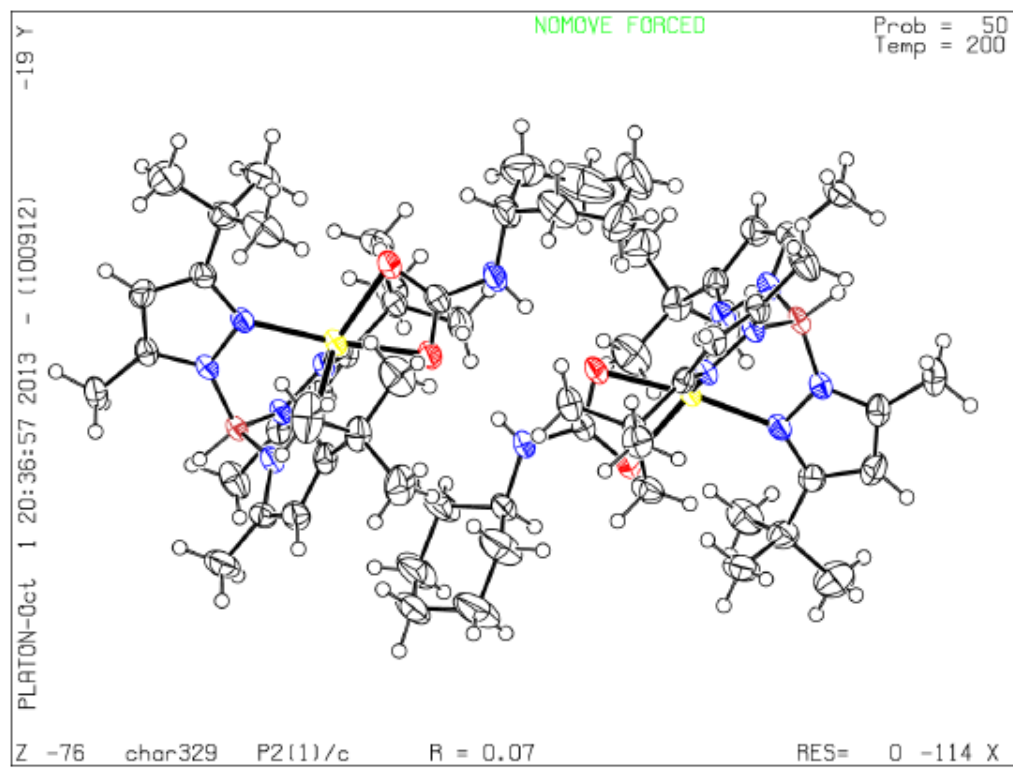
PLAT710 ALERT 4 G Delete 1-2-3 or 2-3-4 Linear Torsion Angle ... # 60 Do !

N3 -N11 -C25 -N7 160.00 8.00 1.555 1.555 1.555 1.555

PLAT710 ALERT 4 G	Delete 1-2-3 or 2-3-4 Linear Torsion Angle ... #	61 Do !
N1 -N11 -C25 -N7	33.00 8.00 1.555 1.555 1.555	1.555
PLAT710 ALERT 4 G	Delete 1-2-3 or 2-3-4 Linear Torsion Angle ... #	62 Do !
N5 -N11 -C25 -N7	-84.00 8.00 1.555 1.555 1.555	1.555
PLAT710 ALERT 4 G	Delete 1-2-3 or 2-3-4 Linear Torsion Angle ... #	63 Do !
O1 -N11 -C25 -N7	160.00 8.00 1.555 1.555 1.555	1.555
PLAT710 ALERT 4 G	Delete 1-2-3 or 2-3-4 Linear Torsion Angle ... #	114 Do !
N10 -N12 -C56 -N14	-74.00 22.00 1.555 1.555 1.555	1.555
PLAT710 ALERT 4 G	Delete 1-2-3 or 2-3-4 Linear Torsion Angle ... #	115 Do !
N12 -N12 -C56 -N14	157.00 22.00 1.555 1.555 1.555	1.555
PLAT710 ALERT 4 G	Delete 1-2-3 or 2-3-4 Linear Torsion Angle ... #	116 Do !
N8 -N12 -C56 -N14	44.00 22.00 1.555 1.555 1.555	1.555
PLAT710 ALERT 4 G	Delete 1-2-3 or 2-3-4 Linear Torsion Angle ... #	117 Do !
O4 -N12 -C56 -N14	158.00 22.00 1.555 1.555 1.555	1.555
PLAT710 ALERT 4 G	Delete 1-2-3 or 2-3-4 Linear Torsion Angle ... #	118 Do !
O3 -N12 -C56 -N14	-22.00 22.00 1.555 1.555 1.555	1.555
PLAT710 ALERT 4 G	Delete 1-2-3 or 2-3-4 Linear Torsion Angle ... #	157 Do !
O2 -N11 -N3 -C9	-6.80 1.10 1.555 1.555 1.555	1.555
PLAT710 ALERT 4 G	Delete 1-2-3 or 2-3-4 Linear Torsion Angle ... #	162 Do !
O2 -N11 -N3 -N4	172.50 0.80 1.555 1.555 1.555	1.555
PLAT710 ALERT 4 G	Delete 1-2-3 or 2-3-4 Linear Torsion Angle ... #	207 Do !
N11 -C25 -N7 -C31	-161.00 8.00 1.555 1.555 1.555	1.555
PLAT710 ALERT 4 G	Delete 1-2-3 or 2-3-4 Linear Torsion Angle ... #	269 Do !
O3 -N12 -N12 -C48	9.80 1.00 1.555 1.555 1.555	1.555
PLAT710 ALERT 4 G	Delete 1-2-3 or 2-3-4 Linear Torsion Angle ... #	274 Do !
O3 -N12 -N12 -N13	-165.50 0.70 1.555 1.555 1.555	1.555
PLAT710 ALERT 4 G	Delete 1-2-3 or 2-3-4 Linear Torsion Angle ... #	290 Do !
N12 -C56 -N14 -C62	-153.00 21.00 1.555 1.555 1.555	1.555

0 ALERT level A = Most likely a serious problem - resolve or explain
3 ALERT level B = A potentially serious problem, consider carefully
13 ALERT level C = Check. Ensure it is not caused by an omission or oversight
23 ALERT level G = General information/check it is not something unexpected

1 ALERT type 1 CIF construction/syntax error, inconsistent or missing data
13 ALERT type 2 Indicator that the structure model may be wrong or deficient
2 ALERT type 3 Indicator that the structure quality may be low
22 ALERT type 4 Improvement, methodology, query or suggestion
1 ALERT type 5 Informative message, check

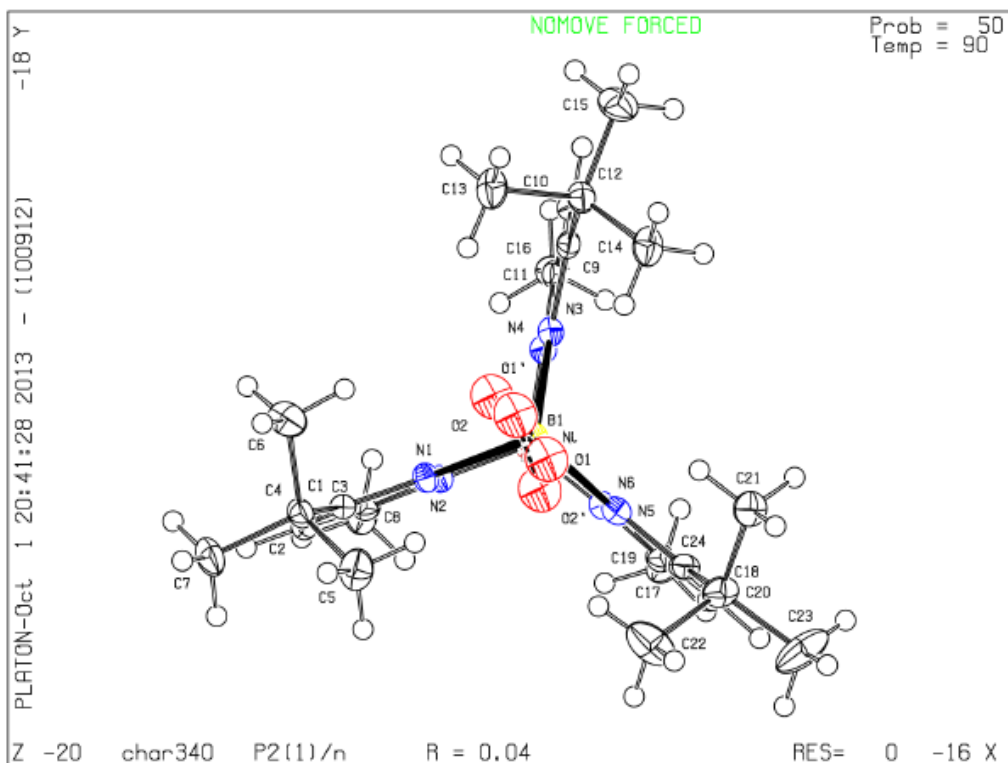


Alert level G

PLAT002	ALERT 2	G	Number of Distance or Angle Restraints on AtSite	5	Note
PLAT005	ALERT 5	G	No _iucr_refine_instructions_details in the CIF		Please Do !
PLAT232	ALERT 2	G	Hirshfeld Test Diff (M-X) Ni -- O1 ..	7.7	su
PLAT232	ALERT 2	G	Hirshfeld Test Diff (M-X) Ni -- O2 ..	8.5	su
PLAT232	ALERT 2	G	Hirshfeld Test Diff (M-X) Ni -- O1' ..	5.7	su
PLAT232	ALERT 2	G	Hirshfeld Test Diff (M-X) Ni -- O2' ..	13.0	su
PLAT301	ALERT 3	G	Main Residue Disorder	Percentage =	6 Note
PLAT860	ALERT 3	G	Number of Least-Squares Restraints		3 Note

0 **ALERT level A** = Most likely a serious problem - resolve or explain
 0 **ALERT level B** = A potentially serious problem, consider carefully
 0 **ALERT level C** = Check. Ensure it is not caused by an omission or oversight
 8 **ALERT level G** = General information/check it is not something unexpected

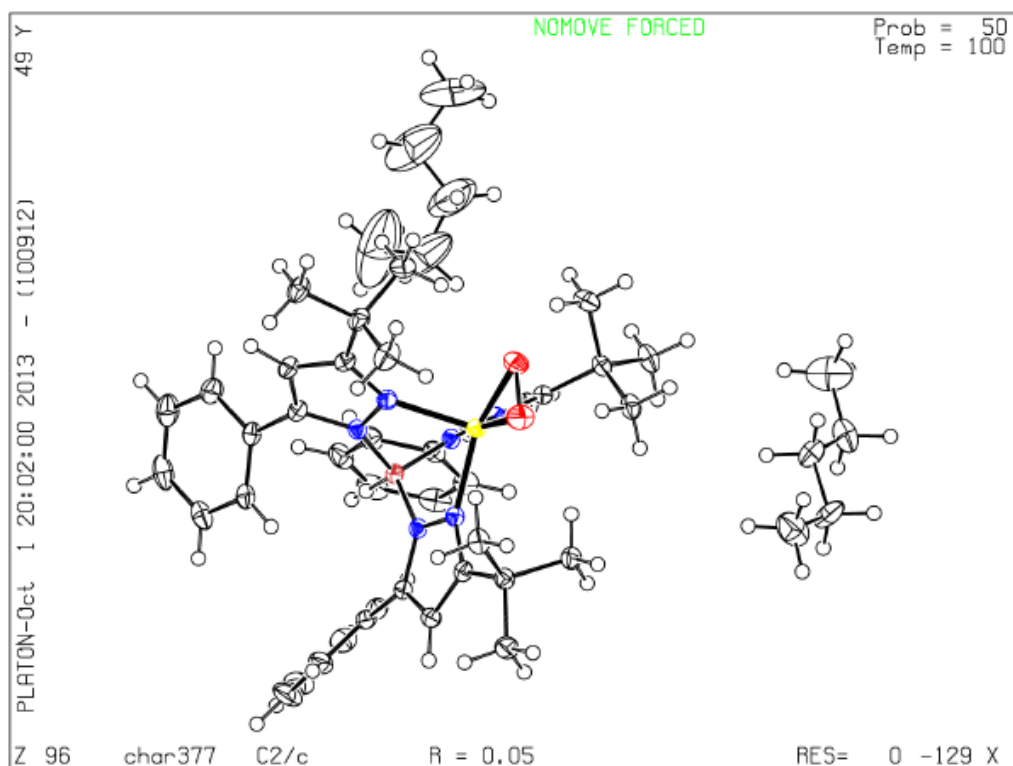
0 ALERT type 1 CIF construction/syntax error, inconsistent or missing data
 5 ALERT type 2 Indicator that the structure model may be wrong or deficient
 2 ALERT type 3 Indicator that the structure quality may be low
 0 ALERT type 4 Improvement, methodology, query or suggestion
 1 ALERT type 5 Informative message, check



Alert level G

PLAT002	ALERT 2 G	Number of Distance or Angle Restraints on AtSite	10	Note
PLAT003	ALERT 2 G	Number of Uiso or Uij Restrained non-H Atoms ...	10	
PLAT005	ALERT 5 G	No <code>_iucr_refine_instructions_details</code> in the CIF	Please Do !	
PLAT083	ALERT 2 G	SHELXL Second Parameter in WGHT Unusually Large.	9.38	
PLAT128	ALERT 4 G	Alternate Setting for Input Space-Group C2/c	I2/a	Note
PLAT152	ALERT 1 G	The Supplied and Calc. Volume s.u. Differ by ...	2	Units
PLAT302	ALERT 4 G	Anion/Solvent Disorder Percentage =	100	Note
PLAT790	ALERT 4 G	Centre of Gravity not Within Unit Cell: Resd. #	2	
		C5 H12		
PLAT860	ALERT 3 G	Number of Least-Squares Restraints	101	Note

-
- 0 **ALERT level A** = Most likely a serious problem - resolve or explain
 0 **ALERT level B** = A potentially serious problem, consider carefully
 0 **ALERT level C** = Check. Ensure it is not caused by an omission or oversight
 9 **ALERT level G** = General information/check it is not something unexpected
- 1 ALERT type 1 CIF construction/syntax error, inconsistent or missing data
 3 ALERT type 2 Indicator that the structure model may be wrong or deficient
 1 ALERT type 3 Indicator that the structure quality may be low
 3 ALERT type 4 Improvement, methodology, query or suggestion
 1 ALERT type 5 Informative message, check



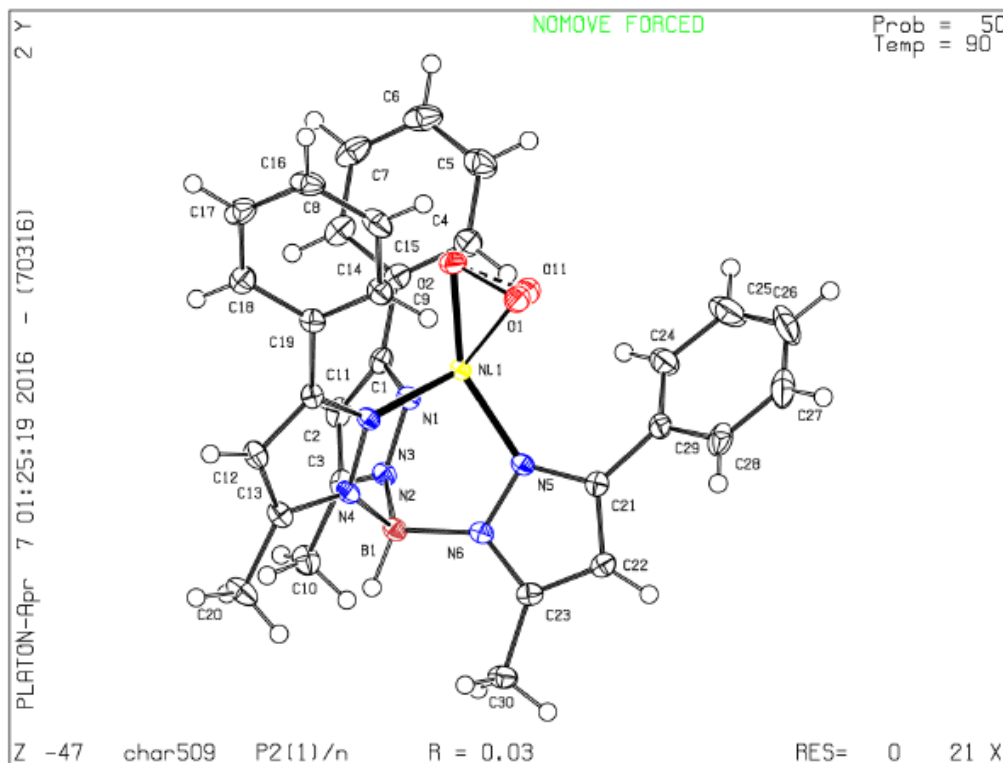
Alert level C

PLAT220 ALERT 2 C Non-Solvent Resd 1 C Ueq(max)/Ueq(min) Range 3.4 Ratio

Alert level G

PLAT002 ALERT 2 G	Number of Distance or Angle Restraints on AtSite	4	Note
PLAT003 ALERT 2 G	Number of Uiso or Uij Restrained non-H Atoms ...	3	Report
PLAT005 ALERT 5 G	No Embedded Refinement Details found in the CIF		Please Do !
PLAT063 ALERT 4 G	Crystal Size Likely too Large for Beam Size	0.75	mm
PLAT301 ALERT 3 G	Main Residue Disorder Percentage =	3	Note
PLAT779 ALERT 4 G	Suspect or Irrelevant (Bond) Angle in CIF #	24	Check
	O11 -O2 -O1 1.555 1.555 1.555	20.00	Deg.
PLAT860 ALERT 3 G	Number of Least-Squares Restraints	24	Note
PLAT899 ALERT 4 G	SHELXL97 is Deprecated and Succeeded by SHELXL	2014	Note

- 0 ALERT level A = Most likely a serious problem - resolve or explain
 0 ALERT level B = A potentially serious problem, consider carefully
 1 ALERT level C = Check. Ensure it is not caused by an omission or oversight
 8 ALERT level G = General information/check it is not something unexpected
- 0 ALERT type 1 CIF construction/syntax error, inconsistent or missing data
 3 ALERT type 2 Indicator that the structure model may be wrong or deficient
 2 ALERT type 3 Indicator that the structure quality may be low
 3 ALERT type 4 Improvement, methodology, query or suggestion
 1 ALERT type 5 Informative message, check



Alert level B

PLAT230 ALERT 2 B Hirshfeld Test Diff for C30 -- C31 .. 7.3 su

Author Response: These are atoms on the cyclohexyl ring and their identities as C-atoms are consistent with synthesis.

PLAT230 ALERT 2 B Hirshfeld Test Diff for C57 -- C62 .. 10.3 su

Author Response: These are atoms on the cyclohexyl ring and their identities as C-atoms are consistent with synthesis.

Alert level C

PLAT230 ALERT 2 C Hirshfeld Test Diff for C61 -- C62 .. 5.2 su

Author Response: These are atoms on the cyclohexyl ring and their identities as C-atoms are consistent with synthesis.

PLAT241 ALERT 2 C High Ueq as Compared to Neighbors for C57 Check
PLAT242 ALERT 2 C Low Ueq as Compared to Neighbors for C31 Check
PLAT242 ALERT 2 C Low Ueq as Compared to Neighbors for C62 Check
PLAT413 ALERT 2 C Short Inter XH3 .. XHN H24A .. H24A .. 2.12 Ang.

Alert level G

PLAT005 ALERT 5 G No _iucr_refine_instructions_details in the CIF Please Do !
PLAT230 ALERT 2 G Hirshfeld Test Diff for N7 -- C25 .. 7.7 su

Author Response: These are atoms on the cyclohexyl ring and their identities as C-atoms are consistent with synthesis.

PLAT230 ALERT 2 G Hirshfeld Test Diff for N14 -- C56 .. 8.0 su

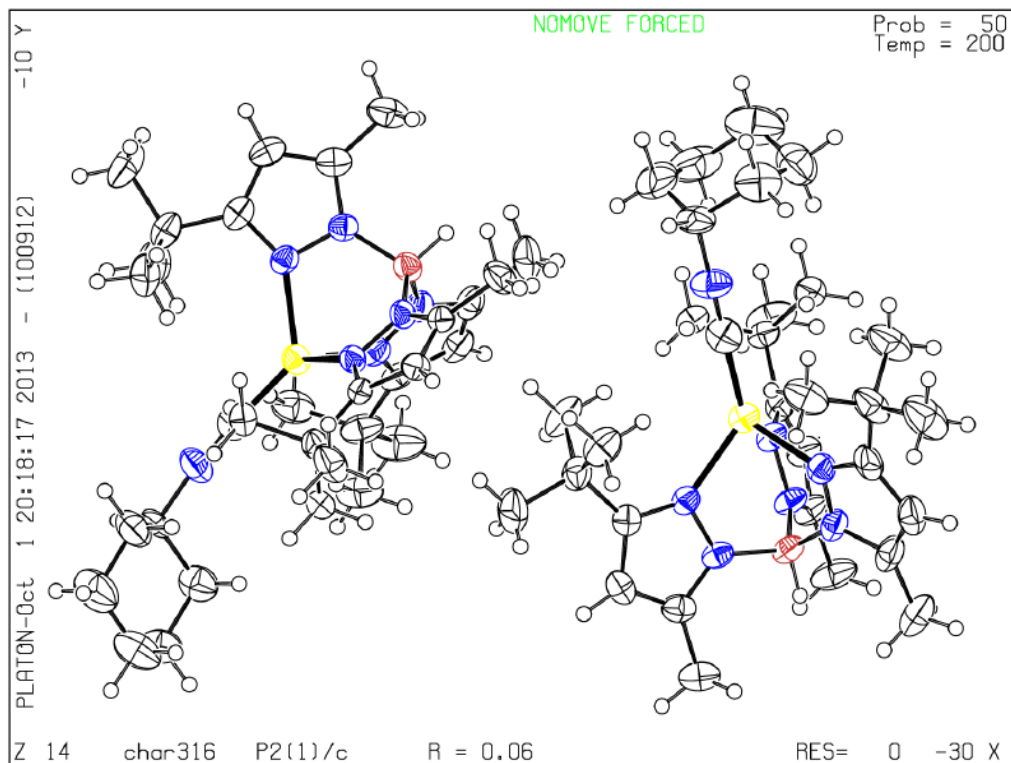
Author Response: These are atoms on the cyclohexyl ring and their identities as C-atoms are consistent with synthesis.

PLAT232 ALERT 2 G Hirshfeld Test Diff (M-X) N11 -- C25 .. 10.0 su
PLAT232 ALERT 2 G Hirshfeld Test Diff (M-X) N12 -- C56 .. 9.5 su
PLAT710 ALERT 4 G Delete 1-2-3 or 2-3-4 Linear Torsion Angle ... # 139 Do !
C31 -N7 -C25 -N11 -3.00 7.00 1.555 1.555 1.555 1.555
PLAT710 ALERT 4 G Delete 1-2-3 or 2-3-4 Linear Torsion Angle ... # 140 Do !
N3 -N11 -C25 -N7 -125.00 5.00 1.555 1.555 1.555 1.555
PLAT710 ALERT 4 G Delete 1-2-3 or 2-3-4 Linear Torsion Angle ... # 141 Do !
N5 -N11 -C25 -N7 -7.00 5.00 1.555 1.555 1.555 1.555
PLAT710 ALERT 4 G Delete 1-2-3 or 2-3-4 Linear Torsion Angle ... # 142 Do !
N1 -N11 -C25 -N7 109.00 5.00 1.555 1.555 1.555 1.555
PLAT710 ALERT 4 G Delete 1-2-3 or 2-3-4 Linear Torsion Angle ... # 207 Do !
C62 -N14 -C56 -N12 9.00 0.00 1.555 1.555 1.555 1.555
PLAT710 ALERT 4 G Delete 1-2-3 or 2-3-4 Linear Torsion Angle ... # 208 Do !
N10 -N12 -C56 -N14 6.00 0.00 1.555 1.555 1.555 1.555
PLAT710 ALERT 4 G Delete 1-2-3 or 2-3-4 Linear Torsion Angle ... # 209 Do !
N12 -N12 -C56 -N14 18.00 0.00 1.555 1.555 1.555 1.555

PLAT710 ALERT 4 G	Delete 1-2-3 or 2-3-4 Linear Torsion Angle ... #	210 Do !
N8 -N12 -C56 -N14	6.00 0.00 1.555 1.555 1.555 1.555	
PLAT710 ALERT 4 G	Delete 1-2-3 or 2-3-4 Linear Torsion Angle ... #	215 Do !
C56 -N14 -C62 -C57	14.00 0.00 1.555 1.555 1.555 1.555	
PLAT710 ALERT 4 G	Delete 1-2-3 or 2-3-4 Linear Torsion Angle ... #	216 Do !
C56 -N14 -C62 -C61	1.00 0.00 1.555 1.555 1.555 1.555	

0 ALERT level A = Most likely a serious problem - resolve or explain
 2 ALERT level B = A potentially serious problem, consider carefully
 5 ALERT level C = Check. Ensure it is not caused by an omission or oversight
 15 ALERT level G = General information/check it is not something unexpected

0 ALERT type 1 CIF construction/syntax error, inconsistent or missing data
 11 ALERT type 2 Indicator that the structure model may be wrong or deficient
 0 ALERT type 3 Indicator that the structure quality may be low
 10 ALERT type 4 Improvement, methodology, query or suggestion
 1 ALERT type 5 Informative message, check



Appendix B

PERMISSION FOR JOURNAL ARTICLE REPRINT



RightsLink®

Home

Account
Info

Help



Title: Cleavage of DNA by nickel complexes
Author: Janet R. Morrow, Kimberly A. Kolasa
Publication: Inorganica Chimica Acta
Publisher: Elsevier
Date: 15 May 1992
Copyright © 1992 Published by Elsevier B.V.

Logged in as:
William Green

LOGOUT

Order Completed

Thank you very much for your order.

This is a License Agreement between William L Green ("You") and Elsevier ("Elsevier"). The license consists of your order details, the terms and conditions provided by Elsevier, and the [payment terms and conditions](#).

[Get the printable license.](#)

License Number	3827310122990
License date	Mar 13, 2016
Licensed content publisher	Elsevier
Licensed content publication	Inorganica Chimica Acta
Licensed content title	Cleavage of DNA by nickel complexes
Licensed content author	Janet R. Morrow, Kimberly A. Kolasa
Licensed content date	15 May 1992
Licensed content volume number	195
Licensed content issue number	2
Number of pages	4
Type of Use	reuse in a thesis/dissertation
Portion	figures/tables/illustrations
Number of figures/tables/illustrations	1
Format	both print and electronic
Are you the author of this Elsevier article?	No
Will you be translating?	No
Original figure numbers	2
Title of your thesis/dissertation	Dioxygen Activation with Monovalent Nickel: Trispyrazolylborate Supported Ni(I) Complexes and Superoxide Derivatives
Expected completion date	May 2016
Estimated size (number of pages)	180
Elsevier VAT number	GB 494 6272 12
Permissions price	0,00 USD
VAT/Local Sales Tax	0,00 USD / 0,00 GBP
Total	0,00 USD



RightsLink®

Home

Create Account

Help



Title: Nickel-mediated sequence-specific oxidative cleavage of DNA by a designed metalloprotein
Author: David P. Mack, Peter B. Dervan
Publication: Journal of the American Chemical Society
Publisher: American Chemical Society
Date: May 1, 1990
Copyright © 1990, American Chemical Society

LOGIN

If you're a **copyright.com user**, you can login to RightsLink using your copyright.com credentials. Already a **RightsLink user** or want to [learn more?](#)

PERMISSION/LICENSE IS GRANTED FOR YOUR ORDER AT NO CHARGE

This type of permission/license, instead of the standard Terms & Conditions, is sent to you because no fee is being charged for your order. Please note the following:

- Permission is granted for your request in both print and electronic formats, and translations.
- If figures and/or tables were requested, they may be adapted or used in part.
- Please print this page for your records and send a copy of it to your publisher/graduate school.
- Appropriate credit for the requested material should be given as follows: "Reprinted (adapted) with permission from (COMPLETE REFERENCE CITATION). Copyright (YEAR) American Chemical Society." Insert appropriate information in place of the capitalized words.
- One-time permission is granted only for the use specified in your request. No additional uses are granted (such as derivative works or other editions). For any other uses, please submit a new request.

If credit is given to another source for the material you requested, permission must be obtained from that source.

BACK

CLOSE WINDOW

Copyright © 2016 [Copyright Clearance Center, Inc.](#) All Rights Reserved. [Privacy statement](#). [Terms and Conditions](#). Comments? We would like to hear from you, E-mail us at customer@copyright.com